

# **Engineering the tumour microenvironment *in vitro* using self-assembling peptide hydrogels**

A thesis submitted to The University of Manchester for the degree of

Doctor of Philosophy

in the Faculty of Science and Engineering

2021

Helen C Clough

Department of Materials

School of Natural Sciences

# Table of Contents

<b>List of Equations</b> .....	7
<b>List of Tables</b> .....	7
<b>List of Figures</b> .....	7
<b>List of Abbreviations</b> .....	11
<b>Abstract</b> .....	15
<b>Declaration</b> .....	16
<b>Copyright Statement</b> .....	16
<b>Acknowledgements</b> .....	17
<b>The Author</b> .....	19
<b>CHAPTER 1 – Introduction</b> .....	20
1.1. Overview .....	20
1.2. Hypothesis .....	22
1.3. Aims of the Project .....	22
1.4. Outline of Thesis .....	24
<b>CHAPTER 2 – Literature Review</b> .....	25
2.1. Tissue Engineering .....	25
2.1.1. Overview .....	25
2.1.2. Use in Disease Modelling .....	25
2.2. The Tumour Microenvironment .....	25
2.2.1. Overview .....	25
2.2.2. Extracellular Matrix .....	27
2.2.3. Immune Cells .....	29
2.2.4. Hypoxia and Vasculature .....	29
2.2.5. Epithelial to Mesenchymal Transition and Cancer Stem Cells .....	31
2.2.6. Importance in the Clinic and in Drug Development .....	33
2.3. Modelling Cancer .....	35
2.3.1. Overview .....	35
2.3.2. 2D <i>In Vitro</i> Models .....	35
2.3.3. Animal Models .....	36
2.3.4. 3D <i>In Vitro</i> Models .....	38
2.4. Hydrogels .....	43
2.4.1. Overview .....	43
2.4.2. Naturally Derived Hydrogels .....	43
2.4.3. Synthetic Hydrogels .....	45
2.5. Self-Assembling Peptide Hydrogels (SAPHs) .....	49
2.5.1. Overview .....	49

2.5.3. $\beta$ -Hairpin SAPHs .....	56
2.5.4. Short Peptide Derivatives.....	56
2.5.5. Peptide Amphiphiles .....	57
2.5.6. Ionic Complementary SAPHs .....	58
2.5.7. SAPHs for <i>In Vitro</i> Cancer Modelling.....	61
2.6. Modelling Vasculature Formation <i>In Vitro</i> .....	64
2.6.1. Overview .....	64
2.6.2. Co-Culture using HUVECs and MSCs .....	65
2.6.3. Designing Hydrogels for Vasculature <i>In Vitro</i> .....	65
2.6.4. SAPHs for Vasculature Formation <i>In Vitro</i> .....	67
2.7. Conclusions.....	70
<b>CHAPTER 3 – Materials and Methods</b> .....	<b>71</b>
3.1. Hydrogel Preparation .....	71
3.1.1. Self-Assembling Peptide Hydrogels .....	71
3.1.2. Collagen I.....	71
3.1.3. Matrigel.....	72
3.2. Attenuated Total Reflectance – Fourier Transform Infrared Spectroscopy .....	72
3.3. Oscillatory Shear Rheometry .....	72
3.4. Transmission Electron Microscopy .....	73
3.5. Doxorubicin Diffusion through PeptiGelAlpha1 .....	74
3.6. Cell Culture and Maintenance.....	75
3.7. Transduction of HUVECs and MSCs with Fluorescent Proteins .....	76
3.7.1. Fluorescence-Activated Cell Sorting .....	76
3.8. Cell Staining using Cell Membrane Linker Stains.....	76
3.9. 2D Cell Culture .....	77
3.9.1. SAPHs.....	77
3.9.2. Collagen I.....	77
3.9.3. TCP .....	78
3.9.4. Image Quantification.....	78
3.10. 3D Cell Culture .....	78
3.10.1. SAPHs.....	78
3.10.2. Collagen I.....	79
3.11. Cell Viability Assays .....	80
3.11.1. AlamarBlue .....	80
3.11.2. LIVE/DEAD .....	80
3.11.3. PicoGreen.....	80
3.12. Phalloidin Staining of F-actin Filaments .....	82
3.13. Histological Staining.....	82
3.13.1. Processing and Sectioning .....	82

3.13.2. Haematoxylin and Eosin Staining .....	83
3.13.3. Gomori Trichome Staining .....	83
3.13.4. Immunohistochemistry.....	84
3.14. MMP-2 ELISA Assay .....	86
3.15. Hypoxia Detection in Cells .....	87
3.16. Embedded Invasion Assay .....	88
3.17. Anti-Cancer Drug Efficacy .....	88
3.17.1. Dose-Response Curves .....	89
3.18. Matrigel Tube Formation Assay with Conditioned Media .....	90
3.19. $\alpha 5\beta 1$ Integrin Blocking .....	91
3.20. Statistical Analysis.....	91
3.21. Materials .....	92
<b>CHAPTER 4 – Characterisation of Biomaterials used for <i>In Vitro</i> Cancer Research</b>	<b>95</b>
4.1. Introduction.....	95
4.2. Results.....	97
4.2.1. Determining $\beta$ -sheet Structure of PeptiGelAlpha1, 2 and 4 .....	97
4.2.2. Mechanical Properties of PeptiGelAlpha1, 2 and 4 .....	98
4.2.3. Charge of PeptiGelAlpha1, 2 and 4 .....	99
4.2.4. Viability of MCF-7 cells in PeptiGelAlpha1 & PeptiGelAlpha2 .....	101
4.2.5. Choosing a SAPH Candidate .....	101
4.2.6. Fibre Formation of PeptiGelAlpha1, Collagen I and Matrigel .....	102
4.2.7. Viscoelastic Behaviour of PeptiGelAlpha1, Collagen I and Matrigel .....	104
4.2.8. Doxorubicin Penetration of PeptiGelAlpha1 .....	111
4.3. Discussion .....	114
4.3.1. Comparison of PeptiGelAlpha1, 2 and 4 .....	114
4.3.2. Fibre Formation of PeptiGelAlpha1, Collagen I and Matrigel .....	115
4.3.3. Viscoelastic Behaviour of PeptiGelAlpha1, Collagen I and Matrigel .....	117
4.3.4. Doxorubicin Penetration of PeptiGelAlpha1 .....	119
4.4. Conclusions.....	121
<b>CHAPTER 5 – Development of <i>In Vitro</i> Models of Breast Cancer using Self-Assembling Peptide Hydrogels</b>	<b>123</b>
5.1. Introduction.....	123
5.2. Results.....	125
5.2.1. Viability of MCF-7 & MDA-MB-231 Cells in PeptiGelAlpha1 .....	125
5.2.2. Proliferation of MCF-7 & MDA-MB-231 Cells in PeptiGelAlpha1 .....	127
5.2.3. Organisation of MCF-7 & MDA-MB-231 Cells in PeptiGelAlpha1 .....	130
5.2.4. Extracellular Matrix Deposition by MCF-7 and MDA-MB-231 Cells .....	137
5.2.5. Cell-Material Interactions .....	140
5.2.6. Hypoxia Development .....	143



5.2.7. Epithelial to Mesenchymal Transition .....	147
5.2.8. Invasive Potential of MCF-7 & MDA-MB-231 Cells in PeptiGelAlpha1.....	150
5.2.9. Cell Response to Anti-Cancer Drugs in PeptiGelAlpha1 .....	153
5.3. Discussion .....	164
5.3.1. Viability and Proliferation of MCF-7 & MDA-MB-231 Cells within PeptiGelAlpha1 .....	164
5.3.2. Organisation of MCF-7 & MDA-MB-231 Cells within PeptiGelAlpha1.....	166
5.3.3. Extracellular Matrix Deposition.....	167
5.3.4. Cell-Material Interactions .....	168
5.3.5. Hypoxia Development .....	170
5.3.6. Epithelial to Mesenchymal Transition .....	172
5.3.7. Invasive Potential of MCF-7 & MDA-MB-231 Cells in PeptiGelAlpha1.....	173
5.3.8. Cell Response to Anti-Cancer Drugs in PeptiGelAlpha1 .....	174
5.4. Conclusions.....	177
<b>CHAPTER 6 – Stimulating Vasculature Formation by HUVECs and MSCs within Self-Assembling Peptide Hydrogels.....</b>	<b>179</b>
6.1. Introduction.....	179
6.2. Results.....	181
6.2.1. Effect of Cancer Cell Conditioned Media on HUVEC Tube Formation .....	181
6.2.2. Effect of Laminin Enrichment and Hydrophobicity of SAPHs on HUVEC Behaviour .....	184
6.2.3. Effect of RGD Functionalisation on HUVEC and MSC Morphology.....	187
6.2.4. Effect of RGD Functionalisation on HUVEC and MSC Proliferation .....	194
6.2.5. Effect of RGD Functionalisation on HUVEC Phenotype.....	195
6.2.6. Effect of RGD and IKVAV Functionalisation on HUVEC and MSC Behaviour .....	196
6.2.7. Exploring HUVEC and MSC Interactions with RGD Functionalised PeptiGelAlpha1 via Integrin Binding .....	198
6.2.8. Effect of RGD Functionalisation on PeptiGelAlpha1 Material Properties .....	200
6.3. Discussion .....	204
6.3.1. Effect of Cancer Cell Conditioned Media on HUVEC Tube Formation .....	204
6.3.2. Influence of Laminin Enrichment of SAPHs on HUVEC Behaviour.....	205
6.3.3. Influence of SAPH Hydrophobicity on HUVEC Behaviour .....	205
6.3.4. Influence of Functionalisation of SAPHs on HUVEC and MSC Behaviour .....	206
6.3.5. RGD Functionalisation and Physico-Chemical Properties .....	209
6.4. Conclusions.....	212
<b>CHAPTER 7 – Overall Conclusions and Future Work .....</b>	<b>214</b>
7.1. Overall Conclusions.....	214
7.2. Future Work.....	219
<b>CHAPTER 8 – References .....</b>	<b>222</b>

<b>CHAPTER 9 – Appendix</b> .....	255
Appendix 1. Positive control for Gomori Trichome staining. ....	255
Appendix 2. Representative negative controls of MCF-7 and MDA-MB-231 cells encapsulated in PeptiGelAlpha1.....	256
Appendix 3. Acellular PeptiGelAlpha1 controls for immunohistochemistry staining. ....	257
Appendix 4. MCF-7 and MDA-MB-231 cell pellet controls for E-cadherin, N-cadherin, pan cytokeratin, vimentin and HIF1 $\alpha$ . ....	258
Appendix 5. Positive control images for immunohistochemistry. ....	259
Appendix 6. Contraction of collagen I by MCF-7 cells.....	260
Appendix 7. Dose-response curves without normalisation of Y values. ....	261
Appendix 8. Steps for sorting GFP-MSCs and RFP-HUVECs using fluorescence activated cell sorting (FACS).....	262
Appendix 9. Tri-lineage differentiation of MSCs and GFP-MSCs.....	263
Appendix 10. RFP-HUVECs cultured on top of Matrigel in the presence of DMEM. ....	264
Appendix 11. LIVE/DEAD staining of HUVECs seeded on TCP $\pm$ 5, 25 and 50 $\mu$ g/mL laminin over 7 days. ....	265
Appendix 12. Metabolic activity of HUVECs seeded on laminin-coated TCP over 7 days.....	266
Appendix 13. Contraction of collagen I by HUVECs and MSCs.....	267

Word count: 59,335

## List of Equations

Equation 3.1. Modulus of rigidity. ....	73
Equation 3.2. 4-parameter logistical model used to calculate IC <sub>50</sub> values. ....	90
Equation 4.1. Calculation of theoretical charge using pH and pKa values of amino acids. ....	99

## List of Tables

Table 2.1. The ability of 2D <i>in vitro</i> , 3D <i>in vitro</i> and animal models to mimic ideal characteristics in cancer modelling. ....	39
Table 2.2. Summary of strategies used to mimic cancer <i>in vitro</i> using hydrogels. ....	47
Table 2.3. Naturally occurring L-amino acids and their properties. ....	50
Table 2.4. Summary of strategies used to mimic cancer <i>in vitro</i> using SAPHs. ....	63
Table 2.5. Summary of strategies used to create vasculature <i>in vitro</i> using SAPHs. ....	69
Table 3.2. Materials and reagents used in experimental sections. ....	92
Table 4.1. Summary of charge and storage moduli at 1 Hz of PeptiGelAlpha1, 2 and 4. ....	100
Table 4.2. Summary of mean fibre diameters and storage moduli at 1 Hz of PeptiGelAlpha1, collagen I and Matrigel. ....	111
Table 5.1. IC <sub>50</sub> values for MCF-7 and MDA-MB-231 cells cultured in 2D and 3D in PeptiGelAlpha1. ....	163
Table 6.1. Summary of mean fibre diameters and storage moduli at 1 Hz of PeptiGelAlpha1 ± 1 %, 10 %, 40 % RGD. ....	203

## List of Figures

Figure 2.1. Original and emerging hallmarks of cancer. ....	26
Figure 2.2. Schematic of the TME. ....	27
Figure 2.3. Mechanism of events underpinning vascularisation of solid tumours <i>in vivo</i> . ....	30
Figure 2.4. Epithelial to mesenchymal transition of cancer cells. ....	32
Figure 2.5. Physical and chemical barriers preventing anti-cancer drug penetration of solid tumours. ....	34
Figure 2.6. Mechanical, structural and morphological differences in 2D and 3D cell culture. ....	40
Figure 2.7. Schematic of structure of amino acids. ....	49
Figure 2.8. Schematic of self-assembly process of SAPHs. ....	54
Figure 2.9. Schematic of $\alpha$ -helix coiled coil assembly. ....	55
Figure 2.10. Self-assembly process and amino acid sequence of MAX1 hydrogel. ....	56
Figure 2.11. Chemical structure of peptide amphiphile hydrogel. ....	58
Figure 2.12. Moduli of ionic complementary SAPHs. ....	59
Figure 2.13. <i>In vitro</i> tube formation by ECs and pericytes within a hydrogel. ....	64
Figure 3.1. Lambda dsDNA standard curve for PicoGreen analysis. ....	81
Figure 3.2. MMP-2 ELISA standard curve. ....	87
Figure 4.1. ATR-FTIR spectra of PeptiGelAlpha1, 2 and 4. ....	97

Figure 4.2. Mechanical properties of PeptiGelAlpha1, 2 and 4.....	98
Figure 4.3. Theoretical net charge of PeptiGelAlpha1, 2 and 4 vs pH. ....	99
Figure 4.4. LIVE/DEAD staining of MCF-7 cells in 2D and 3D culture in PeptiGelAlpha1 and 2 after 7 days. ....	101
Figure 4.5. TEM images of Matrigel, collagen I and PeptiGelAlpha1.....	102
Figure 4.6. Frequency distribution of fibre diameters. ....	103
Figure 4.7. Mean fibre diameters of PeptiGelAlpha1, collagen I and Matrigel.....	103
Figure 4.8. Amplitude sweeps of collagen I (1.5 mg/mL). ....	104
Figure 4.9. Amplitude sweeps of Matrigel (5 mg/mL). ....	105
Figure 4.10. Amplitude sweeps of PeptiGelAlpha1. ....	105
Figure 4.11. Frequency sweeps of (A) collagen I (1.5 mg/mL), (B) Matrigel (5 mg/mL) and (C) PeptiGelAlpha1 in the absence and presence of 18 hours media conditioning. ....	107
Figure 4.12. Recovery profile of collagen I (1.5 mg/mL). ....	108
Figure 4.13. Recovery profile of Matrigel (5 mg/mL). ....	109
Figure 4.14. Recovery profile of PeptiGelAlpha1. ....	109
Figure 4.15. The effect of media conditioning on the stiffness of PeptiGelAlpha1, collagen I (1.5 mg/mL) and Matrigel (5 mg/mL). ....	110
Figure 4.16. Fluorescence images of doxorubicin penetration into PeptiGelAlpha1 and TCP. ....	111
Figure 4.17. Fluorescence quantification of doxorubicin penetration into PeptiGelAlpha1 and TCP.....	112
Figure 4.18. Distribution of 100 $\mu$ M doxorubicin through PeptiGelAlpha1. ....	113
Figure 5.1. LIVE/DEAD staining of MCF-7 and MDA-MB-231 cells in PeptiGelAlpha1 or collagen I over 7 days. ....	126
Figure 5.2. Standard curve of PicoGreen analysis of MCF-7 cells encapsulated in PeptiGelAlpha1 and dPBS. ....	127
Figure 5.3. PicoGreen analysis of MCF-7 and MDA-MB-231 cells encapsulated within PeptiGelAlpha1 over 14 days.....	128
Figure 5.4. Ki67 immunohistochemical staining of MCF-7 and MDA-MB-231 cells in PeptiGelAlpha1 over 14 days.....	129
Figure 5.5. H&E staining of MCF-7 and MDA-MB-231 cells encapsulated in PeptiGelAlpha1 or collagen I over 14 days. ....	131
Figure 5.6. Higher magnification imaging of H&E stained MCF-7 and MDA-MB-231 cell-laden PeptiGelAlpha1 or collagen I sections over 14 days.....	132
Figure 5.7. Quantification of H&E staining of MCF-7 cells encapsulated in PeptiGelAlpha1 or collagen I over 14 days. ....	134
Figure 5.8. F-actin filament staining of MCF-7 and MDA-MB-231 cells encapsulated in PeptiGelAlpha1 or collagen I over 14 days. ....	136
Figure 5.9. Gomori Trichome staining of MCF-7 and MDA-MB-231 cells in PeptiGelAlpha1 over 14 days.....	138
Figure 5.10. Collagen I immunostaining of MCF-7 and MDA-MB-231 cells in PeptiGelAlpha1 over 14 days.....	139
Figure 5.11. TEM images of MCF-7 and MDA-MB-231 cells in PeptiGelAlpha1 or collagen I after 14 days. ....	140
Figure 5.12. TEM images of MCF-7 cells in PeptiGelAlpha1 after 14 days.....	141

Figure 5.13. Mechanical properties of acellular PeptiGelAlpha1 and MCF-7 and MDA-MB-231 cell-laden PeptiGelAlpha1 over 14 days in culture. ....	142
Figure 5.14. MMP-2 production by MCF-7 cells cultured in PeptiGelAlpha1 over 14 days. ....	143
Figure 5.15. Optimisation of the Image-iT Red Hypoxia staining procedure using chemically induced hypoxia and physiologically induced hypoxia (< 5 % (v/v) O <sub>2</sub> ). ....	144
Figure 5.16. Hypoxia detection and staining of MCF-7 and MDA-MB-231 cells in PeptiGelAlpha1 over 14 days. ....	145
Figure 5.17. Immunohistochemical staining of HIF1 $\alpha$ in MCF-7 and MDA-MB-231 cells in PeptiGelAlpha1 over 14 days. ....	146
Figure 5.18. Immunohistochemical staining of EMT markers in MCF-7 cells cultured in PeptiGelAlpha1 over 14 days. ....	148
Figure 5.19. Immunohistochemical staining of EMT markers in MDA-MB-231 cells cultured in PeptiGelAlpha1 over 14 days. ....	149
Figure 5.20. Schematic of steps used for the embedded invasion assay. ....	150
Figure 5.21. Invasion of MCF-7 and MDA-MB-231 cells from PeptiGelAlpha1 into collagen I or Matrigel over 21 days. ....	151
Figure 5.22. Number of invading MCF-7 and MDA-MB-231 cells from PeptiGelAlpha1 into collagen I or Matrigel over 21 days. ....	152
Figure 5.23. Efficacy of anti-cancer drugs tamoxifen and doxorubicin on MCF-7 and MDA-MB-231 cells. ....	155
Figure 5.24. Percentage viability of MCF-7 and MDA-MB-231 cells exposed to tamoxifen and doxorubicin treatment comparing 2D monolayer and 3D PeptiGelAlpha1 culture. ....	157
Figure 5.25. Fluorescence imaging of MCF-7 cells exposed to tamoxifen and doxorubicin treatment after 24 and 48 hours. ....	159
Figure 5.26. Fluorescence imaging of MDA-MB-231 cells exposed to tamoxifen and doxorubicin treatment after 24 and 48 hours. ....	160
Figure 5.27. Dose-response curves for MCF-7 and MDA-MB-231 cells in 2D and 3D in PeptiGelAlpha1. ....	162
Figure 5.28. IC <sub>50</sub> values for MCF-7 and MDA-MB-231 cells cultured in 2D and 3D in PeptiGelAlpha1. ....	163
Figure 6.1. Tube formation of HUVECs on Matrigel using conditioned media from MCF-7 cells. ....	182
Figure 6.2. Quantification of tube formation of HUVECs on Matrigel using conditioned media from MCF-7 cells. ....	183
Figure 6.3. Effect of ECM protein laminin and hydrophobicity of primary amino acid sequence on tube formation of HUVECs. ....	185
Figure 6.4. Percentage area quantification of RFP-HUVECs cultured on different substrates. ....	186
Figure 6.5. Effect of cell-binding motif RGD on HUVEC and MSC behaviour. ....	188
Figure 6.6. Effect of cell-binding motif RGD and cell density on HUVEC and MSC behaviour. ....	189
Figure 6.7. Circularity quantification of (A) HUVECs and (B) MSCs in response to RGD concentration of PeptiGelAlpha1 and cell-seeding density after 7 days. ....	190
Figure 6.8. Effect of RGD concentration and cancer cells on HUVEC and MSC behaviour. ....	192

Figure 6.9. Tri-culture of MCF-7 cancer cells, HUVECs and MSCs in collagen I + 90 $\mu\text{g/mL}$ fibronectin. ....	193
Figure 6.10. PicoGreen analysis of HUVECs and MSCs encapsulated in PeptiGelAlpha1 $\pm$ 1 %, 10 % and 40 % RGD after 4 and 7 days in culture. ....	194
Figure 6.11. CD31 immunostaining of HUVECs encapsulated in PeptiGelAlpha1 $\pm$ 1 %, 10 %, 40 % RGD after 4 days. ....	195
Figure 6.12. Effect of cell-binding motifs RGD and IKVAV on HUVEC and MSC behaviour. ....	197
Figure 6.13. $\alpha 5\beta 1$ integrin blocking in HUVECs and MSCs. ....	199
Figure 6.14. AT-FTIR spectra of PeptiGelAlpha1 $\pm$ 1 %, 10 % and 40 % RGD. ....	200
Figure 6.15. Mechanical properties of PeptiGelAlpha1 $\pm$ 1 %, 10 % and 40 % RGD with 18 hours media incubation. ....	201
Figure 6.16. TEM images of PeptiGelAlpha1 $\pm$ 1 %, 10 % and 40 % RGD. ....	202
Figure 6.17. Fibre diameters of PeptiGelAlpha1 $\pm$ 1 %, 10 % and 40 % RGD. ....	203

## List of Abbreviations

µg	Microgram
µL	Microlitre
µM	Micromole
2D	Two-dimensional
3D	Three-dimensional
5-FU	5-fluorouracil
A, Ala	Alanine
AFM	Atomic force microscopy
AFM-IR	Atomic force microscopy-infrared spectroscopy
ASC	Adipose derived stem cell
ATP	Adenosine triphosphate
ATR-FTIR	Attenuated total reflectance – Fourier transform infrared spectroscopy
BM-MSC	Bone marrow derived mesenchymal stem cell
BQ13	QQKFQFQFEQEQQ
BSA	Bovine serum albumin
C, Cys	Cysteine
CAC	Critical aggregation concentration
Calcein-AM	Calcein acetoxymethyl
CAF	Cancer-associated fibroblast
CD	Circular dichroism
CD31	Cluster of differentiation 31
CDX	Cell line-derived xenograft
CGC	Critical gelation concentration
CO <sub>2</sub>	Carbon dioxide
CoCl <sub>2</sub>	Cobalt chloride hexahydrate
CSC	Cancer stem cell
CXCL5	C-X-C motif chemokine ligand 5
CXCL12	Stromal cell-derived factor 1
dsDNA	Double stranded DNA
dPBS	Dulbecco's phosphate buffered saline
D, Asp	Aspartate
DAPI	4',6-diamidino-2-phenylindole
DMEM	Dulbecco's modified eagle medium
DMSO	Dimethyl sulfoxide
DNA	Deoxyribonucleic acid
E, Glu	Glutamic acid
EAK16-I	AEAKAEAKAEAKAEAK
EAK16-II	AEAEAKAKAEAEAKAK
EAK16-IV	AEAEAEAEAKAKAKAKAK
EC	Endothelial cell
ECGM-2	Endothelial cell growth medium 2
ECM	Extracellular matrix
EFK8	KFEFKFEF

EGF	Epidermal growth factor
ELISA	Enzyme-linked immunoabsorbant assay
EMT	Epithelial to mesenchymal transition
ER	Oestrogen receptor
F, Phe	Phenylalanine
FACS	Fluorescence activated cell sorting
FBS	Foetal bovine serum
FF	Diphenylalanine
FGF	Fibroblast growth factor
Fmoc	Fluorenylmethoxycarbonyl
Fmoc-FF	Fluorenylmethoxycarbonyl-diphenylalanine
G, Gly	Glycine
$G$	Shear modulus
$G'$	Storage modulus
$G''$	Loss modulus
GAG	Glycosaminoglycan
GelMA	Gelatin methacrylate
GEMM	Genetically engineered mouse model
GFP	Green fluorescent protein
H, His	Histidine
H9e	FLVIGSIIGPGGDGPGGD
H&E	Haematoxylin and eosin
HAEC	Human aortic endothelial cell
HECFC	Human endothelial colony forming cell
HEPES	4-(2-hydroxyethyl)-1-piperazineethanesulfonic acid
HER2	Human epidermal growth factor receptor-2
HIF1 $\alpha$	Hypoxia inducible factor 1 $\alpha$
HMEC-1	Human microvascular endothelial cell-1
HPLC	High performance liquid chromatography
HRP	Horseradish peroxidase
HUVEC	Human umbilical vein endothelial cell
I, Ile	Isoleucine
IC <sub>50</sub>	Concentration of drug needed to inhibit cell viability by 50%
IGF	Insulin-like growth factor
IKVAV	Ile-Lys-Val-Ala-Val
IL	Interleukin
IR	Infrared spectroscopy
K, Lys	Lysine
KFE-8	FKFEFKFE
KLD-12	KLDLKLDLKLDL
L, Leu	Leucine
LDH	Lactate dehydrogenase
LOX	Lysyl oxidase
LVR	Linear viscoelastic region
M, Met	Methionine
MDR1	Multi-drug resistance protein 1



MDSC	Myeloid derived suppressor cell
MET	Mesenchymal to epithelial transition
MMP	Matrix metalloproteinase
MSC	Mesenchymal stem cell
N, Asn	Asparagine
N#	Number of experimental repeats
NaCl	Sodium chloride
NaOH	Sodium hydroxide
NK	Natural killer cell
NSCLC	Non-small cell lung carcinoma
P, Pro	Proline
P#	Cell passage number
Pa	Pascal
PA	Peptide amphiphile
PA-H	VVVAAAH <sub>2</sub> K
PDGF	Platelet derived growth factor
PDX	Patient derived-xenograft
PEG	Poly(ethylene glycol)
PR	Progesterone receptor
Q, Gln	Glutamine
Q11	QQKFQFQFEQQ
R, Arg	Arginine
RADA16	RADARADARADARADA
RCCS	Rotary cell culture system
RFP	Red fluorescent protein
RGD	Arg-Gly-Asp
RNA	Ribonucleic acid
RT-PCR	Reverse transcription-polymerase chain reaction
RYVVLPR	Arg-Tyr-Val-Val-Leu-Pro-Arg
S, Ser	Serine
S.D	Standard deviation
S.E.M	Standard error of mean
SAPH	Self-assembling peptide hydrogel
SEM	Scanning electron microscopy
T, Thr	Threonine
TAGSCLRKFSTM	Thr-Ala-Gly-Ser-Cys-Leu-Arg-Lys-Phe-Ser-Thr-Met
TAM	Tumour associated macrophage
TAN	Tumour associated neutrophil
TAZ	Transcriptional co-activator with PDZ-binding motif
TCP	Tissue culture plastic
TEM	Transmission electron microscopy
TGFβ	Transforming growth factor β
TIMP	Tissue inhibitor of metalloproteinase
TME	Tumour microenvironment
TNBC	Triple negative breast cancer
TWIST1	Twist-related protein 1

UA	Uranyl acetate
V	Poisson's ratio
V, Val	Valine
V8	VEVKVEVK
VEGF	Vascular endothelial growth factor
VEGFR	Vascular endothelial growth factor receptor
W, Trp	Tryptophan
Y, Tyr	Tyrosine
YAP	Yes-associated protein
YIGSR	Tyrosine-isoleucine-glycine-serine-arginine
ZEB1	Zinc finger E-box-binding homeobox 1
ZO-1	Zona occludens 1

## Abstract

Solid tumours comprise of a variety of cell types and components, collectively known as the tumour microenvironment (TME). The TME includes: vasculature, immune cells, extracellular matrix (ECM), hypoxia and lymphatic vessels. The TME is dynamic and complex, but essential for tumours to grow, metastasise and withstand anti-cancer drugs. To create effective anti-cancer drugs that target the TME, representative models are needed. Traditional two-dimensional (2D) *in vitro* models lack translatability to *in vivo*, due to the absence of a three-dimensional (3D) environment and physical components such as the ECM. The ECM is a 3D network of proteins and macromolecules and provides structural and biochemical support for cells. The development and use of 3D *in vitro* models can augment and expand the quality of data collected in *in vitro* studies, by culturing cells within a 3D environment that mimic the physical and chemical barriers observed within the TME. Hydrogels, 3D networks of hydrophilic chains that can retain large quantities of water, are popular biomaterials used for disease modelling purposes, due to their biocompatibility and ability to mimic the 3D environment. However, naturally derived hydrogels are limited by their batch-to-batch variability, rendering them inappropriate for pharmaceutical use. A class of synthetic hydrogels, self-assembling peptide hydrogels (SAPHs), are gaining popularity in tissue engineering applications due to their chemical definition, biocompatibility and tuneable properties. A SAPH system has not been used previously for modelling breast cancer and vasculature; this would allow more representative *in vitro* modelling of the TME using a synthetic platform. This thesis aims to explore the use of a commercially available SAPH for modelling breast cancer and vasculature *in vitro*, thereby better recapitulating the TME in addition to using a synthetic hydrogel system. Features of the TME studied were: hypoxia, epithelial to mesenchymal transition (EMT), cell invasion, anti-cancer drug resistance and vasculature formation. The breast cancer cell lines MCF-7 and MDA-MB-231, representing early-stage and metastatic breast cancer respectively were studied, in parallel to using human umbilical vein endothelial cells (HUVECs) and mesenchymal stem cells (MSCs), to create tubes resembling vasculature. Compared with collagen I and Matrigel, the SAPH PeptiGelAlpha1 exhibited superior mechanical properties and was formed from uniformly sized nanofibres. MCF-7 and MDA-MB-231 cells were viable and proliferated within PeptiGelAlpha1 over a 14-day period. MCF-7 cells formed spheroids within SAPH, similar to that of collagen I, whilst MDA-MB-231 cells tended to remain dispersed. PeptiGelAlpha1 appeared to be more appropriate for *in vitro* modelling of early breast cancer, such as with MCF-7 cells, as shown by ECM deposition, their highly invasive potential, and evidence of remodelling the peptide matrix, which were not observed with MDA-MB-231 cells. Preliminary data showed that encapsulation in PeptiGelAlpha1 resulted in a greater percentage of viable cells when treated with tamoxifen, compared with 2D culture. HUVECs and MSCs were not able to form tube-like structures within the hydrogel, although RGD functionalisation did positively influence cell morphology and proliferation. This benefit was concentration-dependent. The work in this thesis shows that a commercially available SAPH has potential to be a suitable candidate for *in vitro* modelling of breast cancer, and has important implications for studying tumour biology and tissue engineering vasculature *in vitro*.

## **Declaration**

I declare that what portion of the work referred to in the thesis has been submitted in support of an application for another degree or qualification of this or any other university or other institute of learning.

## **Copyright Statement**

- i. The author of this thesis (including any appendices and/or schedules to this thesis) owns certain copyright or related rights in it (the “Copyright”) and s/he has given The University of Manchester certain rights to use such Copyright, including for administrative purposes.
- ii. Copies of this thesis, either in full or in extracts and whether in hard or electronic copy, may be made only in accordance with the Copyright, Designs and Patents Act 1988 (as amended) and regulations issued under it or, where appropriate, in accordance with licensing agreements which the University has from time to time. This page must form part of any such copies made.
- iii. The ownership of certain Copyright, patents, designs, trademarks and other intellectual property (the “Intellectual Property”) and any reproductions of copyright works in the thesis, for example graphs and tables (“Reproductions”), which may be described in this thesis, may not be owned by the author and may be owned by third parties. Such Intellectual Property and Reproductions cannot and must not be made available for use without the prior written permission of the owner(s) of the relevant Intellectual Property and/or Reproductions.
- iv. Further information on the conditions under which disclosure, publication and commercialisation of this thesis, the Copyright and any Intellectual Property and/or Reproductions described in it may take place is available in the University IP Policy (see <http://documents.manchester.ac.uk/DocuInfo.aspx?DocID=24420>), in any relevant Thesis restriction declarations deposited in the University Library, The University Library’s regulations (see <http://www.library.manchester.ac.uk/about/regulations/>) and in The University’s policy on Presentation of Theses.

## **Acknowledgements**

Firstly, I would like to thank Dr Olga Tsigkou, Prof Alberto Saiani and Prof Aline Miller for conception of this project and providing me with supervision, financial assistance, direction and mentorship. Thank you for allowing me to disseminate my work at numerous international conferences and giving me the freedom and flexibility to tune my project accordingly.

This project would not have been possible without financial support from the EPSRC and MRC funded CDT in Regenerative Medicine (EP/L014904/1). This programme has been invaluable for providing me with additional opportunities and pastoral support. I also thank the Sir Henry Royce Institute for funding several pieces of equipment, which were vital for my work (EP/R00661X/1, EP/S019367/1, EP/P025021/1 and EP/P025498/1).

A number of people have provided their time for technical support. I am grateful to Dr Aleksandr Mironov and Mrs Samantha Forbes from the FBMH EM Facility for all of their help with TEM sample processing and image collection. Thank you to Mrs Pauline Baird and Dr Stephen Richardson for allowing me to use the hypoxia chamber in their lab for optimising the hypoxia assay. A huge thank you goes to Mrs Marie O'Brien for all of her histology wisdom and technical support, and to Dr Louise Carney for general cell culture advice and help with experimental disasters. Thank you also for setting up the Royce lab for us in the middle of a pandemic. My thanks also goes to Dr Kate Maksimcuka for all of her help with the HUVECs and MSCs work, as well as being a great friend and office buddy. Thank you also to my other office mate Dr Ian Wimpenny, for thoughtful discussions about my research and project and pointing me in the right direction to people who were able to help me further.

The CDT has also provided me with a cohort of colleagues and friends, thank you to you all for your continuous support over the last 4.5 years. A shout out goes to Drs to be Paul Humphreys and Geoffrey Potjewyd, our Kyotoya trips were much needed to decompress and vent about the trials and tribulations of our projects. To members of the Polymers and Peptides and Biomaterials research groups, past and present, thank you all for experimental and moral support and helping me out and providing invaluable advice when needed. A particular thank you goes to Dr Xinyi Zhu for all of her help with TEM data collection. Thank you also to Dr Victoria Workman, Dr Kyle Burgess and Dr to be Cosimo Ligorio for all of your advice and help with using the hydrogels. I have gained many cherished friends from these groups, who have been there for me both inside and outside of the lab,

thank you to you all for your friendship and kindness. Thank you especially to Dr Biranche Tandon, Dr William Ambler and Dr Annchalee Eade for proofreading my thesis.

To Oli, thank you so much for looking after me and putting up with me whilst I was finishing my PhD and stressing out about my project and writing up, especially during the first lockdown period when we were thrown into the unknown. I will forever be grateful for your unconditional love, patience and support and always being there for me. I will try to be the best that I can be in return.

Last but not least, thank you to my parents, sister and grandpa for always being my cheerleaders, celebrating my smallest victories and forever supporting me throughout my academic endeavours. Thank you for believing in me and I hope I have made you proud!

## The Author

Prior to my PhD, I received my Bachelor of Science and Master of Biology (MBiol) integrated Master's degree in Medical Sciences from the University of Leeds in 2016.

In September 2016, I joined the CDT in Regenerative Medicine PhD programme and started my PhD project in April 2017.

I have presented the work in this thesis at the following conferences:

- **11<sup>th</sup> World Biomaterials Congress**, held virtually. 11<sup>th</sup> – 15<sup>th</sup> December 2020. Oral presentation.
- **RSC Biomaterials Chemistry Group Meeting**, Manchester, UK. 8<sup>th</sup> – 10<sup>th</sup> January 2020. Oral presentation.
- **TERMIS-EU Chapter Meeting**, Rhodes, Greece. 27<sup>th</sup> – 31<sup>st</sup> May 2019. Oral presentation.

I have been awarded several travel grants to aid attendance and presentation at the above conferences:

- **Armourers & Brasiers Travel Grant:** £500 awarded in March 2020 to attend World Biomaterials Congress (2020) conference.
- **Tissue and Cell Engineering Society (TCES) Travel Bursary:** £300 awarded to attend TERMIS EU Chapter Meeting (2019) in April 2019.
- **RSC Biomaterials Chemistry Group Travel Grant:** £300 awarded to attend TERMIS EU Chapter Meeting (2019) in April 2019.

My flash presentation at the RSC Biomaterials Translation Workshop (2019) was awarded Best Oral Presentation.

The work outlined in Chapters 4 and 5 has been compiled into a manuscript entitled: *“Neutrally Charged Self-Assembling Peptide Hydrogel Recapitulates In Vitro Mechanisms of Breast Cancer Progression.”* It is currently under review.

During my PhD, I have been proactive with public engagement and outreach activities, particularly Women in STEM events.

Outside of the lab, I have written several blog posts about fighting climate change in the lab as well as making the most of your research grants, which can be found below:

[Fighting climate change... in the lab – Research Hive \(wordpress.com\)](#)

[Make the most of your research grants - Tipbox \(abcam.com\)](#)

# CHAPTER 1 – Introduction

## 1.1. Overview

Cancer is currently the leading cause of mortality worldwide, which is increasing in prevalence, with breast cancer accounting for 1 in 4 diagnosed cancer cases among women in 2018 [1]. Incidence and mortality are increasing worldwide due to population growth as well as a growing ageing population, resulting in an increased diagnosis rate. Survival depends upon the tumour location, stage of disease and therapy available [2]. Metastatic breast cancer has a 5-year survival rate of 25 %, whilst at the localised stage this improves to 99 % [3,4].

Solid cancers or tumours are complex and heterogeneous. They comprise of a variety of components, including: non-cancerous cells, extracellular matrix (ECM), vasculature and lymphatic vessels. These components form the tumour microenvironment (TME), or the stromal component of tumours [5]. Tumour growth and eventual metastasis, if advanced, relies on the interplay between these different components. From a drug development perspective, the TME provides physical and chemical barriers that prevent drug penetration and result in minimal efficacy. Physical barriers include the highly linearised ECM and interstitial fluid pressure, whilst chemical barriers include acidic pH [6]. On the other hand, the TME also provides drug targets; each individual component can be attacked and thus disturbing the dynamic environment. This would hinder tumour growth and halt disease progression.

To understand the mechanisms behind disease progression and find efficacious treatment options, disease models are needed. Disease models, both *in vitro* and *in vivo*, are essential in the initial stages of drug development as they provide preliminary data collected regarding the efficacy and safety profile of the drug candidate. Traditionally, two-dimensional (2D) *in vitro* models and animal models are used to test novel drugs [7]. 2D *in vitro* models are characterised by a monolayer of cells growing on a plastic substrate. Whereby with *in vivo* models, compounds are tested at the organism level and systemic effects can be observed. 2D *in vitro* models are limited by the lack of a three-dimensional (3D) environment, resulting in homogenous application of cancer drugs to the cells [8]. This causes an overestimation of efficacy of the drug candidates, leading to further study in animal models only to find they are ineffective. Furthermore, 2D *in vitro* models cannot replicate the complex nature of the TME, and interactions of tumour cells with the other residing cell types and components are absent.



3D *in vitro* models have been regarded as an important stepping-stone in the drug development cascade, combining the simplicity and control of 2D *in vitro* models with the complexities of *in vivo* models [9]. The first 3D model for tumours was developed in 1971, in which Chinese hamster V9 lung cells were cultured in plastic Petri dishes and formed spheroids similar to that of nodular carcinomas [10].

3D *in vitro* modelling would also allow for the vasculature component of the TME to be modelled, which is a significant hallmark of cancer [11]. Tumour angiogenesis enables tumour growth alongside circulation of cancer cells to secondary sites, promoting metastasis. Modelling vasculature alongside tumour cells *in vitro* would be a further step to bridge the gap between traditional *in vitro* and *in vivo* systems.

Advancing technologies such as tissue engineering have expanded the field of 3D *in vitro* models enormously, with the inclusion of natural or synthetic materials that are biocompatible, to recapitulate the ECM and the environment in which the cells thrive [12]. The development of 3D *in vitro* models also allows the stromal component of tumours to be modelled, further mimicking tumour progression and tumour-stroma interactions. Naturally derived hydrogels, such as Matrigel [13], collagen I [14], alginate [15] and hyaluronic acid [16] are widely used for the 3D culture of cancer cells. However, these materials are limited by their batch-to-batch variability, weak mechanical properties and exaggerated concentrations of growth factors and ECM proteins, hindering translatability [17]. By utilising a synthetic system to form the 3D *in vitro* model, the reproducibility between studies could be greatly improved, whilst also removing the influence of the overabundant growth factors and ECM proteins found in naturally derived hydrogels.

One branch of synthetic hydrogels are self-assembling peptide hydrogels (SAPHs), which are formed from naturally occurring amino acids which self-assemble into secondary structures such as  $\beta$ -sheets or  $\alpha$ -helices under aqueous conditions. These in turn self-assemble further to form nanofibres which create a self-supporting hydrogel [18]. These nanofibres are able to mimic that of the ECM, therefore representing an ECM-mimicking platform. These hydrogels are largely made of water, rendering them biocompatible. From a tissue engineering perspective, biocompatibility can be defined as the ability of a biomaterial to support appropriate cellular activity [19]. By adjusting the peptide concentration, amino acid composition and length, the mechanical properties can be tuned to mimic the stiffness of the tissue in question [20]. A family of ionic complementary  $\beta$ -sheet forming SAPHs commercialised by Manchester BIOGEL for cell

culture and tissue engineering applications, have successfully been utilised in previous studies [21–23], and are potential candidates for this use.

MCF-7 and MDA-MB-231 are cell lines representing early stage and metastatic breast cancer respectively. MCF-7 cells display the oestrogen receptor (ER), progesterone receptor (PR) and human epidermal growth factor receptor-2 (HER2) [24], whilst MDA-MB-231 cells are characterised by the absence of these receptors, therefore mimicking triple negative breast cancer (TNBC) [25]. To create vasculature *in vitro*, the primary cell types, human umbilical vein endothelial cells (HUVECs) and mesenchymal stem cells (MSCs), are one potential method which can be used. This method of forming vasculature utilises HUVECs to differentiate and organise themselves to form tubule structures, and the MSCs adopt a perivascular niche and stabilise the tubes formed [26]. To my knowledge, few studies have used MCF-7 and MDA-MB-231 cells within a SAPH for *in vitro* modelling of cancer [27–29], whilst only one study has utilised the co-culture of HUVECs and MSCs to create tissue engineered blood vessels within SAPHs [30]. Tri-culture systems with HUVECs, MSCs and breast cancer cells have been studied using collagen I [31], whilst a SAPH has been used previously for the tri-culture system of ovarian cancer cells, HUVECs and MSCs [30]. A SAPH system has not been used for the tri-culture of breast cancer cells, HUVECs and MSCs, to my knowledge.

## **1.2. Hypothesis**

SAPHs have been used previously for 3D culture of cancer cell lines [28,32,33] and primitive blood vessel formation by HUVECs [34–36], and are inherently chemically defined and have tuneable properties, which is advantageous over using naturally derived hydrogel systems [20]. It was therefore hypothesised that an ionic complementary SAPH system would be able to support the 3D culture, growth and *in vitro* modelling of the MCF-7 and MDA-MB-231 breast cancer cell lines, as well as supporting vasculature formation of HUVECs and MSCs, with appropriate material modifications if needed.

## **1.3. Aims of the Project**

This project aimed to explore the use of a commercially available ionic complementary  $\beta$ -sheet forming SAPH for modelling breast cancer and tumour angiogenesis *in vitro*, mimicking the TME more closely. Two different breast cancer cell lines, MCF-7 and MDA-MB-231, representing different stages of breast cancer were used. Tumour angiogenesis was investigated using HUVECs and MSCs, to create blood vessel-like

structures within the SAPH system. Broadly, the aims of this thesis correspond to the three results chapters:

- 1) **To identify the most appropriate SAPH candidate as well as characterise and compare the physical and mechanical properties of the chosen SAPH, PeptiGelAlpha1, with collagen I and Matrigel.**

Chapter 4 Focus: Matrigel and collagen I are naturally occurring hydrogels used in cancer modelling *in vitro* due to the abundance of growth factors and ECM proteins for cell growth, yet the physical properties of these hydrogels have not been well characterised. There are several commercially available SAPHs for cell culture purposes, which differ in charge and mechanical properties. The focus of Chapter 4 will therefore be to choose a commercially available SAPH for downstream experiments based on initial studies. Further, how the chosen SAPH, PeptiGelAlpha1, compared with Matrigel and collagen I in regards to the physical properties and suitability for mimicking tumours *in vitro* from a materials perspective is also shown in this chapter.

- 2) **To investigate the growth and behaviour of MCF-7 and MDA-MB-231 breast cancer cell lines within the chosen SAPH, by exploring cell viability, phenotype, and organisation, as well as investigating if features of solid tumours could be mimicked.**

Chapter 5 Focus: Solid tumours are characterised by features and events such as hypoxia, epithelial to mesenchymal transition (EMT), metastasis and resistance to anti-cancer drugs. MCF-7 and MDA-MB-231 are two of the most commonly used cell lines in breast cancer research, and are used to model early stage and metastatic breast cancer respectively [37]. The focus of Chapter 5 is to explore the suitability of the chosen SAPH as a platform for *in vitro* modelling of cancer. This is achieved by studying the response and behaviour of both cell lines when encapsulated in the SAPH, by investigating cell viability, phenotype and organisation.

- 3) **To determine what modifications are needed to support HUVEC and MSC growth and tube formation within the chosen SAPH.**

Chapter 6 Focus: Vasculature formation is an important hallmark of the TME, as it allows metastasis to occur and also provides an additional barrier to drug penetration of the tumour mass [11]. Tissue engineering vasculature *in vitro* has been achieved via co-culture of HUVECs and MSCs, which form capillary-like structures [26]. It is

unknown if a SAPH alone would be able to support the phenotype of both cell types, and if the cells would spontaneously form tube-like structures. Previous studies using synthetic hydrogels have shown that modification to the hydrogel is needed to promote HUVEC attachment and capillary morphogenesis [38,39]. Therefore, the focus of Chapter 6 will be to determine what modifications to the SAPH were necessary to promote and facilitate cell attachment, elongation, and subsequent tube formation. Achieving vasculature formation *in vitro* using a SAPH system would be a major advance in tissue engineering applications, by using a chemically defined platform.

#### **1.4. Outline of Thesis**

The thesis is comprised of this introduction chapter, Chapter 1, followed by Chapter 2, which discusses and summarises the literature regarding the TME, modelling cancer using 2D *in vitro*, *in vivo* and 3D *in vitro* systems, and hydrogels and SAPHs for *in vitro* modelling cancer and vasculature formation. Chapter 3 outlines the experimental protocols used to carry out the research undertaken. There are three results chapters, Chapters 4, 5 and 6, which have been summarised in section 1.3.

Chapter 7 will provide a summary of these findings and conclusions, as well as discuss future work. Chapter 8 contains the references cited in this thesis and Chapter 9 contains the appendices.

## **CHAPTER 2 – Literature Review**

### **2.1. Tissue Engineering**

#### **2.1.1. Overview**

Tissue engineering can be described as an interdisciplinary process involving the replacement and regeneration of damaged or diseased tissues, using a combinatory approach of cells, biomaterials and bioactive molecules [40]. A biomaterial can be defined as a material designed to interact with biological systems to evaluate, treat, improve or replace any tissue, organ or function of the body [41]. Bioactive can be described, on the other hand, as eliciting a specific biological response [42]. This approach to ‘rebuild’ biological tissues is a promising solution to chronic and degenerative diseases, where the focus is on disease management rather than treating the underlying condition. By using a scaffold-based system, cells can thrive in a 3D environment, mimicking the *in vivo* condition.

#### **2.1.2. Use in Disease Modelling**

Traditional disease models are animal models, where the organism-level effects can be determined, and 2D *in vitro* models, which provide a more simplistic viewpoint. Tissue engineering enables the development of more realistic *in vitro* models, by culturing cells in a 3D environment, which provides a more accurate representation of the situation *in vivo* [43]. In regards to disease models of cancer, tissue engineering offers the sophistication needed to recapitulate the TME *in vitro*; the complexity of which will now be discussed.

### **2.2. The Tumour Microenvironment**

#### **2.2.1. Overview**

Hanahan and Weinberg have previously described the characteristics acquired during tumour development which clearly distinguish malignant cells from their non-malignant counterparts; these characteristics were described as the ‘hallmarks of cancer’ [11]. These hallmarks include: resisting cell death, inducing angiogenesis, enabling replicative immortality, activating invasion and metastasis, evading growth suppressors and sustaining proliferative signalling [44]. Since the discovery of the ‘original’ hallmarks, emerging hallmarks and enabling factors of cancer have also been discovered, including:

deregulating cellular energetics, avoiding immune destruction, genome instability and tumour-promoting inflammation (**Figure 2.1**) [11].

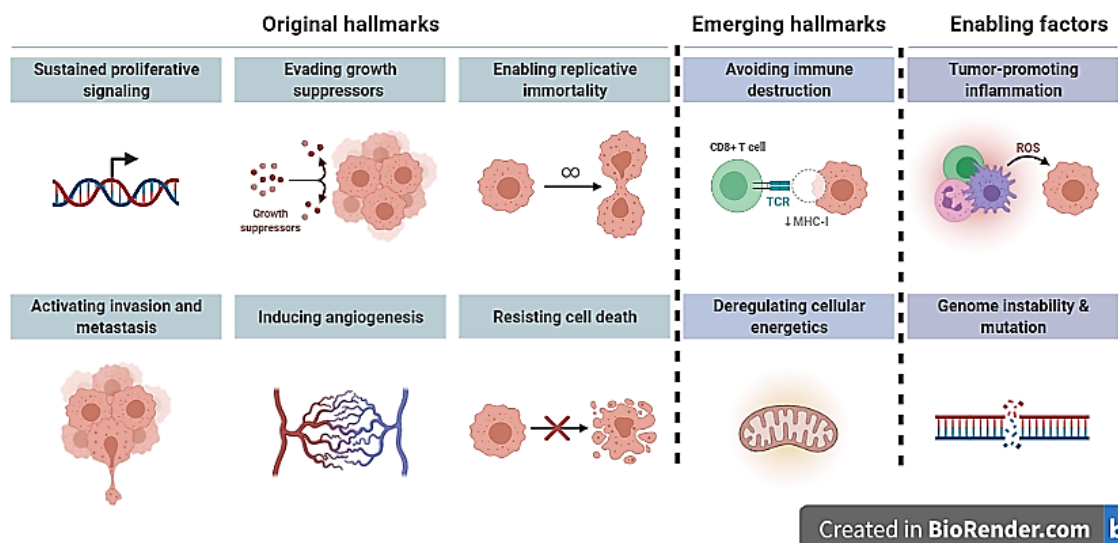


**Figure 2.1. Original and emerging hallmarks of cancer.** Adapted from “Hallmarks of Cancer” by BioRender.com (2020). Retrieved from: <https://app.biorender.com/biorender-templates>

It is now understood that acquiring these hallmarks requires not only tumour cells, but also the surrounding environment in which these tumour cells reside. Tumours are not comprised solely of malignant cells, but also contain heterogeneous populations of different cell types and networks, which altogether play an important role in tumour progression. The collection and organisation of these stromal cells form the TME (**Figure 2.2**) [45]. These cells may ordinarily reside within the tumour or may have been recruited to aid tumour development, such as endothelial cells (ECs) [5]. The interactions between the tumour cells and the surrounding environment not only dictate the growth and advancement of the tumour and patient prognosis, but also provide physical and chemical barriers to penetration of chemotherapeutic drugs [46]. This ultimately results in resistance to anti-cancer drugs, making development of efficacious chemotherapeutic drugs challenging.

The cell types and components forming the TME will be discussed in the following sections. This thesis aims to model breast cancer specifically. However, the components of the TME will be discussed generally with specific references to breast cancer where necessary.

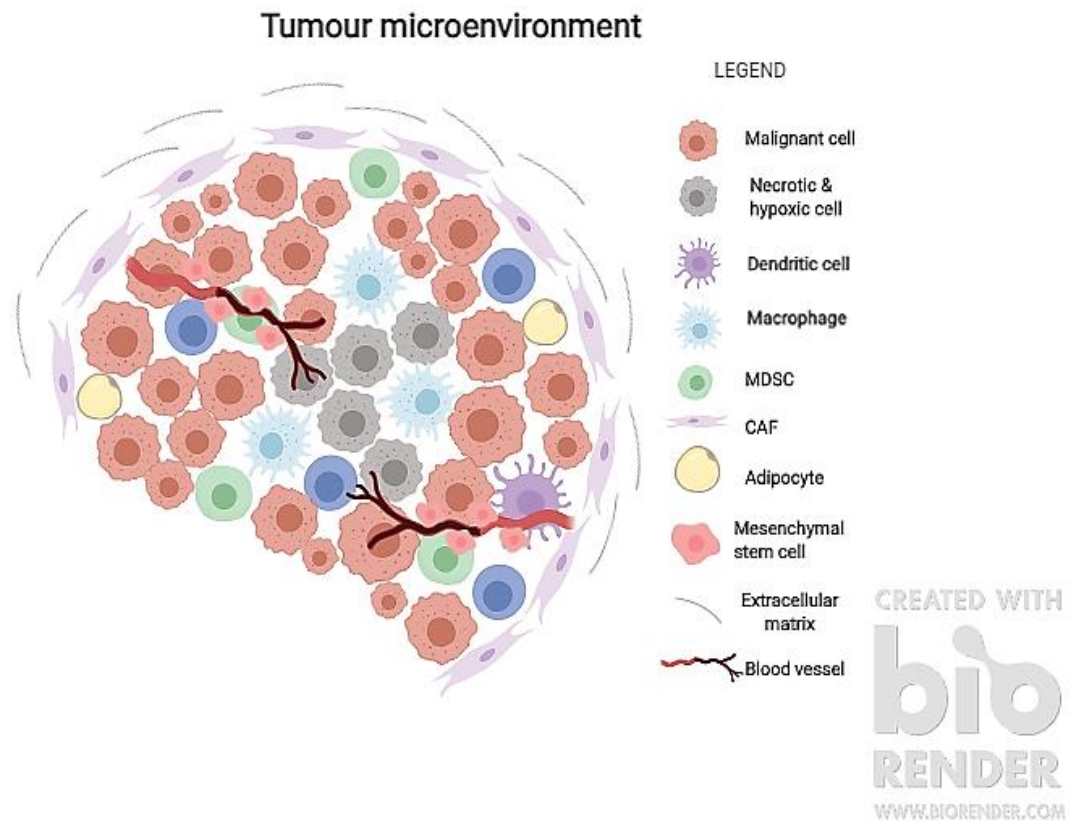


**Figure 2.2. Schematic of the TME.** Cells and components of the TME are labelled. It is noted that necrotic and malignant cells are not the same and represent different types of cells. Created with BioRender.com.

### 2.2.2. Extracellular Matrix

In normal mammary tissue, the ECM is comprised of two components: the basement membrane and the interstitial matrix [47]. The basement membrane is largely formed of type IV collagen, laminin, fibronectin and linker proteins including entactin and nidogen [48]. The interstitial matrix is comprised of fibrillary collagen, proteoglycans, glycoproteins and fibronectin, and is responsible for the tensile strength of the tissue [49]. The ECM is highly dynamic and is constantly being remodelled through deposition and degradation. ECM turnover is tightly regulated by control of degrading matrix metalloproteinase (MMP) enzymes and tissue inhibitor of metalloproteinase (TIMP) enzymes [49]. In the case of tumour progression, ECM dynamics become disordered; there is increased deposition of collagens I, II, III, V and IX, as well as increased cross-linking due to overproduction of the lysyl oxidase (LOX) enzyme [49,50]. The increased linearisation of collagen fibres, as well as cross-linking, results in increased stiffness and stromal density of the breast tissue. Atomic force microscopy (AFM) testing was used to compare the elasticity of ‘normal’ stroma and the invasive region in patients with invasive luminal ductal carcinoma; the stiffness of normal tissue was measured to be 400 Pa, whereas the cancerous tissue was measured to be 5 kPa [51]. It was also found that the

collagen content in mammary tumours in a xenograft mouse model correlated with compliance of the tumour, highlighting the importance of collagen in the stiffness of breast tumours [52]. Macroscopic stiffness, indicated by palpation, gives rise to the diagnosis of early stage breast cancer, due to cancerous tissue feeling more rigid compared with healthy breast tissue [53].

Moreover, in tumours there is an increased production of ECM degrading enzymes, in particular MMP enzymes. MMP expression is increased in almost all types of cancer and is associated with poor prognosis. MMPs can be produced by the cancer cells themselves or by the stromal cells within the TME [54]. Collagen IV degradation via MMP-2 and -9 activity is vital for cancer cells to cross the basement membrane and invade surrounding tissue in order to metastasise [55]. The shift in ECM dynamics towards degradation gives rise to the notion that cancer cells are remodelling the surrounding matrix [56]. ECM degradation by increased MMP activity also results in the release of cell surface-located growth factors, which are activated by MMP production [55]. One example is transforming growth factor- $\beta$  (TGF $\beta$ ) as a result of fibronectin degradation by MMP-9 [57]. These growth factors further contribute to tumour growth and development. MMP production is also important for angiogenesis: MMPs break down the basement membrane and release bound vascular endothelial growth factors (VEGFs), causing ECs to sprout in response to the VEGF gradient [58,59].

ECM within the tumour can be deposited by the resident cancer cells, but also by recruited fibroblasts, known as cancer-associated fibroblasts (CAFs) [60]. Normal fibroblasts are recruited to the tumour mass by cancer cells, and thought to undergo 'activation' in order to become CAFs, by mechanisms such as TGF $\beta$  signalling, increased ECM stiffness and inflammatory modulators including interleukin (IL) -1 and -6 [61]. It has also been postulated that CAFs can derive from bone marrow-derived mesenchymal stem cells (BM-MSCs) [62]. The functions of CAFs are multi-faceted: they are primarily responsible for the high ECM turnover described previously, catalysing invasion of surrounding tissues and aiding metastasis [63]. However, they also produce a variety of growth factors including VEGF, TGF $\beta$  and IL-6, which has implications for both angiogenesis and immune cell evasion of the TME [64]. CAFs and tumour cells have a synergistic relationship, as cross-talk between the two cell types promotes growth and progression of the tumour. For example, cancer cells produce platelet-derived growth factor (PDGF) which influences CAF proliferation and insulin-like growth factor (IGF) expression by CAFs, which in turn promotes cancer cell proliferation and PDGF production [65]. CAFs



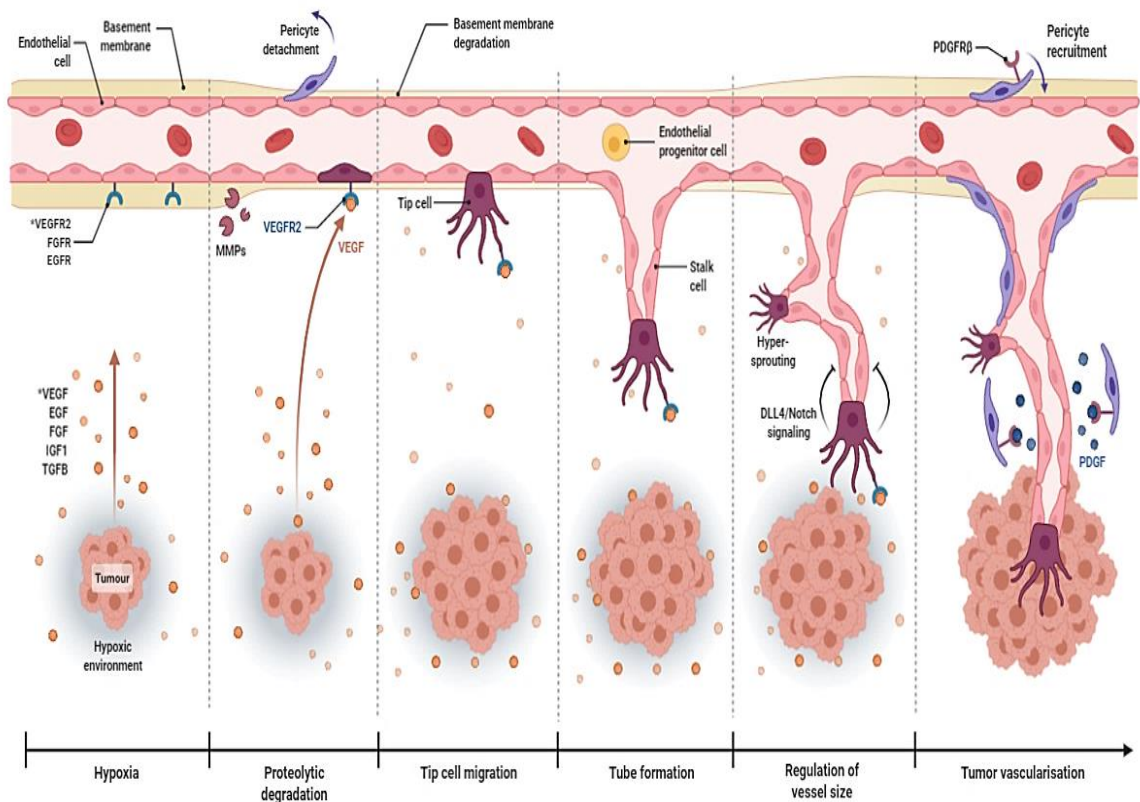
also produce multiple cytokines such as chemokine ligand 5 (CCL5) and stromal cell-derived factor 1 (CXCL12) which recruit BM-MSCs into the TME, aiding metastasis by differentiation into CAFs [66].

### **2.2.3. Immune Cells**

The TME hosts a variety of different immune cells representing both the innate and adaptive immune systems, including: T lymphocytes, B lymphocytes, mast cells, natural killer (NK) cells, tumour associated macrophages (TAMs), myeloid-derived suppressor cells (MDSCs), dendritic cells and tumour associated neutrophils (TANs) [5]. The immune component is important for both tumour inhibition, in the initial stages of tumour growth, and tumour progression [67]. NK cells and T cells are responsible for detecting foreign tumour antigens on cancer cells and destroying them. Dendritic cells subsequently express these antigens and combined with the production of T- and B-memory cells, result in immune surveillance of the tumour [68]. Eventually, the more aggressive tumour cells overpower the immune cells by mutating their surface antigens to evade detection by the immune system. As the TME becomes more complex, the migration of T cells into the tumour mass is inhibited by the disordered and leaky vasculature which further exacerbates the situation [67]. As opposed to lymphoid-derived T cells, which are observed to oppress tumour progression, myeloid-derived immune cells such as TAMs and mast cells are associated with promoting tumour development [69].

### **2.2.4. Hypoxia and Vasculature**

Initially, tumours rely on diffusion for access to oxygen and glucose. The diffusion limit for oxygen is 200  $\mu\text{m}$  and this leads to hypoxia typically occurring in the centre when tumours reach 1–2 mm in diameter [70,71]. As the centre of the tumour begins to undergo hypoxia, primitive blood vessels begin to form in response to the lack of oxygen to help the tumour meet its metabolic demands. Angiogenesis is a crucial component of the TME, as not only do the blood vessels provide a source of oxygen and glucose, it is a primary route of escape for invading cancer cells to metastasise in secondary sites [72]. Hypoxia and nutrient deprivation result in an angiogenic ‘switch’, resulting in the recruitment of ECs via production of VEGF and hypoxia-inducible factor 1-alpha (HIF1 $\alpha$ ) [73]. Increased production of matrix degrading enzymes results in proteolytic degradation of the basement membrane. The steps involved in vascularisation of tumours are depicted in **Figure 2.3**.



Created in BioRender.com

**Figure 2.3. Mechanism of events underpinning vascularisation of solid tumours *in vivo*.** Adapted from “Tumor Vascularization” by BioRender.com (2020). Retrieved from: <https://app.biorender.com/biorender-templates>

Recruited ECs proliferate and sprout to form immature blood vessels, which provide a short-lived supply in oxygen and nutrients. Pericytes are recruited by ECs to stabilise and mature the primitive blood vessels by the release of CAF-derived PDGF [73]. The formation of blood vessels to meet oxygen demand is paradoxical, as the blood vessels are leaky and primitive resulting in irregular blood flow and inability to meet the increased metabolic demands of the tumour. Blood vessels in tumours are characterised by widened interendothelial junctions, a poorly defined basement membrane and a chaotic and tortuous structure [74]. The blood vessels are also described as mosaic due to the patchy immunohistochemical staining of cluster of differentiation 31 (CD31), which is a characteristic marker for ECs [75]. This patchiness can be explained by a phenomenon known as ‘vascular mimicry’, by which tumour cells masquerade as ECs and line the blood vessels [70,76].

In physiological vasculature, one of the primary functions is to remove waste products away from the tissue to be excreted. Due to the poor perfusion and function of tumour blood vessels, this process is inefficient and results in an accumulation of lactic acid and hydrogen ions, resulting in decreased pH, and thus an acidic microenvironment [77]. This acidity, combined with low glucose and oxygen concentrations and a high accumulation of waste products, provides a harsh environment for cells to thrive. However, these cells are adapted to withstand these environmental pressures and are thus still able to grow and proliferate, therefore expanding the hypoxic core further [78].

### **2.2.5. Epithelial to Mesenchymal Transition and Cancer Stem Cells**

For metastasis to occur, cancer cells must undergo a process known as epithelial to mesenchymal transition (EMT). EMT occurs under normal physiological conditions in embryogenesis, for differentiation of epiblast cells into mesenchymal cells [79]. However, in cancer, EMT is required for malignant cells to adopt a more invasive phenotype to escape the primary tumour, invade the ECM and occupy a secondary site [80]. The main sites of metastasis for breast cancer are bones, the lungs, liver and the brain [81].

Contextual signals from the TME are thought to be responsible for the activation of EMT in individual cancer cells, mediated via cell-cell signalling molecules including: Wnt, TGF $\beta$  and Notch, and growth factors such as PDGF, epidermal growth factor (EGF), fibroblast growth factor (FGF) and HIF1 $\alpha$  and inflammatory cytokines [82]. The release of these growth factors, and subsequent EMT, can be catalysed by hypoxia, tissue stiffness, low pH and immune cell infiltration [83]. The complex nature of the TME is essential for the differentiation of malignant epithelial cells to a more mesenchymal and thus aggressive phenotype.

EMT is characterised by a loss of epithelial markers, such as E-cadherin, cytokeratin and zona-occludens 1 (ZO-1), and upregulation in mesenchymal markers including vimentin, N-cadherin, and fibronectin [80]. In conjunction, cells also change morphology, from epithelial to spindle-like, due to reorganisation of actin filaments in the cytoskeleton, as well as a loss of tight junctions between cells and apical-basal polarity. ECM components also differ between both states, with an abundance of laminin and collagen IV in epithelial cells and collagen I and fibronectin in mesenchymal cells [84]. The gene expression required for EMT to occur is regulated by a collection of EMT-inducing transcription factors, including: Snail, Slug, zinc finger E-box-binding homeobox 1 (ZEB1) and twist-related protein 1 (TWIST1) [84].

The activation of these factors results in repression of genes associated with the epithelial phenotype and upregulation of genes associated with the mesenchymal phenotype [85]. A summary of the events occurring in EMT in cancer is outlined in **Figure 2.4**.

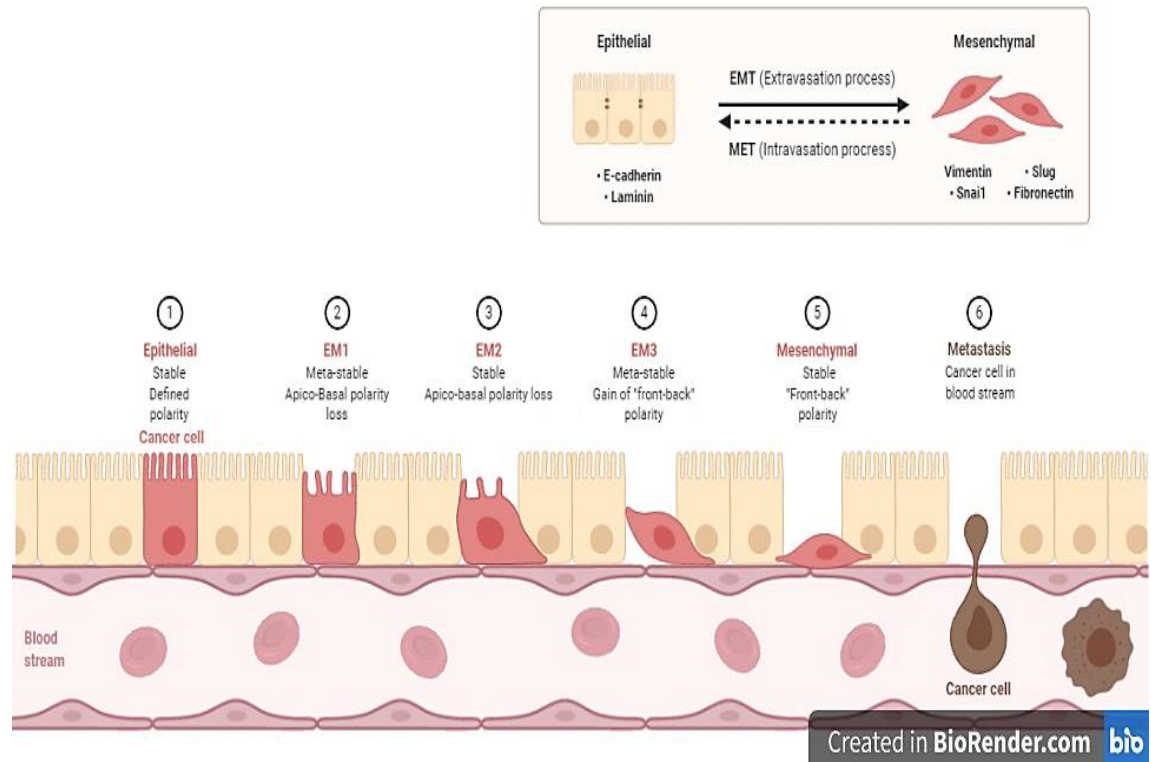


**Figure 2.4. Epithelial to mesenchymal transition of cancer cells.** Adapted from “Epithelial to Mesenchymal Transition” by BioRender.com (2020). Retrieved from: <https://app.biorender.com/biorender-templates>

EMT was long thought to be a binary process, but is now believed to be highly dynamic and heterogeneity is often observed within a cancer cell population; described as phenotypic plasticity [82]. As such, partial EMT may be observed whereby cells have not completely undergone EMT, but still retain epithelial markers and therefore adopt an intermediate phenotype. Tumour buds isolated from invasive ductal breast cancer, lung adenocarcinoma and pancreatic ductal adenocarcinoma displayed co-expression of E-cadherin and ZEB1, indicative of a partial EMT state [86]. Moreover, the fluid state of EMT also shows that the process is reversible, and that cells may also de-differentiate to an epithelial phenotype, known as mesenchymal to epithelial transition (MET) [82]. The EMT ‘state’ of the cancer cell is thought to dictate the likelihood of metastasis, as tumour cells with a more mesenchymal phenotype will be more invasive. EMT also gives rise to a population of malignant cells with increased tumorigenic capability and have the ability to self-renew, known as cancer stem cells (CSCs) [87].

CSCs are similar to normal stem cells, due to their self-renewing potential, but differentiate into separate cancer cell populations and are thus able to restore the original cancer cell population [88]. CSCs can be divided into subsets dependent upon the EMT state of the cell; mesenchymal-like CSCs express cell surface markers CD24<sup>-</sup>CD44<sup>+</sup> and are normally located at the tumour-stromal border [89]. On the other hand, epithelial-like CSCs express aldehyde dehydrogenase and are typically found in the core of the tumour. CSCs and the TME are in a dynamic state of cross-talk with one another, and as such, one will influence the other. For example, the cells located in the TME produce a variety of cytokines and growth factors, such as VEGF by ECs and C-X-C motif chemokine ligand 5 (CXCL5) by MSCs which are thought to promote the self-renewal of CSCs [90]. This is thought to be achieved by activation of Wnt/ $\beta$ -catenin and Notch pathways [91]. CSCs are adapted to survive in all aspects of the heterogeneous tumour mass, including the hypoxic core where nutrient and oxygen is lacking, to differentiate into the cell type required to further drive hypoxia, necrosis, invasion and metastasis of the tumour [78].

#### **2.2.6. Importance in the Clinic and in Drug Development**

The components of the TME, as described previously, play an important role in preventing the penetration of cytotoxic drugs and are responsible for chemotherapeutic resistance, which is observed in cancer patients. For a drug to be effective, it must penetrate the periphery of the tumour and distribute homogeneously throughout the entire tumour [92]. Tumours are notoriously heterogeneous in terms of their size, structure and stromal density. As a consequence of this heterogeneity, an anti-cancer drug will not be distributed homogeneously and will only kill a small proportion of cancer cells that are encountered. Barriers preventing diffusion of chemotherapeutic drugs into the tumour mass can be divided into either physical or chemical. Physical barriers include the ECM; the increased density and linearisation decreases the ECM mesh size, hence preventing infiltration of drug molecules [48]. The stiffness of the ECM also offers resistance to anti-cancer drugs; matrix stiffness is known to promote nuclear localisation of yes-associated protein (YAP) and transcriptional co-activator with PDZ-binding motif (TAZ), which in turn increase resistance to chemotherapeutic drugs in pancreatic cancer cells [93]. The increased interstitial fluid pressure exerted by inefficient blood and lymphatic vessels, along with increased contractile forces by fibroblasts of the tumour stroma, also contribute to reduced penetration [94]. Chemical barriers include the acidic microenvironment and hypoxia; upregulation of HIF1 $\alpha$ , in turn, upregulates expression of multi-drug resistance protein 1 (MDR1) and its product P-glycoprotein, which is known for its contribution to

chemotherapeutic resistance [95]. Weak basic chemotherapeutic drugs can become protonated in the acidic environment and can also become sequestered within acidic organelles [96]. Protonation occurs due to ‘ion trapping’, whereby the acidic extracellular component of tumours prevents the uptake of weakly basic drugs due to the large membrane permeability difference between the ionised and non-ionised portions of a drug. A change in cellular pH can therefore reduce the cellular uptake of a basic drug [97]. The barriers preventing drug penetration of tumours have been depicted in **Figure 2.5**.

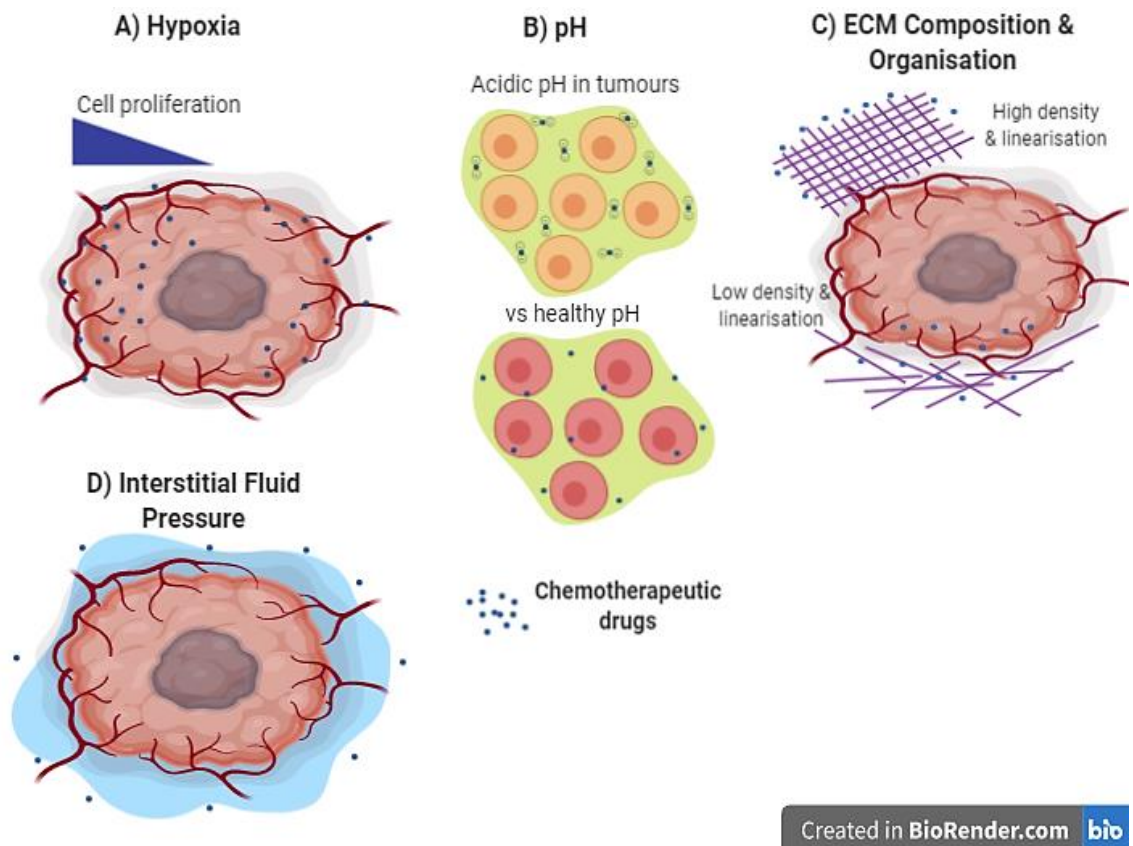


**Figure 2.5. Physical and chemical barriers preventing anti-cancer drug penetration of solid tumours.** Adapted from [98]. Created with BioRender.com.

The barriers described have subsequent implications for patients undergoing chemotherapeutic treatment and survival rates. Components of the TME described previously impact patient prognosis. The presence of vasculogenic mimicry has been shown to result in poor prognosis in breast cancer patients [99,100] and TNBC patients with stroma-rich breast tumours had poorer prognosis scores compared with patients with stroma-poor tumours [101]. A high density of TAMs has also been shown to be associated with poorer survival rates in breast cancer patients [102].

However, not only does the TME act as a barrier to drugs entering the mass, but it also provides important targets for drug development. Cancer cells rely on cross-talk between

all the different components of the TME to promote the growth and expansion of the tumour. If one of the components is eliminated or made ineffective, this will affect the survival of the tumour cells. Numerous drug compounds have been developed targeting the TME; tumour vasculature has been one such target by developing anti-angiogenic drugs that inhibit VEGF and the VEGF receptor (VEGFR). Apatinib, a VEGFR inhibitor, is currently being investigated in a phase II clinical trial in patients with thyroid cancer [103] (ClinicalTrials.gov number: NCT03048877). Other VEGF targeting compounds include the clinically approved anti-fibrotic drug Pirfenidone, which was found to 'normalise' the TME in orthotopic mammary models by reducing ECM components collagen and hyaluronan via TGF $\beta$  signalling as well as improving tumorigenic blood vessel function [104]. Another anti-fibrotic agent has demonstrated potential in targeting the tumour ECM; Losartan was able to reduce collagen I production in primary fibroblasts and stromal density in animal models of breast, skin, and pancreatic cancer [105]. The drug was also found to prevent breast cancer progression in a separate animal study [106].

Tumour fate and progression ultimately rely on the components of the TME. To study the development of tumours and efficacy of novel drug compounds, the complexity and heterogeneity of the TME must be mimicked in experimental cancer models. Such models used will be discussed in the next section.

## **2.3. Modelling Cancer**

### **2.3.1. Overview**

Before a drug is tested in human volunteers and patients, it must be tested pre-clinically using both *in vitro* and *in vivo* platforms. This is to ensure that the drug has no adverse side effects, and is safe to use. As well, efficacy must be demonstrated, such as improved survival, symptom amelioration or a complete cure. Standard *in vitro* models used for drug development purposes consist of a monolayer of cells seeded in 2D on tissue culture plastic (TCP), whereas *in vivo* models involve inducing the disease in animals such as rodents [107]. This section will summarise the uses of both platforms in the drug development cascade as well as discuss their limitations.

### **2.3.2. 2D *In Vitro* Models**

The use of cell lines for drug toxicity testing allows complete control over the experimental conditions by the researchers as well as ensuring reproducibility of data [108]. The

simplicity involved in culturing cells and subsequent exposure to cytotoxic compounds enables high throughput screening to be utilised, meaning a large amount of data can be generated quickly [109]. For cancer cell lines, in particular, chemo-sensitivity in response to increasing the drug concentration in the cell culture medium is an important measure to provide initial data on drug efficacy [110].

However, the 2D culture of cells results in the loss of tumour-stroma interactions due to the absence of ECM in the system. The lack of external cues from the tissue culture environment then results in the loss of *in vivo* phenotype typically observed [111]. Besides, cells cultured in a monolayer are exposed uniformly to anti-cancer drugs, as there are no physical barriers such as the ECM and blood vessels preventing the penetration of the drug [112]. This can result in overestimation of a drug's therapeutic capability and can also lead to promising drug candidates being ruled out, as the actions of the drug may be missed due to the culture method [112]. Cells are uniformly exposed to nutrients and oxygen, resulting in homogeneous cell populations which is unlike those observed in tumours [110]. TCP is extremely rigid and has a stiffness of 2–4 GPa, which is several orders of magnitude greater than breast tumour. Ultimately, a monolayer culture is not able to replicate the intricacies and complexity of the TME. The stark differences between 2D culture and *in vivo* contribute to the high failure rate in drug development, particularly in cancer which is estimated to be 95 % [113]. Due to the array of limitations associated with 2D culture, as of 2016, the National Cancer Institute has stopped using cancer cell lines to test novel drugs and instead is focussing on animal models for drug development [114]. For cell lines to be used, a suitable platform must be utilised.

### **2.3.3. Animal Models**

To determine the systemic effect of a novel drug, the compound must be tested *in vivo* before proceeding to clinical trials. In cancer studies, animal models can be classed into one of two broad groups: xenograft models, where human tumour cells are implanted into a host organism, or genetically engineered models [115]. Both types of animal models will be discussed in the following sections.

#### **2.3.3.1. Xenograft Models**

Xenograft models of cancer incorporate implanting tumour cells either subcutaneously or orthotopically into immunodeficient mice. Mice lacking an immune system are used to avoid an immune response against the foreign tissue [116]. Xenografts can employ either established cell lines (cell-line derived xenografts; CDX) [117] or autologous patient cells



(patient-derived xenograft; PDX) [118]. Traditional cell lines carry the caveat of undergoing de-differentiation with their genetic and molecular behaviour altered [117]. As well, cancer cells implanted subcutaneously do not metastasise [119] and metastasis can only be mimicked via implantation into the tail vein [120]. Orthotopic implantation offers the advantage of spontaneous metastasis from the primary tumour elsewhere, however, the incidence of this is very low, with one study reporting only 3 out of 144 mice displaying spontaneous metastasis from the implanted tumour [121].

Using patients' cells allows more representative features of *in vivo* tumours to be mimicked and provides a personalised approach to finding the most suitable chemotherapeutic for an individual. Moreover, the inherent genetic and histological heterogeneity can also be mimicked, resulting in drug responses which are more characteristic of the clinical situation [122]. PDXs have been used in high throughput applications for preclinical drug screening applications; 1075 PDX models encompassing a range of different solid tumour types were used to predict therapy response as well as patient heterogeneity to a variety of anti-cancer drugs [123]. The panel was able to predict patient response in clinical trials, highlighting the importance of physiologically relevant pre-clinical models. One of the major limitations of using PDX models is the presence of mouse stroma within the propagated tumour. Over time, the human-derived stroma will degrade and be replaced with mouse stromal tissue [124,125]. This limits the translatability of xenograft tumours, as aspects of the human TME will be lost as well as cell-stroma interactions. This mixture of mouse and human cells can make the genomic characterisation of PDXs challenging due to contamination by the murine stromal cells [126]. Moreover, drugs targeting the immune system cannot be tested nor will the immune cell component of the TME be mimicked as immunocompromised mice are used.

### **2.3.3.2. Genetically engineered models**

To overcome the issues with mouse stroma and immunodeficiency, genetically engineered mouse models (GEMMs) offer an alternative. These mice have been genetically transformed via activation of oncogenes and inactivation of tumour suppressor genes; this can be achieved either in the germline which affects expression in the entire animal, or specifically in the tissue or organ of interest by using a Cre-Lox system [116,127]. The ideal GEMM should contain tumours that are initially propagated in a small population of cells within an organ of interest by a genetic fault, and the steps in tumour progression should mimic the human condition [128].

The literature regarding similarities between GEMMs and human breast cancer is mixed. The US National Institute of Health Breast Cancer Think Tank and Annapolis Pathology Panel compared 39 breast cancer GEMMs with human breast tumours [129]. It was found that the morphology of human breast tumours and tumours found in the mammary pads of GEMMs were not directly comparable [129]. In addition, GEMM tumours were predominantly found to be hormone-independent whereas almost half of all human breast tumours depend on hormones. On the other hand, another study found that histological and genetic analysis of GEMMs was faithful to the human tumour it was mimicking, with the conservation of gene signatures between species [130].

Moreover, *in vivo* studies are expensive to undertake, due to the high costs involved in maintaining the animals used [110].

Bearing in mind the faults of both 2D and animal models, the development and application of 3D models for cancer research will now be discussed.

#### **2.3.4. 3D *In Vitro* Models**

Although both 2D *in vitro* models and animal models provide a wealth of information regarding a potential drug compound's efficacy profile, the caveats in both do question if the data collected are representative of the human condition or not. To bridge the gap between the two systems, the development and use of 3D *in vitro* models for cancer research have been employed. By combining the simplicity and control of 2D models with the 3D microenvironment of animal models, one hopes that the pre-clinical data collected will be more predictive. Therefore, resources will be invested in compounds that are likely to provide an efficacious outcome in later stages of the drug development cascade. A summary of the advantages and caveats of 2D *in vitro*, 3D *in vitro* and *in vivo* models is depicted in **Table 2.1**.

**Table 2.1. The ability of 2D *in vitro*, 3D *in vitro* and animal models to mimic ideal characteristics in cancer modelling.** Information was collated from the following sources [9,110,131].

Characteristic	2D <i>in vitro</i> models	Animal Models	3D <i>in vitro</i> models
Cell-cell interaction	Yes	Yes	Yes
Cell-ECM interaction	No	Yes	Yes
Systemic effect	No	Yes	Yes
Mimics <i>in vivo</i> environment	No	Yes	Yes
Low cost	Yes	No	Yes
Control of external parameters	Yes	No	Yes
Response to chemotherapeutic drug	Yes	Yes	Yes
Personalised screening of patients' cells	Yes	No	Yes

By encapsulating or incorporating cells within a biomaterial, the 3D microenvironment is mimicked and cell-ECM interactions can be studied, due to cells binding to the matrix fibres via proteins known as integrins [132]. Integrin mediated adhesion influences cell shape and polarity by cytoskeletal organisation [133]. Whilst in 2D culture, cells are constrained to a flattened morphology due to forced adhesion to one plane, cells in 3D culture can spread in all dimensions and polarity is unrestricted [133]. This impacts cell function and behaviour, reflecting cell phenotype *in vivo*. Furthermore, the stiffness of biomaterials is more varied than that of TCP or glass, resulting in cells responding to dynamic mechanical forces, ultimately influencing cell fate and behaviour [134]. For example, Engler *et al*, famously reported that the substrate stiffness influences MSC fate and lineage, with softer elasticity resulting in differentiation to a neurogenic lineage, and more stiffer matrices resulting in a tendency towards an osteogenic lineage [135]. The main differences between 2D and 3D culture are summarised in **Figure 2.6**.

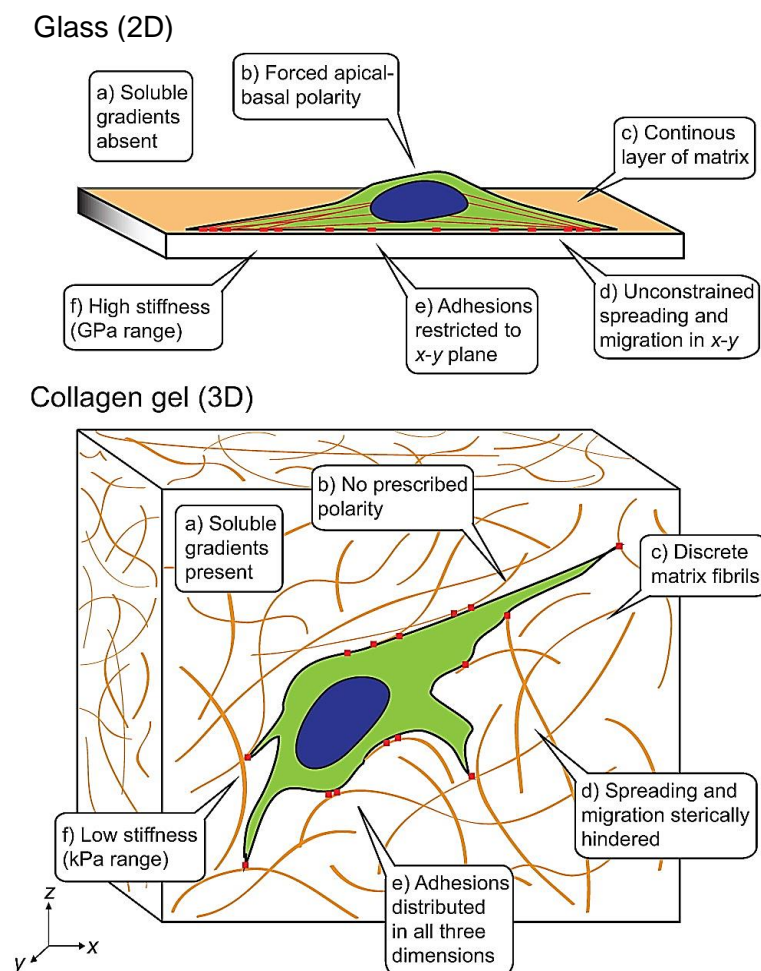


**Figure 2.6. Mechanical, structural and morphological differences in 2D and 3D cell culture.** This diagram has been reprinted and modified with copyright permission from The Company of Biologists [133].

Although the advantages of using a biomaterial for culturing cells in 3D has just been described, there are many different platforms that are used to create 3D *in vitro* models of cancer. These include liquid-based methods such as suspension culture and material-based methods such as scaffolds and hydrogels, which can either be naturally derived or synthetically produced. The different strategies used to develop 3D *in vitro* models of cancer will be discussed next.

### 2.3.4.1. Liquid-Based Methods

Tumour spheroids can be produced using scaffold-free methods; in liquid-based systems, cancer cells are suspended to allow the self-assembly of the cells, resulting in the production of a spheroid [136]. One of the most commonly used liquid-based approaches is the hanging drop method; cells within the pipetted droplets become concentrated due to the effect of gravity at the liquid-air interface when suspended from a flat surface [137]. One

of the main advantages of the hanging drop method is that spheroids produced are of homogenous size; a range of cell lines including MCF-7 (breast cancer), Caco-2 (colon cancer), HeLa (cervical cancer) and DU-145 (prostate cancer) were cultured using this technique and it was observed that all cell lines formed tightly packed and rounded spheroids of similar size [138]. This study shows the value of using the hanging drop technique for high throughput screening, where reproducibility is vital. However, viability was not assessed and thus it is uncertain if the cells maintained a high viability when cultured using this method. Non-small cell lung carcinoma (NSCLC) cancer lines 549 and Colo699 cultured using the hanging drop method were observed to have differences in cell viability and proliferation, suggested that some cell lines are more suited to culture using this method than others [139]. Increased expression of vimentin and decreased expression of E-cadherin showed that the cells were adopting a mesenchymal phenotype during the culture period, implying that this method can be used to model tumour progression. This method has also been used for high throughput screening of anti-cancer drugs; the epithelial carcinoma cell line A431.H9 was used to produce spheroids using a 384 hanging drop array plate, of which the majority were still viable after 7 days of culture [140]. Moreover, when compared with 2D culture, the cells were highly resistant to treatment with the anti-cancer drug 5-fluorouracil (5-FU); this is because this drug exerts anti-proliferative activity and so would have had no effect on the quiescent cells in the spheroids.

The rotary cell culture system (RCCS) was developed by NASA to simulate the effects of microgravity on cells, however, the formation of spheroids by random collision allows the RCCS to be used for cancer research [141]. Fluid turbulence and shear stress are minimised by filling the system completely with culture media, providing a still environment for cell culture and efficient mass transport [142]. A total of sixteen different cancer cell lines including those representing breast cancer, prostate cancer, malignant gliomas and urinary bladder cancer were used to form spheroids using the RCCS; a maximum diameter of 0.5 mm was reached and upregulation of cell adhesion molecules E-cadherin and CD44 was observed [143]. However, the spheroids formed were heterogeneous in shape and size, limiting reproducibility of data.

Another liquid-based method is the use of magnetic beads or Nanoshuttles™. Incubating cancer cells with fibroblasts and magnetic beads or Nanoshuttles™ resulted in the cells aggregating via magnetic levitation at the air-liquid interface [144]. MDA-MB-231 breast cancer cells and fibroblasts incubated with Nanoshuttles™ formed spheroids of 1 mm

diameter within 24 hours of culture with a fibrotic capsule surrounding the tumour cells; comprised of collagen, vimentin and laminin [145]. Treatment of the spheroids with anti-cancer drugs doxorubicin and Doxil® resulted in greater viability of the cells compared with 2D culture, showing the magnetic levitation system can mimic physical barriers seen *in vivo*. Human glioblastoma cells incubated with a hydrogel containing magnetic iron oxide particles formed spheroids of approximately 1 mm diameter within 24 hours, with necrosis occurring in the centre of the spheroids [146]. Cell viability was maintained for up to 12 weeks, confirming this method can be used for long-term studies of spheroids. Magnetic levitation is, however, limited by the loss of cells due to incomplete attachment to the magnetic particles [144]. A study comparing the different liquid-based systems for developing tumour spheroids using the lung cancer cell line A549, showed that the pellet culture method is most suitable for developing spheroids greater than 500 µm with a spheroid shape, and that the shape of the spheroid determines the viability of the cells, due to heterogeneous proliferative activity [147].

Low-attachment plates are a simple and reliable way of creating tumour spheroids. Using this method, tumour cells are unable to attach to the surface and thus are forced to aggregate together forming spheroids. It was recently discovered that tumour spheroids produced using this technique have more similar genetic profiles to *in vivo* tumours than 2D monolayer cultures, and genetic mutations involved in lung cancer displayed a higher frequency and stronger phenotype in 3D culture, highlighting the need for 3D culture for more representative modelling [148].

The main limitation with using liquid-based methods for modelling of cancer *in vitro* is the absence of an ECM-mimicking platform, resulting in the loss of cell-ECM interactions. Using a material-based method is able to replicate this interaction, and strategies used will be discussed in the next section.

#### **2.3.4.2. Material-Based Methods**

The use of a material or scaffold within an *in vitro* model allows the cells to adhere to a matrix, thus mimicking cell-ECM interactions. Scaffold based models can be generated by incorporating cells into a liquid matrix with subsequent solidification techniques, by physically mixing cells into the material, or by seeding cells directly onto the scaffold and allowing them to infiltrate the material [107]. The use of a biomaterial allows physical variables such as stiffness and porosity to be controlled and varied, mimicking the native ECM and microenvironment more closely [149]. Electrospun scaffolds such as

poly(lactide-co-glycolide) (PLG) with the bone mineral hydroxapatite (HA) have been used to model breast cancer metastasis to bone [150]. Another polymeric scaffold, poly( $\epsilon$ -caprolactone) (PCL), has been used for studying breast CSCs, as well as modelling the bone cancer Ewing sarcoma *in vitro* [151,152]. The main limitations with using solution blow spun scaffolds are that the synthesis method used typically results in cytotoxicity due to the harsh chemicals used, and cell adhesion is low, resulting in a loss of bioactivity [153]. Cell adhesion on polymeric scaffolds can be achieved, however, by surface modification techniques such as incorporating ECM proteins [154]. Hydrogels are a promising tissue engineering strategy for creating an *in vitro* model of cancer, due to their tuneable mechanical properties and biocompatibility [155], and can be naturally derived or synthetically produced. These will be discussed in the following sections.

## 2.4. Hydrogels

### 2.4.1. Overview

Hydrogels can be defined as hydrophilic networks capable of absorbing large quantities of water, yet behaving as solid materials [156]. The remaining content consists of polymer chains. Hydrogels are tuneable in nature due to their design and therefore desired parameters, such as stiffness [157], porosity [158], functionalisation [159] and stability/degradation [160] can be mimicked. The high water content and ‘softness’ makes them similar to living tissue and thus renders these materials biocompatible [161]. Consequently, they have been used in a variety of biomedical applications, including cell culture. Hydrogels can be classed according to the stimulus causing gelation: temperature, pH and light [156]. Their uses in tissue engineering and regenerative medicine include: drug delivery, biosensors and scaffolds for cell therapies and *in vitro* modelling [161]. A summary of the use of hydrogels for *in vitro* modelling of cancer is provided in **Table 2.2**, and will be discussed in more detail in the following sections.

### 2.4.2. Naturally Derived Hydrogels

The most commonly used naturally sourced hydrogel is Matrigel, a commercially available basement membrane extract derived from Engelbreth-Holm-Swarm mouse tumour tissue [162]. The hydrogel contains a variety of ECM proteins such as laminin-111, collagen IV, entactin and heparin sulphate and therefore provides cells with naturally occurring stimuli [163]. Matrigel also contains large quantities of growth factors such as EGF, FGF and PDGF, enabling growth and angiogenesis of tumour cells [164]. Due to the

tumorigenic qualities of Matrigel, it is considered the ‘gold standard’ biomaterial for modelling cancer [165]. Breast, lung and prostate cancer cells cultured in Matrigel alongside fibroblasts were found to be protected by chemotherapeutic drug treatment when co-cultured with fibroblasts, highlighting the importance of replicating the stromal component *in vitro* [166]. Breast cancer cell lines MCF-7 and MDA-MB-231 were found to be more resistant to doxorubicin treatment when cultured in Matrigel compared with 2D culture, and this resistance was mediated by cell attachment to ECM proteins in the material via  $\beta 1$  integrin binding [13]. Interestingly, one study found that JIMT1 and MCF-7 breast cancer cells cultured in Matrigel exhibited greater sensitivity to anti-cancer drugs methotrexate and alantolactone than 2D culture, but showed a similar gene expression profile to that of JIMT1 xenografts compared with 2D culture [167]. As the concentration of growth factors is not defined and varies from one batch to the next, this results in irreproducibility of data. Moreover, the material is animal-derived, meaning chemical definition cannot be controlled, and has ethical implications. The high concentration of growth factors present is greatly inflated compared with what is found *in vivo*, resulting in an exaggerated response. Methods to overcome the limitations of Matrigel include creating composite materials with: alginate [168–170], poly(ethylene glycol) (PEG) [171] and collagen I [172,173]. However, hybrid materials made with Matrigel do not fully overcome the limitations presented herein, such as weak mechanical properties and lack of chemical definition.

Collagen I, which can be derived from murine and bovine sources, is another naturally sourced hydrogel that is popularly used for cancer modelling. As an animal source, collagen I contains cell-binding ligands such as the arginine-glycine-aspartate (RGD) motif, which facilitates cell adhesion to the ECM [174]. Colorectal tumoroids produced using collagen I hydrogels and ECM protein laminin, containing HT29/HCT116 cancer cell lines and fibroblasts and ECs were able to recapitulate the stromal component of the TME with disrupted vasculature formed [14]. Collagen I was used to create bioprintable models of vascularised neuroblastoma using SH-SY5Y cells, HUVECs and MSCs [175]. Cells produced a vimentin-rich matrix, indicative of cancer progression and an aggressive phenotype, although HUVECs and MSCs were unable to form tubes. A mixture of Matrigel and collagen I hydrogels was used to combine pre-formed HUVEC tubes with spheroids composed of MDA-MB-231 cells and MSCs; the authors found that simply adding HUVECs to the spheroids was not sufficient to promote tube formation [176]. As a naturally sourced hydrogel, collagen I suffers from similar limitations to Matrigel such as lack of definition and animal origin.



Polysaccharide-based hydrogels bridge the gap between animal-derived and synthetic hydrogels, as they are formed from naturally occurring polymers such as alginate [177,178] and hyaluronic acid [16,179]. The main caveat with using alginate especially, is that it is biologically inert so needs to be functionalised with cell-binding motifs and moieties to facilitate cell attachment [180,181]. It was found that HCT116 colorectal cancer cells exhibited the highest proliferation and viability in alginate blended with gelatin, compared with alginate alone [182], most likely due to the cell-binding motifs provided by gelatin.

The use of synthetic hydrogels for *in vitro* modelling of cancer will be explored next.

### **2.4.3. Synthetic Hydrogels**

To overcome the challenges posed by naturally sourced hydrogels, such as animal origin, weak mechanical properties and batch-to-batch variability, synthetic hydrogels provide a viable solution. The advantages of using such materials include: chemical definition, tuneable mechanical properties and controlled degradation [183]. PEG blended with fibrinogen was used to create 3D models of breast cancer cell lines MCF-7, MDA-MB-231 and SK-BR-3; it was found that all three cell lines were viable and proliferated over 15 days in culture [184]. MCF-7 cells encapsulated in PEG hydrogels behaved similarly to Matrigel and collagen I, and cell response to oestrogen was reproducible between experimental repeats, whereas Matrigel and collagen I exhibited high variability [185]. Breast cell lines (MCF-7/MDA-MB-231) and prostate cancer cell lines (LNCaP/PC3) were cultured alongside HUVECs and MSCs within hydrogels formed from starPEG, heparin and RGD binding motifs [186]. Tri-cultures were carried out in soft hydrogels (200 Pa), alongside the RGD motif and growth factors VEGF, FGF-2 and CXCL12 [186]. Interactions between tumour cells and vascular cells were observed towards the periphery of the tumour spheroids, but tumour angiogenesis models were found to be slightly more sensitive to anti-cancer drugs epirubicin and paclitaxel compared with tumour only models. This could be due to the softer stiffness in tumour angiogenesis models used, resulting in increased drug diffusion. The use of a chemically defined hydrogel aids reproducibility and consistency between experiments and researchers. A hydroxyethyl chitosan/glycidyl methacrylate hydrogel was used to encapsulate MCF-7 breast cancer cells [187]. It was found that angiogenic markers CD34, VEGF, PDGF and FGF were expressed in xenograft tumours derived from 3D hydrogel cultures, and were resistant to Bevacizumab compared with 2D cultures. Polyacrylamide is another synthetic hydrogel used as a substrate for

cancer cell growth; the main caveat with this material, however, is that it can only be used for 2D culture and thus the 3D environment is not mimicked [188,189].

SAPHs will be discussed in the next section.

**Table 2.2. Summary of strategies used to mimic cancer *in vitro* using hydrogels.** The hydrogel used, mechanical properties (if measured), cell type(s), features of cancer studied, response to chemotherapeutic drugs (if studied) and the reference are noted.

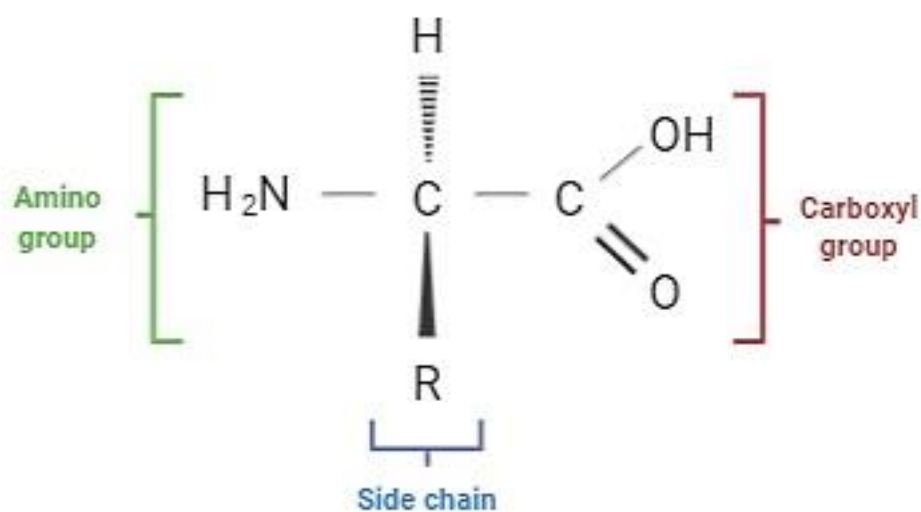
Hydrogel used	Mechanical Properties	Cell type(s)	Features of cancer studied	Response to chemotherapeutic drugs	Reference
Hydroxyethyl chitosan/glycidyl methacrylate	10 kPa	MCF-7 (breast)	<b>Angiogenesis</b> – Upregulation of angiogenic markers CD34, VEGF-A, PDGF-B, bFGF.	Sensitivity to Endostar, resistance to Bevacizumab.	Wang <i>et al</i> , 2015 [16].
PEG-fibrinogen	Acellular: 250 Pa ± 40 Pa. MCF-7 cell-laden: 4700 Pa ± 650 Pa	MCF-7/MDA-MB-231/SK-BR-3 (breast)/PC-3/PC-3-Met (prostate)/HT29 (colon)	n/a	n/a	Pradhan <i>et al</i> , 2017 [184]
starPEG	1500 Pa for tumour only models, 200 Pa for tumour angiogenesis models	MCF-7/MDA-MB-231 (breast), LNCaP/PC3 (prostate), HUVECS, MSCs	<b>Hypoxia</b> – hypoxia observed in MCF-7 and LNCaP models. <b>Tumour angiogenesis</b> – tube formation by HUVECs and MSCs.	Tumour angiogenesis models slightly more sensitive to chemotherapeutic drugs than tumour only models. 2D tumour cultures more sensitive to doxorubicin, epirubicin and paclitaxel treatment than 3D culture.	Bray <i>et al</i> , (2015) [186].
Collagen I	n/a	HT29/HCT116 (colon), HDF (fibroblasts), HUVECs	<b>EMT</b> – Upregulation of mesenchymal marker vimentin. <b>Angiogenesis</b> – Pathogenic angiogenesis.	n/a	Magdeldin <i>et al</i> , 2017 [14].
Basement membrane extract/collagen I	n/a	MCF-7/MDA-MB-231 (breast), HUVECs, MSCs	<b>Angiogenesis</b> – tube formation by HUVECs and MSCs. <b>Hypoxia</b> – hypoxic (5 % O <sub>2</sub> ) conditions mimicked.	Disruption of endothelial network with paclitaxel treatment, MCF-7 cells unaffected by paclitaxel or fluororacil.	Benton <i>et al</i> , 2015 [176].
Alginate	n/a	HCT116 (colorectal)	<b>Hypoxia</b> – hypoxic core observed.	n/a	Kesarwala <i>et al</i> , 2017, Read <i>et al</i> , 2018 [177,178].
Alginate-Matrigel	24–76 kPa	MDA-MB-231 (breast)	<b>Invasion</b> – transwell invasion assay showed presence of entrapped cells.	n/a	Cavo <i>et al</i> , 2018 [169].

Hydrogel used	Mechanical Properties	Cell type(s)	Features of cancer studies	Response to chemotherapeutic drugs	Reference
Alginate-gelatin	n/a	HCT116 (colorectal)	<b>EMT</b> – no change in mesenchymal marker vimentin, retention of epithelial phenotype. <b>Invasion</b> – wound healing migration assay.	n/a	Ivanovska <i>et al.</i> , 2016 [182].
Matrigel	n/a	MCF-7 (breast), LNCaP (prostate), NCI-H1437 (lung) ± HDF (fibroblasts)	<b>Stromal component</b> – incorporation of fibroblasts. <b>EMT</b> – retention of epithelial phenotype, negative vimentin staining.	Sensitivity to doxorubicin and fulvestrant in 3D embedded and 2D cultures, co-culture with fibroblasts protected tumour cells from drug treatment	Stock <i>et al.</i> , 2016 [166].
Matrigel	n/a	MCF-7 (breast), MDA-MB-231 (breast cancer)	<b>Resistance to anti-cancer drugs.</b>	Decreased sensitivity to doxorubicin compared with 2D culture.	Lovitt <i>et al.</i> , 2018 [13].
Matrigel	n/a	MCF-7/ JIMT1 (breast)	<b>EMT</b> – no change in vimentin expression compared with 2D culture.	Increased sensitivity to methotrexate and alantolactone compared with 2D culture.	Hongisto <i>et al.</i> 2013 [167]
Hyaluronic acid	n/a	MDA-MB-231 (breast), HMEC-1	<b>Angiogenesis</b> – increases in VEGF and MMP-9 expression.	n/a	Kassim <i>et al.</i> , 2017 [179].
Hyaluronic acid	7.4–18.9 kPa	MCF-7 (breast)	<b>Angiogenesis</b> – increased expression of VEGF, IL-8 and FGF compared with 2D culture. <b>Invasion</b> – increased migration and invasion of cells compared with 2D culture.	n/a	Suo <i>et al.</i> , 2019 [16].

## 2.5. Self-Assembling Peptide Hydrogels (SAPHs)

### 2.5.1. Overview

Molecular self-assembly is described as the spontaneous and reversible organisation of molecules without any external cues [190]. It provides a ‘bottom-up’ approach to building and designing novel biomaterials [191]. Self-assembly of peptides is governed by weak, non-covalent forces including: hydrogen bonds, ionic bonds, van der Waals interactions and hydrogen bonds with water molecules [192]. SAPHs consist of short-chain peptides which organise themselves first into secondary structures and consequently into supramolecular structures that contain large volumes of water [18]. These short-chain peptides are comprised of amino acids; the monomers of proteins. There are 20 naturally occurring amino acids, which have a common structure of a chiral carbon atom, an amino group, a carboxyl group, an R group and a hydrogen atom (**Figure 2.7**). Amino acids vary by the composition of the side chain, denoted as the R group, which determine the consequent chemical properties.

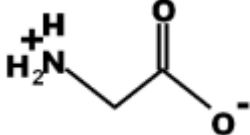
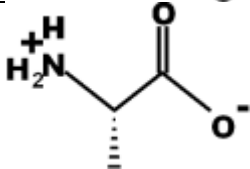
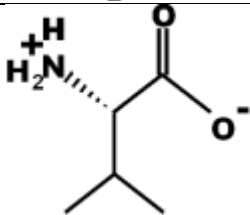
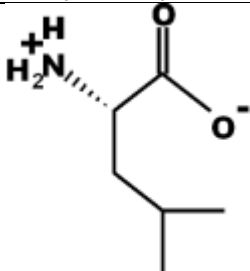
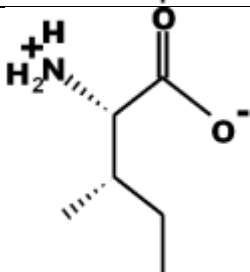


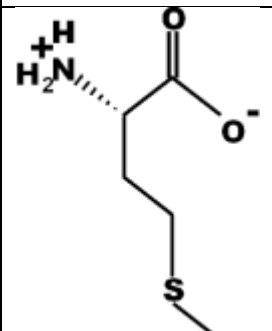
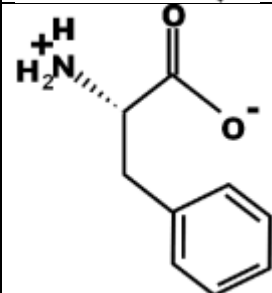
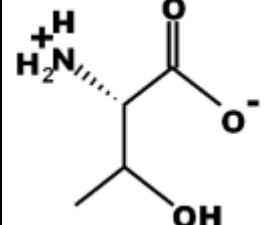
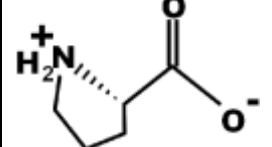
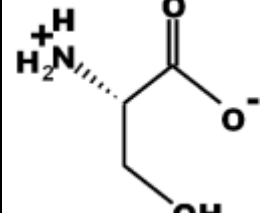
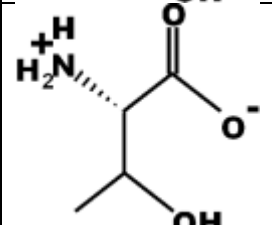
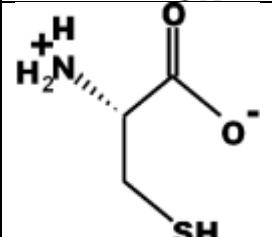
Created in BioRender.com 

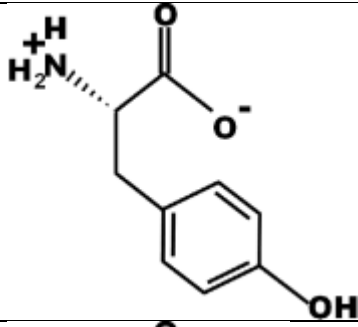
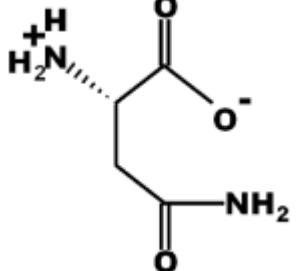
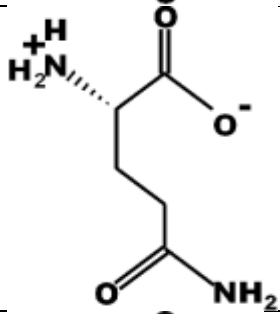
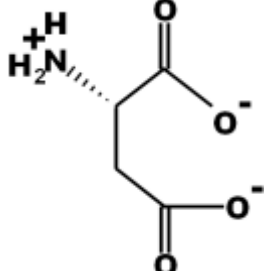
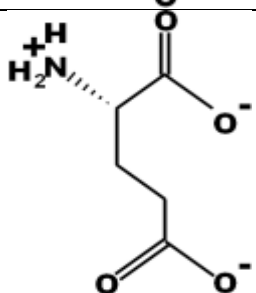
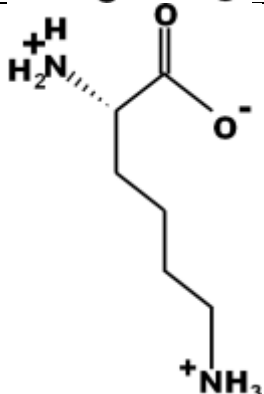
**Figure 2.7. Schematic of structure of amino acids.** A chiral carbon atom is at the centre, surrounded by an amino group, a carboxyl group, a hydrogen atom and a side chain denoted as the ‘R’ group. Created with BioRender.com.

A peptide bond is formed between two amino acids via covalent bonding, where the carboxyl group of one amino acid shares electrons with the amino group of a second amino acid, resulting in the removal of water [193]. The side chains can be acidic, basic, negatively charged, positively charged or uncharged (**Table 2.3**). The number of amino acids available results in a huge number of peptide chains to be designed, with the desired properties incorporated. The sequence of amino acids formed via peptide bonds is thus known as the primary structure of proteins and peptides.

**Table 2.3. Naturally occurring L-amino acids and their properties.** The 3-letter and 1-letter code of each amino acid is provided alongside the chemical structure of each side chain and the resulting properties.

Amino acid	3-letter code	1-letter code	Side chain	Property
Glycine	Gly	G		Non-polar (hydrophobic)
Alanine	Ala	A		Non-polar (hydrophobic)
Valine	Val	V		Non-polar (hydrophobic)
Leucine	Leu	L		Non-polar (hydrophobic)
Isoleucine	Ile	I		Non-polar (hydrophobic)

Amino acid	3-letter code	1-letter code	Side chain	Property
Methionine	Met	M		Non-polar (hydrophobic)
Phenylalanine	Phe	F		Non-polar (hydrophobic)
Tryptophan	Trp	W		Non-polar (hydrophobic)
Proline	Pro	P		Non-polar (hydrophobic)
Serine	Ser	S		Polar, uncharged (hydrophilic)
Threonine	Thr	T		Polar, uncharged (hydrophilic)
Cysteine	Cys	C		Polar, uncharged (hydrophilic)

Amino acid	3-letter code	1-letter code	Side chain	Property
Tyrosine	Tyr	Y		Polar, uncharged (hydrophilic)
Asparagine	Asn	N		Polar, uncharged (hydrophilic)
Glutamine	Gln	Q		Polar, uncharged (hydrophilic)
Aspartate	Asp	D		Polar, negatively charged (hydrophilic)
Glutamate	Glu	E		Polar, negatively charged (hydrophilic)
Lysine	Lys	K		Polar, positively charged (hydrophilic)



Amino acid	3-letter code	1-letter code	Side chain	Property
Arginine	Arg	R		Polar, positively charged, (hydrophilic)
Histidine	His	H		Polar, positively charged (hydrophilic)

Hydrogen bonding between the amino acids results in conformational changes of the peptide structure. The types of secondary structure that can be formed are:  $\beta$ -sheet,  $\alpha$ -helix and  $\beta$ -hairpin. Beta-sheets can form from neighbouring polypeptide chains that run in the same direction, known as parallel  $\beta$ -sheets, or from polypeptide chains that run in opposite directions, which is described as anti-parallel [193]. The polypeptide chains forming the  $\beta$ -sheet are known as  $\beta$ -strands. An  $\alpha$ -helix is formed when a polypeptide chain twists on itself forming a cylindrical structure [194]. A  $\beta$ -hairpin results from two anti-parallel  $\beta$ -sheets separated by 2–5 amino acid residues, resulting in a loop or turn [195].

Beta-sheets self-assemble as a result of hydrogen bonding along the fibres and link one  $\beta$ -sheet to the next, resulting in high stability [196]. Whereas with  $\alpha$ -helices, self-assembly is driven by hydrophobic interactions. A schematic outlining the self-assembly process is depicted in **Figure 2.8**.

This thesis is focussed on the use of ionic complementary  $\beta$ -sheet forming SAPHs; however, other types of self-assembling peptides are discussed below.

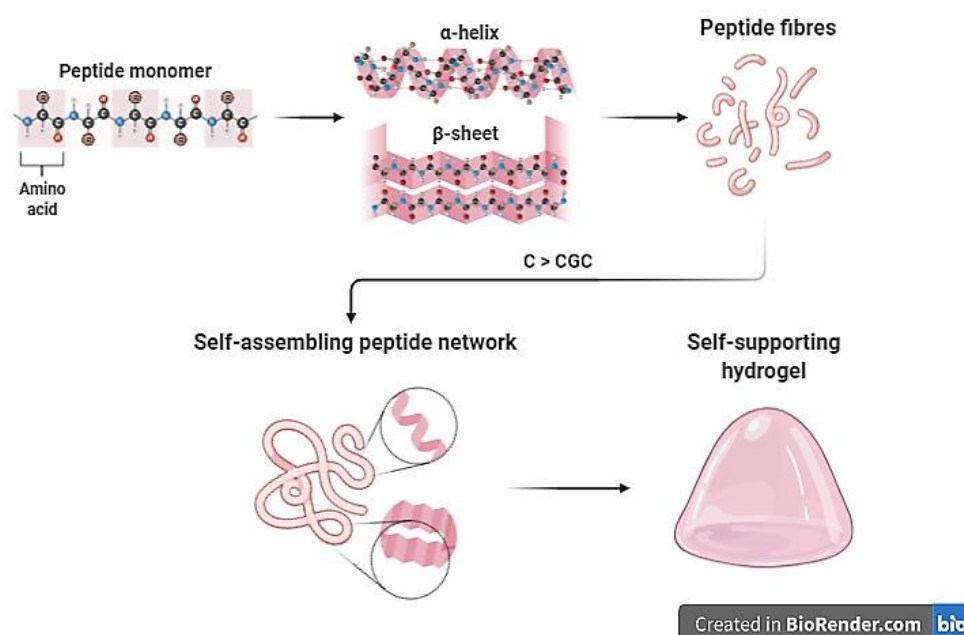


**Figure 2.8. Schematic of self-assembly process of SAPHs.** Peptide monomers aggregate to form peptide fibres rich in one of several secondary structures. Above the critical gelation concentration (CGC), these fibres form an entangled network within a self-supporting hydrogel. Created with BioRender.com.

### 2.5.2. $\alpha$ -Helix forming SAPHs

The  $\alpha$ -helix is formed by winding the amino acid backbone into a helix with 3.6 amino acids per turn, with helical stability achieved by hydrogen bonding between the carbonyl oxygen atoms of residues and the amide hydrogen atoms of residues four amino acids along the chain [197].

Alpha-helical SAPHs are components of coiled-coils, which are governed by hydrophobic interactions as well as electrostatic interactions between charged amino acids. These interactions are responsible for the cylindrical structure observed [198]. Coiled coils have a repeating heptad structure  $(abcdefg)_n$ , where  $n$  is the number of repeats and  $a-g$  signify the positions of the amino acids in a helical diagram (**Figure 2.9**) [194]. The repeating heptad structure is composed of hydrophobic (h) and polar (p) amino acids in a hpphppp pattern. The hydrophobic interactions between the 'a' and 'd' amino acids of multiple  $\alpha$ -helices give rise to the coiled-coil structure, due to the burial of residues forming a hydrophobic core to minimise interaction with water [199]. The charges of the 'e' and 'g' charged residues affect stability of the coiled coil: oppositely charged residues result in

stabilisation, whereas like charges result in repulsion [194]. The residues at ‘b’, ‘c’ and ‘f’ are exposed on the surface of the coiled coil and vary in design [200].

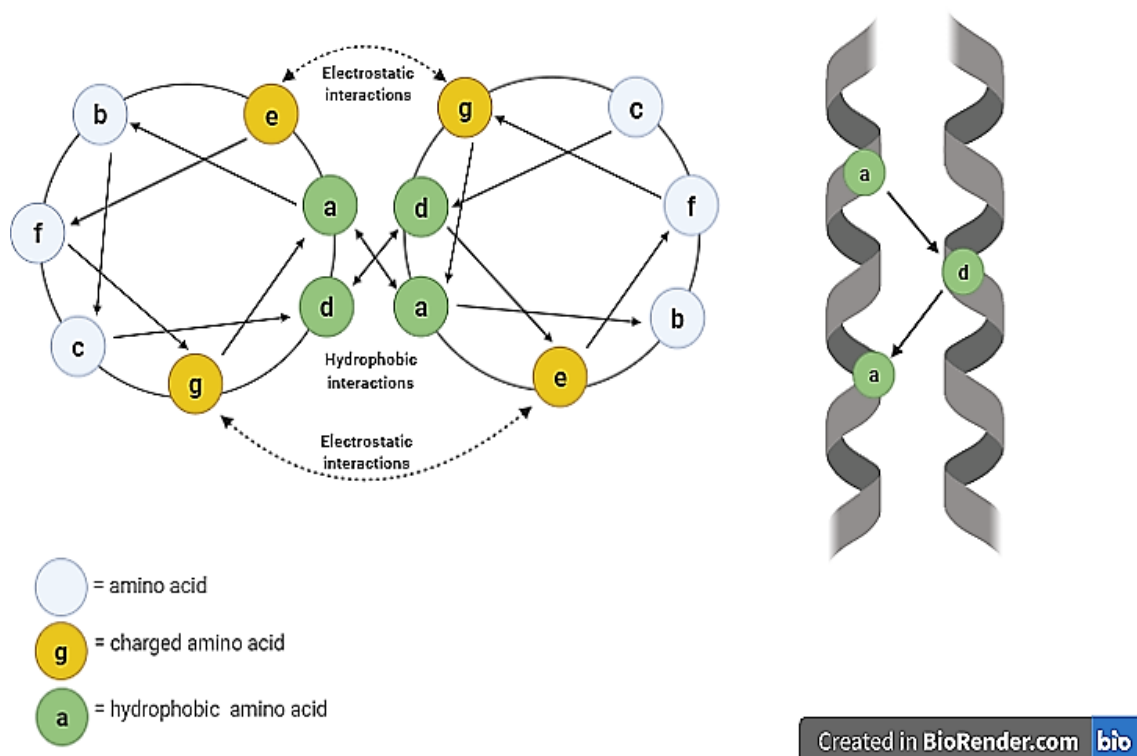


**Figure 2.9. Schematic of  $\alpha$ -helix coiled coil assembly.** Created with BioRender.com.

Alpha-helical SAPH AEAKAEAK (A = alanine, E= glutamine, K = phenylalanine) was unable to self-assemble, whereas AEAEAKAK self-assembled into fibrils with a diameter of 6 nm, which aggregated laterally to form a ‘pearl-necklace’ morphology [196]. However, gelation was not observed. It was suggested that the position of polar groups along the peptide chain affects self-assembly, due to hydrophobic interactions being highly sensitive to polar groups [196]. A series of  $\alpha$ -helical SAPHs were successfully formed based on repeats and alternations of alanine and glutamine residues, with hydrogels having strong hydrogen bonding melting upon heating, whereas those with strong hydrophobic interactions strengthening upon heating [201]. These hydrogels were found to support murine neural stem cell growth and viability [202]. A disadvantage of  $\alpha$ -helical SAPHs is that typically a large number of amino acids are required in the polypeptide chain to stabilise the helical structure [203].

### 2.5.3. $\beta$ -Hairpin SAPHs

The  $\beta$ -hairpin is formed by two anti-parallel  $\beta$ -sheets which are joined by a turn or loop [204]. An example of a  $\beta$ -hairpin SAPH is MAX1, which is 20 amino acids in length and composed of alternating lysine and glutamate residues with an intermittent tetrapeptide which adopts a  $\beta$ -turn structure (**Figure 2.10**) [205].

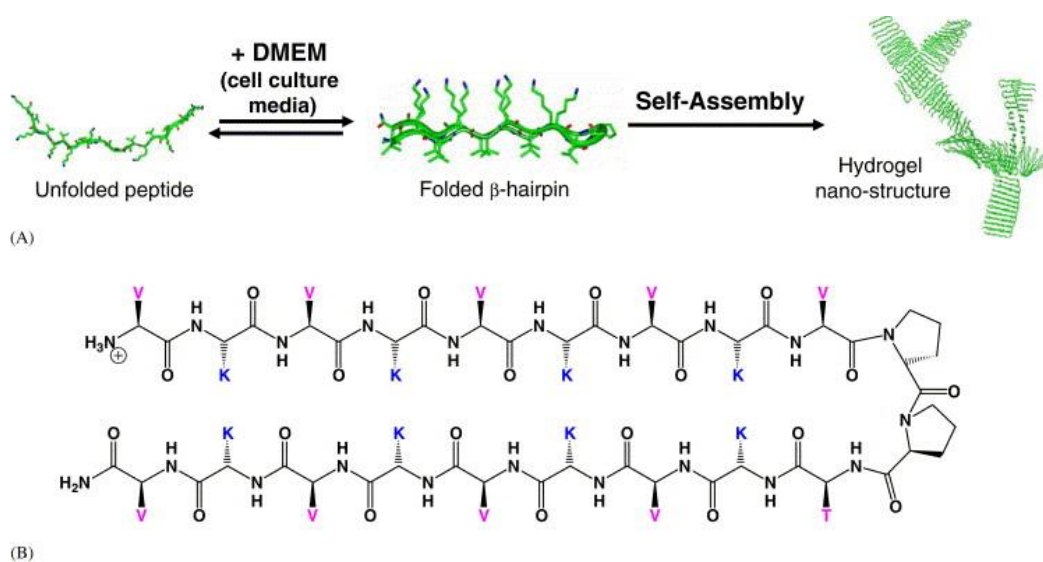


**Figure 2.10. Self-assembly process and amino acid sequence of MAX1 hydrogel.** This diagram has been reprinted with copyright permission from Elsevier [206].

This hydrogel is amphiphilic, due to the hydrophobic valine residues forming a hydrophobic face and the hydrophilic face composed of glutamate residues [205]. In acidic pH, the protonated lysine residues prevent peptide folding and self-assembly. However, the material is able to self-assemble upon the addition of salt resulting in charge screening of the positively charged lysine residues, as well as increasing the pH [207,208]. It can self-assemble and form a hydrogel under cell culture conditions (pH 7.4, cell culture media) and support the attachment of fibroblasts [206]. A derivative of MAX1, MAX8, was shown to support the 3D culture of medulloblastoma cells and was suitable for high throughput screening of chemotherapeutic drugs [32].

### 2.5.4. Short Peptide Derivatives

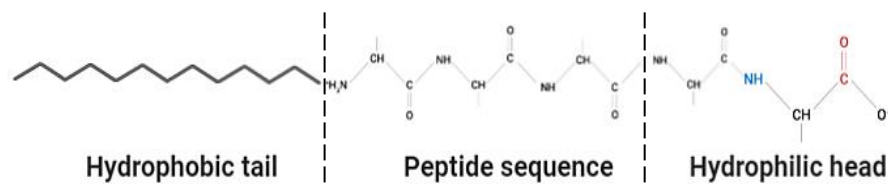
Short peptide derivatives are made up of less than 8 amino acids in length. Their self-assembly depends upon the groups attached, with aromatic groups contributing to  $\pi$ - $\pi$  interactions and bulky protecting groups such as fluorenylmethoxycarbonyl (Fmoc) leading to self-assembly [209]. A popular short peptide derivative, diphenylalanine (FF), derived from the  $\beta$ -amyloid protein involved in the pathophysiology of Alzheimer's disease, is able to self-assemble into nanotubes formed from  $\beta$ -sheets [210]. Aromatic

dipeptide systems formed from tryptophan-tryptophan, a combination of tryptophan and/or phenylalanine or tyrosine, were not able to self-assemble into the marked tubular structures formed in the FF system [210]. Under aqueous conditions, the addition of salts causes the formation of longer and wider FF nanotubules, due to the formation of salt bridges between the head and tail of the peptide monomers [211]. The salt bridges formed act as alternatives to peptide bonds due to the reduced energy required, resulting in radial and longitudinal growth of the nanofibres [211]. A series of Fmoc-dipeptide hydrogels have been shown to support the viability and phenotype of chondrocytes [212]. Fmoc-FF and Fmoc-RGD were used successfully for the encapsulation of dermal fibroblasts, resulting in cell viability and cell spreading in the presence of RGD [213].

### **2.5.5. Peptide Amphiphiles**

Peptide amphiphiles (PAs) are composed of three parts: a peptide chain containing a charged /hydrophilic head and a hydrophobic alkyl tail (**Figure 2.11**), rendering them similar to surfactants [214]. The peptide chain is mainly composed of hydrophobic amino acids, which results in a high degree of hydrogen bonding in the form of  $\beta$ -sheets. Changing this region of the PA molecule has been shown to alter the mechanical properties of the resulting hydrogel, with blocking hydrogen bonding at specific amino acid locations resulting in the inability of the molecule to form a hydrogel network [215]. The peptide chain is typically terminated by a bioactive epitope group, such as the RGD domain, to aid biocompatibility [215]. The advantage of attaching surfactant-like structures to the peptide chain is that the nanostructure can be controlled. Such an example is by altering the lipid tail length and number of charged sequences, resulting in modification of the length and diameter of the nanofibres [198].

A series of peptide amphiphilic hydrogels were developed whereby gelation was triggered by adding a peptide solution to cell culture media containing heavy metal ions [216]. The addition of heavy metal ions caused the PA to self-assemble into cylindrical structures, with the hydrophobic tails hidden in the core and hydrophilic peptide sequences displayed on the surface [217]. These hydrogels were formed of peptide segments of 6–12 amino acids in length coupled with a hydrophobic chain of 10–22 carbon atoms. It was found that the amino acid sequence of the C-terminal had a profound effect on cell viability, with mouse osteoblasts dying in glutamate-glutamine-serine (EQS) terminated fibrils, but proliferating and surviving for 3 weeks in lysine-glycine-glutamine (KGE) terminated fibrils.



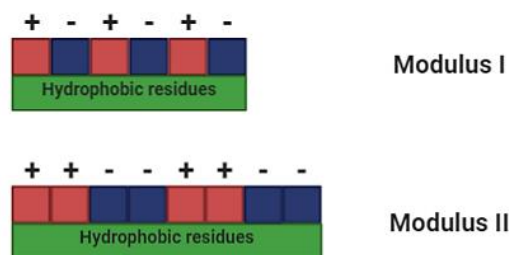
Created in BioRender.com 

**Figure 2.11. Chemical structure of peptide amphiphile hydrogel.** Created with BioRender.com.

### 2.5.6. Ionic Complementary SAPHs

This class of peptides was discovered in the 1980s by Zhang and colleagues, who isolated AEAEAKAKAEAEAKAK (EAK16-II; A = alanine, E = glutamic acid, K = lysine) from the yeast protein zuotin as a left-handed Z-DNA binding protein [218]. This peptide was found to self-assemble into a membrane which was unusually stable and adopted a  $\beta$ -sheet structure, consisting of alternating hydrophilic and hydrophobic residues [219]. The addition of salt in the form of cell culture media was also shown to induce formation of a stable hydrogel [220]. It was found that substituting positively charged lysine with positively charged arginine of throughout EAK16-II did not affect self-assembly. However, replacing positively charged amino acids with negatively charged residues resulted in  $\beta$ -sheet structures formed in the presence of salt, although hydrogels were not formed [18]. Ionic complementary SAPHs are characterised by periodic repeats of alternating hydrophilic and hydrophobic amino acids forming  $\beta$ -sheet structures with hydrophilic residues on the interior and hydrophobic residues on the exterior [221]. This ultimately results in a hydrophobic face and a hydrophilic face; with two  $\beta$ -sheets stacking together to form a hydrophobic core and the hydrophilic faces readily interacting with water molecules [221]. The complementary ionic sides are categorised into several moduli (modulus I, modulus II etc.), which is due to the repeating hydrophilic amino acids

alternating by one residue, two residues etc. [192]. Modulus I thus has a charge arrangement of  $+ - + - + -$  (**Figure 2.12**).



Created in BioRender.com 

**Figure 2.12. Moduli of ionic complementary SAPHs.** Created with BioRender.com.

Altering the peptide length, concentration and pH are methods used to alter the hydrogel properties [222]. Changing one amino acid has a remarkable effect on the overall charge, fibre structure and mechanical properties of the hydrogel formed.

AEAKAEAKAEAKAEAK (EAK16-I), EAK16-II and AEAEAEAEAKAKAKAK (EAK16-IV) have the same amino acid composition but different amino acid arrangement, resulting in different charge distribution [223]. The work completed by Jun *et al* proposed the charged worm-like chain model to explain the effect of charge on self-assembly; whereby the presence of a  $\beta$ -turn in the molecule shows that this is the most stable equilibrium for EAK16-IV and thus prefers a bent conformation. EAK16-II was also shown to form nanofibers at neutral pH, whereas EAK16-IV forms globular assemblies [224]. The different charge distributions result in stronger intramolecular attractions between the carboxyl groups of glutamic acid residues and the amino groups of lysine residues of EAK16-IV, causing exposure of the hydrophobic residues to the aqueous environment and bending of the EAK16-IV molecules. Increasing the hydrophobicity of the amino acids, from alanine to leucine, isoleucine or phenylalanine, results in the critical aggregation concentration (CAC) decreasing, which increases the likelihood of self-assembly by decreasing the minimum amount of energy needed to form a hydrogel [225].

Increasing the peptide concentration results in a reduced mesh and increased intermolecular hydrogen bonding due to more peptide monomer present, which manifests as a stiffer hydrogel being formed [226]. Increasing the peptide concentration of EFK8 (KFEFKFEF; K = lysine, F = phenylalanine, E = glutamate) from 2.7 to 10 mg/mL resulted in an increase in measured elastic modulus from  $1.59 \text{ kPa} \pm 0.06 \text{ kPa}$  to  $14.7 \text{ kPa} \pm 1.0 \text{ kPa}$ , which corresponded with a denser matrix observed with a larger number of fibres per volume [222].

The pH of the peptide system has also been shown to impact the self-assembly process; FEFK was demonstrated to form a hydrogel over the pH range of 2.0–12.0, however changing the pH value resulted in differing nanostructures formed [227]. At pH 6.0–8.0, electrostatic interactions between the charged residues and  $\pi$ - $\pi$  interactions resulted in lateral association, causing a hydrogel to form. At pH 2.0 and 12.0, electrostatic repulsion occurred between the charged amino acid residues, reducing lateral attraction between the peptide fibres. Hydrogels were still formed due to the  $\pi$ - $\pi$  interactions in the aromatic residues overcoming the electrostatic repulsion.

Based on the sequence of EAK16, Zhang designed the peptide RADARADARADARADA (RADA16; R = arginine, A = alanine, D = aspartic acid) by replacing positively charged lysine residues with arginine and negatively charged glutamic acid residues with aspartic acid [209,220]. This hydrogel has been commercialised as PuraMatrix™, a 3D scaffold capable of encapsulating cells and has been used successfully for tissue engineering and regenerative medicine purposes [228,229]. RADA16 also has been functionalised with various cell-binding motifs [230]. Ionic complementary SAPHs are non-toxic, biocompatible, degrade to form naturally occurring amino acids as waste products and can be functionalised to incorporate desired biological motifs and thus have great potential as a scaffold for 3D cell culture [190]. They have also been shown not to induce an inflammatory response *in vitro* [231]. Moreover, SAPHs are more able to mimic the ECM over commonly used biomaterials, due to the formation of nanofibers and pore sizes which are of the same scale as the ECM and the ability to modulate the mechanical properties [20].

The next section will discuss using SAPHs for the culture and *in vitro* modelling of cancer cells.



### 2.5.7. SAPHs for *In Vitro* Cancer Modelling

Various types of SAPHs have been used to create *in vitro* models of cancer, which have been summarised in **Table 2.4**. RADA16-I, previously discussed in **section 2.5.6**, is one of the most popular SAPH for this application. Ovarian cancer cell lines A2780, A2780/DDP and SK-OV-3 cultured using RADA16-I formed colonies typical of glandular epithelial tumours, however, the SK-OV-3 cell line did not form spheroids [232]. When treated with anti-cancer drugs paclitaxel and curcumin, a two to five times higher concentration was needed to inhibit cell growth by 50 %, compared with 2D cultured cells, showing that 3D cultured tumours using a SAPH exhibited the same chemotherapeutic resistance seen clinically [232]. Several studies using RADA16 for breast cancer research have shown that the material reduces malignancy of the cancer cells. One such study using RADA16-I to culture the breast cancer cell line MDA-MB-435S, which contains a large abundance of the breast CSC population, observed that the breast cancer cells exhibited a ‘reversed’ phenotype, indicated by basally-located nuclei and organised cytoskeletons, resembling non-cancerous breast acini [233]. Whereas in collagen I, cells exhibited a mesenchymal phenotype with elongated cell bodies and projections, and in Matrigel, the cells were observed to have disorganised nuclei. Another similar study investigating the breast cancer cell line MDA-MB-231 found that cells cultured in RADA16-I exhibited a reduced malignant phenotype, as shown by reduced migratory capacity compared with collagen I [28]. SMMC7721 liver cancer cells exhibited positive fibronectin staining in RADA16, alongside expression of angiogenesis related growth factors VEGFA, EGF and FGF [234].

The  $\beta$ -sheet forming FEFEFKFK, which has previously been used for 3D culture of nucleus pulposus cells [235] and chondrocytes [236], was shown to support viability and collagen I production of MCF-7 cells for up to 10 days in culture [29]. Another  $\beta$ -sheet SAPH, named h9e (FLIVIGSIIGPGGDGPGGD; F = phenylalanine, L = leucine, I = isoleucine, V = valine, G = glycine, S = serine, P = proline, D = aspartic acid) [237], has been used for culturing a number of cancer cell lines [27,238]. It was found that liver and colon cancer cells exhibited decreased sensitivity to chlorogenic acid treatment when compared with 2D culture, showing that the SAPH can act as a physical barrier to chemotherapeutic drug penetration. bQ13 (QQKFQFQFEQEQQ, Q = glutamine, K = lysine, F = phenylalanine), derived from the SAPH Q11 (QQKFQFQFEQQ) [239], was used to culture LNCaP prostate cancer cells, which formed spheroids after 7 days in culture and were found to be as equally sensitive to enzalutamide treatment as Matrigel embedded cells [240]. A series of amphiphilic SAPHs based on the VVVAAAH<sub>2</sub>K (PA-H;

V = valine, A = alanine, H = histidine, K = lysine) functionalised with different cell binding moieties were found to support the growth and intercellular network formation of the ovarian cancer cell line OVCAR-4, HUVECs and MSCs, resulting in the formation of a vascularised ovarian cancer model [30].

*In vitro* modelling of cancer has been discussed in detail in the previous sections. The remainder of this chapter will focus on modelling vasculature and tumour angiogenesis *in vitro* using hydrogels and SAPHs in particular.

**Table 2.4. Summary of strategies used to mimic cancer *in vitro* using SAPHs.** The class of SAPH used, mechanical properties (if measured), cell type(s), features of cancer studied, response to chemotherapeutic drugs (if studied) and the reference are noted.

Class of SAPH	Mechanical Properties	Cell type(s)	Features of cancer studied	Response to chemotherapeutic drugs	Reference
Ionic complementary $\beta$ -sheet	50–220 Pa	A549 (lung cancer)	n/a	n/a	Sheikholeslam <i>et al.</i> , 2018 [241].
$\beta$ -hairpin	100 Pa	DAOY/ONS-76 (medulloblastoma)	n/a	Increased sensitivity to cisplatin and vorinostat compared with 2D.	Worthington <i>et al.</i> , 2017 [32].
$\beta$ -sheet	100–700 Pa	MCF-7 (breast)	n/a	Decreased viability when treated with cisplatin (no 2D control).	Huang <i>et al.</i> , 2013 [242].
$\beta$ -sheet	n/a	HepG2 (liver)/ SW480 (colon)	n/a	Decreased sensitivity to chlorogenic acid compared with 2D.	Xu <i>et al.</i> , 2019 [238].
Ionic complementary $\beta$ -sheet	3300 Pa	MDA-MB-231 (breast cancer)	n/a	n/a	Mi <i>et al.</i> , 2009 [28].
Ionic complementary $\beta$ -sheet	n/a	A2780, A2780/DDP, SK-OV-3 (ovarian)	<b>Invasion</b> – no difference in invaded cells between RADA16 and collagen I.	Decreased sensitivity to 5-FU, paclitaxel and curcumin compared with 2D.	Yang & Zhao, 2011 [232].
Ionic complementary $\beta$ -sheet	n/a	SMMC7721 (liver)	<b>Angiogenesis</b> – Expression of VEGF, EGF and FGF, no difference in expression levels between RADA16, collagen I and Matrigel. <b>ECM deposition</b> – no fibronectin or laminin production.	n/a	Song <i>et al.</i> , 2015 [234].
$\beta$ -sheet	1000–10,000 Pa	LNCaP (prostate)	n/a	Increased sensitivity to enzalutamide, compared with Matrigel and RADA16-I.	Hainline <i>et al.</i> , 2019 [240].
Peptide amphiphile	2133 Pa $\pm$ 111 Pa	OVCAR-4 (ovarian), HUVECs, MSCs	<b>Angiogenesis</b> – intercellular network formed by tri-cultures.	Resistance to carboplatin and paclitaxel treatment.	Hedegaard <i>et al.</i> , (2020) [30].
Ionic complementary $\beta$ -sheet	500 Pa – 5 kPa	MCF-7	<b>ECM deposition</b> – collagen I production	n/a	Ashworth <i>et al.</i> , (2020) [29].

## 2.6. Modelling Vasculature Formation *In Vitro*

### 2.6.1. Overview

Tissue engineering blood vessel-like structures *in vitro*, resembling tubes, has been achieved using naturally derived hydrogels, such as collagen I [26,243] and Matrigel [244]. The main cell type used to create tubular structures is ECs, notably HUVECs [245], as they are easy to handle and isolate [246]. As discussed in **section 2.2.4**, within the vasculature system, ECs are supported by mural cells. The ECs benefit from the chemokines and growth factors produced by the secondary cell source, resulting in stabilisation and maturation of the endothelial network. To represent this *in vitro*, HUVECs are often co-cultured with another cell line representing mural cells providing structural support to the vascular network [247]. Such cell types used as supporting cells include: MSCs, fibroblasts, smooth muscle cells, osteoblasts and pericytes [247]. This section will focus on co-culture of HUVECs and MSCs, as this method will be used in experimental sections. When encapsulated within a hydrogel, ECs and supporting cells will attach to the surrounding matrix, resulting in an elongated morphology (**Figure 2.13**). The ECs differentiate and reorganise themselves into tubes. Supporting cells stabilise the formed structures in response to increased production of angiogenic factors.

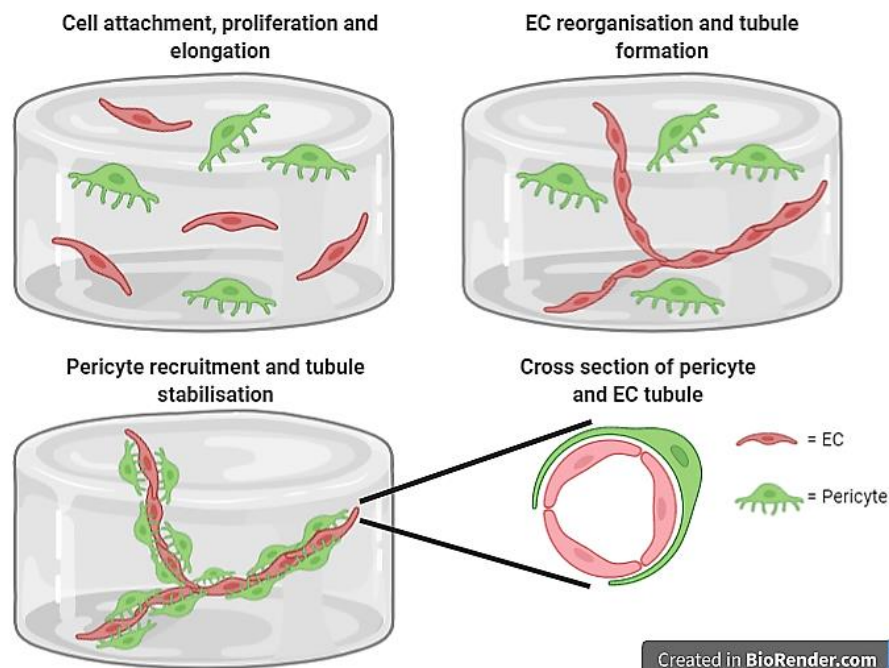


**Figure 2.13.** *In vitro* tube formation by ECs and pericytes within a hydrogel. Created with BioRender.com.

### **2.6.2. Co-Culture using HUVECs and MSCs**

MSCs are multipotent stem cells that can self-renew and differentiate into several lineages, namely: osteogenic, chondrogenic and adipogenic [248]. MSCs are derived from several sources within the body, including the bone marrow, adipose tissue, placenta, peripheral blood, umbilical cord and cord blood [249]. There is evidence to suggest that BM-MSCs adopt a perivascular niche and thus behave as pericytes [250]. When co-cultured with ECs in a collagen I/fibronectin hydrogel, MSCs produce  $\alpha$ -smooth muscle actin, desmin and sm22 $\alpha$ , which are known pericyte markers [251,252]. It has also been observed that ECs implanted alone *in vivo* could form blood vessel-like structures but regressed quickly, whereas when implanted alongside MSCs could form vessels which lasted much longer [26,252]. Moreover, tubes formed from MSCs and ECs were longer in length with branching observed, compared with EC only tubes [253]. Clearly, the cell-cell interactions between ECs and MSCs result in maturation and stabilisation of the tubes formed. Co-culture of HUVECs and MSCs has been shown to upregulate expression of VE-cadherin, an endothelial-specific marker, compared with HUVEC monocultures [254,255].

Parameters used to influence HUVEC behaviour in hydrogels are discussed in the next section.

### **2.6.3. Designing Hydrogels for Vasculature *In Vitro***

For ECs to attach, organise and differentiate into tube-like structures, the material used must be able to mimic the ECM and stimulate this behaviour. To achieve this, the hydrogel used must be designed accordingly. Parameters such as matrix stiffness, functionalisation with ECM derived binding motifs and creating hybrid composites with natural hydrogels have been employed, and will be discussed in this section.

#### **2.6.3.1. Matrix Stiffness**

It is well established that the mechanical properties of a biomaterial can influence cell behaviour [135]. For HUVECs, the stiffness of the hydrogel used can alter behaviour too. Several studies have found that HUVECs will form tubes on soft hydrogels, notably in 2D culture. HUVECs cultured on polyacrylamide hydrogels with a Young's modulus of 140 Pa formed interconnected networks, but increasing the hydrogel stiffness to 2500 Pa reduced the tendency to form tubular structures [39]. Bovine aortic endothelial cells formed a network of tubes on compliant hydrogels (Young's modulus of 200 Pa), but not on stiffer (10 kPa) hydrogels [256]. For 3D culture, the impact of matrix stiffness is more

varied. PEG hydrogels containing MMP-sensitive sites and RGD binding sites were used to co-culture HUVECs and mesenchymal progenitor cells; it was found that the polymer weight of the hydrogel affected cell behaviour, with softer, compliant (7.5 % polymer weight) hydrogels forming tubule structures which quickly regressed, and stiff (12.5–15 % polymer weight) hydrogels failing to induce cell-cell contacts [257]. For collagen I hydrogels, increasing the matrix stiffness resulted in denser EC networks [258] and increased angiogenic sprouting and EC outgrowth [259] compared with softer hydrogels.

The effect of matrix stiffness on ECs cultured in 3D is ambiguous. It could be possible that in 2D culture, the impact of stiffness is more prominent due to the cells being constrained to one dimension. Whereas in 3D culture, cells do not experience such constraints and are able to remodel their surrounding environment [260]. Moreover, increasing matrix stiffness results in reduced porosity, increasing the number of bioactive molecules available to cells [260].

#### **2.6.3.3. Functionalisation**

Due to their design, synthetic hydrogels lack bioactive cues that are needed for ECs to attach and differentiate into tubular structures. Therefore, functionalisation with ECM-derived binding motifs is often used in designing hydrogels for tissue engineering of blood vessels. Functionalisation of hyaluronic acid-tyramine hydrogel with RGD domains resulted in HUVEC adhesion and cell-cell contacts resulting in capillary formation, compared with hydrogels without RGD functionalisation [261]. Interestingly, HUVECs cultured within gellan-gum hydrogels functionalised with RGD domains were only able to form interconnected tubules in the presence of adipose derived stem cells (ASCs), highlighting the importance of a supporting cell type when creating blood vessel-like structures *in vitro* [262]. PEG cross-linked gelatin hydrogels functionalised with peptides mimicking VEGF and the YIGSR (Y = tyrosine, I = isoleucine, G = glycine, S = serine, R = arginine) domain derived from laminin were able to induce differentiation of HUVECs into capillary-like structures after 5 days, whereas the hydrogel alone could not stimulate this behaviour [263].

#### **2.6.3.4. Hybrid Composites with Natural Hydrogels**

The combination of a synthetic and a natural hydrogel provide the cells with native cell binding motifs, alongside tuneable properties and a degree of chemical definition. Gelatin methacrylate (GelMA) and pluronic 127 were combined to create a hydrogel composite which was able to support the viability and phenotype of HUVECs after 10 days [264].

However, the tube formation was not observed, suggesting that the hydrogel composite could not support the underpinning events leading to tube formation by HUVECs. Conjugation of collagen I to PEG resulted in capillary formation of HUVECs and MSCs when encapsulated, with higher concentrations of PEG resulting in HUVEC death [265]. The degree of methacrylation in GelMA hydrogels has also been shown to affect tube formation, with the lowest methacrylation (1 M) resulting in more vasculogenesis and interconnections of human endothelial colony forming cells (HECFs) and MSCs, with the highest methacrylation (10 M) resulting in fewer cell-cell contacts and branch points [266]. The use of SAPHs for developing vasculature will be discussed in the next section.

#### **2.6.4. SAPHs for Vasculature Formation *In Vitro***

As discussed in **section 2.5.6 & 2.5.7**, RADA16 has been a popular SAPH to use for creating tube-like structures *in vitro*, due to its use in other tissue engineering applications [17]. HUVECs encapsulated within RADA16-I and RADA16-II were able to organise and form tubes with primitive lumens in response to decreasing the matrix stiffness [36]. However, another study using RADA16 for culture of microvascular ECs showed that increasing the peptide concentration, resulting in a greater hydrogel stiffness, resulted in larger and more extended networks of tubes [34]. VEGF gene expression was also upregulated compared with collagen gels, and ECs were able to survive within the peptide matrix for 2 weeks and formed 3D tubular structures. A study comparing RADA16-I and RADA16-II with FKFEFKFE (KFE-8) and KLDLKLDL (KLD-12) for tissue engineering structures resembling blood vessels, found increased adhesion of HUVECs to the RADA16 gels with formation of capillary structures, which did not occur in either KFE-8 or KLD-12 [267]. The authors attributed this finding to the differences in hydrophobicity between the hydrogels, although other factors such as matrix stiffness were not investigated. Functionalisation of RADA16 with RGD or a VEGF receptor agonist resulted in increased adhesion, survival, elongation and capillary morphogenesis of HUVECs compared with RADA16 alone [268]. Functionalised RADA16 with laminin derived motifs YIGSR, RYVVLPR (R = arginine, Y = tyrosine, V = valine, L = leucine, P = proline) or the collagen IV motif TAGSCLRKFSTM (T = threonine, A = alanine, G = glycine, S = serine, L = leucine, R = arginine, K = lysine, F = phenylalanine, M = methionine) resulted in increased growth and proliferation of human aortic endothelial cells (HAECs) and increased production of laminin and collagen IV, indicative of basement membrane deposition [269].

Functionalisation of SAPHs for vasculature formation has also been investigated using another system: Q11 was functionalised with either RGD or laminin-derived IKVAV (I = isoleucine, K = lysine, V = valine, A = alanine) binding motifs [239]. RGD modified Q11 was able to positively influence the elongation and spreading of HUVECs, whilst IKVAV did not exert major benefits to HUVEC morphology. Q11 functionalised with RGD, IKVAV and YIGSR domains was further investigated for HUVEC culture; it was found that a combination of RGD and IKVAV resulted in optimal HUVEC growth, whilst combining RGD and YIGSR resulted in an antagonistic interaction [38]. The strategies used to tissue engineer tubular structures *in vitro* using SAPHs has been summarised in **Table 2.5**.



**Table 2.5. Summary of strategies used to create vasculature *in vitro* using SAPHs.** The class of SAPH, SAPH modifications (if any), cell type(s), outcomes and reference are provided.

<b>Class of SAPH</b>	<b>Modifications made to SAPH</b>	<b>Cell type(s) used</b>	<b>Presence of growth factors and other stimuli</b>	<b>Outcome</b>	<b>Reference</b>
Ionic complementary $\beta$ -sheet	Decreasing matrix stiffness.	HUVECs	VEGF (50 ng/mL) and phorbol-myristate acetate (50 ng/mL).	Tubule structures with lumens.	Sieminski <i>et al</i> , 2007 [36].
Ionic complementary $\beta$ -sheet	Increasing peptide concentration.	Microvascular ECs	1% endothelial cell growth supplement (contents not disclosed).	Increased VEGF expression, 3D tubule structures formed.	Narmoneva <i>et al</i> , 2005 [34].
Ionic complementary $\beta$ -sheet	Changing hydrophobicity of amino acid sequence.	HUVECs	VEGF (50 ng/mL) and phorbol-myristate acetate (50 ng/mL).	Increased cell adhesion, formation of capillary structures in RADA16 hydrogels.	Sieminski <i>et al</i> , 2008 [267].
Ionic complementary $\beta$ -sheet	Functionalisation with RGD or VEGF receptor.	HUVECs	n/a	Increased adhesion, survival and elongation compared with RADA16 alone.	Wang <i>et al</i> , 2008 [268].
Ionic complementary $\beta$ -sheet	Functionalisation with RGD or IKVAV.	HUVECs	n/a	RGD modified SAPH promoted spreading and elongation of HUVECs, IKVAV did not affect cell morphology.	Jung <i>et al</i> , 2009 [239].
Ionic complementary $\beta$ -sheet	Functionalisation with YIGSR, RYVVLPR or TAGSCLRKFSTM.	HAECs	n/a	Increased survival, proliferation and basement membrane deposition on functionalised hydrogels.	Genové <i>et al</i> , 2005 [269].
Ionic complementary $\beta$ -sheet	Functionalisation with RGD, IKVAV or YIGSR.	HUVECs	n/a	Increased growth and attachment on RGD & IKVAV functionalised hydrogels.	Jung <i>et al</i> , 2011 [38].

## 2.7. Conclusions

The TME is complex and dynamic by nature, with the cross-talk of different components required to perpetuate tumour growth, disease progression and resistance to anti-cancer drugs. *In vitro* models recapitulating the TME are therefore necessary to aid development of efficacious anti-cancer drugs, as well as drugs that target components of the TME. 3D *in vitro* models utilise both liquid-based and material-based methods; the latter utilise an ECM mimicking platform, which offers cell-ECM interactions to be emulated.

Biomaterials, and in particular hydrogels, are becoming increasingly popular in tissue engineering applications due to their ability to mimic the ECM and 3D environment, as well as modifiable physical and chemical properties. For drug discovery, chemical definition is vital for ensuring reproducibility. Choosing a platform for 3D *in vitro* modelling must meet the requirements of exhibiting minimal batch-to-batch variability as well as being able to support cell attachment and growth.

Synthetic hydrogels, specifically SAPHs, are therefore promising candidates as platforms for mimicking solid tumours and the TME *in vitro*. SAPHs are able to meet the aforementioned requirements, as they are composed of naturally occurring amino acid sequences, and are hydrophilic, resulting in biocompatibility. In addition, their nanofibrous architecture mimics that of the ECM. A class of SAPHs designed by Zhang and colleagues is of particular interest; known as ionic complementary SAPHs [219]. These SAPHs are  $\beta$ -sheet rich and self-assemble under aqueous conditions to form nanofibres forming a macromolecular structure. SAPH systems have previously been used for 3D culture of breast cancer cell lines [29,32,232,238,242]. However, initial cell viability, growth and anti-cancer drug efficacy is mainly explored without investigating events of tumour progression and features of the TME [28,241]. Vasculature is an important feature of solid tumours, and choosing or designing a hydrogel to promote assembly of HUVECs into a tubular network should be carried out with consideration. Modifications to synthetic hydrogels, such as functionalisation, are often implemented to aid HUVEC growth. Although SAPHs have been utilised to create vasculature, the majority of studies solely use ECs without a supporting cell type [30].

Chapter 3 will outline the methods and materials used in this thesis to explore the use of SAPHs for *in vitro* modelling of solid tumours and the vasculature component of the TME.

## CHAPTER 3 – Materials and Methods

### 3.1. Hydrogel Preparation

#### 3.1.1. Self-Assembling Peptide Hydrogels

PeptiGelAlpha1 ± 0.1 %, 1 %, 10 % and 40 % RGD, PeptiGelAlpha1 + 15 % RGD & 15 % IKVAV, PeptiGelAlpha2 and PeptiGelAlpha4 SAPHs (Manchester BIOGEL, UK) were provided as ready-to-use hydrogels. The amino acid sequences and peptide concentrations of the hydrogels are proprietary information and therefore cannot be disclosed.

VEVKVEVK (V8) (Biomatik, USA) was provided as lyophilised powder in a hydrochloric acid salt. Samples were prepared by dissolving V8 powder in high performance liquid chromatography (HPLC) grade water to a final concentration of 10 mg/mL and titration using 0.5 M sodium hydroxide (NaOH) until gelation occurred (~ pH 5.5). A pH probe was used to measure the pH of the peptide solution. The peptide hydrogel was supplemented with additional HPLC grade water until a final volume of 1 mL was reached. The hydrogel was vortexed to ensure homogeneity and stored at 4 °C overnight to allow the hydrogel to stabilise before use.

Laminin-enriched SAPHs were used to investigate if the IKVAV and YIGSR motifs found within the protein would stimulate HUVEC behaviour. For laminin supplemented SAPH, laminin extracted from Engelbreth-Holm-Swarm tumours (Sigma-Aldrich, UK) was used. Laminin (1 mg/mL) was physically mixed into hydrogels at concentrations of 5, 25 and 50 µg/mL.

#### 3.1.2. Collagen I

Rat-tail collagen I (ThermoFisher, UK) was prepared on ice to prevent spontaneous gelation. Collagen I (stock concentration 3 mg/mL) was added to 4-(2-hydroxyethyl)-1-piperazineethanesulfonic acid (HEPES) buffer and Dulbecco's Modified Eagle Medium (DMEM) media (Sigma-Aldrich, UK) and titrated with 1 M NaOH. The optimal pH for gelation was 7.4, which was confirmed using Hydrion Brilliant pH-testing strips (Sigma-Aldrich, UK). Gelation of the hydrogel was achieved by incubation at 37 °C, 20 % (v/v) O<sub>2</sub>, 5 % (v/v) CO<sub>2</sub> for 1 hour, whereby the material appeared white and opaque.

### 3.1.3. Matrigel

Growth factor reduced Matrigel (Corning, USA) was prepared on ice to prevent spontaneous gelation. Matrigel (stock concentration: 10 mg/mL) was diluted using cold DMEM media to a final concentration of 5 mg/mL. Gelation was achieved by incubation at 37 °C, 20 % (v/v) O<sub>2</sub>, 5 % (v/v) CO<sub>2</sub> for 1 hour.

## 3.2. Attenuated Total Reflectance – Fourier Transform Infrared Spectroscopy

Attenuated total reflectance – Fourier transform infrared spectroscopy (AT-FTIR) was used to characterise the secondary structure of the SAPHs used. AT-FTIR measures the wavelength and absorption of IR radiation; this absorption results in vibrations of molecular bonds. For peptides, amide bands recorded on IR spectra represent different molecular vibrations [270]. The amide I band, found between 1600–1700 cm<sup>-1</sup>, is the most sensitive to structural change and is the most commonly used in secondary structural characterisation of protein and peptide samples [271].

A ThermoFisher Nicolet 5700 spectrometer equipped with an attenuated total reflectance diamond accessory was used to record the spectra of SAPHs. A volume of 50 µL of hydrogel was placed onto the crystal of the spectrophotometer. A resolution of 4 cm<sup>-1</sup> was used and absorbance spectra were obtained between 400 and 4000 cm<sup>-1</sup> over 256 scans. HPLC grade water was used as a background control and removed from all spectra. OMNIC software was used to collect the spectra. Data were smoothed using 2<sup>nd</sup> order smoothing with an average number of 5 neighbours using GraphPad Prism 9.0 software.

## 3.3. Oscillatory Shear Rheometry

Small amplitude oscillatory shear rheometry was used to measure the mechanical properties of the hydrogels used. Rheological studies provide two values based on the shear modulus: the storage modulus (G') and loss modulus (G''). The G' indicates how solid-like a material is, whilst the G'' indicates how liquid a material is. These values are measured as a function of time, strain and frequency [272]. When G' > G'', the material is considered to be solid, and when G'' > G', the material is no longer considered to behave as solid-like [273]. The shear modulus can be indirectly compared to the Young's modulus or elastic modulus, which is typically measured with AFM or indentation, using the following equation:

$$E = 2G(1 + \nu)$$

### Equation 3.1. Modulus of rigidity.

Where  $E$  = elastic modulus,  $G$  = shear modulus and  $\nu$  = Poisson's ratio.

An oscillatory rheometer (Discovery Hybrid 2, TA Instruments, USA) equipped with a Peltier plate to control temperature was used to measure the viscoelastic properties of the hydrogels. A parallel plate geometry of 20 mm was used. For each run, 250  $\mu$ L of sample was pipetted into 12 well ThinCert cell culture inserts (Greiner Bio-One, UK) and loaded onto the stage and the upper plate was lowered to a 500  $\mu$ m gap. For media conditioning experiments, samples were exposed to 1 mL of DMEM surrounding the insert and 250  $\mu$ L on top of the hydrogel. The samples were incubated at 37 °C, 20 % (v/v) O<sub>2</sub>, 5 % (v/v) CO<sub>2</sub>. Cell culture media was removed from the samples prior to loading on the stage. Amplitude sweeps were used to determine the linear viscoelastic region (LVR) and yield strain of the hydrogel, within the range of 0.02–30 % using a constant frequency of 1 Hz. Frequency sweeps were performed within the range of 0.01–10 Hz at a constant strain of 0.2 %. To assess the shear-thinning properties of the hydrogel, samples were exposed to time sweeps with alternating cycles of recovery (5 minutes at 0.2 % strain with 1 Hz frequency) and high shear (5 minutes at 100 % strain with 1 Hz frequency) for 35 minutes. A solvent trap was used to prevent evaporation and all samples were measured at 37 °C.

For cell-laden samples, the mechanical properties were measured at designated time points using the same parameters as described. Frequency sweeps within the range of 0.01–10 Hz at a constant strain of 0.2 % were carried out, with the  $G'$  at 1 Hz used to indicate the stiffness of the sample. Acellular samples were used as controls and were incubated under the same conditions as cell-laden samples, including the same volume of media mixed into the hydrogel, media changes and exposure to a 37 °C and 20 % (v/v) O<sub>2</sub>, 5 % (v/v) CO<sub>2</sub> environment.

### 3.4. Transmission Electron Microscopy

Transmission electron microscopy (TEM) imaging was carried out to observe both fibre morphology and network architecture of hydrogels, and to visualise cell-material interactions. TEM works by focussing a beam of electrons onto a sample and a monotonic image is produced by the transmission difference in electron density [274]. Staining the sample with a heavy metal, such as uranyl, is used to provide contrast to the sample.

For acellular samples, hydrogels with no exposure to cell culture media were diluted 100-fold using HPLC grade water to observe network formation of the fibres.

Carbon-coated copper grids with a 400 mesh size were exposed to positive charge for

2 minutes. A volume of 10  $\mu\text{L}$  of diluted sample was pipetted onto Parafilm and a grid was placed film-side down on the sample for 30 seconds. Grids were washed twice with water. The grids were exposed to 1 % (w/v) uranyl acetate (UA) for 30 seconds, before washed with water once again. Samples were air-dried for 24 hours prior to imaging. The FEI Tecnai 12 Biotwin Transmission Electron Microscope was used to image samples. Images were collected digitally using the Gatan Orius SC1000 CCD camera.

For cell-laden samples, cell culture media was removed from all samples and washed with Dulbecco's phosphate buffered saline (dPBS) (Sigma-Aldrich, UK). Samples were subsequently fixed with 4 % (v/v) formaldehyde + 2.5 % (v/v) glutaraldehyde in 0.1 M HEPES buffer (pH 7.2) for 1 hour. Samples were stored at 4 °C until further processing. The samples were post-fixed with 1 % (w/v) osmium tetroxide + 1.5 % (w/v) potassium ferrocyanide in 0.1 M cacodylate buffer (pH 7.2) for 1 hour, followed by 1 % (v/v) tannic acid in 0.1 M cacodylate buffer (pH 7.2) for 1 hour, and finally in 1 % (w/v) UA in water for 1 hour. The samples were then dehydrated in a series of increasing ethanol concentrations, infiltrated with TAAB Low Viscosity resin and polymerised for 24 hours at 60 °C. Sections were cut using a Reichert Ultracut ultramicrotome. The FEI Tecnai 12 Biotwin Transmission Electron Microscope was used to image samples. Images were collected digitally using the Gatan Orius SC1000 CCD camera.

### **3.5. Doxorubicin Diffusion through PeptiGelAlpha1**

Doxorubicin hydrochloride (Sigma-Aldrich, UK) was dissolved in dimethyl sulfoxide (DMSO) (VWR International, UK) to provide a stock solution of 10 mg/mL. The stock solution was diluted in complete cell culture media to concentrations of 5, 10, 50 and 100  $\mu\text{M}$ , using the molecular weight of doxorubicin (543.52 g/mol) to calculate final concentrations. A vehicle control of 1 % (v/v) DMSO was also used. PeptiGelAlpha1 was dispensed into 24 well ThinCert inserts (100  $\mu\text{L}$ /insert) using a positive displacement pipette, exposed to the supplemented media and incubated at 37 °C, 20 % (v/v) O<sub>2</sub>, 5 % (v/v) CO<sub>2</sub> for 24 hours. Control TCP samples using the same concentrations and conditions were used as a comparison as there are no physical barriers preventing drug penetration. Confocal imaging was used to visualise doxorubicin penetration into the hydrogel. Images were collected using the CQ1 spinning disk inverted confocal microscope (Yokogawa, Japan) using excitation/emission wavelengths of 488 nm and 520 nm. Penetration of the drug through the hydrogel was observed via 3D rendering of the 100  $\mu\text{M}$  sample, using both fluorescence and multi-photon imaging with a Leica SP8 confocal microscope using excitation/emission wavelengths of 488 nm and 525 nm.

### 3.6. Cell Culture and Maintenance

All cells were maintained under standard cell culture conditions (37 °C; 20 % (v/v) O<sub>2</sub>, 5 % (v/v) CO<sub>2</sub>) in T75 flasks unless stated otherwise.

MCF-7 breast adenocarcinoma cells (ATCC, USA) were maintained in low glucose DMEM supplemented with 10 % (v/v) foetal bovine serum (FBS) (Sigma-Aldrich, UK), 1 % (v/v) penicillin and 1 % (v/v) streptomycin (Sigma-Aldrich, UK).

MDA-MB-231 human breast adenocarcinoma cells (ATCC, USA) were maintained in high glucose DMEM with 10 % (v/v) FBS, 1 % (v/v) penicillin and 1 % (v/v) streptomycin.

HUVECs were obtained from a pooled donor (Promocell, Germany). HUVECs and red fluorescent protein labelled HUVECs (RFP-HUVECs) were maintained in flasks pre-treated with 0.1 % (v/v) gelatin with Endothelial Cell Growth Medium 2 (ECGM-2; Promocell, Germany). This media contained supplements of 5 ng/mL EGF, 10 ng/mL FGF, 20 ng/mL IGF and 0.5 ng/mL VEGF.

MSCs were obtained from a single human bone marrow-derived donor (Promocell, Germany). MSCs and green fluorescent protein labelled MSCs (GFP-MSCs) were maintained in flasks treated with 0.1 % (v/v) gelatin with Mesenchymal Stem Cell Medium 2 (Promocell, Germany).

RFP-HUVECs and GFP-MSCs were kindly gifted by Jekaterina Maksimcuka. The protocol used to transduce both cell types is described in **section 3.7**.

All cell types were passaged 1 in 3. Cells were passaged when they had reached 70–80 % confluence. To detach the cells from the TCP, cells were washed once with dPBS and 1 mL of trypsin-EDTA solution (Sigma-Aldrich, UK) was added to each flask. Cells were incubated at 37 °C for 3 minutes. The flask was gently tapped to promote detachment of the cells and at least twice the volume of complete cell culture medium was added to neutralise the trypsin-EDTA solution. Aliquots of cell suspension were pipetted into new T75 flasks for sub-culturing. Excess cells were resuspended in FBS with 10 % (v/v) DMSO and collected into cryovials. Cells were frozen at -80 °C in a Mr Frosty container until later use. For experiments, p5–20 were used for MCF-7 cells, p5–19 for MDA-MB-231 cells, p4–15 for HUVECs and p3–6 for MSCs were used, unless stated otherwise.

### **3.7. Transduction of HUVECs and MSCs with Fluorescent Proteins**

Second generation lentiviral transduction of cells was used to permanently label HUVECs with CopRFP and MSCs with TagGFP. This was undertaken in order that cells would fluoresce throughout passages and enabled live cell imaging without the need for membrane staining prior to encapsulation. To produce the virus, 70–80 % confluent human embryonic kidney 293T cells were used. Briefly, one 15 mL falcon tube containing 6 µg of Pcdh lentivirus vector, 4.5 µg of PsPAX2, 3 µg of PMD2G, and 50 µL of serum free DMEM was added to one tube containing 27 µL x1 polyethylenamine (100 mg/mL diluted 100 fold in 150 mM sodium chloride (NaCl)) and 250 µL of serum free DMEM. The solution was incubated for 30 minutes at room temperature. A volume of 500 µL of solution was added to one T75 flask of cells and incubated overnight at 37 °C. On the following day, the cells were viewed using a fluorescence microscope to assess transduction efficiency. The media was replaced with standard cell media containing 10 mM sodium phenyl butyrate and incubated for 4–8 hours. The media was replaced again after 4–8 hours. Media was removed the following day and 5 µg/mL protamine sulphate was added. The media was filtered through a 0.45 µm syringe filter and used at a 1:5 virus to media ratio to infect confluent p1 HUVECs or p1 MSCs.

#### **3.7.1. Fluorescence-Activated Cell Sorting**

A BD Biosciences Aria Fusion sorter was used to sort the cells. Diva 8 software was used to produce a histogram of forward scatter height versus scatter area to select single cells by drawing region P1. A histogram of forward scatter vs side scatter was used to draw region P2 around the intact cells. The combination of P1 and P2 was used to gate the histograms displaying the fluorescence so that only single intact cells were shown. The GFP-MSCs were imaged using excitation/emission wavelengths of 488 nm and 530 nm. The RFP-HUVECs were imaged using excitation/emission wavelengths of 561 nm and 610 nm.

### **3.8. Cell Staining using Cell Membrane Linker Stains**

To enable imaging non-transduced cells over time, cell linker membrane stains were utilised. The PKH26 Red Fluorescent Cell Linker Kit and CellVue Claret Far Red Fluorescent Cell Linker Kit (Sigma-Aldrich, UK) were used to stain the cell membrane. Cells were collected in a centrifuge tube and centrifuged at 1500 rpm for 5 minutes. The cell pellet was resuspended in 1 mL of Diluent C from the kit. A volume of 4 µL of PKH26/CellVue dye solution was added to 1 mL of Diluent C in a separate centrifuge



tube. The diluted dye solution was then added to the cell suspension and pipetted rapidly to ensure adequate mixing. The cells were incubated in the dye solution for 5 minutes at room temperature. Complete media containing FBS was added to the cells to stop the staining process. Cells were centrifuged at 1500 rpm for 10 minutes with the supernatant removed and 10 mL of fresh medium added. Cells were transferred to a new centrifuge tube to ensure removal of unbound dye, centrifuged and washed a further 2 times to reduce background staining. Cells were imaged using a Yokogawa CQ1 spinning disk inverted confocal microscope at excitation/emission wavelengths of 561/617 nm and 640/685 nm for PKH26 and CellVue respectively.

### **3.9. 2D Cell Culture**

#### **3.9.1. SAPHs**

For SAPHs, 100  $\mu$ L of hydrogel was dispensed into wells of a 96 well plate using a positive displacement pipette. The hydrogel was left for 5 minutes to recover from the shear exerted by pipetting. Cell culture media (100  $\mu$ L) was placed on top of the hydrogel and the plate was incubated overnight under standard cell culture conditions to allow the pH of the hydrogel to equilibrate to pH 7. After trypsinisation and cell counting using trypan blue staining and a C-chip haemocytometer, cells were adjusted to the desired seeding density and centrifuged at 1500 rpm for 5 minutes. A cell-seeding density of  $1 \times 10^5$  cells/mL was used for 2D cell culture. Cells were adjusted to the required density and 100  $\mu$ L of cell suspension was pipetted onto 100  $\mu$ L of equilibrated hydrogel. The plate was incubated under standard cell culture conditions and media was changed every 2 days for HUVECs and every 3 days for MCF-7 cells.

#### **3.9.2. Collagen I**

For collagen I, the hydrogel was prepared as described in **section 3.1.2**. The solution was dispensed into wells of a 96 well plate (100 $\mu$ L/well) and incubated at 37 °C for 1 hour for gelation to occur. After trypsinisation and cell counting using trypan blue staining and a C-chip haemocytometer, cells were adjusted to the desired seeding density and centrifuged at 1500 rpm for 5 minutes. A cell-seeding density of  $1 \times 10^5$  cells/mL was used for 2D cell culture. Cells were adjusted to the required density and 100  $\mu$ L of cell suspension was pipetted onto 100  $\mu$ L of hydrogel. The plate was incubated under standard cell culture conditions and media was changed every 2 days for HUVECs.

### **3.9.3. TCP**

For laminin-coated TCP controls, the laminin stock solution (1 mg/mL) was diluted to 5, 25 and 50  $\mu\text{g/mL}$  with dPBS and pipetted onto wells of a 96 well plate, ensuring that the entire surface was coated. Plates were incubated with the laminin solution at 4 °C overnight to ensure adsorption of the laminin protein to the TCP. Wells were washed with dPBS 3 times and cells were then seeded.

### **3.9.4. Image Quantification**

To quantify percentage area of HUVECs cultured on hydrogels, the ‘Analyze Particles’ plugin on ImageJ was used (v1.53g) using the following steps:

- Run (“ 8-bit ”);
- Run (“ Threshold ”);
- “ Analyze Particles ”

## **3.10. 3D Cell Culture**

### **3.10.1. SAPHs**

For MCF-7 and MDA-MB-231 cells alone, a cell-seeding density of  $1 \times 10^6$  cells/mL was used. For co-cultures of HUVECs and MSCs, a total cell-seeding density of  $1 \times 10^6$  cells/mL ( $8 \times 10^5$  HUVECs/mL and  $2 \times 10^5$  MSCs/mL) was used. For tri-cultures, a cell-seeding density of  $1.5 \times 10^6$  cells/mL ( $8 \times 10^5$  HUVECs/mL,  $5 \times 10^5$  MCF-7 cells/mL and  $2 \times 10^5$  MSCs/mL) was used.

After trypsinisation and cell counting using trypan blue staining and a C-chip haemocytometer, cells were adjusted to the desired seeding density and centrifuged at 1500 rpm for 5 minutes. The supernatant was removed from the cell pellet and cells were resuspended in a volume of complete media that was 10 % of the desired hydrogel volume. The desired volume of hydrogel was pipetted into a 15 mL centrifuge tube using a positive displacement pipette. Using a P1000 pipette tip with a cut end, the cells were mixed into the hydrogel slowly in all dimensions at least 10 times until a homogenous mixture was achieved. A P1000 pipette tip with a cut end was again used to pipette 100  $\mu\text{L}$  of the hydrogel/cell mixture into 24 well ThinCert cell culture inserts with a 1.0  $\mu\text{m}$  pore size (Greiner Bio-One, UK) or wells of a 96 well plate. The hydrogel/cell mixture was incubated for 5 minutes at room temperature to allow the hydrogel to recover from the shear exerted during cell encapsulation. If inserts were used, 600  $\mu\text{L}$  of media was added to

the well surrounding the insert and incubated for 5 minutes at room temperature. This was to allow bulk reinforcement of the hydrogel. A volume of 100  $\mu\text{L}$  of media was added on top of each hydrogel and the plate was incubated under standard cell culture conditions. Media changes were carried out 1–3 times within an hour until the hydrogel had turned pink, indicative of a neutral pH.

Media changes were carried out the next day and every 2 days for HUVEC/MSC co-cultures and HUVEC/MSC/MCF-7 tri-cultures, and every 3 days for MCF-7/MDA-MB-231 cultures. HUVEC/MSC co-cultures and HUVEC/MSC/MCF-7 tri-cultures were maintained with ECGM-2 media, whilst MCF-7/MDA-MB-231 cultures were maintained with DMEM. Due to the fragile nature of the hydrogels, 50  $\mu\text{L}$  of media was removed from the top of the hydrogel and replenished with 50  $\mu\text{L}$  of fresh media.

### **3.10.2. Collagen I**

Rat-tail collagen I (1.5 mg/mL) was used as a positive control for MCF-7 and MDA-MB-231 cells and collagen I (1.5 mg/mL) enriched with 90  $\mu\text{g/mL}$  human fibronectin (Sigma-Aldrich, UK) was used as a positive control for HUVEC/MSC co-cultures and HUVEC/MSC/MCF-7 tri-cultures. The cell-seeding densities used were the same as described in **section 3.10.1**. Collagen solution was prepared as described in **section 3.1.2**.

After trypsinisation and cell counting using trypan blue staining and a C-chip haemocytometer, cells were adjusted to the desired seeding density and centrifuged at 1500 rpm for 5 minutes. All of the supernatant was removed and the pellet was resuspended in the cold collagen solution using slow pipetting. The hydrogel solution containing cells was pipetted into 24 well inserts with a 1.0  $\mu\text{m}$  pore size or wells of a 96 well plate (100  $\mu\text{L}$  per well/insert). The hydrogels were transferred to a 37  $^{\circ}\text{C}$  incubator to allow gelation of the collagen for 1 hour. Gelation was deemed successful if the hydrogel had turned white and opaque. A volume of 100  $\mu\text{L}$  of media was added on top of the hydrogel, and 600  $\mu\text{L}$  surrounding the hydrogel if inserts were used. The samples were incubated under standard cell culture conditions.

HUVEC/MSC co-cultures and HUVEC/MSC/MCF-7 tri-cultures were maintained with ECGM-2 media, whilst MCF-7/MDA-MB-231 cultures were maintained with DMEM. Media changes were carried out the next day and every 2 days for HUVEC/MSC co-cultures and HUVEC/MSC/MCF-7 tri-cultures, and every 3 days for MCF-7/MDA-MB-231 cultures.

## **3.11. Cell Viability Assays**

### **3.11.1. AlamarBlue**

For the laminin study, resazurin-based AlamarBlue was used to assess the metabolic activity of HUVECs cultured on laminin coated TCP. Viable cells metabolise the resazurin to the highly fluorescent resofurin via reduction. AlamarBlue reagent was added directly to the cell culture media at a ratio of 1:10. Plates were incubated under standard cell culture conditions for 2 hours. After incubation, the supernatant was collected and dispensed into wells of a black bottomed 96 well plate. Fluorescence was measured using a BMG Labtech Optima FluoStar plate reader with Optima software (v1.26) with excitation/emission wavelengths of 560 nm and 590 nm. Cell culture media was used as a blank control and removed from all values.

### **3.11.2. LIVE/DEAD**

To qualitatively assess viability of encapsulated cells, the LIVE/DEAD assay (ThermoFisher, UK) was used. Live cells are stained green by calcein acetoxymethyl (calcein-AM) due to intracellular esterase activity and dead cells are stained red by ethidium homodimer due to loss of plasma membrane integrity. 2  $\mu$ M calcein-AM and 4  $\mu$ M ethidium homodimer were diluted in 10 mL dPBS on the day of usage and stored in the dark. Media was aspirated from all samples and dPBS was used to wash the samples for 5 minutes at 37 °C. The LIVE/DEAD solution was then added to all samples and incubated at 37 °C for 1 hour in the dark. Samples were transferred to a glass slide and a Leica SP5 confocal microscope was used to obtain images using excitation/emission wavelengths of 488/525 nm and 561/625 nm for live cells and dead cells respectively.

### **3.11.3. PicoGreen**

To quantitatively assess proliferation of cells within SAPHs, the PicoGreen assay (ThermoFisher, UK) was used. PicoGreen is a fluorescent probe which binds to the backbone of double stranded DNA (dsDNA) and produces a fluorescent compound which is proportional to the concentration of DNA present [275]. To digest the SAPH, the enzyme pronase was used. Its use has been validated for cell recovery from SAPHs in previous studies [276].

To determine if encapsulation in PeptiGelAlpha1 affected DNA recovery, a standard curve of known cell concentrations was produced from cells encapsulated in PeptiGelAlpha1 and dPBS. Cell concentrations of  $1 \times 10^5$  cells/mL,  $5 \times 10^5$  cells/mL,  $1 \times 10^6$  cells/mL and

$2 \times 10^6$  cells/mL were prepared and suspended in either PeptiGelAlpha1 or dPBS in 1.5 mL Eppendorf tubes and incubated for 30 minutes under standard cell culture conditions. For samples at designated time points, media was removed from all samples and the membrane of the inserts were removed using a pair of tweezers. The inserts were placed into 1.5 mL Eppendorfs and tapped against the base of the cell culture hood until the cell/hydrogel mixture reached the bottom of the Eppendorf. A volume of 400  $\mu$ L of pronase (10 mg/mL) was added and the samples were triturated until the mixture was homogeneous. The samples were incubated in a 37 °C water bath for 5 minutes to activate the pronase enzyme, with inversion every minute. A volume of 500  $\mu$ L of 1x TE buffer with 1 % (v/v) Triton-X was then added to lyse the cells and incubated for 30 minutes at room temperature. Samples were then exposed to one freeze-thaw cycle at -20 °C and vortexing to ensure cell lysis.

For analysis, 100  $\mu$ L of sample was added to wells of a black bottomed 96 well plate and incubated with an equal volume of PicoGreen reagent (200x dilution in 1x TE buffer) for 5 minutes. A BMG Labtech Optima FluoStar plate reader with Optima software (v1.26) was used to measure fluorescence with excitation/emission wavelengths of 480 nm and 520 nm. Acellular samples were used as blanks and subtracted from sample values. Fluorescence values were compared with a lambda dsDNA standard curve (0–1000 ng/mL) (**Figure 3.1**).

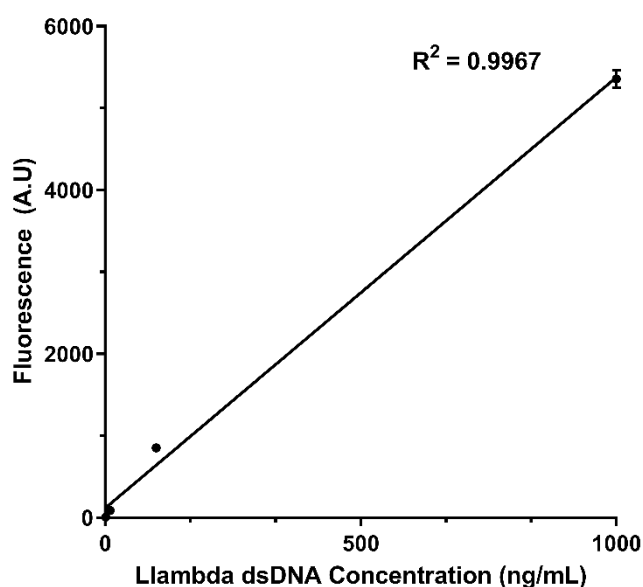


**Figure 3.1. Lambda dsDNA standard curve for PicoGreen analysis.** The PicoGreen assay was used to measure the fluorescence of known DNA concentrations (0, 10, 100 and 1000 ng/mL). Data are mean  $\pm$  S.D.  $R^2$  = coefficient of determination.

### **3.12. Phalloidin Staining of F-actin Filaments**

To visualise F-actin filaments of the cytoskeleton of cells, phalloidin staining was used. Cell culture media was aspirated and samples were washed in dPBS for 5 minutes at 37 °C. Samples were subsequently fixed with 10 % (v/v) formalin for 1 hour at room temperature. The fixative was aspirated and samples were washed with dPBS for 5 minutes in triplicate. 0.1 % (v/v) Triton-X diluted in dPBS was added to the sample for 5 minutes to extract the sample. The samples were washed in dPBS for 5 minutes in triplicate. 1 % (w/v) bovine serum albumin (BSA) diluted in dPBS was added to the sample and incubated for 30 minutes. Alexa Fluor 568 Phalloidin (ThermoFisher, UK) was diluted 1:50 using dPBS with 1 % (v/v) BSA and samples were incubated overnight at 4 °C. The following day, samples were washed with dPBS for 5 minutes in triplicate. 300 nM 4',6-diamidino-2-phenylindole (DAPI) was added to counterstain the nuclei and samples were incubated overnight at 4 °C. Images were collected using a Yokogawa CQ1 spinning disk inverted confocal microscope using excitation/emission wavelengths of 405 nm and 447 nm for DAPI and 561 nm and 617 nm for phalloidin.

### **3.13. Histological Staining**

#### **3.13.1. Processing and Sectioning**

At designated time points, cell culture media was aspirated from all samples and dPBS was used to wash the samples for 5 minutes at 37 °C. Acellular PeptiGelAlpha1 controls were also included. Cell pellet controls were prepared by trypsinising a large volume of cells and centrifugation at 1500 rpm for 5 minutes to create a large cell pellet. Samples were fixed with 10 % (v/v) formalin incubation for 1 hour at room temperature. After fixation, the formalin solution was replaced with dPBS and stored at 4 °C until further processing. The inserts were placed in histology cassettes lined with foam biopsy pads and placed in the Tissue Tek VIP 2000 tissue processor and exposed to cycles of 70 % (v/v), 90 % (v/v) and 100 % (v/v) ethanol followed by xylene and wax. After processing, samples were embedded in paraffin wax using a HistoStar embedding centre (ThermoFisher, UK). A Leica RM2145 microtome was used to section the hydrogels at a thickness of 5.0 µm. Sections were floated in a floatation bath (ThermoFisher, UK) and collected onto poly-L-lysine coated glass slides (ThermoFisher, UK). Sections were placed into a section dryer (ThermoFisher, UK) at 60 °C for 30 minutes.

### **3.13.2. Haematoxylin and Eosin Staining**

Haematoxylin and eosin (H&E) staining was used to observe the overall histoarchitecture and cellular organisation within PeptiGelAlpha1 and collagen I. To prepare the haematoxylin solution, 1 g of haematoxylin was dissolved in 1 L of distilled water using gentle heat, followed by the addition of 50 g of potassium alum, which was dissolved again using gentle heat. Once the solution had cooled, 0.2 g of sodium acetate was added. Once dissolved, the solution was filtered and 20 mL of glacial acetic acid was added. To prepare the eosin Y solution, 50 mL of 1 % (v/v) eosin was mixed with 390 mL of 95 % (v/v) ethanol and 2 mL of glacial acetic acid.

Slides were dewaxed in xylene followed by rehydration with 100 % (v/v), 95 % (v/v), 85 % (v/v), 70 % (v/v) ethanol and tap water. Slides were stained in Mayer's haematoxylin to stain cell nuclei for 5 minutes and washed in tap water for a further 5 minutes. Slides were then stained in eosin Y for 3 minutes. Samples were then dehydrated using the same grades of ethanol and xylene as used before. Sections were mounted using DMX mountant. Images were collected using a Leica DM2700 brightfield upright microscope and Leica LAS X software. Cell nuclei were stained blue whilst the surrounding hydrogel was stained pink.

To quantify area and number of cells present in MCF-7 spheroids, 10X images were analysed using ImageJ (v.152p). A circle was drawn around each spheroid and the 'Analyze Particles' plugin was used to quantify the area. For the number of cells, the 'Cell counter' plugin was used to measure the number of cells present per spheroid. A group of > 3 cells was considered to be a spheroid.

### **3.13.3. Gomori Trichome Staining**

Gomori Trichome staining was used to detect the presence of non-specific collagen production by MCF-7 and MDA-MB-231 cells within PeptiGelAlpha1. The Gomori solution was prepared by adding 0.6 g of chromotrope 2R, 0.3 g of fast green FCF and 0.6 g of phosphotungstic acid to 100 mL of distilled water, followed by 1 mL of glacial acetic acid.

Slides were dewaxed in xylene followed by rehydration with 100 % (v/v), 95 % (v/v), 85 % (v/v), 70 % (v/v) ethanol and tap water. Sections were stained using Mayer's haematoxylin for 5 minutes and blued in tap water for a further 5 minutes to stain cell nuclei. Sections were stained with Gomori solution for 5 minutes. Sections were then rinsed using 0.2 % (v/v) acetic acid for 1 minute, followed by dehydration with absolute

ethanol and xylene. Sections were mounted using DMX mountant. Images were collected using a Leica DM2700 brightfield upright microscope and Leica LAS X software. A positive control of pig anterior cruciate ligament was used (**Appendix 1**). Collagen was stained green whilst cell nuclei were stained blue.

#### **3.13.4. Immunohistochemistry**

Immunohistochemical staining was used to determine the presence of proteins and markers typically produced by cancer cells and HUVECs. Slides were dewaxed in xylene followed by rehydration with 100 % (v/v), 95 % (v/v), 85 % (v/v), 70 % (v/v) ethanol and tap water. Antigen retrieval consisted of pre-treatment with low pH for 20 minutes, except for CD31 staining which required high pH for 20 minutes. All subsequent steps were carried out using the Thermo Fisher Lab Vision Autostainer 480S. Sections were treated using the UltraVision Quanto Detection System (ThermoFisher, UK), consisting of a hydrogen peroxide block, primary antibody amplifier and horseradish peroxidase (HRP) polymer. This system has anti-mouse and anti-rabbit specificity. After pre-treatment, sections were blocked using the hydrogen peroxide block for 10 minutes to reduce non-specific background staining. Sections were then treated with the diluted antibodies (**Table 3.1**). Primary antibodies were diluted in Antibody Diluent OP Quanto (ThermoFisher, UK) using the dilutions specified in **Table 3.1**. Sections were washed with wash buffer. The primary antibody amplifier was added to sections for 10 minutes, followed by a wash step. HRP Polymer was added to the sections for 10 minutes. Sections were washed using wash buffer and distilled water. Sections were incubated with the DAB Quanto Chromogen detection system to reveal positive staining for 5 minutes. Cell nuclei were counterstained by haematoxylin, followed by washing with distilled water. Sections were subsequently dehydrated with absolute ethanol and xylene followed by mounting using DMX mountant. Images were collected using a Leica DM2700 brightfield upright microscope and Leica LAS X software. Positive staining was indicated by brown staining, whilst nuclei were stained blue.

Negative controls were included for each sample, in which the primary antibody was omitted from the protocol (**Appendix 2**). Acellular controls for each antibody were also included (**Appendix 3**). MCF-7 and MDA-MB-231 cell pellet controls were included for cytokeratin, vimentin, E-cadherin, N-cadherin and HIF1 $\alpha$  (**Appendix 4**). Images of positive controls for each antibody are depicted in **Appendix 5**.



Quantification of Ki67 positive cells was carried out by marking the nuclei of Ki67 positive and negative cells using the Multi-point tool in ImageJ (v.152p) and calculating the percentage of Ki67 positive cells.

**Table 3.1. Antibodies and protocols used in immunohistochemical staining of MCF-7, MDA-MB-231 cells and HUVECs in hydrogel sections.**

Marker	Antigen retrieval	Primary Antibody	Dilution used	Secondary Antibody	Positive control
Ki67	Low pH	Ab15580 Rabbit polyclonal to Ki67 (Abcam)	1:2000	UltraVision Quanto Detection System (ThermoFisher)	Pig liver
E-cadherin	Low pH	24E10 Rabbit monoclonal to E-cadherin (Cell Signalling Technology)	1:2000	UltraVision Quanto Detection System (ThermoFisher)	LNCaP cell pellet
Cytokeratin (pan)	Low pH	NB600-579 Rabbit polyclonal to pan cytokeratin (Novus Biologicals)	1:1000	UltraVision Quanto Detection System (ThermoFisher)	Pig kidney
N-cadherin	Low pH	D4R1H Rabbit monoclonal to N-Cadherin (Cell Signalling Technology)	1:200	UltraVision Quanto Detection System (ThermoFisher)	PC3 cell pellet
Vimentin	Low pH	6030330-1 Mouse monoclonal to Vimentin (Proteintech)	1:2000	UltraVision Quanto Detection System (ThermoFisher)	Rat oesophagus
Collagen I	Low pH	Ab34710 Rabbit polyclonal to collagen I (Abcam)	1:200	UltraVision Quanto Detection System (ThermoFisher)	Rat lung
HIF1 $\alpha$	Low pH	ADI-OSA-602 Mouse monoclonal to HIF1 $\alpha$ (Enzo)	1:200	UltraVision Quanto Detection System (ThermoFisher)	LNCaP cell pellet
CD31	High pH	Ab9498 Mouse monoclonal to CD31 (Abcam)	1:2000	UltraVision Quanto Detection System (ThermoFisher)	HUVEC pellet

### 3.14. MMP-2 ELISA Assay

The LEGEND MAX Human total MMP-2 sandwich enzyme-linked immunoabsorbant assay (ELISA) kit (BioLegend, USA) was used to measure the concentration of MMP-2 produced by MCF-7 cells encapsulated in PeptiGelAlpha1. Sandwich ELISAs rely on the target antigen being trapped between the capture antibody and the detection antibody, rendering this type of ELISA highly sensitive and specific [277].

Supernatant was collected from cell-laden rheology samples at desired time points and frozen at -20 °C until later use. Supernatant from acellular samples were also collected. To perform the ELISA, samples were diluted two-fold in DMEM. A standard curve was produced from human total MMP-2 standard included in the kit by serial dilution. Equal volumes of cell culture media were added to wells of the 96 well plate supplied containing standards, and equal volumes of assay buffer were added to wells containing samples. The plate was sealed and incubated at room temperature for 2 hours shaking at 200 rpm. The contents of the plate were discarded and the plate was washed 4 times with wash buffer. Human Total MMP-2 Detection Antibody was added to each well (100 µL) and the plate was sealed and incubated at room temperature for 30 minutes while shaking. The plate contents were discarded and the plate was washed 4 times using wash buffer. Avidin-HRP solution was added to each well (100 µL) and the plate was incubated for 30 minutes shaking at room temperature. The plate contents were discarded and the plate was washed 5 times with wash buffer. Substrate solution was added to each well (100 µL) and the plate was incubated in the dark for 15 minutes at room temperature. The reaction was stopped by adding 100 µL of Stop Solution to each well.

Absorbance was measured using excitation/emission wavelengths of 492 nm and 590 nm using a BMG Labtech Optima FluoStar plate reader with Optima software (v1.26). Acellular samples were removed from all sample values as a background control. Fluorescence values were compared and interpolated with a human total MMP-2 standard curve (0–40 ng/mL) (**Figure 3.2**).

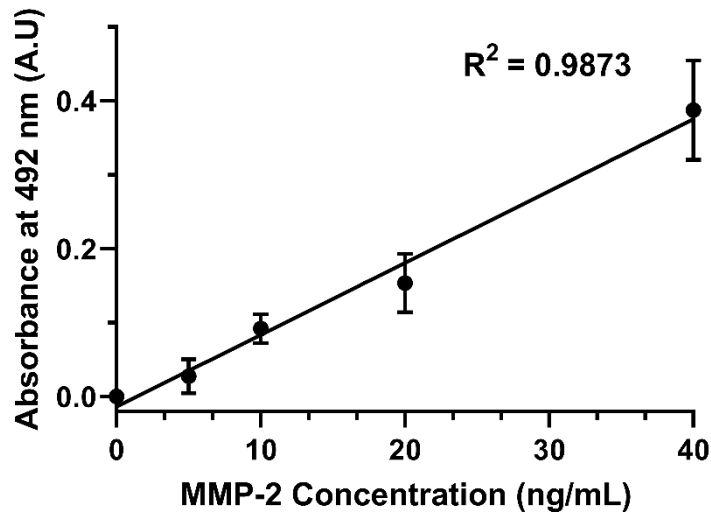


**Figure 3.2. MMP-2 ELISA standard curve.** Known concentrations of human total MMP-2 ELISA were used to produce a standard curve for unknown values. Data are mean  $\pm$  S.D.  $R^2$  = coefficient of determination.

### 3.15. Hypoxia Detection in Cells

Fluorescence-based detection was used initially to determine if cancer cells encapsulated within PeptiGelAlpha1 were becoming hypoxic. The Image-iT™ Red Hypoxia Reagent (ThermoFisher, UK) was used, whereby the probe fluoresces when the oxygen concentration is less than 5 % (v/v) and is non-fluorescent under normoxic conditions. At designated time points, the reagent was added to the supernatant of samples at a concentration of 10  $\mu$ M. The samples were incubated at 37 °C for 1 hour in the dark. The samples were then transferred to a glass slide for imaging. Images were acquired using a Yokogawa CQ1 spinning disk inverted confocal microscope with excitation/emission wavelengths of 488 nm and 617 nm. To optimise the assay and establish a suitable positive control, MCF-7 cell-laden samples and acellular samples were exposed to either 150  $\mu$ M cobalt chloride hexahydrate (CoCl<sub>2</sub>) (Sigma-Aldrich, UK) or incubation in 4 % (v/v) O<sub>2</sub> for 48 hours.

To quantify the number of hypoxic cells and percentage area, the ‘Analyze Particles’ plugin in ImageJ was used (v1.52p) using the following steps:

- Run (“ 8-bit ”);
- Run (“ Threshold ”);
- “ Analyze Particles ”

### **3.16. Embedded Invasion Assay**

To assess the invasion of MCF-7 and MDA-MB-231 cells encapsulated in PeptiGelAlpha1 into another biomaterial, cell-laden hydrogel samples were embedded into either collagen I or Matrigel. Cells were stained with the PKH26 Red Fluorescent Cell Linker Kit, as described previously (**section 3.8**), to enable live cell imaging. MCF-7 and MDA-MB-231 cells were encapsulated in PeptiGelAlpha1 in 24 well plate inserts as described previously (**section 3.10.1**) and incubated for 2 days to allow the cells to recover from the encapsulation process.

After 2 days, collagen I (1.5 mg/mL) and Matrigel (5 mg/mL) solutions were prepared on ice as described previously (**sections 3.1.2 & 3.1.3**). The membrane of each insert was removed using tweezers and the insert containing the cell-laden hydrogel was placed in the well of a 24 well plate. The insert was carefully removed leaving the hydrogel in the well. The liquid collagen I/Matrigel was pipetted around the hydrogel and the plate was incubated at 37 °C to allow gelation of the surrounding hydrogel. Cell culture media was placed on top of the embedded samples and the plate was incubated under standard cell culture conditions. Images were acquired at desired time points using the Yokogawa CQ1 spinning disk inverted confocal microscope using excitation/emission wavelengths of 561 nm and 617 nm.

The number of cells which invaded collagen I/Matrigel from PeptiGelAlpha1 was quantified using the ‘Analyze Particles’ plugin in ImageJ (v1.52a) using the following steps:

- Run (“ 8-bit ”);
- Run (“ Threshold ”);
- “ Analyze Particles ”

### **3.17. Anti-Cancer Drug Efficacy**

The efficacy of anti-cancer drugs tamoxifen (Cayman Chemicals, USA) and doxorubicin were assessed with MCF-7 and MDA-MB-231 cells encapsulated in PeptiGelAlpha1 and 2D monolayer culture. Doxorubicin and tamoxifen were both dissolved in DMSO to provide stock concentrations of 10 mg/mL. The stock solutions were then diluted into cell culture media to concentrations of 100  $\mu$ M and 500  $\mu$ M for tamoxifen and 500  $\mu$ M for doxorubicin, using the molecular weights of 371.515 g/mol and 543.52 g/mol for

tamoxifen and doxorubicin respectively. A 1 % (v/v) DMSO control was included as a vehicle control for cells seeded on TCP.

MCF-7 and MDA-MB-231 cells were prepared as described previously in **section 3.10.1** and encapsulated in PeptiGelAlpha1 at a density of  $1 \times 10^6$  cells/mL in 24 well inserts. As 2D controls, cells were seeded as a monolayer in wells of 24 well plates at a density of  $1 \times 10^5$  cells/mL. Samples were incubated for 1 day to allow the cells to recover from the encapsulation process. After 1 day, samples were exposed to doxorubicin and tamoxifen treatments and cultured for 24 hours or 48 hours. A no treatment control of cell culture media alone was also included.

At the desired time point, hydrogel samples were prepared for PicoGreen analysis as described in **section 3.11.3**. For TCP samples, cell culture media was aspirated and 1 mL of lysis buffer (1x TE buffer with 1 % (v/v) Triton-X) was added to each sample and incubated for 30 minutes. Samples were then exposed to a freeze-thaw cycle at  $-20$  °C and the wells were scraped using a pipette tip. Cell lysate samples were collected in Eppendorf tubes and analysed using the PicoGreen assay as described in **section 3.11.3**. As different cell-seeding concentrations were used for 2D and 3D culture, data were presented as percentage cell viability compared with untreated cells.

### **3.17.1. Dose-Response Curves**

Dose-response curves for both doxorubicin and tamoxifen were established to determine the concentration of drug needed to inhibit cell viability by 50 % ( $IC_{50}$ ) for both MCF-7 and MDA-MB-231 cells. Concentrations of 0.0001  $\mu$ M, 0.001  $\mu$ M, 0.01  $\mu$ M, 0.1  $\mu$ M, 1  $\mu$ M, 10  $\mu$ M, 100  $\mu$ M and 500  $\mu$ M were prepared for both tamoxifen and doxorubicin, as described in **section 3.17**. MCF-7 and MDA-MB-231 cells were prepared as described previously in **section 3.10.1** and encapsulated in PeptiGelAlpha1 at a density of  $1 \times 10^6$  cells/mL in 24 well inserts. As 2D controls, cells were seeded as a monolayer in wells of 96 well plates at a density of  $1 \times 10^5$  cells/mL. Samples were cultured for 1 day to allow the cells to recover from the encapsulation process. After 1 day, samples were exposed to doxorubicin and tamoxifen treatments and cultured for 48 hours. After 48 hours, hydrogel samples were prepared for PicoGreen analysis as described in **section 3.11.3** and TCP samples were prepared as described in **section 3.17**. As different cell-seeding concentrations were used for 2D and 3D culture, data were presented as percentage cell viability compared with untreated cells. To calculate the  $IC_{50}$  values, GraphPad Prism 9 software was used with the following steps:

- Normalise Y values to percentages.
- Analysis: Fit curve with non-linear regression.
- Equation: [Inhibitor] vs. normalised response – Variable slope (four parameters).

The IC<sub>50</sub> values were measured using the following equation:

$$Y = \frac{a - d}{1 + \left(\frac{X}{c}\right)^b} + d$$

**Equation 3.2. 4-parameter logistical model used to calculate IC<sub>50</sub> values.**

Where Y = response, X = concentration, d = bottom of curve, a = top of curve, c = IC<sub>50</sub> and b = slope.

### **3.18. Matrigel Tube Formation Assay with Conditioned Media**

MCF-7 cells were seeded at a density of 1x10<sup>6</sup> cells/mL. Conditioned media was collected from MCF-7 cells cultured in the following platforms:

- a. Spheroids in Nunclon Sphera 96 well round bottomed plates (ThermoFisher, UK) in either DMEM or ECGM-2 for 4 days.
- b. Within PeptiGelAlpha1 in either DMEM or ECGM-2 for 4 days.
- c. Cultured in TCP for 4 days in either DMEM or ECGM-2.

As a material control, acellular PeptiGelAlpha1 was cultured in either DMEM or ECGM-2 for 4 days and collected. Conditioned media was frozen at -20 °C until later use. Matrigel solution (10 mg/mL) was prepared on ice and 100 µL was pipetted into each well of a 96 well plate. The plate was incubated for 1 hour at 37 °C to allow gelation to occur. P7 RFP-HUVECs cultured in complete media without FBS overnight were used for this experiment at a density of 1x10<sup>5</sup> cells/mL. RFP-HUVECs were resuspended in ECGM-2 or 50:50 DMEM:ECGM-2 from each MCF-7 cell condition. A positive control of fully supplemented ECGM-2 and a negative control of ECGM-2 with 30 µM suramin, an inhibitor of angiogenesis, were used. Cells were cultured for 18 hours before fixation with 10 % (v/v) formalin. Images were collected using a Leica SP5 confocal microscope. The ImageJ (v1.52p) ‘Angiogenesis Analyzer’ plugin was used to analyse the images to collect quantitative data, using the following steps:

- Run (“ 8-bit ”);
- Run (“ RGB Color ”);
- Run (“ Brightness/Contrast ”, “ saturated = 0.35 ”);
- Run (“ Non-local means denoising “)
- “ Analyze HUVEC phase contrast ”
- Min. object size: 25 pixels, Min. branch size: 40 pixels, Loop size: 1000 pixels

Tube length, number of nodes and number of branches were measured.

### 3.19. $\alpha 5\beta 1$ Integrin Blocking

To assess whether HUVECs and MSCs were responding to the RGD stimulus via  $\alpha 5\beta 1$  integrin activity, the  $\alpha 5\beta 1$  integrins were blocked using a mouse anti-human integrin  $\alpha 5\beta 1$  monoclonal antibody. RFP-HUVECs and GFP-MSCs were trypsinised and collected in a 15 mL centrifuge tube and centrifuged at 1500 rpm leaving a cell pellet. Cell density was adjusted and an antibody dilution of 1:50 was used, with 10  $\mu$ L of antibody added to 490  $\mu$ L serum-free DMEM containing 800,000 RFP-HUVECs and 200,000 GFP-MSCs. The cells and antibody were incubated at 37 °C for 45 minutes. This protocol has been modified from a similar study [213]. Cells were adjusted to the required density and encapsulated in PeptiGelAlpha1 + 10 % RGD. Unblocked cells were used as a negative control. As a positive control, TCP coated with 50  $\mu$ g/mL human plasma fibronectin was used. TCP alone was used as an additional control. Samples were imaged after 4 days in culture using a Yokogawa CQ1 spinning disk inverted confocal microscope with excitation/emission wavelengths of 488/520 nm for GFP-MSCs and 561/617 nm for RFP-HUVECs.

### 3.20. Statistical Analysis

Experiments were carried out a minimum of two times, unless stated otherwise. The experimental repeat number (N#) is provided in the figure caption. Data were presented as mean  $\pm$  standard deviation (S.D), except for IC<sub>50</sub> values, which were presented as mean  $\pm$  standard error of mean (S.E.M). Data were analysed using one-way or two-way ANOVA with post-hoc Tukey’s tests, and post-hoc Sidak’s tests for IC<sub>50</sub> values and the PicoGreen hydrogel vs dPBS standard curve, using GraphPad Prism 9 software. Statistical significance was observed when  $p < 0.05$ , with \* =  $p < 0.05$ , \*\* =  $p < 0.01$ , \*\*\* =  $p < 0.001$  and \*\*\*\* =  $p < 0.0001$ .

### 3.21. Materials

The materials described and used herein are listed in **Table 3.2**.

**Table 3.2. Materials and reagents used in experimental sections.**

Item name		Catalogue number
	<b>Manchester BIOGEL</b>	
PeptiGelAlpha1		18010101
PeptiGelAlpha2		18010102
PeptiGelAlpha4		18010104
PeptiGelAlpha1 + 0.1 % RGD		18010101RGD0.1%
PeptiGelAlpha1 + 1 % RGD		18010101RGD1%
PeptiGelAlpha1 + 10 % RGD		18010101RGD10%
PeptiGelAlpha1 + 40 % RGD		18010101RGD40%
PeptiGelAlpha1 + 15 % RGD & 15 % IKVAV		Bespoke order
	<b>Thermo Fisher Scientific (Life Technologies)</b>	
Collagen I Rat Tail, 20 mL		A1048301
LIVE/DEAD Cell Viability Assay		L3224
Image-iT Red Hypoxia Reagent		H10498
Quant-iT PicoGreen dsDNA Assay kit		P11496
HRP Polymer Quanto		TL-060-QPH
Ultra Vision Protein Block		TA-060-PBQ
Antibody Diluent OP Quanto		TA-125-ADQ
DAB Quanto		TA-060-QHDX
AlexaFluor 568 phalloidin		A12380
DAPI		D1306
Polysine adhesion slides		10219280
Nunclon Sphera 96 well round-bottom plates		174925
	<b>Sigma-Aldrich</b>	
Gelatin solution, 2 % in H <sub>2</sub> O		G1393-100ML
Fibronectin from human plasma		F2006-2MG
Dulbecco's Modified Eagle Medium – low glucose		D6046-500ML
Dulbecco's Modified Eagle Medium – high glucose		D5761-500ML
Foetal bovine serum		F9665-500ML
Penicillin Streptomycin		P0781-100ML
Trypsin-EDTA solution		SLBZ7364
PKH26 Red Fluorescent Cell Linker Mini Kit		MINI26
CellVue Claret Far Red Fluorescent Cell Linker Kit		MINICLARET
Protease from <i>Streptomyces griseus</i> (Pronase)		P5147-1G
Doxorubicin hydrochloride		021790
HEPES buffer		83264



<b>Item name</b>	<b>Catalogue number</b>
Laminin from Engelbreth-Holm-Swarm murine sarcoma basement membrane	L2020-1MG
Hydrion Brilliant pH dip stiks (pH range 5.0–9.0)	Z264784
Cobalt chloride hexahydrate	C8661
	<b>Lonza</b>
HUVEC pooled donor EGM2 amplified	C2517A
Human bone marrow MSCs from 36 year old Caucasian female	(Lot no. 0000632996) C-12974
	<b>Promocell</b>
Endothelial Cell Growth Medium 2	C-22111
Mesenchymal Stem Cell Growth Medium 2	C-28009
	<b>Abcam</b>
Rabbit polyclonal to Ki67	ab15580
Rabbit polyclonal to collagen I	ab34710
Rabbit polyclonal to CD31	ab9498
	<b>Corning</b>
Matrigel Matrix Basement Membrane Growth Factor Reduced	356230 (Lot no. 634/015)
	<b>Greiner Bio-One</b>
Thincert 24 well plate inserts, 1.0 µm pore membrane	662610
Thincert 12 well plate inserts, 1.0 µm pore membrane	665610
	<b>ATCC</b>
MDA-MB-231 human breast adenocarcinoma cells	HTB-26
MCF-7 human breast adenocarcinoma cells	HTB-22
	<b>Merck Millipore</b>
Mouse anti-human integrin $\alpha 5\beta 1$ monoclonal antibody	MAB1969
	<b>Cell Signalling Technology</b>
Rabbit monoclonal to E-cadherin	24E10
Rabbit monoclonal to N-cadherin	D4R1H
	<b>Proteintech</b>
Mouse monoclonal to vimentin	6030330-1
	<b>Novus Biologicals</b>
Rabbit polyclonal to cytokeratin (pan)	NB600-579
	<b>Enzo</b>
Mouse monoclonal to HIF1 $\alpha$	ADI-OSA-602
	<b>BioLegend</b>
LEGEND MAX Human Total MMP-2 ELISA kit	444607

---

<b>Item name</b>		<b>Catalogue number</b>
DMSO cell culture grade	<b>VWR International</b>	A3672.0100
Tamoxifen	<b>Cayman Chemicals</b>	13258

---

## CHAPTER 4 – Characterisation of Biomaterials used for *In Vitro* Cancer Research

### 4.1. Introduction

There is a breadth of different biomaterials commercially available to include within an *in vitro* model, used as an ECM-mimicking platform to support cell growth. With *in vitro* models of cancer, naturally derived hydrogels Matrigel [278,279] and collagen I [14,280] are commonly used, with Matrigel considered the ‘gold standard’ [183]. In spite of their popularity, few studies are available regarding the physical properties of these materials. Moreover, a synthetic hydrogel is deemed more appropriate for *in vitro* modelling of the TME, due to minimal batch-to-batch variability as well as chemical definition.

SAPHs are emerging as attractive biomaterials for cell culture purposes, due to their synthetic design and tuneability. Within the SAPH family,  $\beta$ -sheet forming ionic complementary SAPHs have been used extensively for tissue engineering and regenerative medicine purposes [21,235,281]. This type of SAPH has also previously been used for *in vitro* modelling of cancer [28,241], providing a foundation for using this type of hydrogel. Moreover, optimisation of downstream RNA and protein isolation protocols for gene expression and Western Blotting have expanded the wealth of data that can be obtained from these hydrogels [276,282]. SAPHs vary based on their primary amino acid sequence, which ultimately results in differences in charge, mechanical properties and hydrophobicity [267,283,284]. As a result, there are a variety of SAPHs to choose for cell culture applications.

Cells are known to respond to the environment in which they are cultured, and therefore choosing a hydrogel that emulates the native cellular environment is paramount. Hydrogels act as substitute for the ECM and therefore cell-ECM interactions can be mimicked. Hydrogel fibres should therefore be on the same scale as native ECM. Laminin fibres measure 2–7 nm, whilst fibronectin varies from 2–22 nm [20]. Moreover, tissue stiffness varies widely, from soft tissues such as the brain and fat (~ 10 Pa) to rigid tissues like cartilage and bone (10–100 kPa) [134]. The chosen material should also mimic the stiffness of the tissue in question. Cancerous tissue is often characterised by an increase in matrix stiffness, due to increased cell proliferation and ECM deposition, as well as increased pressure resulting from growth of the tumour in a constrained volume [134]. Emulating this stiffness is vital for faithfully recapitulating solid tumours *in vitro*.

Moreover, a hydrogel should also act as a physical barrier to drug penetration and diffusion, to replicate *in vivo* drug kinetics. The chosen hydrogel should hinder drug efficacy, by either the hydrogel structure or the 3D growth of cells and associated ECM production.

This chapter will focus on determining which SAPH to use for cell culture experiments based on mechanical properties, charge and initial cell viability results, as well as comparing and characterising the fibre structure and viscoelastic behaviour of the chosen SAPH with Matrigel and collagen I. The SAPHs trialled were: PeptiGelAlpha1, PeptiGelAlpha2 and PeptiGelAlpha4, all sourced from Manchester BIOGEL.

The aims of the chapter are thus as follows:

- 1. To determine which SAPH is most suitable for *in vitro* modelling of cancer cells, HUVECs and MSCs, by examining  $\beta$ -sheet secondary structure, mechanical properties and cell viability.**
- 2. To compare the viscoelastic behaviour and fibre architecture and diameter of the chosen SAPH with Matrigel and collagen I.**
- 3. To observe if the chosen SAPH can act as a physical barrier to anti-cancer drugs, using doxorubicin as a test compound.**

## 4.2. Results

### 4.2.1. Determining $\beta$ -sheet Structure of PeptiGelAlpha1, 2 and 4

ATR-FTIR spectroscopy was used to determine the secondary structures of the panel of SAPHs chosen: PeptiGelAlpha1, PeptiGelAlpha2 and PeptiGelAlpha4 from Manchester BIOGEL. All three hydrogels produced peaks at  $1620\text{ cm}^{-1}$  in the amide I region, which is indicative of  $\beta$ -sheet formation (**Figure 4.1**) [270,285]. This shows that the hydrogels all contained a  $\beta$ -sheet secondary structure. A shoulder peak observed at approximately  $1690\text{ cm}^{-1}$  also shows the  $\beta$ -sheets formed were in an anti-parallel conformation. For PeptiGelAlpha4, this peak was observed to be broader. A broad peak was observed at approximately  $1540\text{ cm}^{-1}$  in all hydrogels, characteristic of C-N stretching in the amide II region.

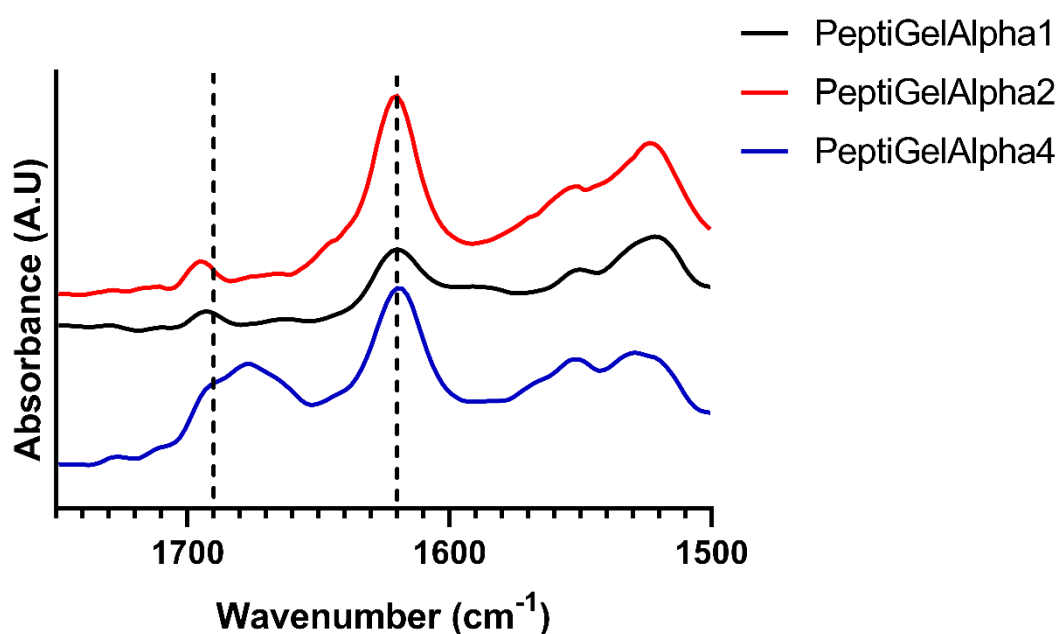


**Figure 4.1. ATR-FTIR spectra of PeptiGelAlpha1, 2 and 4.** Dashed lines refer to presence of  $\beta$ -sheets ( $1620\text{ cm}^{-1}$ ) and anti-parallel  $\beta$ -sheets ( $1690\text{ cm}^{-1}$ ). Spectra were collected over 256 scans using a resolution of  $4\text{ cm}^{-1}$ . HPLC grade water was used as a background control and removed from all spectra. OMNIC software was used to collect the spectra. Spectra were smoothed using 2<sup>nd</sup> order smoothing with an average number of 5 neighbours using GraphPad Prism 9.0 software. Data are representative spectra. N = 2.

#### 4.2.2. Mechanical Properties of PeptiGelAlpha1, 2 and 4

The  $G'$  at 1 Hz, or 'stiffness' of all three peptide hydrogels was determined using oscillatory shear rheology, by carrying out frequency sweeps from 0.01–10 Hz at a constant strain of 0.2 % after 18 hours incubation of media conditioning under standard cell culture conditions.

The stiffness of PeptiGelAlpha1 and PeptiGelAlpha2 were similar, with PeptiGelAlpha1 measured to be  $12679.5 \text{ Pa} \pm 3224.0 \text{ Pa}$ , and PeptiGelAlpha2 measured to be  $12559.7 \text{ Pa} \pm 9647.3 \text{ Pa}$  (**Figure 4.2**). PeptiGelAlpha4, on the other hand, was significantly weaker than PeptiGelAlpha1 and PeptiGelAlpha4, with a stiffness of  $275.1 \text{ Pa} \pm 84.2 \text{ Pa}$  ( $p < 0.05$ ).

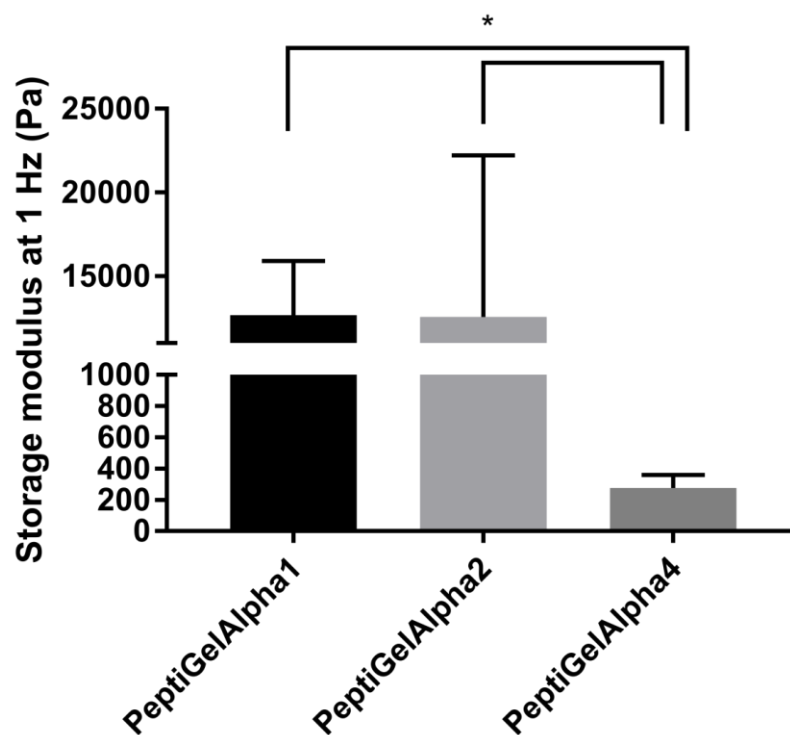


**Figure 4.2. Mechanical properties of PeptiGelAlpha1, 2 and 4.** Storage moduli taken at 1 Hz from frequency sweeps from 0.01–10 Hz at 0.2 % strain. Gap size = 500  $\mu\text{m}$ . Temperature = 37 °C. Samples were exposed to cell culture media and incubated at 37 °C prior to measurement. Data are mean  $\pm$  S.D. \* =  $p < 0.05$  using one-way ANOVA and post-hoc Tukey's test. N = 3.

### 4.2.3. Charge of PeptiGelAlpha1, 2 and 4

The overall charge of each hydrogel versus pH was calculated using the following equation:

$$|Z| = \sqrt{\left( \sum_i N_i \frac{10^{pK_{a_i}}}{10^{pH} + 10^{pK_{a_i}}} - \sum_j N_j \frac{10^{pH}}{10^{pH} + 10^{pK_{a_j}}} \right)^2}$$

**Equation 4.1. Calculation of theoretical charge using pH and pKa values of amino acids.**

Where  $N_{i/j}$  are the numbers of amino acid residues and  $pK_{a_{i/j}}$  the pKa values of the basic ( $i - pK_a > 7$ ) and acidic ( $j - pK_a < 7$ ) groups present on the peptide [281,286]. At pH 7, PeptiGelAlpha1 was neutral with a charge of 0, whilst both PeptiGelAlpha2 and PeptiGelAlpha4 were positively charged, with charges of + 1 and + 2 respectively (Figure 4.3).

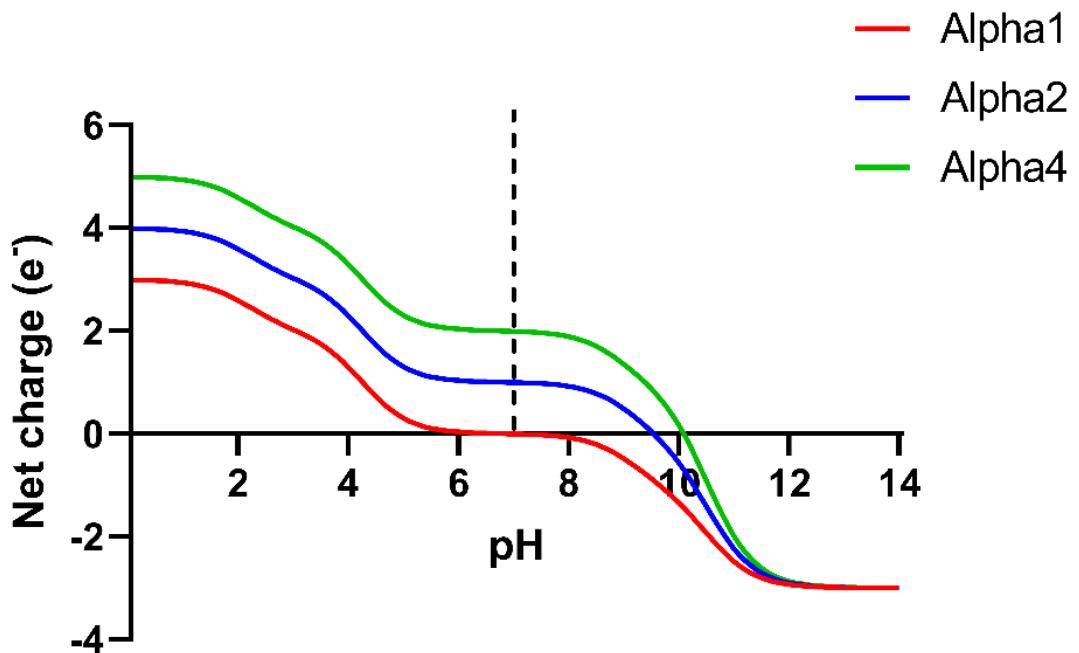


**Figure 4.3. Theoretical net charge of PeptiGelAlpha1, 2 and 4 vs pH.** Dashed line indicates physiological pH (pH 7.0).

From the rheology and charge data alone, it is clear that PeptiGelAlpha4 would not be suitable as a peptide hydrogel platform for TME modelling, due to its weak mechanical properties and relatively high positive charge (**Table 4.1**). Consequently, PeptiGelAlpha1 and 2 were pursued further for investigating 2D and 3D culture of MCF-7 breast cancer cells as a preliminary study, whilst PeptiGelAlpha4 was ruled out for further studies.

**Table 4.1. Summary of charge and storage moduli at 1 Hz of PeptiGelAlpha1, 2 and 4.** Data are mean  $\pm$  S.D.

<b>SAPH</b>	<b>Charge at pH 7</b>	<b>Storage Modulus at 1 Hz (Pa)</b>
PeptiGelAlpha1	0	12679.5 $\pm$ 3224.0
PeptiGelAlpha2	+ 1	12559.7 $\pm$ 9647.3
PeptiGelAlpha4	+ 2	275.1 $\pm$ 84.2



#### 4.2.4. Viability of MCF-7 cells in PeptiGelAlpha1 & PeptiGelAlpha2

It was hypothesised that the positively charged PeptiGelAlpha2 would result in cell adhesion and elongation, whilst a neutral charge would render the cells inert. LIVE/DEAD staining was used to observe the viability of MCF-7 cancer cells cultured on top of and within PeptiGelAlpha1 and PeptiGelAlpha2 after 7 days (**Figure 4.4**). MCF-7 cells cultured on top of both hydrogels were sparse in density, but exhibited a high viability. Cell morphology was observed to be rounded. In 3D culture, cells in both hydrogels maintained a high viability with a small number of dead cells present. Cells tended to aggregate in both PeptiGelAlpha1 and PeptiGelAlpha2. A higher number of cells were found in PeptiGelAlpha1, with a greater fluorescence intensity in the clusters formed.

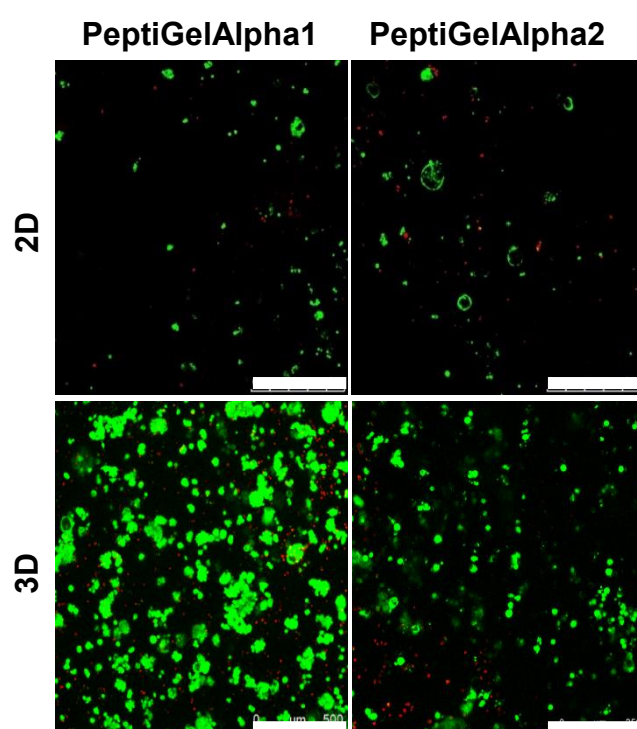


**Figure 4.4. LIVE/DEAD staining of MCF-7 cells in 2D and 3D culture in PeptiGelAlpha1 and 2 after 7 days.** Cells were stained with calcein-AM and ethidium homodimer-1 and incubated for 1 hour at 37 °C. Images were collected using a Leica SP5 confocal inverted microscope. Green = live cells. Red = dead cells. Scale bar = 500  $\mu$ m. N = 2.

#### 4.2.5. Choosing a SAPH Candidate

From the rheology data (**Figure 4.2**) and viability data (**Figure 4.4**), both PeptiGelAlpha1 and PeptiGelAlpha2 were similar in regards to their mechanical properties and ability to support MCF-7 cell growth. However, they differed in regards to their charge (**Figure 4.3**). As revealed in **section 4.2.3**, PeptiGelAlpha1 was neutrally charged whereas PeptiGelAlpha2 was positively charged at pH 7. On this basis, PeptiGelAlpha1 was chosen

as the most suitable peptide hydrogel for further investigation. The neutral charge of PeptiGelAlpha1 would render it more compatible with the majority of cell culture assays, as the hydrogel charge can interfere with negatively charged macromolecules such as DNA [276].

#### 4.2.6. Fibre Formation of PeptiGelAlpha1, Collagen I and Matrigel

TEM was used to visualise fibre formation of all three hydrogels (**Figure 4.5**). Matrigel was observed to form large bundles of fibres with a high density. Collagen I formed smaller fibrils, which were irregular in shape and structure. Some of these fibrils appeared to have disassembled with a fragmented network observed, suggesting that the material exhibited weak structural integrity. PeptiGelAlpha1, on the other hand, formed long thin fibres resembling ribbons, which were structurally intact and entangled to form a network.

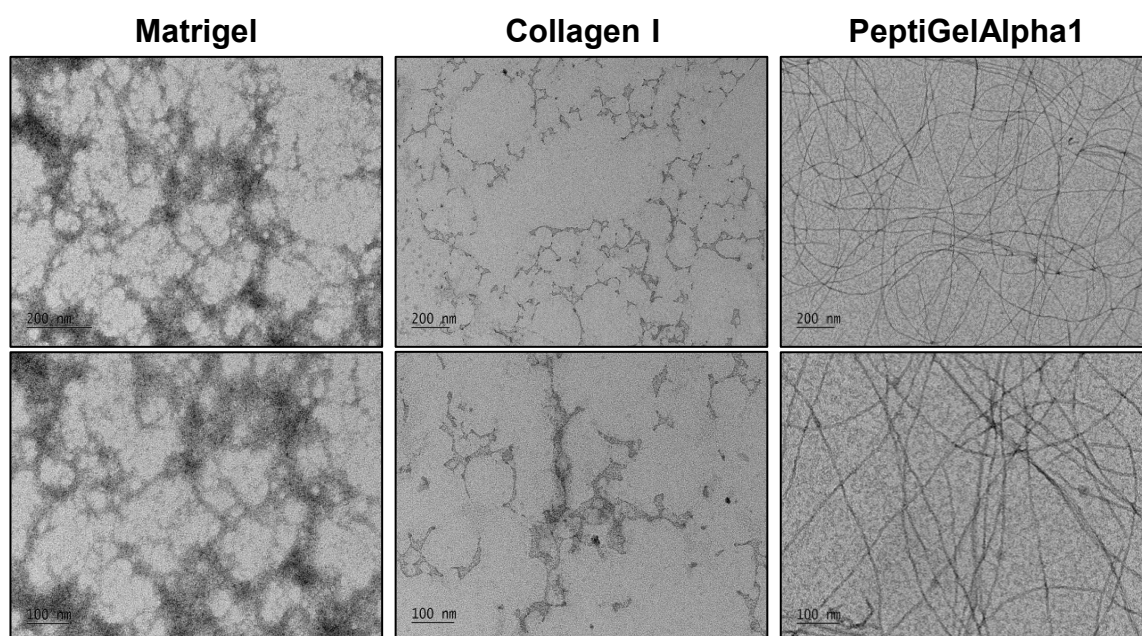


**Figure 4.5. TEM images of Matrigel, collagen I and PeptiGelAlpha1.** Hydrogels were diluted 100x with HPLC grade water and placed onto a copper grid and exposed to 1 % (w/v) UA to improve contrast. Images were collected using a Gatan Orius SC1000 CCD camera. N = 2. Scale bar = 200 nm for top row and 100 nm for bottom row.

The diameter of the fibres were measured using ImageJ software and plotted as a histogram to observe the distribution and variation (**Figure 4.6**). PeptiGelAlpha1 contained fibres that were uniform in size, varying from 2.6–14.2 nm in diameter (**Figure 4.6A**). Collagen I was formed of fibres that were more varied in size, ranging from 2.1–65.4 nm (**Figure 4.6B**). Matrigel also consisted of denser fibres that were incredibly varied in diameter, ranging from 3.9–120.7 nm (**Figure 4.6C**).

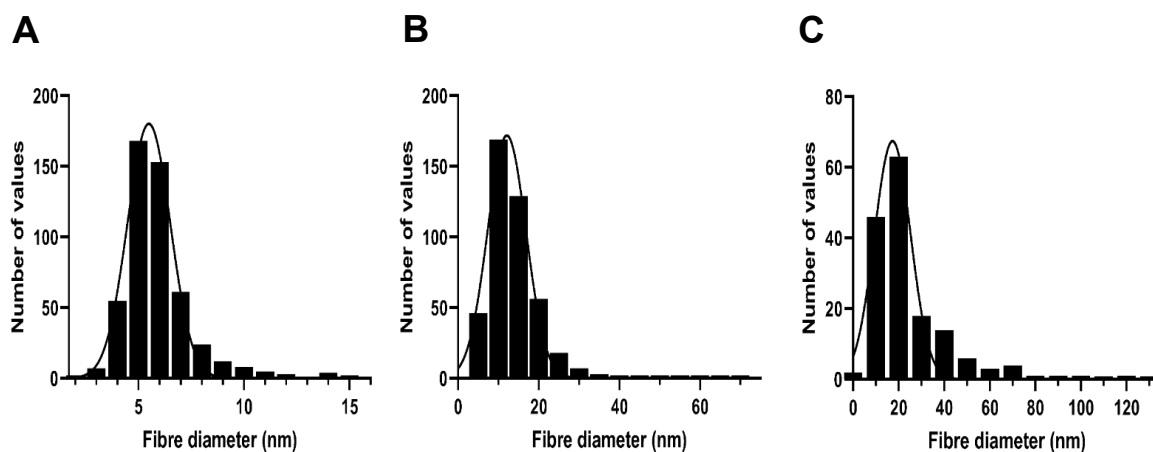


**Figure 4.6. Frequency distribution of fibre diameters.** (A) PeptiGelAlpha1, (B) collagen I and (C) Matrigel. ImageJ was used to measure and plot the fibre diameters as a histogram.

The thinnest fibres of each hydrogel were averaged and compared (**Figure 4.7**). For PeptiGelAlpha1, fibres with a diameter of < 10 nm, collagen I; < 20 nm and Matrigel; < 50 nm were analysed. Fibres of these diameters were used due to the large variation observed in fibre width. PeptiGelAlpha1 contained fibres with a mean of  $5.7 \text{ nm} \pm 1.4 \text{ nm}$ , whilst collagen I and Matrigel had a mean fibre diameter of  $12.0 \text{ nm} \pm 3.9 \text{ nm}$  and  $20.1 \text{ nm} \pm 9.6 \text{ nm}$  respectively. The mean fibre diameter of PeptiGelAlpha1 was significantly lower than collagen I and Matrigel ( $p < 0.0001$ ), whilst the fibre diameter of Matrigel was significantly larger than that of collagen I ( $p < 0.0001$ ). The mean fibre diameters of the three hydrogels have been summarised in **Table 4.2**.

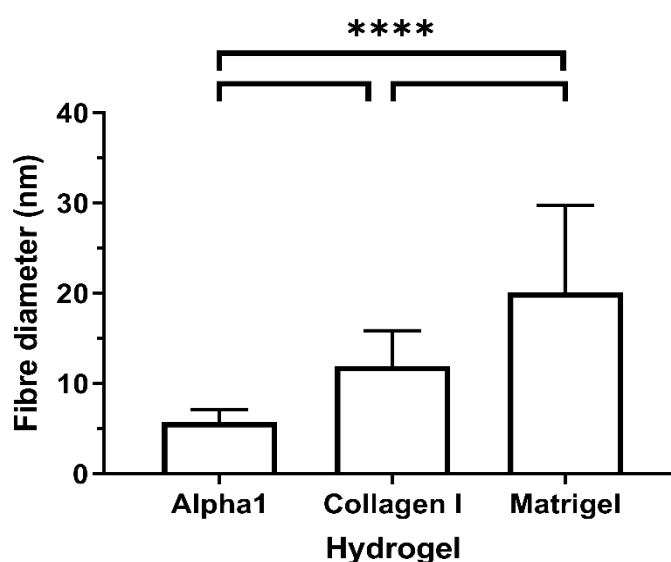


**Figure 4.7. Mean fibre diameters of PeptiGelAlpha1, collagen I and Matrigel.** For PeptiGelAlpha1, fibres with a diameter of < 10 nm, collagen I; < 20 nm and Matrigel; < 50 nm were analysed. Data are mean  $\pm$  S.D. \*\*\*\* =  $p < 0.0001$  using one-way ANOVA and post-hoc Tukey's test. N = 2.

#### 4.2.7. Viscoelastic Behaviour of PeptiGelAlpha1, Collagen I and Matrigel

Oscillatory rheometry was used to compare the mechanical properties of all three hydrogels. Firstly, amplitude sweeps were carried out in order to determine the LVR of the hydrogel, as well as the strain at which the hydrogel deforms. The LVR is defined as the range of stress in which measurements can be carried out without compromising the structural integrity of the sample. The yield strain is defined as the strain at which the  $G''$  exceeds the  $G'$  and the material is no longer considered solid-like [287]. Amplitude sweeps were carried out at a frequency of 1 Hz in the range of 0.02–30 % strain in the absence and presence of 18 hours media incubation.

For all hydrogels in the absence and presence of media conditioning, the applied strain of 0.2 % was within the LVR, showing that this strain can be used for further rheological experiments (**Figure 4.8–4.10**). This was shown by the  $G'$  remaining stable as the strain was increased. Collagen I without media conditioning exhibited linear behaviour until 6 % strain, with the observed increase in  $G''$  and decline in  $G'$ , although breakage was not observed. While with media conditioning, the material experienced breakage at a yield strain of 20 % (**Figure 4.8**). Matrigel did not deform in either condition (with and without media conditioning), with both  $G'$  and  $G''$  remaining linear throughout the strain range applied (**Figure 4.9**). For PeptiGelAlpha1 without media conditioning, linear behaviour was observed until 2 % strain, marked by  $G''$  exceeding  $G'$ , whilst with media conditioning the yield strain increased to 9 % (**Figure 4.10**). It was also observed that the material exhibited a linear strain region until 1 %, in the absence and presence of cell culture media.

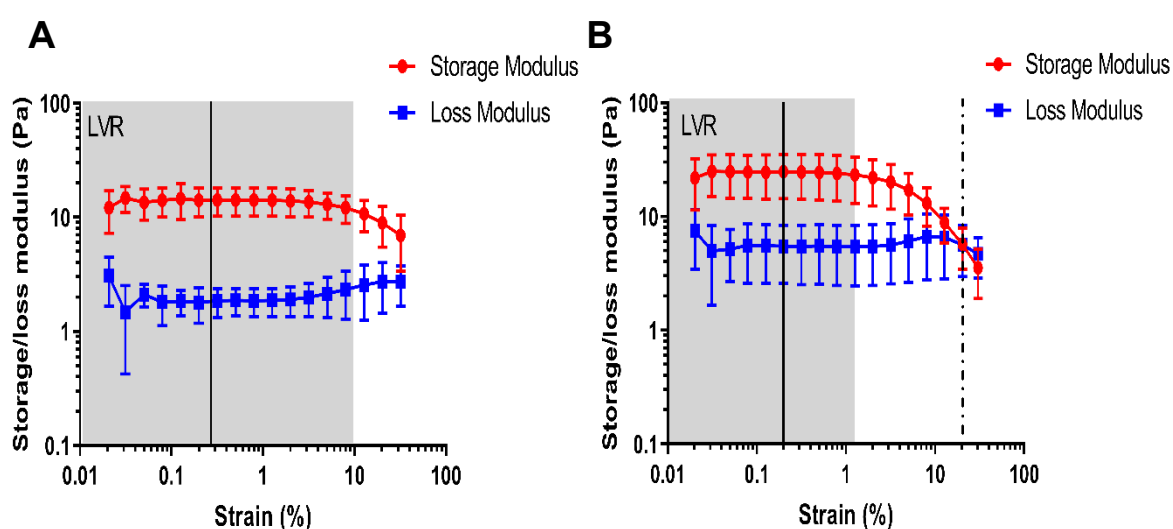


**Figure 4.8. Amplitude sweeps of collagen I (1.5 mg/mL).** (A) Without media conditioning. (B) After 18 hours of media incubation. A strain of 0.02–30 % at a frequency of 1 Hz was used. Solid line represents applied strain (0.2 %). Dashed line represents yield strain. Gap size = 500  $\mu$ m. Temperature = 37  $^{\circ}$ C. Data are mean  $\pm$  S.D. N = 3.

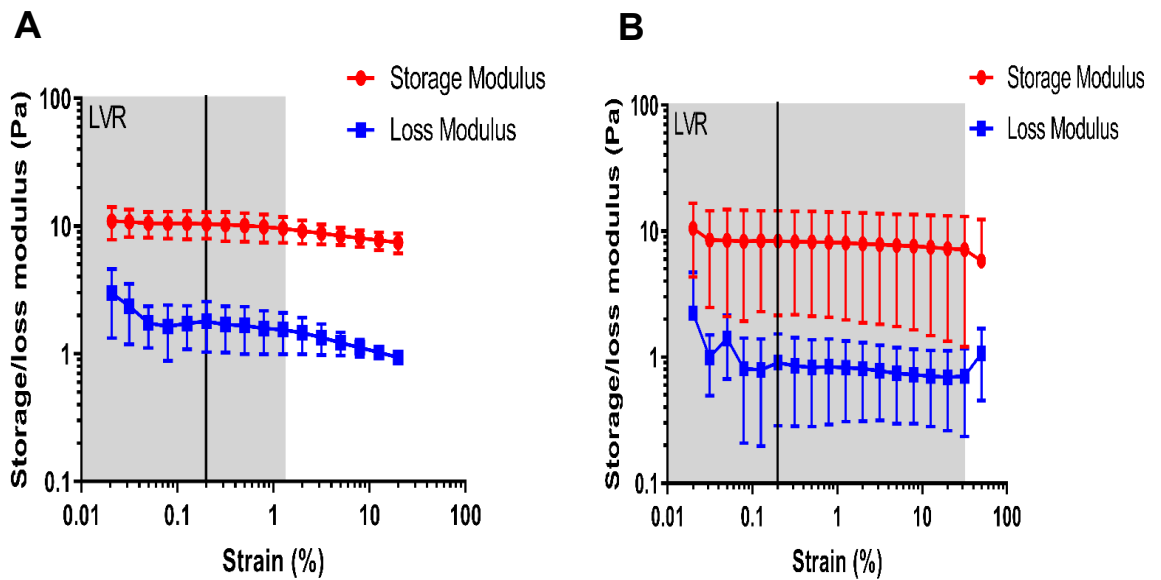


**Figure 4.9. Amplitude sweeps of Matrigel (5 mg/mL).** (A) Without media conditioning. (B) After 18 hours of media incubation. A strain of 0.02–30 % at a frequency of 1 Hz was used. Solid line represents applied strain (0.2 %). Gap size = 500  $\mu\text{m}$ . Temperature = 37  $^{\circ}\text{C}$ . Data are mean  $\pm$  S.D. N = 3.

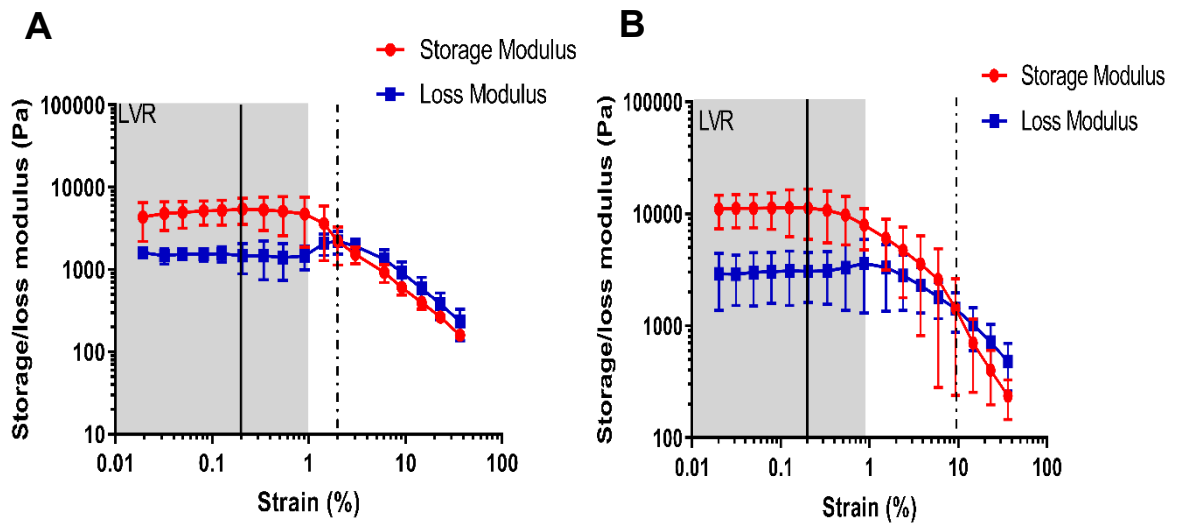


**Figure 4.10. Amplitude sweeps of PeptiGelAlpha1.** (A) Without media conditioning. (B) After 18 hours of media incubation. A strain of 0.02–30 % at a frequency of 1 Hz was used. Solid line represents applied strain (0.2 %). Gap size = 500  $\mu\text{m}$ . Temperature = 37  $^{\circ}\text{C}$ . Data are mean  $\pm$  S.D. N = 3.

Frequency sweeps were next carried out within the range of 0.01–10 Hz using 0.2 % strain (**Figure 4.11**). This strain was previously determined, in **Figure 4.8–10**, to be within the LVR for all hydrogels. For collagen I, the  $G'$  increased in response to increasing frequency, in the absence and presence of media conditioning (**Figure 4.11A**). In media conditioned Matrigel, the  $G'$  declined initially in response to increasing frequency, before plateauing (**Figure 4.11B**). The  $G'$  was then observed to increase slightly at the highest frequencies. Without media, a small frequency-dependent increase in  $G'$  was observed. For PeptiGelAlpha1, a slight frequency-dependent increase in  $G'$  was observed when conditioned with media (**Figure 4.11C**). Without media, the  $G'$  also exhibited a small frequency-dependent increase. It was also noted that the  $G'$  for all materials under both conditions were consistently greater than the  $G''$  at all frequencies, confirming that the materials were elastic. It was also noted that the shear moduli for PeptiGelAlpha1 (**Figure 4.11C**) were two orders of magnitude higher than that of collagen I (**Figure 4.11A**) and Matrigel (**Figure 4.11B**).

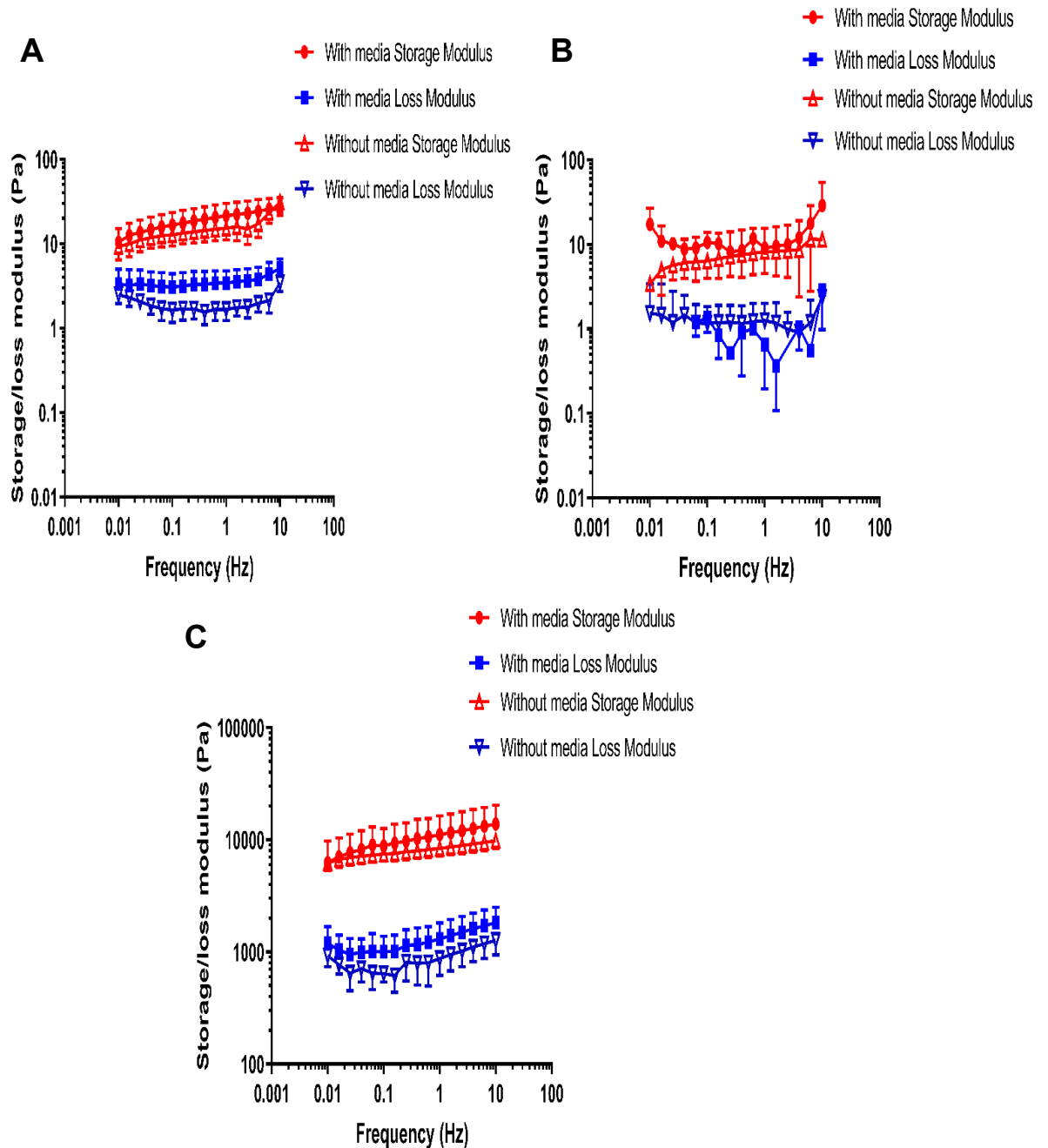


**Figure 4.11. Frequency sweeps of (A) collagen I (1.5 mg/mL), (B) Matrigel (5 mg/mL) and (C) PeptiGelAlpha1 in the absence and presence of 18 hours media conditioning.** Frequency sweeps were carried out from 0.01–10 Hz at a constant strain of 0.2 %. Gap size = 500  $\mu$ m. Temperature = 37  $^{\circ}$ C. Data are mean  $\pm$  S.D. N = 3.

Time sweeps with alternating cycles of high shear and low shear were carried out to observe if each of the materials, both in the absence and presence of media conditioning, were able to recover. Hydrogel samples were exposed to alternating 5-minute cycles of 0.2 % and 100 % strain at 1 Hz frequency. Under low strain (0.2 %), the  $G'$  exceeds the  $G''$  and the material is considered to be solid-like. Whilst under high strain (100 %), the  $G''$  exceeds the  $G'$  and thus the material is no longer solid-like. Recovery was observed if  $G' > G''$  following a cycle of high shear. Without media, collagen I was able to recover sufficiently, as shown by the  $G'$  exceeding the  $G''$  after each high shear cycle (**Figure 4.12A**). With media conditioning, the data appeared to be quite noisy (**Figure 4.12B**). Although collagen I was able to recover following each cycle of high shear, the  $G'$  appeared to decline after each successive cycle of high and low shear.

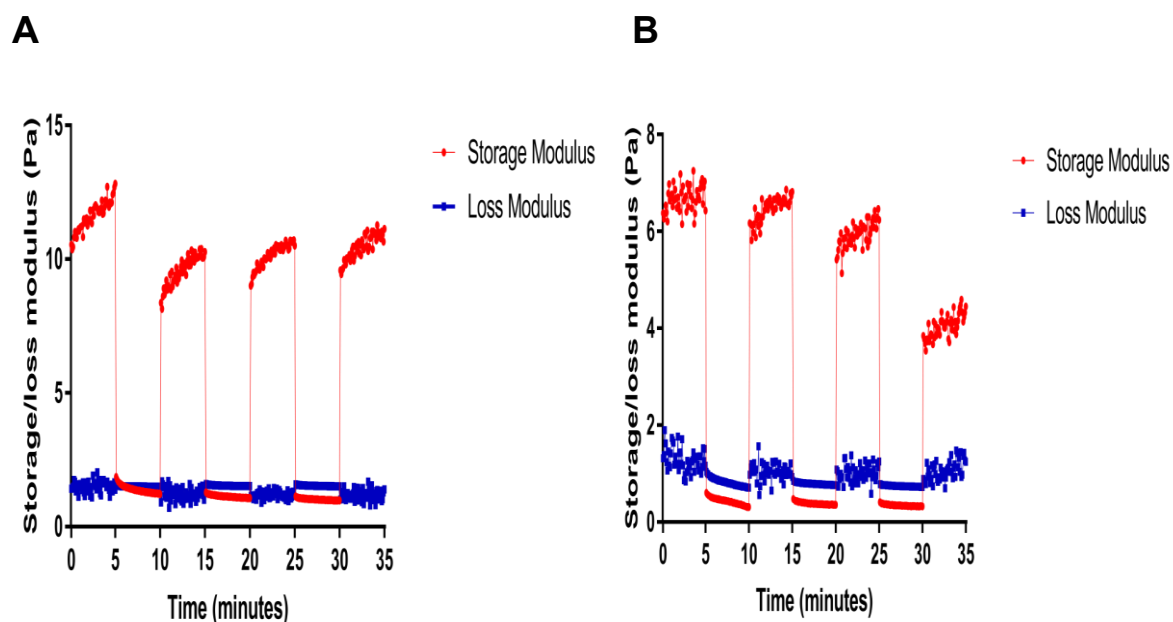


**Figure 4.12. Recovery profile of collagen I (1.5 mg/mL).** (A) Without media conditioning and (B) with 18 hours media conditioning. Time sweeps were carried out with alternating 5-minute cycles of recovery (0.2 % strain, 1 Hz frequency) and 5-minute cycles of high shear (100 % strain, 1 Hz frequency) for 35 minutes. Gap = 500  $\mu\text{m}$ . Temperature = 37  $^{\circ}\text{C}$ . Data shown are representative. N = 2.

Matrigel, interestingly, did not deform at all when high shear was applied, as the  $G'$  exceeded the  $G''$  without media (**Figure 4.13A**). With media, this event was also observed, although the  $G'$  was observed to decline after each successive cycle (**Figure 4.13B**).



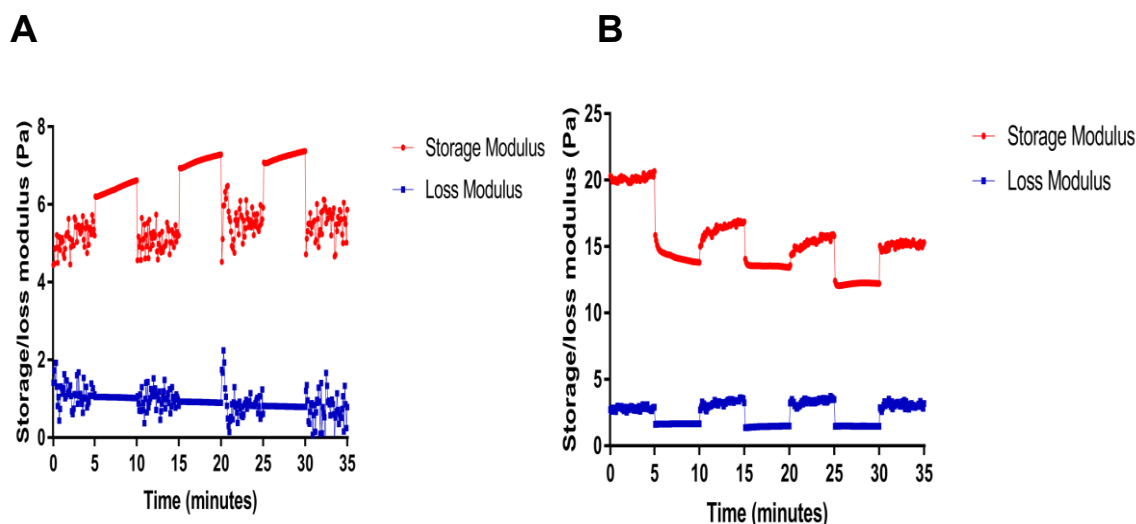


**Figure 4.13. Recovery profile of Matrigel (5 mg/mL).** (A) Without media conditioning and (B) with 18 hours media conditioning. Time sweeps were carried out with alternating 5-minute cycles of recovery (0.2 % strain, 1 Hz frequency) and 5-minute cycles of high shear (100 % strain, 1 Hz frequency) for 35 minutes. Gap = 500  $\mu\text{m}$ . Temperature = 37  $^{\circ}\text{C}$ . Data shown are representative. N = 2.

PeptiGelAlpha1 was able to successfully deform and recover following cycles of high and low shear without media (**Figure 4.14A**). The  $G'$  was also observed to increase after each successive low shear cycle. With media conditioning, PeptiGelAlpha1 was initially able to deform and recover after alternating cycles, with an increase in  $G'$  evident after several cycles (**Figure 4.14B**). However, after several cycles, the material appeared to lose its ability to recover, as shown by the  $G''$  exceeding the  $G'$  when low shear was applied.

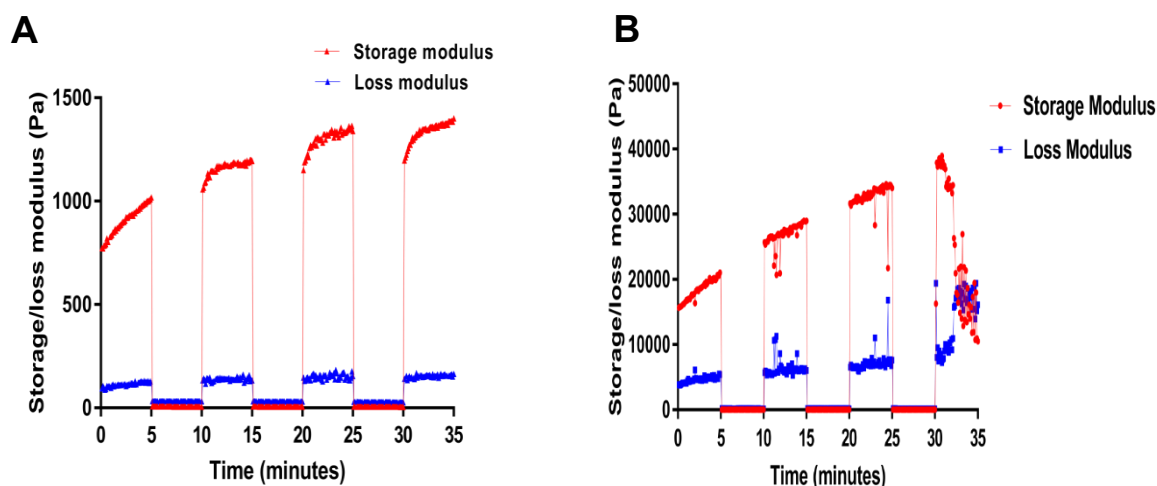


**Figure 4.14. Recovery profile of PeptiGelAlpha1.** (A) Without media conditioning and (B) with 18 hours media conditioning. Time sweeps were carried out with alternating 5-minute cycles of recovery (0.2 % strain, 1 Hz frequency) and 5-minute cycles of high shear (100 % strain, 1 Hz frequency) for 35 minutes. Gap = 500  $\mu\text{m}$ . Temperature = 37  $^{\circ}\text{C}$ . Data shown are representative. N = 2.

The  $G'$  at 1 Hz taken from frequency sweeps displayed in **Figure 4.11** were used to compare the overall stiffness of the three hydrogels, with and without media conditioning (**Figure 4.15**). Media incubation did not significantly affect the storage moduli of collagen I ( $15.3 \text{ Pa} \pm 4.0 \text{ Pa}$  vs  $27.8 \text{ Pa} \pm 0.8 \text{ Pa}$ ;  $p > 0.05$ ) nor Matrigel ( $8.2 \text{ Pa} \pm 3.0 \text{ Pa}$  vs  $9.0 \text{ Pa} \pm 6.6 \text{ Pa}$ ;  $p > 0.05$ ) (**Figure 4.15A**). The addition of cell culture media to PeptiGelAlpha1, however, significantly increased the stiffness from  $9048.3 \text{ Pa} \pm 1352.4 \text{ Pa}$  to  $12679.5 \text{ Pa} \pm 3224.0 \text{ Pa}$  ( $p < 0.01$ ).

Comparing all three hydrogels with media incubation, PeptiGelAlpha1 was significantly stiffer than both collagen I and Matrigel ( $p < 0.001$ ) (**Figure 4.15B**). There was no significant difference in stiffness between collagen I and Matrigel ( $p > 0.05$ ).

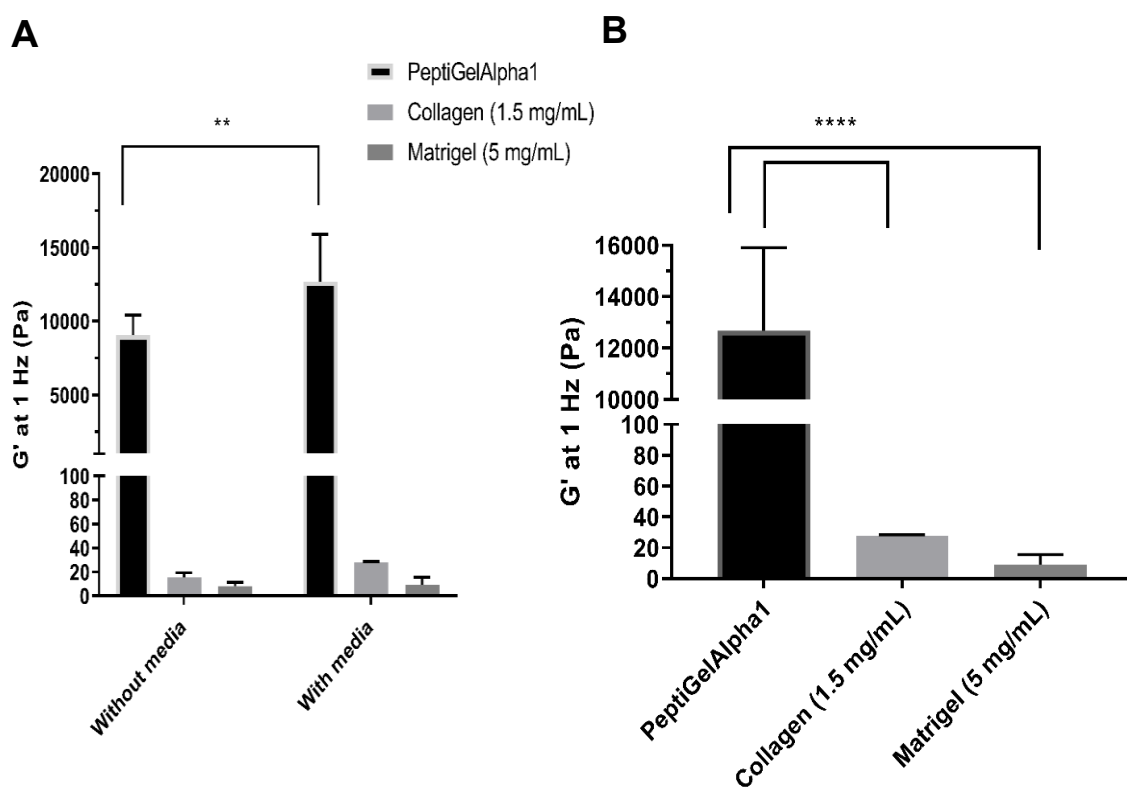


**Figure 4.15. The effect of media conditioning on the stiffness of PeptiGelAlpha1, collagen I (1.5 mg/mL) and Matrigel (5 mg/mL).** (A) With and without 18 hours media conditioning. (B) After 18 hours media conditioning. Values were taken from frequency sweeps from 0.01–10 Hz at 0.2 % strain. Gap size = 500  $\mu\text{m}$ . Temperature = 37  $^{\circ}\text{C}$ . Data are mean  $\pm$  S.D. \*\* =  $p < 0.01$ , \*\*\*\* =  $p < 0.0001$  using one-way ANOVA and post-hoc Tukey’s test. Data presented in (B) are a duplicate of rheology data with media conditioning presented in (A).

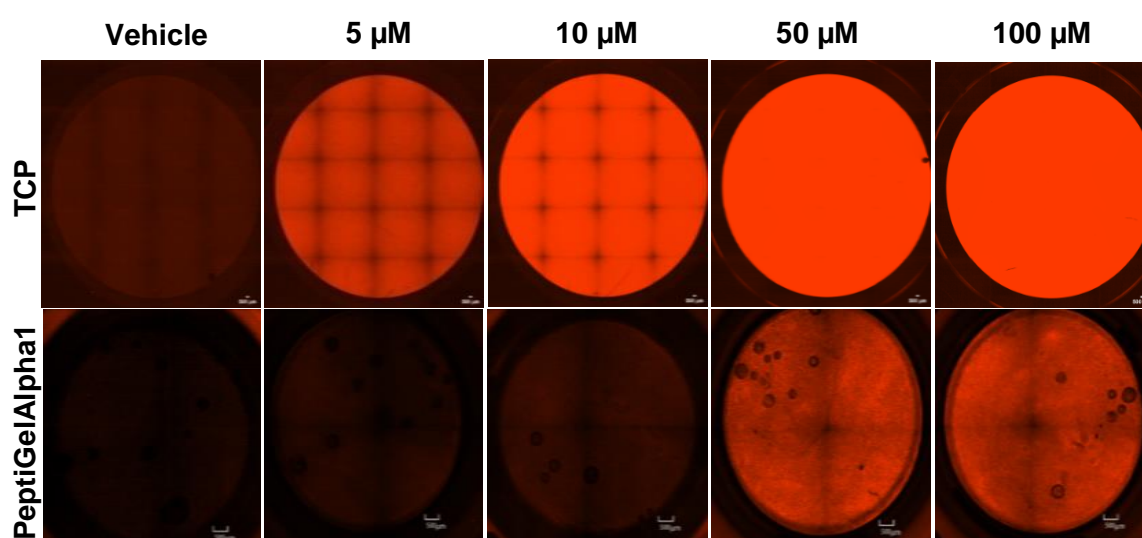
The mean storage moduli at 1 Hz of PeptiGelAlpha1, collagen I and Matrigel, in the absence and presence of media conditioning, have been summarised in **Table 4.2**.

**Table 4.2. Summary of mean fibre diameters and storage moduli at 1 Hz of PeptiGelAlpha1, collagen I and Matrigel. Data are mean  $\pm$  S.D.**

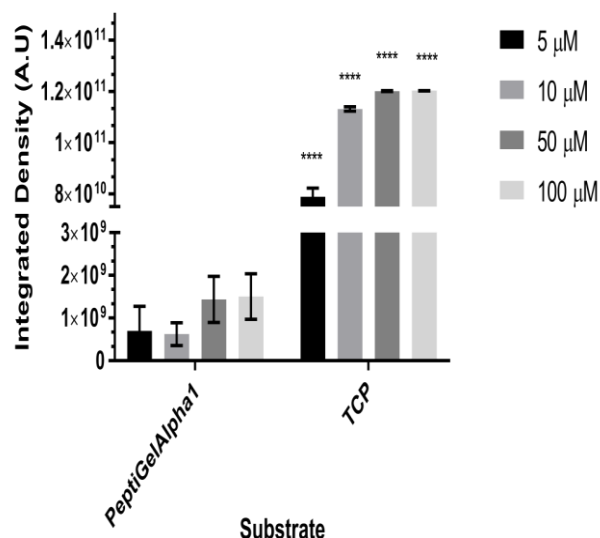
Hydrogel	Mean fibre diameter (nm)	Storage modulus at 1 Hz (Pa)	
		Without media conditioning	With media conditioning
PeptiGelAlpha1	5.7 $\pm$ 1.4	9048.3 $\pm$ 1352.4	12679.5 $\pm$ 3224.0
Collagen I (1.5 mg/mL)	12.0 $\pm$ 3.9	15.3 $\pm$ 4.0	27.8 $\pm$ 0.8
Matrigel (5 mg/mL)	20.1 $\pm$ 9.6	8.2 $\pm$ 3.04	9.0 $\pm$ 6.6

#### 4.2.8. Doxorubicin Penetration of PeptiGelAlpha1

To observe if PeptiGelAlpha1 acted as a physical barrier to chemotherapeutic drugs, confocal microscopy was used to visualise distribution of doxorubicin through the hydrogel. Doxorubicin was used as a test compound as it is inherently fluorescent. TCP was used as a control as distribution would be homogenous. PeptiGelAlpha1 and TCP samples were exposed to doxorubicin prepared in cell culture media at concentrations of 5, 10, 50 and 100  $\mu$ M and incubated overnight under standard cell culture conditions. A vehicle control of 1 % DMSO was also included. The vehicle controls showed very little fluorescence, showing that the DMSO solvent does not contribute towards the fluorescent properties of the compound (**Figure 4.16**). Doxorubicin was clearly visible in the TCP samples with 5  $\mu$ M doxorubicin, with the fluorescence becoming saturated by 10  $\mu$ M. With PeptiGelAlpha1, minimal fluorescence was observed with 5  $\mu$ M and 10  $\mu$ M doxorubicin. PeptiGelAlpha1 samples exposed to 100  $\mu$ M and 500  $\mu$ M doxorubicin appeared visually brighter but when quantified, were still significantly lower than their TCP counterparts ( $p < 0.0001$ ), (**Figure 4.17**).

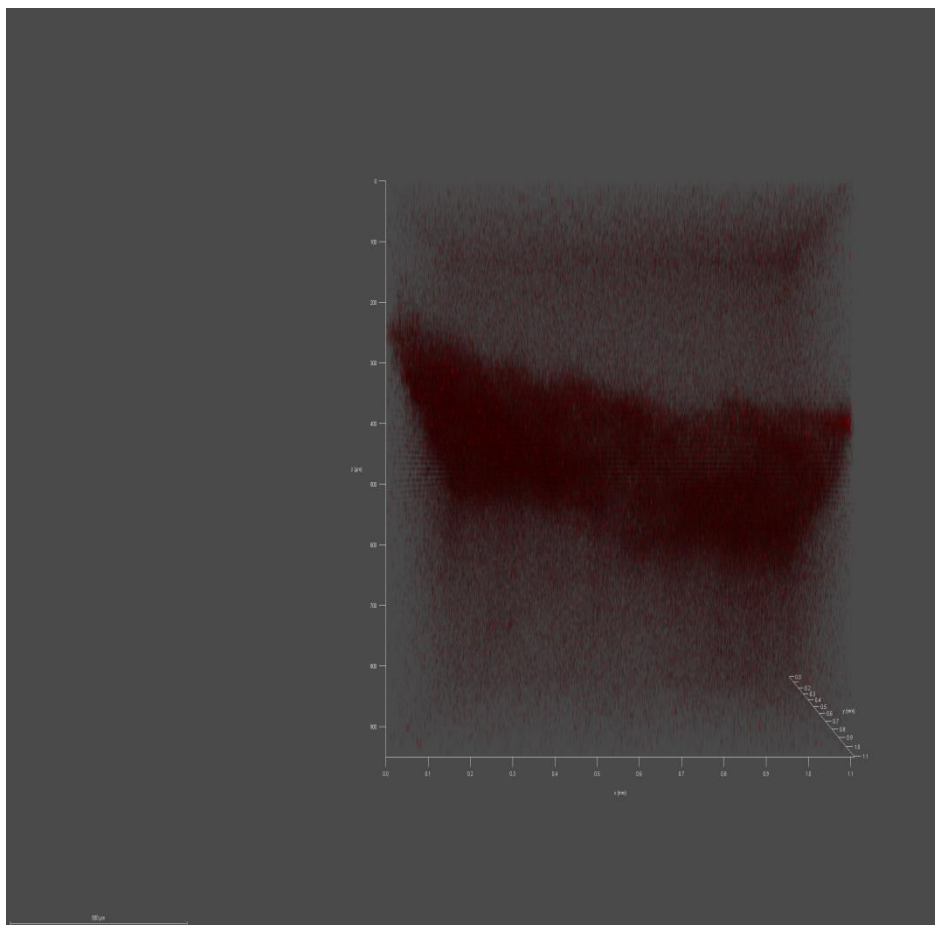
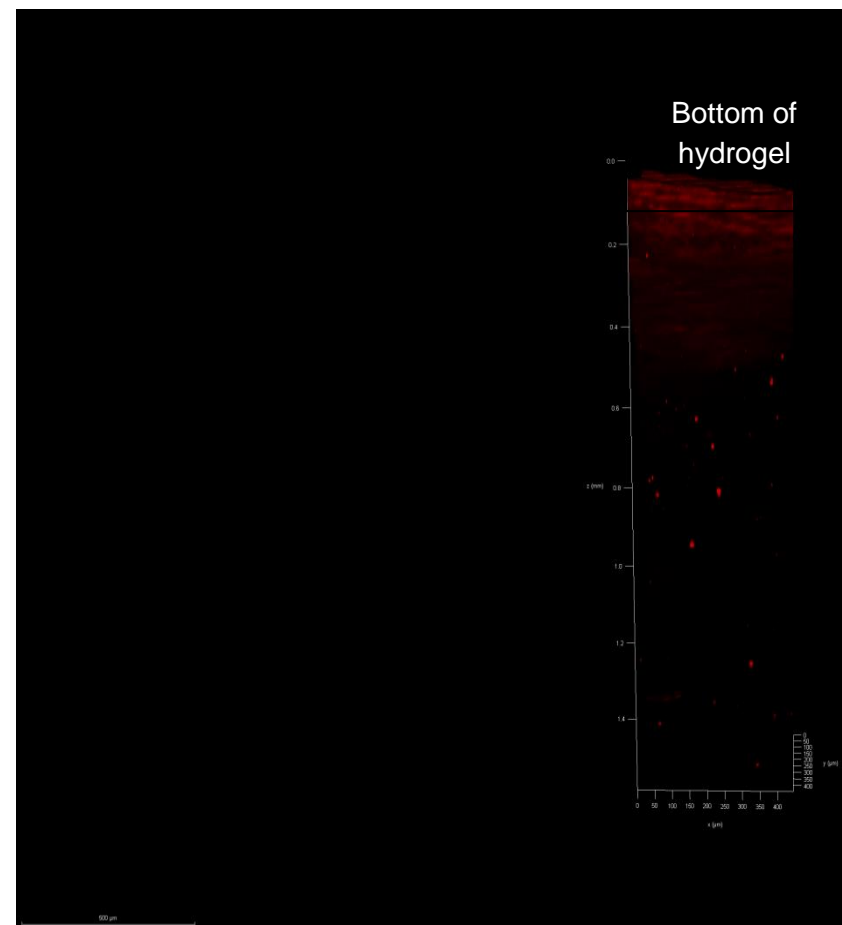


**Figure 4.16. Fluorescence images of doxorubicin penetration into PeptiGelAlpha1 and TCP.** PeptiGelAlpha1 and TCP were exposed to 5, 10, 50 and 100  $\mu$ M doxorubicin and incubated for 24 hours at 37  $^{\circ}$ C, 20 % (v/v) O<sub>2</sub>, 5 % (v/v) CO<sub>2</sub>. A vehicle control of 1 % DMSO was used. Red = doxorubicin. N = 2.



**Figure 4.17. Fluorescence quantification of doxorubicin penetration into PeptiGelAlpha1 and TCP.** Vehicle control values were subtracted from sample values. Data are mean  $\pm$  S.D. \*\*\*\* =  $p < 0.0001$  using one-way ANOVA and post-hoc Tukey's test. N = 2.

Distribution of doxorubicin through PeptiGelAlpha1 on the z-axis was next observed using both confocal microscopy and multi-photon imaging (**Figure 4.18**). Based on results presented in **Figure 4.16**, 100  $\mu$ M was used to ensure visualisation of the compound in the hydrogel. Confocal 3D rendering of the drug-laden hydrogel showed that doxorubicin tended to accumulate within the centre of the hydrogel, and distribution was much sparser towards the top and bottom of the hydrogel (**Figure 4.18A**). Multi-photon imaging was used to observe doxorubicin distribution much deeper into the sample (**Figure 4.18B**). Compared with confocal imaging, which was only able to image 900  $\mu$ m deep into the sample, multi-photon imaging enabled much deeper penetration of the sample, with 1400  $\mu$ m imaged. It was also observed that 'pockets' of doxorubicin were present in the hydrogel, showing that distribution was not homogenous and that the hydrogel prevented diffusion of the drug into the system.

**A****B**

**Figure 4.18. Distribution of 100  $\mu$ M doxorubicin through PeptiGelAlpha1.** (A) Confocal 3D rendering. (B) Multi-photon 3D rendering. Images were taken using a Leica SP8 confocal upright microscope. Red = doxorubicin. N = 2. Scale bar = 50  $\mu$ m.

## 4.3. Discussion

### 4.3.1. Comparison of PeptiGelAlpha1, 2 and 4

To determine which SAPH would be most suitable for culture of MCF-7 and MDA-MB-231 cancer cells, PeptiGelAlpha1, 2 and 4 were first characterised and compared. AT-FTIR analysis was used to confirm that PeptiGelAlpha1, 2 and 4 were composed of anti-parallel  $\beta$  sheets, as shown by peaks at  $1620\text{ cm}^{-1}$  and  $1690\text{ cm}^{-1}$  (**Figure 4.1**), which is consistent with the literature for using  $\beta$ -sheet forming ionic complementary SAPHs [281,288]. The main limitation with using AT-FTIR for protein characterisation is the interference of water molecules, which exhibit an absorbance peak in the amide I region [289]. Hydrogel samples are typically  $> 99\%$  water and so the nature of the sample would surely interfere with infrared spectroscopy (IR). Water is typically used as a background control and subtracted from all sample spectra to remove the interference. To completely eliminate water interfering with IR, deuterium oxide can be used as a solvent instead of water. However, this could potentially change the sample's structure and possibly result in sample loss. An alternative method to AT-FTIR for secondary structure characterisation is circular dichroism (CD), which relies on interaction of molecules with light, giving way to different structural elements having a characteristic CD spectra [290]. Nonetheless, for this study, AT-FTIR was sufficient to characterise the secondary structure of PeptiGelAlpha1, 2 and 4.

The storage moduli of PeptiGelAlpha1, 2 and 4 were measured using oscillatory shear rheology (**Figure 4.2**). PeptiGelAlpha1 and 2 were similar in stiffness ( $12679.5\text{ Pa} \pm 3224.0\text{ Pa}$  vs  $12559.7\text{ Pa} \pm 9647.3\text{ Pa}$  respectively), whereas PeptiGelAlpha4 was significantly softer ( $275.1\text{ Pa} \pm 84.2\text{ Pa}$ ) (**Table 4.1**). The values measured herein do differ from those reported in the literature; one study reported the storage modulus of PeptiGelAlpha1 to be  $15\text{ kPa} \pm 5\text{ kPa}$ , which is comparable to the value reported here ( $12.7\text{ kPa} \pm 3.2\text{ kPa}$ ) [21]. However, the stiffness of PeptiGelAlpha2 was measured as  $21\text{ kPa} \pm 1\text{ kPa}$ , which is almost twice as stiff as reported in this study ( $12.6\text{ kPa} \pm 9.6\text{ kPa}$ ), and PeptiGelAlpha4, depicted as PeptiGelAlphaProB, was measured to be  $0.5\text{ kPa} \pm 0.08\text{ kPa}$  [21]. The disparity in measurements of PeptiGelAlpha2 could arise from different parameters used; in this study 18 hours media conditioning was used rather than 24 hours, and frequency sweeps were carried out at  $0.2\%$  strain in this study, whilst  $1\%$  was used [21]. Rheological measurements are sensitive to the parameters used, which could explain the difference in data obtained [283]. Different ionic concentrations of cell culture media could have also played a role in different storage moduli values measured, as increasing the ionic strength results in an increase in stiffness [21].

The theoretical charges of PeptiGelAlpha1, 2 and 4 versus pH were calculated (**Figure 4.3**). It was determined that at pH 7, physiological pH, PeptiGelAlpha1 was neutrally charged, whereas PeptiGelAlpha2 and 4 were positively charged (+ 1 and + 2 respectively). The high positive charge of PeptiGelAlpha4 explains the relatively low storage modulus; PeptiGelAlpha4 is covered by positively charged residues which reduces hydrophobic fibre interactions, resulting in reduced network crosslinking and ability to form large fibre bundles [286]. This results in an increased mesh size and therefore relatively low stiffness. A positive charge could potentially interfere with cell culture assays, which have been optimised for traditional 2D culture and therefore do not take into consideration the complexities of using 3D systems, which differ in both geometry and charge. A study examining the commercially available PeptiGels from Manchester BIOGEL found that the positive charges of PeptiGelAlpha2 and 4 interfered with RNA extraction resulting in low RNA yield, due to RNA being negatively charged, whilst PeptiGelAlpha1 (neutrally charged) did not interfere [276]. Due to the low stiffness and high charge observed in PeptiGelAlpha4 (**Table 4.1**), this hydrogel was ruled out for further studies.

PeptiGelAlpha1 and 2 were finally used for initial cell viability studies with MCF-7 breast cancer cells. After 7 days in culture, both hydrogels were observed to support cell viability, as observed by a high density of live cells, providing preliminary proof that PeptiGelAlpha1 and 2 can support the growth of breast cancer cells. However, in PeptiGelAlpha1, a greater cell density was observed with a greater cell cluster intensity. Due to the high viability, alongside the neutral charge, PeptiGelAlpha1 was chosen as the sole SAPH to use in further studies.

#### **4.3.2. Fibre Formation of PeptiGelAlpha1, Collagen I and Matrigel**

The physical properties of PeptiGelAlpha1 were next compared to collagen I and Matrigel, popular biomaterials used in cancer research. Fibre formation and morphology of diluted hydrogels was observed using TEM imaging. TEM was used rather than other imaging techniques such as atomic force microscopy (AFM) and scanning electron microscopy (SEM), as it is more suitable for imaging hydrated materials and enables detailed images to be captured. SEM requires dehydration and freeze drying of the sample, which is difficult with hydrogels due to their high water content, causing significant deformation and damage to the hydrogel fibres [291]. Environmental SEM counteracts the issues associated with conventional SEM, by protecting the sample from the vacuum with a partition [292]. AFM requires a probe making contact with the sample, which can result in dragging due to

the ‘wetness’ of hydrogel samples [293]. Diluting of the hydrogels was carried out to visualise individual fibres and their morphologies.

TEM imaging revealed that PeptiGelAlpha1 was formed of long and entangled fibres with a ribbon shape forming a network (**Figure 4.5**). Matrigel was composed of thick fibre bundles forming a mesh, and collagen I was observed as fragmented fibrils with an irregular structure. As the hydrogel networks were diluted prior to further processing and imaging, it is noted that the nanofibres in PeptiGelAlpha1 were still able to maintain an entangled network, whereas collagen I could not retain structural integrity when diluted. The ability of PeptiGelAlpha1 to self-anneal following dilution has been observed with other SAPH systems [281,286]. This self-annealing is due to the rapid and spontaneous self-assembly properties of SAPHs, as well as the stability of  $\beta$ -sheet fibres. Mechanical disruption of the SAPH system impacts the hydrogel formation, but the  $\beta$ -sheet fibres remain undisturbed [221]. Other studies investigating the nanostructure of diluted RADA16, collagen I and Matrigel discovered that RADA16 formed entangled ribbon-like structures, whilst Matrigel was composed of thick fibres that bundled together, and collagen I was formed of heterogeneously sized fibres [28]. The data presented in this current study thus correlate with findings in the literature.

Quantification of all three hydrogels revealed heterogeneity in diameter in collagen I and Matrigel (**Figure 4.6**). PeptiGelAlpha1 contained uniformly sized fibres with a diameter of 2.6–14.2 nm, whilst collagen I and Matrigel fibres were 2.1–65.4 nm and 3.9–120.7 nm respectively. The synthetic nature of PeptiGelAlpha1 would explain the consistency in fibre diameter, whilst collagen I and Matrigel, being naturally derived, would be more heterogeneous. ECM fibres vary widely in diameter, dependent upon the tissue of study and ECM protein. As mentioned in **section 4.1**, laminin fibres measure 2–7 nm, whilst fibronectin varies from 2–22 nm [20]. The mean fibre diameter of PeptiGelAlpha1,  $5.7 \text{ nm} \pm 1.4 \text{ nm}$ , was significantly lower than that of collagen I ( $12.0 \text{ nm} \pm 3.9 \text{ nm}$ ) and Matrigel ( $20.1 \text{ nm} \pm 9.6 \text{ nm}$ ) (**Figure 4.7**). The fibre diameter of PeptiGelAlpha1, therefore, mimicked that of the ECM. Ionic complementary  $\beta$ -forming SAPHs FEFKFEFK and KFEFKFEFKK were shown to have fibres of 3–5 nm in diameter using TEM imaging [286], showing that the measured fibre diameter of PeptiGelAlpha1 was consistent with similar platforms.



### 4.3.3. Viscoelastic Behaviour of PeptiGelAlpha1, Collagen I and Matrigel

The mechanical properties of all three hydrogels were assessed using oscillatory rheology. Oscillatory shear rheometry is used as a reliable technique to measure the storage and loss moduli of hydrogels [273,287,294]. Amplitude sweeps, frequency sweeps and time sweep recovery cycles were all used to observe how the shear moduli of the hydrogels behaved in response to changes in strain, frequency and cycles of high and low shear. Amplitude and frequency sweeps have previously been employed for mechanical characterisation of hydrogels used for biomedical applications [295]. Time sweep cycles are commonly used to determine gelation dynamics and hydrogel formation of naturally derived materials [295,296]. To the author's knowledge, the recovery profiles of collagen I and Matrigel have not previously been investigated using time sweep cycles.

The results of the amplitude sweeps showed that the hydrogels exhibited different linear behaviour profiles within the strain applied (**Figure 4.8–10**). Nonetheless, 0.2 % strain was within the LVR for all three hydrogels, in the absence and presence of media conditioning, and was therefore used in subsequent rheological tests. An appropriate strain to use is an important parameter to generate maximal signal without compromising the sample [295]. It was noted that collagen I, without media conditioning, did not deform within the applied strain range (**Figure 4.8A**). This could be because an insufficient strain range was used, and a higher strain is required to deform the hydrogel. Frequency sweeps showed that all three hydrogels remained solid-like within the frequency range applied, as the  $G'$  was greater than  $G''$  at all frequencies (**Figure 4.11**). The  $G'$  of all three hydrogels exhibited a frequency-dependent increase; this is because the material could not relax at higher frequencies, resulting in an observed increase in  $G'$  [297]. Media conditioning did not affect this behaviour. The  $G'$  at 1 Hz was taken from frequency sweeps and used to describe the overall 'stiffness' of the hydrogel. This value has been used in previous approaches for testing the mechanical properties of hydrogels using rheology [21,281,295].

Regarding the recovery profiles, PeptiGelAlpha1, without media, was able to successfully deform and recover following alternating cycles of low and high shear (**Figure 4.14A**). When high shear (100 %) was applied, the material became liquid ( $G'' > G'$ ) and recovery with low shear (0.2 % strain) resulted in the material becoming solid-like again ( $G' > G''$ ). This demonstrates the pliable nature of the material and shows its versatility for use in different applications, such as 3D printing, injection and cell encapsulation. This recovery is a common feature amongst SAPHs [22,281]. This shear-thinning behaviour is due to breakage of the hydrogel network into separate domains when shear stress is applied;

removal of the shear results in the fibres at the domain boundaries relaxing and entangling, resulting in recovery and solidification of the hydrogel [298]. With media conditioning, however, the system crashed after several cycles, with  $G'' > G'$  when low shear was applied (**Figure 4.14B**). It was noted when handling PeptiGelAlpha1 that without media, the material was easy to handle and could be pipetted without difficulty. When media was added to the gel, the material became fragile and was subject to breakage. The addition of cell culture media to PeptiGelAlpha1 resulted in a charge screening effect from the ions present, promoting physical cross-linking [281]. This charge screening effect could have therefore hindered the self-annealing properties of the hydrogel. Media conditioning has been shown to increase the brittleness of SAPHs in previous studies, by reducing the yield strain [226]. However, the data in this study showed that media conditioning increased the yield strain of PeptiGelAlpha1 (**Figure 4.10**), suggesting that the primary sequence of the SAPH dictates interactions with cell culture media and subsequent viscoelastic properties. Collagen I was able to recover both in the absence and presence of cell culture media; showing that it too has shear-thinning properties and is able to recover (**Figure 4.12A & B**). Media conditioning did result in a decrease in  $G'$  after successive cycles of high and low shear, indicating that the structural integrity was compromised when in the presence of cell culture media. Matrigel, did not deform when high shear was applied, as the  $G'$  was greater than the  $G''$  throughout the cycles, in the absence and presence of media conditioning (**Figure 4.13A & B**). This was also observed with the amplitude sweep data (**Figure 4.9**). This shows that Matrigel did not display any shear-thinning behaviour under high strain. This therefore limits the applications of Matrigel, when the material has solidified as a hydrogel.

The  $G'$  at 1 Hz of PeptiGelAlpha1, collagen I and Matrigel were compared, in the absence and presence of media conditioning (**Figure 4.15A**). PeptiGelAlpha1 was the only material to significantly increase when incubated in cell culture media overnight. Without media, PeptiGelAlpha1 has a pH of 4 [21]. The observed increase in  $G'$  is because, in the addition to the charge screening effect by ions discussed previously, the increase in pH from 4 to 7 results in the absence of electrostatic interactions, increasing hydrophobic crosslinking, resulting in an increase in stiffness [281]. PeptiGelAlpha1 was also found to be significantly stiffer than both collagen I and Matrigel (**Figure 4.15B**). The stiffness of collagen I and Matrigel,  $27.8 \text{ Pa} \pm 0.76 \text{ Pa}$  and  $9.02 \text{ Pa} \pm 6.60 \text{ Pa}$  respectively, are thus more suited to mimicking soft tissues, such as the brain ( $< 1 \text{ kPa}$ ) [299]. The stiffness of breast tumour tissue is under debate, as values reported will depend upon the technique used, the stage of cancer and patient-to-patient variability [300]. One of the main issues

with comparing the stiffness of materials with tissue samples is that hydrogels tend to be measured using techniques investigating the bulk mechanical properties, such as rheology, whereas *ex vivo* samples are typically measured using AFM or nanoindentation. The shear modulus and elastic modulus are measured respectively in rheology and AFM/indentation, which can be indirectly compared using the Poisson's ratio. There have been no studies to date published measuring the stiffness of breast tumour tissue using rheology, although rheology has been performed on colon tumour tissue to provide storage moduli values [301]. A study which is frequently cited for the stiffness of breast tumour states that it is  $4049 \text{ Pa} \pm 938 \text{ Pa}$  (elastic modulus measured, conversion to shear modulus is  $1619 \text{ Pa} \pm 375 \text{ Pa}$  using **Equation 3.1**) [172]. The limitation with this study is that a transgenic mouse model of breast cancer was used, meaning that the value measured is not translatable nor representative of human breast tumour tissue. Other studies using human tissue have provided Young's moduli of  $10.40 \text{ kPa} \pm 2.60 \text{ kPa}$  to  $42.52 \text{ kPa} \pm 12.47 \text{ kPa}$ , dependent upon the stage of cancer [300]. When converted to shear moduli using a Poisson's ratio of 0.5 using **Equation 3.1**, these range from  $4.16 \text{ kPa} \pm 1.04 \text{ kPa}$  to  $17.01 \text{ kPa} \pm 4.99 \text{ kPa}$ . The stiffness of PeptiGelAlpha1 with media conditioning,  $12.7 \text{ kPa} \pm 3.2 \text{ kPa}$ , lies within this range and is therefore more suitable for mimicking the mechanical properties of breast tumour tissue.

In order to directly and accurately compare the stiffness of PeptiGelAlpha1 with breast tumour tissue, oscillatory rheology should be carried out on both sample sets using the same parameters, to ensure consistency in results. Protocols for performing rheological testing on tumour samples have previously been published [302]. Nonetheless, the data in this current study show that PeptiGelAlpha1 is a more appropriate material for mimicking the mechanical properties of breast tumour than collagen I and Matrigel.

#### **4.3.4. Doxorubicin Penetration of PeptiGelAlpha1**

To visualise diffusion and distribution of an anti-cancer drug within PeptiGelAlpha1, and to observe if the hydrogel could prevent the drug entering the system, doxorubicin was used as a test compound. This drug was chosen as it is inherently fluorescent [303]. TCP was chosen as a positive control, as drug distribution would be homogeneous and there are no physical barriers preventing the drug reaching the TCP. Samples were incubated for 18 hours before imaging. Confocal imaging revealed the DMSO vehicle did not contribute towards the fluorescence exerted by the drug. Fluorescence was only observed within the hydrogel at the higher concentrations used ( $50 \mu\text{M}$  and  $100 \mu\text{M}$ ), showing that a higher concentration of drug was needed to penetrate the material (**Figure 4.16**).

Confocal and multi-photon imaging were then used to visualise spatial distribution of 100  $\mu\text{M}$  doxorubicin through the full thickness of the hydrogel (**Figure 4.18**). Confocal imaging was able to image 900  $\mu\text{m}$  of the sample, whereas multi-photon imaging was able to image much deeper into the sample (1400  $\mu\text{m}$ ). Multi-photon imaging offers increased depth penetration of samples, by using longer wavelength photons which are lower in energy and therefore penetrate more deeply [304,305]. Confocal and multi-photon imaging revealed differences in drug accumulation. In multi-photon imaging, doxorubicin appeared to accumulate at the bottom of the hydrogel (**Figure 4.18B**). The hydrogels were kept in their inserts during imaging, to ease handling. It is possible that doxorubicin particles were trapped in the insert membrane pores. However, deeper into the sample ‘pockets’ of doxorubicin were seen, showing that distribution within the hydrogel was not homogeneous. To mimic the TME *in vitro*, it is important that the drug is able to enter the hydrogel, but that distribution is uneven and hindered by the hydrogel. These data show that PeptiGelAlpha1 can prevent uniform penetration and diffusion of anti-cancer drugs. The molecular weight of doxorubicin is 543.52 g/mol; therefore any drug at or below this molecular weight should too be able to penetrate the material.

#### 4.4. Conclusions

When choosing a biomaterial for cell culture and tissue engineering applications, characterisation of the material properties should be carried out to understand how the material behaves, and if its physical properties render it suitable. A choice of commercially available SAPHs are on offer, differing in charge and mechanical properties. Mimicking the mechanical properties of the biological tissue in question is necessary in *in vitro* culture, to support appropriate cell behaviour.

Naturally derived hydrogels, such as collagen I and Matrigel have traditionally been used in *in vitro* modelling of cancer, due to the abundance of growth factors and cell binding cues facilitating cell-cell and cell-ECM interactions. However, these hydrogels have not been well characterised, in spite of their popularity in cell culture applications.

This chapter aimed to select a SAPH to use based on charge, mechanical properties and initial cell viability data. The chosen SAPH, PeptiGelAlpha1, was characterised alongside collagen I and Matrigel in regards to the fibre architecture and mechanical properties. Finally, doxorubicin diffusion into PeptiGelAlpha1 was carried out to determine if the material could mimic an *in vitro* physical barrier.

In summary, PeptiGelAlpha1 was chosen as a suitable candidate due to its mechanical properties, neutral charge and biocompatibility. PeptiGelAlpha1 was found to be formed of uniformly sized nanofibres, whilst Matrigel and collagen I fibres exhibited high variability and were much thicker and irregular in shape. Collagen I and PeptiGelAlpha1 exhibited shear-thinning behaviour, but Matrigel did not. Media conditioning influenced the stiffness of PeptiGelAlpha1 and hindered its ability to recover, but did not affect collagen I or Matrigel. PeptiGelAlpha1 was displayed superior mechanical properties to collagen I and Matrigel and was able to more faithfully mimic the stiffness of breast tumour tissue. Doxorubicin diffusion into PeptiGelAlpha1 was heterogeneous and reduced. These data show that PeptiGelAlpha1 is a more suitable platform for modelling cancer *in vitro* than collagen I or Matrigel, in regards to its physical properties.

The novelty of the work in this chapter is highlighted in the characterisation and comparison of the physical properties and viscoelastic behaviour of collagen I and Matrigel, both popular biomaterials used in 3D cell culture and specifically of cancer cells, with PeptiGelAlpha1. The recovery profiles of both collagen I and Matrigel were revealed for the first time. The viscoelastic behaviour of the commercially available SAPH PeptiGelAlpha1, in the absence and presence of media conditioning, was characterised. It

was also revealed that PeptiGelAlpha1 could act as a physical barrier to an anti-cancer drug, mimicking the *in vivo* environment.

The next steps involve investigating breast cancer cell behaviour within PeptiGelAlpha1, which will be investigated in **Chapter 5**.

# CHAPTER 5 – Development of *In Vitro* Models of Breast Cancer using Self-Assembling Peptide Hydrogels

## 5.1. Introduction

In Chapter 4, the SAPH PeptiGelAlpha1 was chosen to be pursued further for *in vitro* modelling of breast cancer and tube formation by HUVECs and MSCs. It was characterised alongside collagen I and Matrigel in terms of its suitability as a platform to mimic tumour tissue. All data presented in this chapter are thus focussed on PeptiGelAlpha1.

In this Chapter, breast cancer cell lines MCF-7 and MDA-MB-231 encapsulated within PeptiGelAlpha1 were analysed to observe how the cells behaved in the hydrogel, and to determine which features of solid tumours and the TME could be mimicked, without additional cell types. Breast cancer is a progressive disease and different stages will have associated characteristics and phenotypes. It is important that different stages of breast cancer are mimicked *in vitro*, rather than using a ‘one size fits all’ approach. MCF-7 cells represent early-stage cancer [24], whereas MDA-MB-231 cells represent metastatic breast cancer [306]. Using cell lines representing different stages of breast cancer progression allows us to observe if their respective phenotypes and behaviour can be preserved within PeptiGelAlpha1.

Both cell lines have been used previously in peptide hydrogel systems; MCF-7 cells were encapsulated in  $\beta$ -sheet SAPHs h9e [27] and FEFEFKFK [29], and MDA-MB-231 cells in  $\beta$ -sheet forming RADA16, commercially available as PuraMatrix [28]. PeptiGelAlpha1 has been used successfully to culture a variety of cell types in 3D, including: ASCs [23], mammary epithelial cells [307] and oesophageal epithelial cells [21]. It was therefore hypothesised that PeptiGelAlpha1 would be able to maintain the growth of MCF-7 and MDA-MB-231 cancer cells, as well as support features of tumour progression.

The focus of this chapter is to investigate how MCF-7 and MDA-MB-231 cells behave when encapsulated in PeptiGelAlpha1, and to determine what features of solid tumours and the TME are replicated. Moreover, the efficacy of chemotherapeutic drugs when applied to MCF-7 and MDA-MB-231 cells entrapped in PeptiGelAlpha1 was also assessed, to determine if the hydrogel could act as a physical barrier to anti-cancer drugs.

The aims of this chapter are therefore as follows:

- 1. To determine if PeptiGelAlpha1 could support the viability and proliferation of MCF-7 and MDA-MB-231 cells over 14 days.**
- 2. To determine how MCF-7 and MDA-MB-231 cells behaved within the material, regarding their morphology and interactions with PeptiGelAlpha1.**
- 3. To observe if any features of the TME and solid tumours were mimicked in MCF-7 and MDA-MB-231 cell-laden hydrogel samples, including: hypoxia, EMT and invasion.**
- 4. To determine how MCF-7 and MDA-MB-231 cells encapsulated in PeptiGelAlpha1 responded to treatment with chemotherapeutic drugs tamoxifen and doxorubicin.**



## 5.2. Results

### 5.2.1. Viability of MCF-7 & MDA-MB-231 Cells in PeptiGelAlpha1

The LIVE/DEAD assay was used as a qualitative assay to observe if MCF-7 and MDA-MB-231 cells survived and remained viable when encapsulated within PeptiGelAlpha1 over a 7-day period (**Figure 5.1**). Collagen I was used as a control. Live cells were stained green by calcein-AM, indicative of intracellular esterase activity. Dead cells were stained red by ethidium homodimer due to a loss of membrane integrity.

After 1 day in culture, MCF-7 cells were distributed throughout PeptiGelAlpha1 and the majority were viable, with a few dead cells observed (**Figure 5.1A**). A high viability was maintained throughout the 7-day culture period. By day 7, the MCF-7 cells were observed to aggregate to form spheroids. In collagen I, high viability was maintained and aggregation resembling spheroid structures was also seen (**Figure 5.1B**). The cell density appeared higher than that of PeptiGelAlpha1, due to contraction of the hydrogel, as shown in **Appendix 6**. Cell morphology remained rounded in both materials. Quantification could not be carried out due to agglomeration of the cells.

MDA-MB-231 cells remained distributed throughout PeptiGelAlpha1 from days 1–7, with some aggregation observed by day 7 (**Figure 5.1A**). As with the MCF-7 cell line, MDA-MB-231 cells remained viable throughout the culture period, although a few dead cells were present after 1 day in culture. Cell morphology was rounded, with the occasional spindle-shaped cell observed. In collagen I, cell viability was similar to that of PeptiGelAlpha1, although cell morphology appeared more spindle-shaped (**Figure 5.1B**). Again, quantification could not be performed due to cell aggregation.

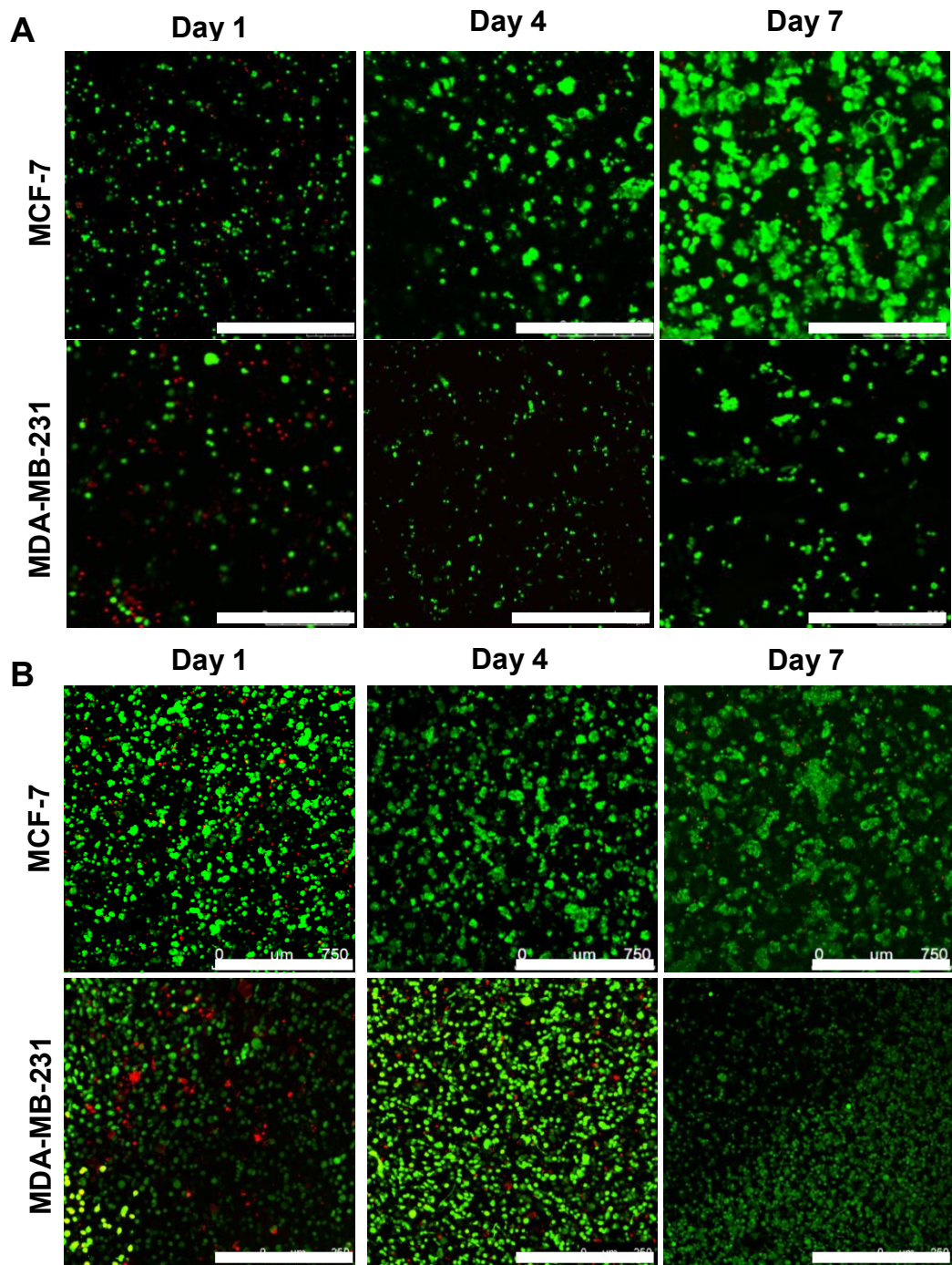


**Figure 5.1. LIVE/DEAD staining of MCF-7 and MDA-MB-231 cells in PeptiGelAlpha1 or collagen I over 7 days.** (A) Cells encapsulated in PeptiGelAlpha1. (B) Cells encapsulated in collagen I. Cells were stained with calcein-AM and ethidium homodimer-1 and incubated for 1 hour at 37 °C. Images were collected using a Leica SP5 confocal inverted microscope. Green = live cells. Red = dead cells. Scale bar = 750 μm. N = 3.

### 5.2.2. Proliferation of MCF-7 & MDA-MB-231 Cells in PeptiGelAlpha1

The PicoGreen assay was used to measure the DNA concentration of MCF-7 and MDA-MB-231 cells encapsulated in PeptiGelAlpha1. To determine if the material would interfere with DNA extraction, a standard curve was produced with MCF-7 cells, using known cell concentrations, encapsulated in either PeptiGelAlpha1 or dPBS (**Figure 5.2**).

A linear relationship was determined between DNA concentration and cell concentration for both PeptiGelAlpha1 ( $r^2 = 0.989$ ) and dPBS ( $r^2 = 0.951$ ). No significant difference was observed between the DNA concentrations of the hydrogel and dPBS ( $p > 0.05$ ), confirming that the hydrogel did not interfere with DNA extraction using the applied method and subsequent analysis.

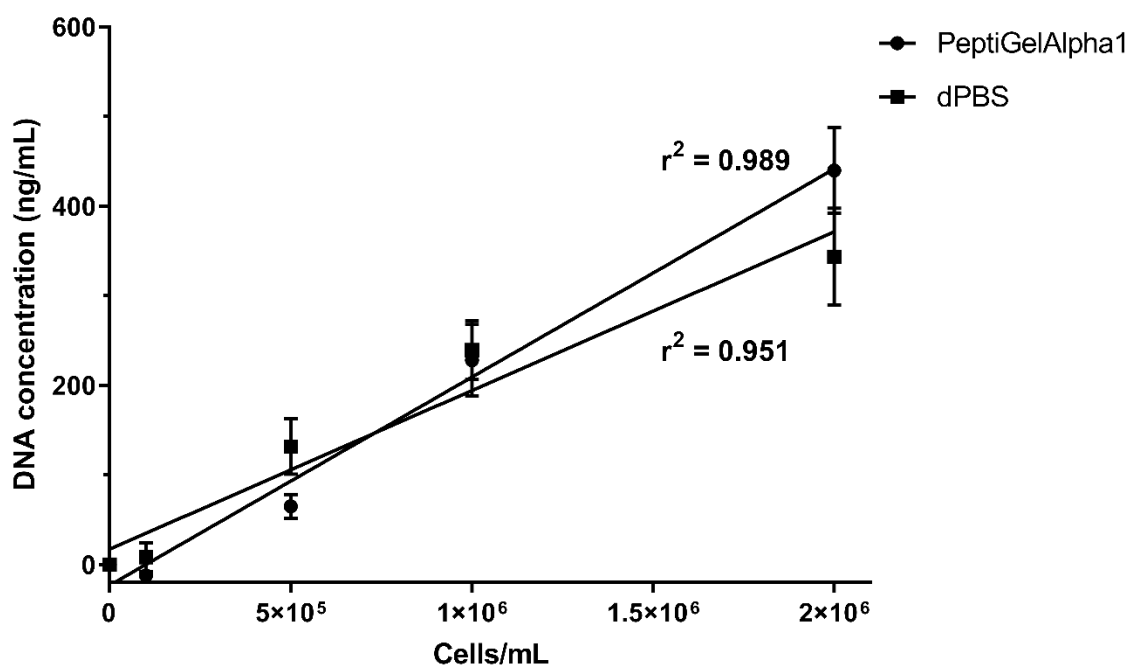


**Figure 5.2. Standard curve of PicoGreen analysis of MCF-7 cells encapsulated in PeptiGelAlpha1 and dPBS.** MCF-7 cells were encapsulated in PeptiGelAlpha1 and dPBS at concentrations from  $1 \times 10^5$ – $2 \times 10^6$  cells/mL for 30 minutes prior to pronase digestion and lysis. PicoGreen solution was added to each sample and fluorescence was measured using wavelengths of 480 nm and 520 nm. Fluorescence values interpolated using a standard curve of known DNA. Acellular samples were used as a background and removed from all samples. Data are mean  $\pm$  S.D.  $R^2$  = coefficient of determination.  $N = 2$ . A two-way ANOVA with post-hoc Sidak's test was used, where  $p > 0.05$ .

PicoGreen analysis was hence carried out on MCF-7 and MDA-MB-231 cell-laden PeptiGelAlpha1 samples over a 14-day period (**Figure 5.3**). The DNA concentration of MCF-7 cells was observed to increase over the 14-day period, with a small increase but non-significant increase from day 1 to day 4 ( $684.4 \text{ ng/mL} \pm 127.0 \text{ ng/mL}$  to  $709.5 \text{ ng/mL} \pm 82.3 \text{ ng/mL}$ ,  $p > 0.05$ ), with significant increases observed after 7 days ( $876.4 \text{ ng/mL} \pm 88.2 \text{ ng/mL}$ ,  $p < 0.01$ ) and 14 days ( $1053.6 \text{ ng/mL} \pm 154.1 \text{ ng/mL}$ ,  $p < 0.0001$ ). For MDA-MB-231 cells, on the other hand, the DNA concentration was observed to increase significantly from day 1 to day 4 ( $504.8 \text{ ng/mL} \pm 107.4 \text{ ng/mL}$  to  $1071.4 \text{ ng/mL} \pm 18.8 \text{ ng/mL}$ ,  $p < 0.0001$ ). The DNA concentration then declined slightly by day 7 ( $890.0 \text{ ng/mL} \pm 82.1 \text{ ng/mL}$ ), before a steep drop was observed by day 14 ( $552.1 \text{ ng/mL} \pm 23.1 \text{ ng/mL}$ ).

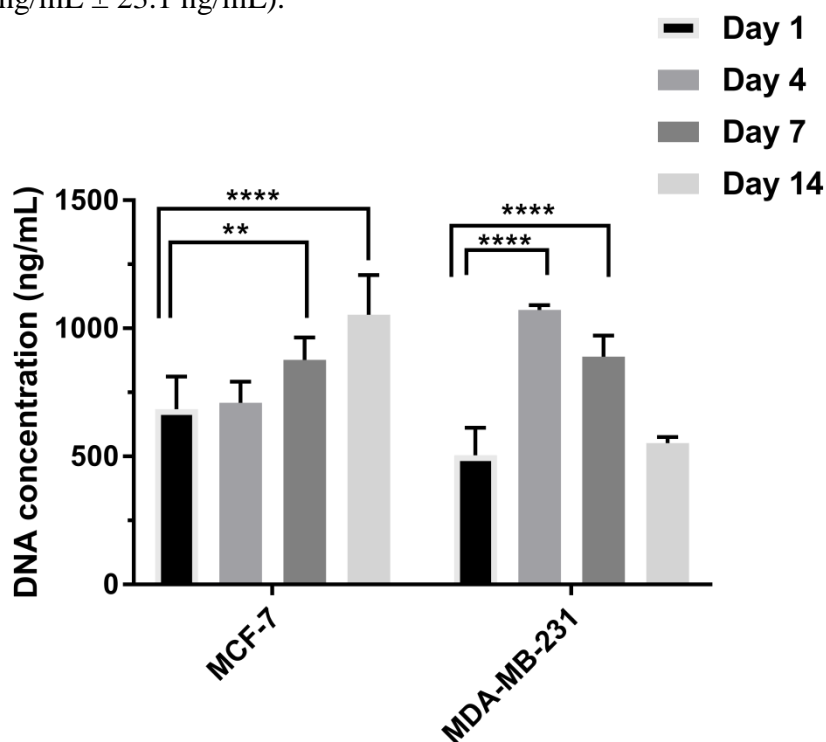


**Figure 5.3. PicoGreen analysis of MCF-7 and MDA-MB-231 cells encapsulated within PeptiGelAlpha1 over 14 days.** PicoGreen solution was added to lysed samples and fluorescence was measured using a plate-reader at wavelengths of 480 nm and 520 nm. Acellular samples were used as blanks and removed from all samples. Data are mean  $\pm$  S.D. \*\* =  $p < 0.01$ , \*\*\*\* =  $p < 0.0001$  using two-way ANOVA and post-hoc Tukey's test. N = 6.

The presence of Ki67, a cellular marker of proliferation, was detected in immunohistochemical staining of MCF-7 and MDA-MB-231 cell-laden PeptiGelAlpha1 sections, to further support the PicoGreen data presented in **Figure 5.3** to provide histological context. Positive nuclear staining indicated that cells were Ki67 positive. Ki67 positive MCF-7 cells were observed from 1 day in culture, and were also detected in the

larger spheroid structures that formed (**Figure 5.4A**). However, by day 14, there appeared to be fewer Ki67 positive cells present. Quantifying these data revealed that MCF-7 cells were  $82.2\% \pm 14.4\%$ ,  $88.3\% \pm 7.1\%$  and  $64.9\% \pm 11.4\%$  Ki67 positive at days 1, 7 and 14 respectively (**Figure 5.4B**). With MDA-MB-231 cells, Ki67 positive cells were detected at all time points (**Figure 5.4A**). The percentages of Ki67 positive cells were measured to be  $78.3\% \pm 10.6\%$ ,  $65.0\% \pm 30.1\%$  and  $75.1\% \pm 19.6\%$  at days 1, 7 and 14 respectively (**Figure 5.4B**).

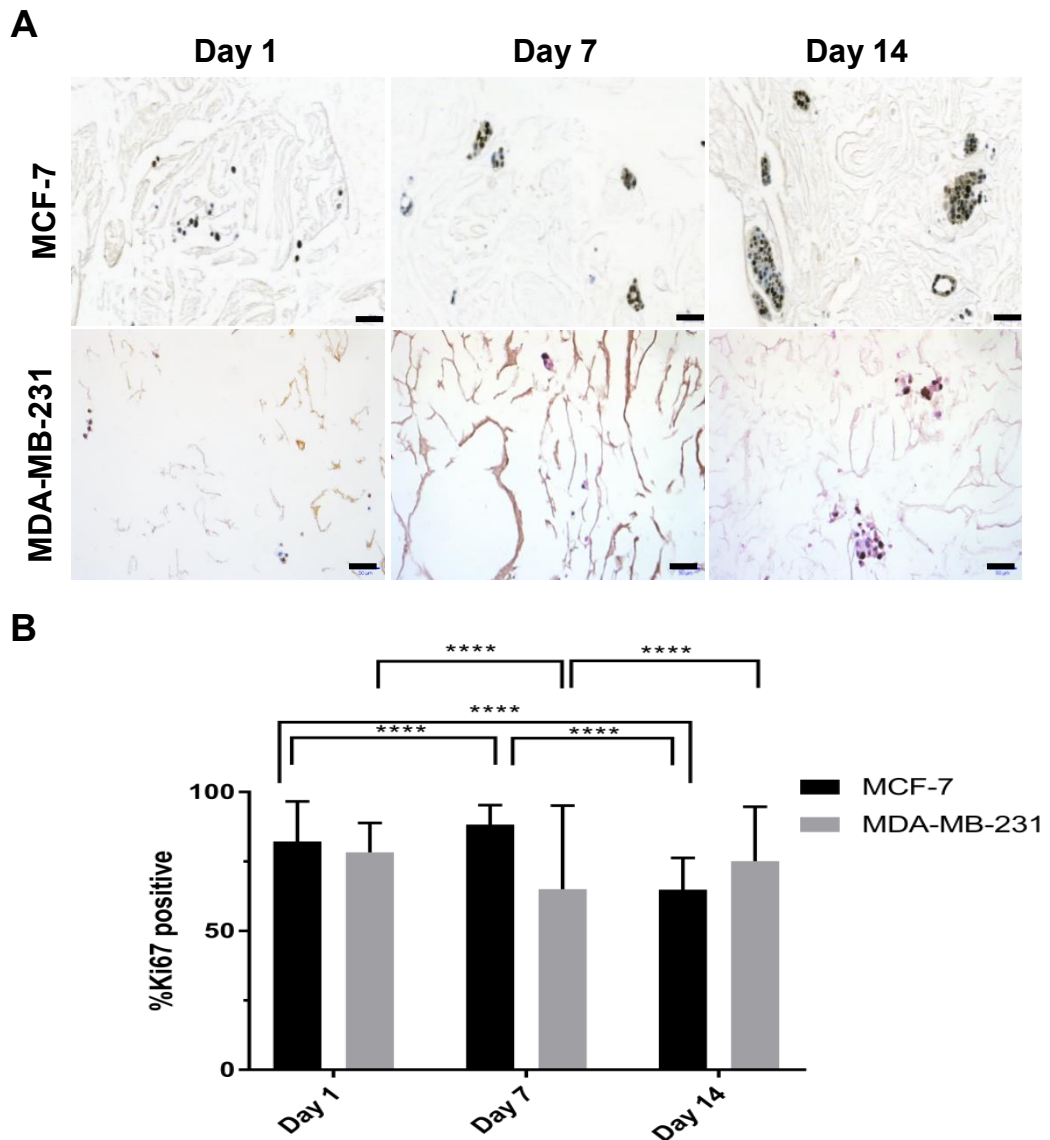


**Figure 5.4. Ki67 immunohistochemical staining of MCF-7 and MDA-MB-231 cells in PeptiGelAlpha1 over 14 days.** (A) Brightfield images of Ki67 staining. Samples were sectioned at a thickness of 5.0  $\mu\text{m}$ . Sections were stained with anti-Ki67 antibody and DAB was used to detect positive staining. Brown = positive staining. Blue = nuclei. Scale bar = 50  $\mu\text{m}$ . (B) Percentage of Ki67 positive cells over 14 days. ImageJ was used to identify and quantify Ki67 positive cells. Data are mean  $\pm$  S.D. \*\*\*\* =  $p < 0.0001$  using two-way ANOVA and post-hoc Tukey's test.  $N = 6$ .

### 5.2.3. Organisation of MCF-7 & MDA-MB-231 Cells in PeptiGelAlpha1

To observe how MCF-7 and MDA-MB-231 cells encapsulated within PeptiGelAlpha1 organised themselves, histological and fluorescence staining was used to observe the overall histoarchitecture and cellular distribution, as well as cell morphology.

H&E staining was used initially to provide a general overview of how MCF-7 and MDA-MB-231 cells interact within the hydrogel. Collagen I was used as a control material. PeptiGelAlpha1 was counterstained pink by eosin, whereas collagen I remained transparent (**Figure 5.5**). Collagen I samples appeared to have a higher cell density due to contraction of the material (**Appendix 6**). MCF-7 cells were dispersed throughout both PeptiGelAlpha1 and collagen I after 1 day in culture. However, the cells started to aggregate and form clusters by day 7 and formed large spheroids by day 14 in both materials. Higher magnification revealed that the spheroids were rounded in structure in PeptiGelAlpha1, whereas in collagen I the structures were more irregularly shaped (**Figure 5.6**).

In contrast, MDA-MB-231 cells tended to behave differently. This cell line remained dispersed throughout both hydrogels by day 7, with loose, irregular structures formed by day 14 in PeptiGelAlpha1 (**Figure 5.5**). In collagen I, MDA-MB-231 cells remained dispersed by day 14. In PeptiGelAlpha1, cell morphology was predominantly rounded throughout the 14-day culture period, whilst in collagen I a mixture of both rounded and elongated cells were observed, particularly by day 7 (**Figure 5.6**).



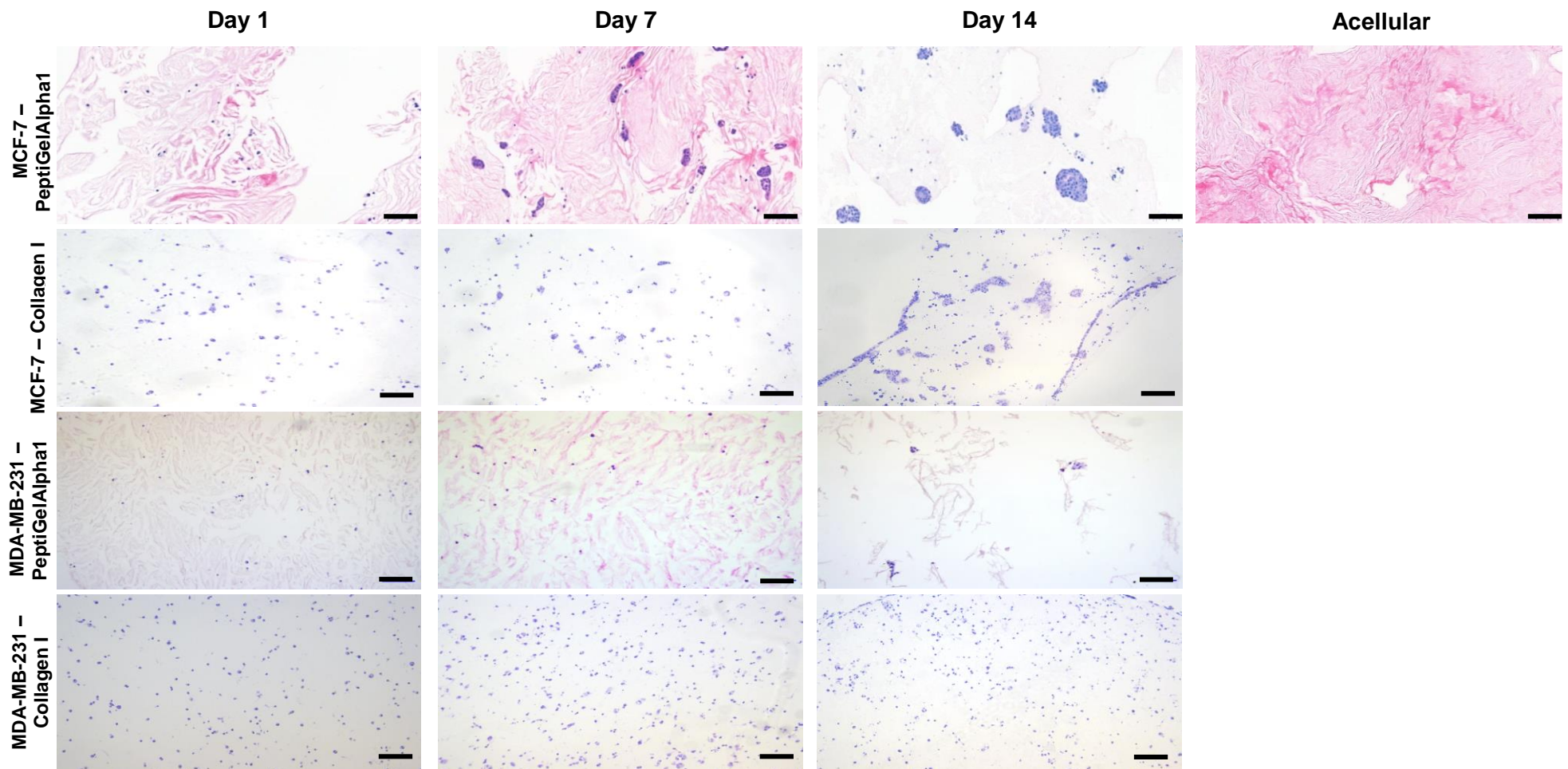


**Figure 5.5. H&E staining of MCF-7 and MDA-MB-231 cells encapsulated in PeptiGelAlpha1 or collagen I over 14 days.** Samples were sectioned at a thickness of 5.0  $\mu\text{m}$  and stained with haematoxylin and eosin. An acellular control for PeptiGelAlpha1 was included. Pink = hydrogel. Blue = cell nuclei. Scale bar = 100  $\mu\text{m}$ . N = 2.

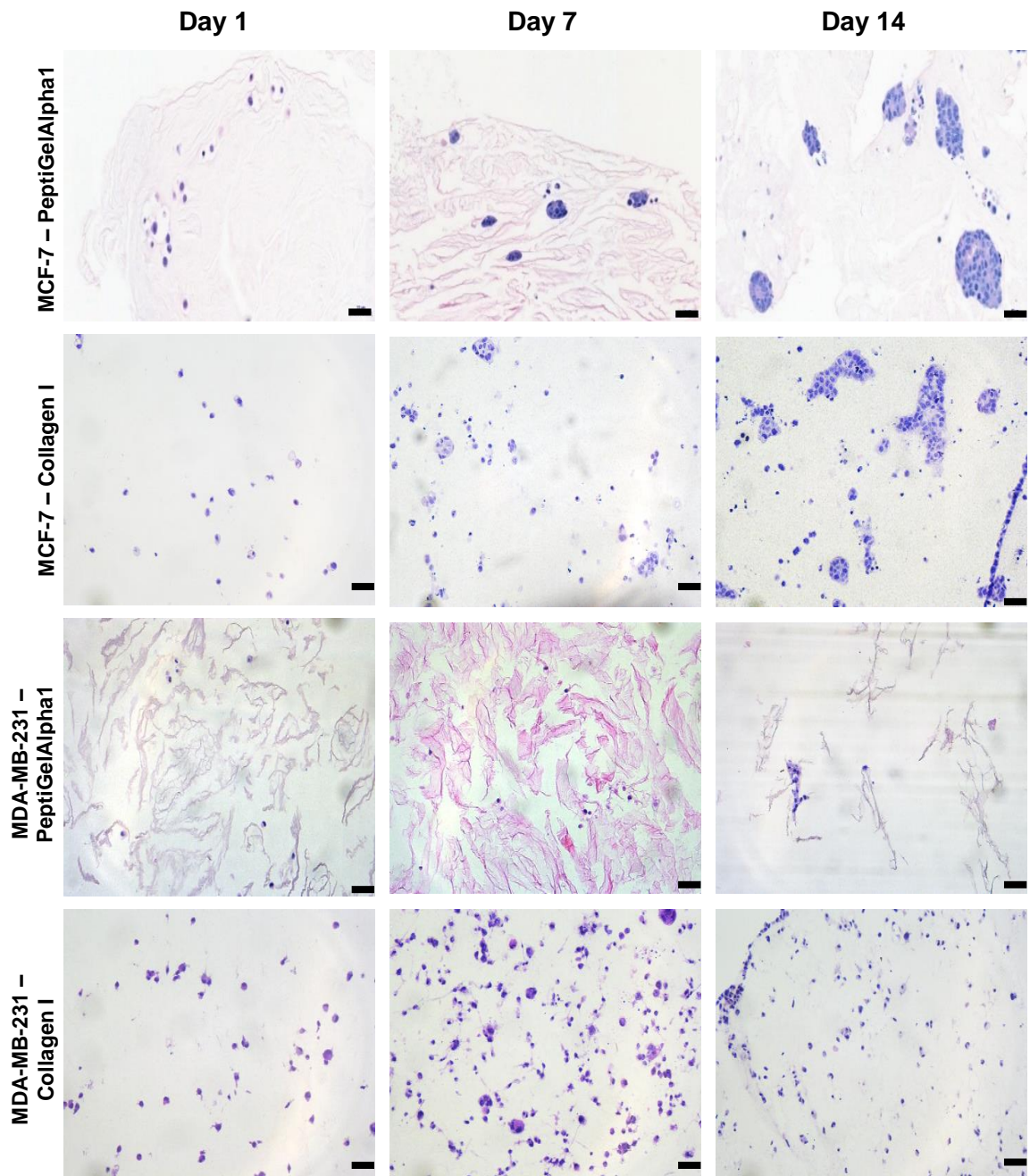


**Figure 5.6. Higher magnification imaging of H&E stained MCF-7 and MDA-MB-231 cell-laden PeptiGelAlpha1 or collagen I sections over 14 days.** Samples were sectioned at a thickness of 5.0  $\mu\text{m}$  and stained with haematoxylin and eosin. Pink = hydrogel. Blue = cell nuclei. Scale bar = 50  $\mu\text{m}$ . N = 2.

Quantification of MCF-7 spheroids in PeptiGelAlpha1 and collagen I was carried out to determine if the area of spheroids, or number of cells per spheroid formed, differed at all between the materials (**Figure 5.7**). In PeptiGelAlpha1, the number cells per spheroid formed by MCF-7 cells significantly increased from day 1 (3.4 cells  $\pm$  1.0 cells) to day 14 (19.5 cells  $\pm$  15.1 cells) ( $p < 0.0001$ ; **Figure 5.7A**). Concordantly, the area of the spheroids was observed to increase significantly from day 1 (503.6  $\mu\text{m}^2 \pm 291.7 \mu\text{m}^2$ ) to day 14 (2919.7  $\mu\text{m}^2 \pm 2492.7 \mu\text{m}^2$ ) ( $p < 0.0001$ ; **Figure 5.7B**).



In collagen I, a significant increase in the number of cells per spheroid was noted from day 1 (4.3 cells  $\pm$  1.1 cells) to day 14 (15.8 cells  $\pm$  14.6 cells) ( $p < 0.0001$ ) (**Figure 5.7C**). A significant increase in spheroid area was only observed between 7 days (843.2  $\mu\text{m}^2 \pm 657.9 \mu\text{m}^2$ ) and 14 days (1380.9  $\mu\text{m}^2 \pm 1416.1 \mu\text{m}^2$ ) ( $p < 0.001$ ) (**Figure 5.7D**). When comparing the number of cells per spheroid and spheroid area between PeptiGelAlpha1 and collagen I, it was observed that MCF-7 cells formed larger spheroids with a greater number of cells per spheroid in PeptiGelAlpha1 than collagen I after 14 days ( $p < 0.05$ ; **Figure 5.7E & F**).

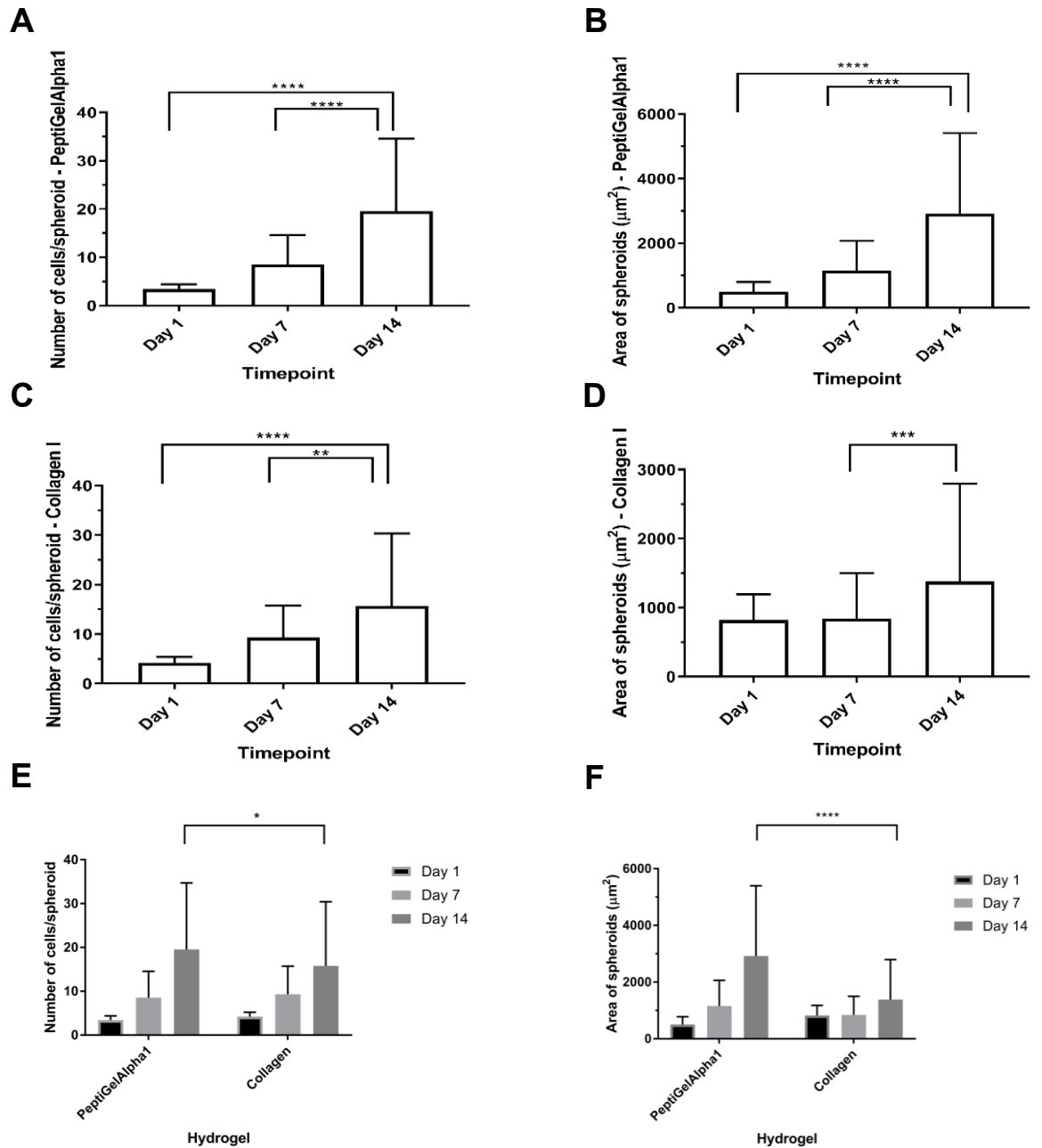


**Figure 5.7. Quantification of H&E staining of MCF-7 cells encapsulated in PeptiGelAlpha1 or collagen I over 14 days.** (A) Number of cells per spheroid in PeptiGelAlpha1 and (B) area ( $\mu\text{m}^2$ ) of MCF-7 spheroids. (C) Number of cells per spheroid in collagen I and (D) area ( $\mu\text{m}^2$ ) of MCF-7 spheroids. (E) Number of cells in PeptiGelAlpha1 vs collagen I and (F) area ( $\mu\text{m}^2$ ) of MCF-7 spheroids in PeptiGelAlpha1 vs collagen I. Data are mean  $\pm$  S.D. ImageJ was used to quantify the number of cells and area of spheroids formed by MCF-7 cells. \* =  $p < 0.05$ , \*\* =  $p < 0.01$ , \*\*\* =  $p < 0.001$ , \*\*\*\* =  $p < 0.0001$  using one-way ANOVA and post-hoc Tukey's test. N = 2.

F-actin staining of the cytoskeleton was used to further confirm how MCF-7 and MDA-MB-231 cells behaved in both PeptiGelAlpha1 and collagen I hydrogels (**Figure 5.8**). DAPI was used to counterstain cell nuclei; however, this was not successful in PeptiGelAlpha1 samples. This was possibly due to the material interfering with the staining. As observed with the H&E images in **Figure 5.5**, MCF-7 cells agglomerated to form spheroids in both collagen I and PeptiGelAlpha1 over the 14 days in culture. MDA-MB-231 cells in PeptiGelAlpha1 appeared to be rounded in general, with few elongated cells present. In collagen I, the cells were evidently elongated in morphology and appeared to have compacted by day 7 to produce a mesh. This was likely due to contraction of the material by the cells, as shown in **Appendix 6**.

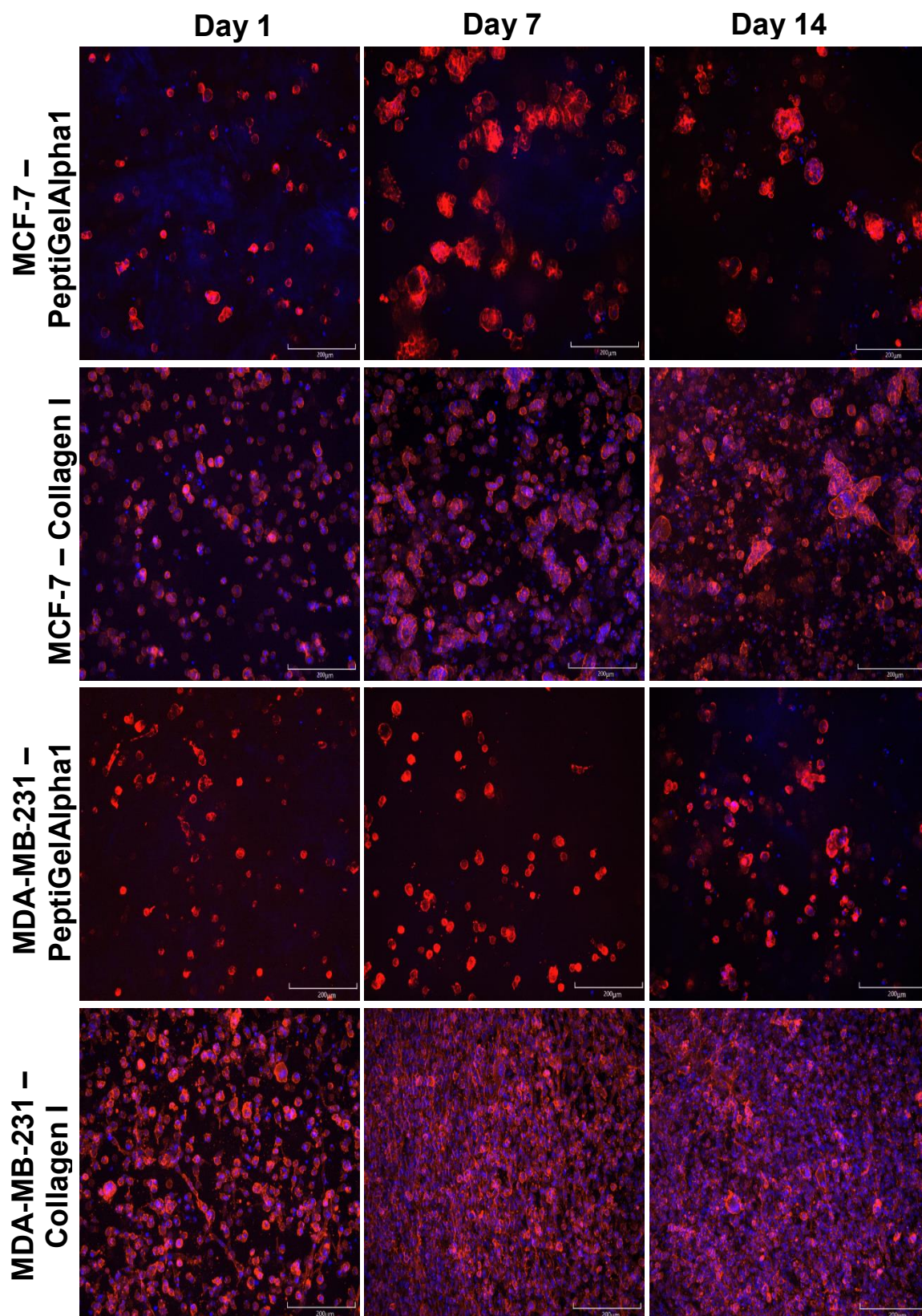


**Figure 5.8. F-actin filament staining of MCF-7 and MDA-MB-231 cells encapsulated in PeptiGelAlpha1 or collagen I over 14 days.** Cell-laden hydrogels were fixed at desired time points and stained with phalloidin and DAPI to stain F-actin filaments and nuclei respectively. Red = F-actin, blue = DNA. Scale bar = 200  $\mu\text{m}$ . N = 3.

#### **5.2.4. Extracellular Matrix Deposition by MCF-7 and MDA-MB-231 Cells**

Gomori Trichrome staining, which detects non-specific collagen production, and collagen I immunohistochemistry were used in combination to detect ECM production by MCF-7 and MDA-MB-231 cells in PeptiGelAlpha1 (**Figure 5.9**).

In Gomori Trichrome stained sections, the material was stained blue by the reagents used. For the MCF-7 cell line, green staining, indicative of collagen production, was observed around nuclei of the cells from day 1 in culture (**Figure 5.9**). As the cells aggregated and formed spheroids, the ECM could clearly be observed. With MDA-MB-231 cells, it was much harder to distinguish pericellular ECM from the surrounding peptide matrix, due to the hydrogel being counterstained. However, the loose aggregates formed at day 14 were observed to exhibit pericellular ECM surrounding the cells.



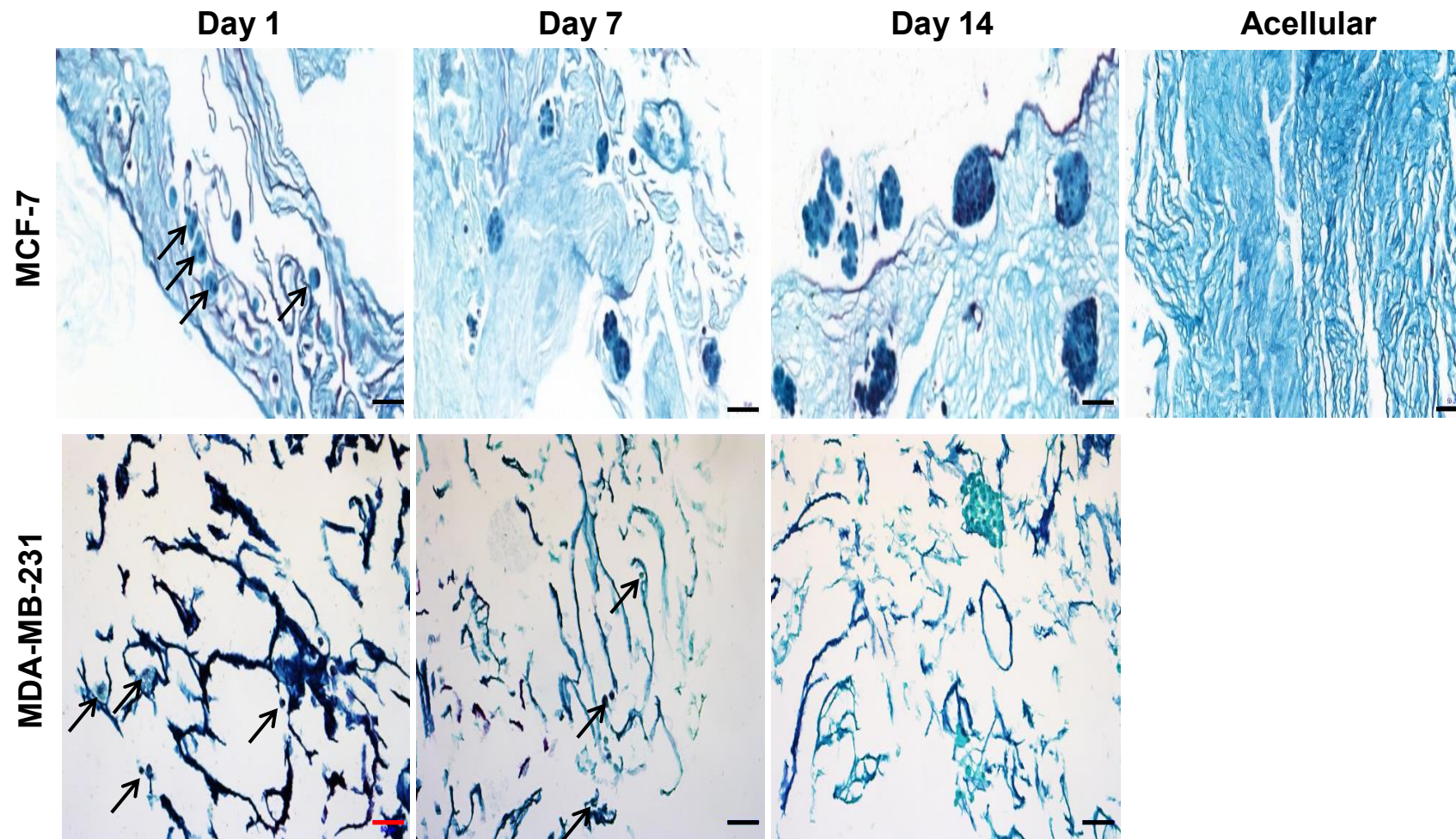


**Figure 5.9. Gomori Trichrome staining of MCF-7 and MDA-MB-231 cells in PeptiGelAlpha1 over 14 days.** Samples were sectioned at a thickness of 5.0  $\mu\text{m}$  and stained with Gomori Trichrome solution. An acellular control was included. Arrows indicate cells within the hydrogel. Dark blue = nuclei. Green/light blue = pericellular extracellular matrix. Scale bar = 50  $\mu\text{m}$ . N = 2.

Immunohistochemistry was performed (**Figure 5.10**) to confirm that the pericellular ECM produced by MCF-7 and MDA-MB-231 cells was collagen I, as expected due to the protein's abundant production in cancer cells. Positive staining was detected using a DAB chromagen, in which brown staining appeared if the protein was present.

After 1 day in culture, positive staining was not easily identifiable with MCF-7 cells (**Figure 5.10**). As the cells aggregated by day 7 to form spheroids, the collagen I deposition was more prominent, as indicated by abundant positive staining. By day 14, large amounts of protein were observed surrounding the cells within the spheroids, confirming that collagen I production was maintained. No positive staining was observed for MDA-MB-231 cells, on the other hand, over the 14 days in culture.

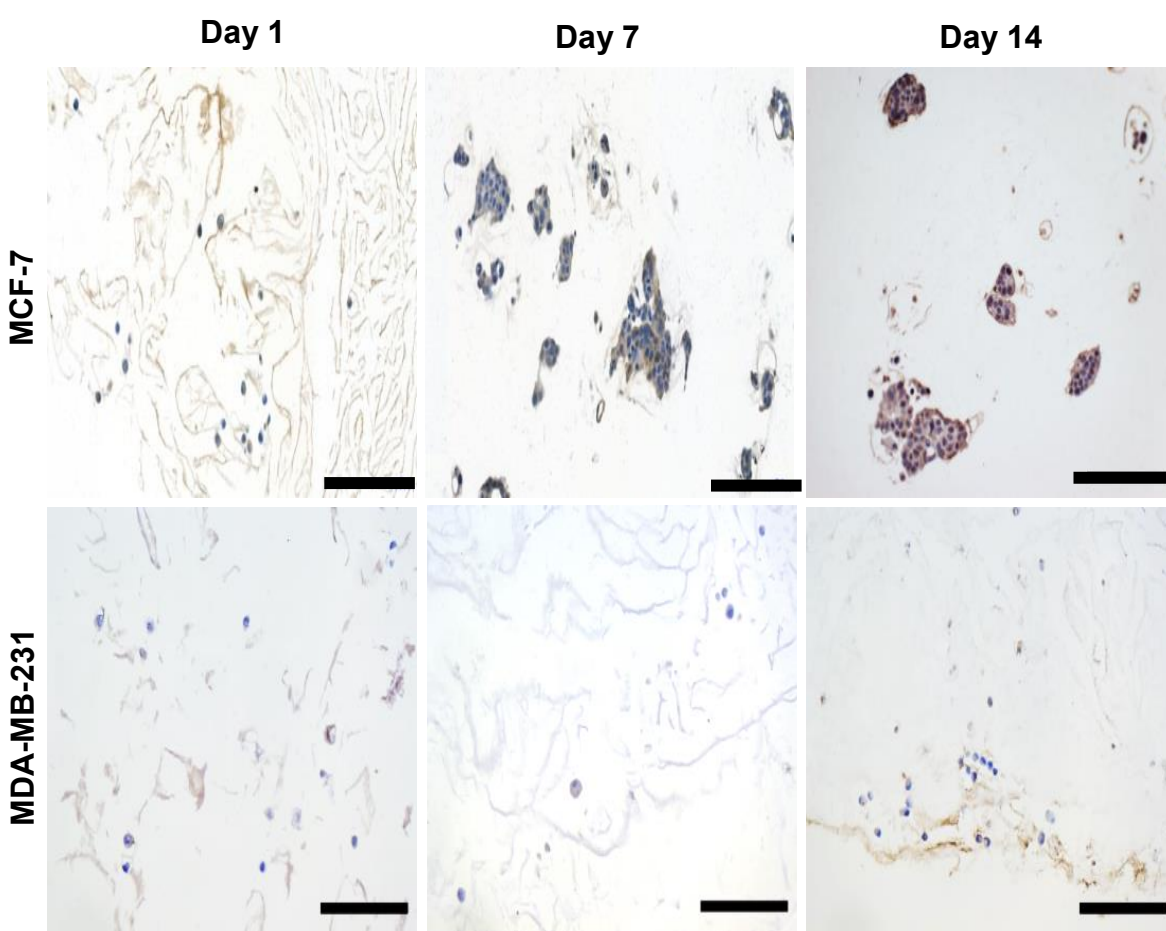


**Figure 5.10. Collagen I immunostaining of MCF-7 and MDA-MB-231 cells in PeptiGelAlpha1 over 14 days.** Samples were sectioned at a thickness of 5.0  $\mu\text{m}$  and stained with anti-collagen I antibody. Positive staining was detected using a DAB substrate stain and counterstained using haematoxylin. Brown = positive staining. Blue = nuclei. Scale bar = 200  $\mu\text{m}$ . N = 2.

### 5.2.5. Cell-Material Interactions

To explore how MCF-7 and MDA-MB-231 cells were responding to encapsulation within PeptiGelAlpha1, TEM imaging was used. Samples cultured for 14 days were used due to the MCF-7 cells forming large spheroids by this time point. Collagen I was used as a control material. The PeptiGelAlpha1 material appeared to be dense and fibrous, whereas collagen I was observed as large fibrils (**Figure 5.11**). MCF-7 cells were observed to engulf PeptiGelAlpha1 in large pockets, with cell processes wrapped around the peptide material. MDA-MB-231 cells did not take up the material but extended processes into the hydrogel, indicative of exploration and interaction by the cells. In collagen I hydrogels, uptake of the material was not observed with either MCF-7 or MDA-MB-231 cells. Instead, anchoring of the collagen fibrils to the cells was observed.

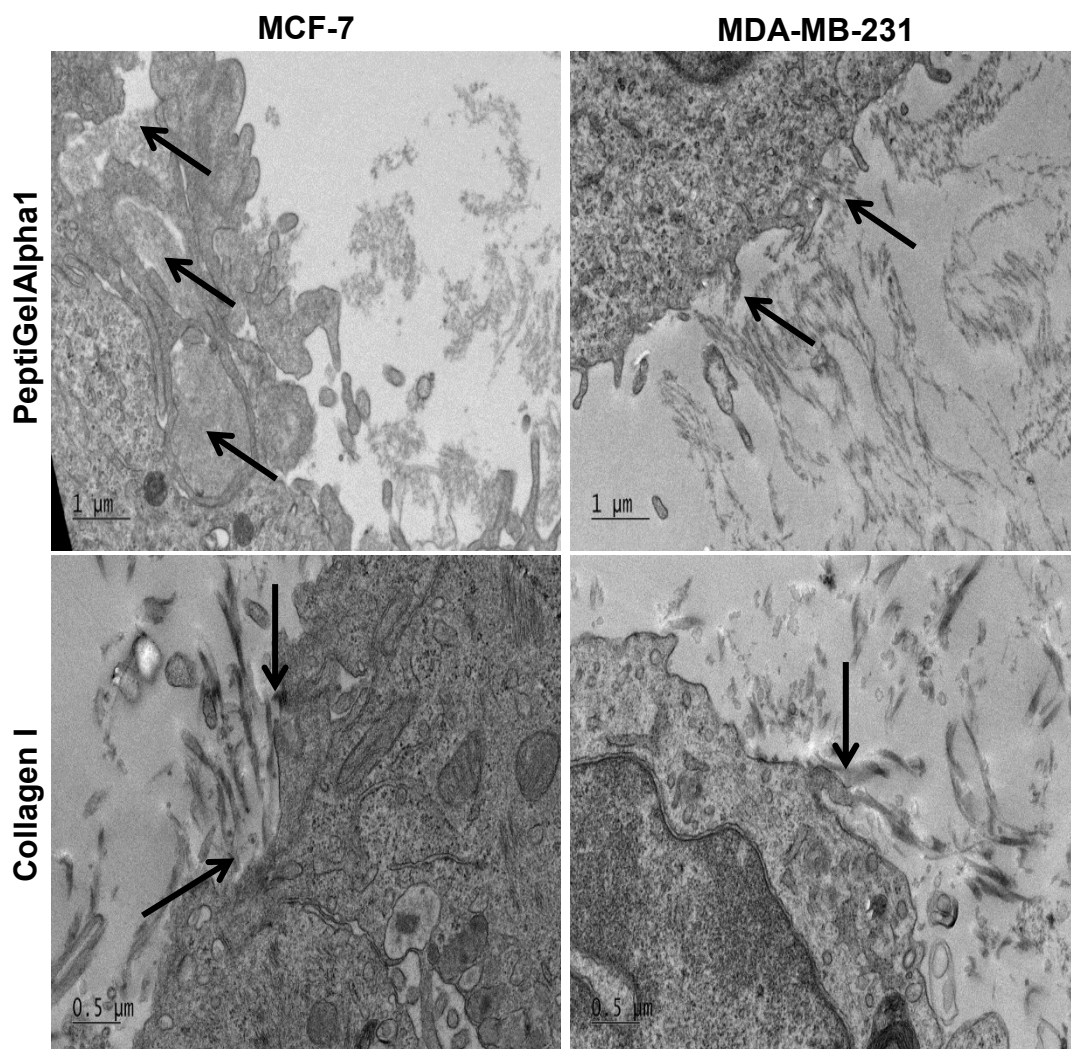


**Figure 5.11. TEM images of MCF-7 and MDA-MB-231 cells in PeptiGelAlpha1 or collagen I after 14 days.** Cell-laden hydrogels were fixed and processed for TEM imaging. Arrows denote interaction of cells with material. Scale bar = 1 μm for PeptiGelAlpha1 images and 0.5 μm for collagen I images. N = 3.



TEM imaging of MCF-7 cells within PeptiGelAlpha1 additionally revealed the large size of the spheroids formed (**Figure 5.12**). It was also noted that enveloped material was found within the centre of the cells. The hydrogel appeared to be stored within vesicles, some of which contained a double membrane. Organelles resembling autophagosomes were located near to the stored material.

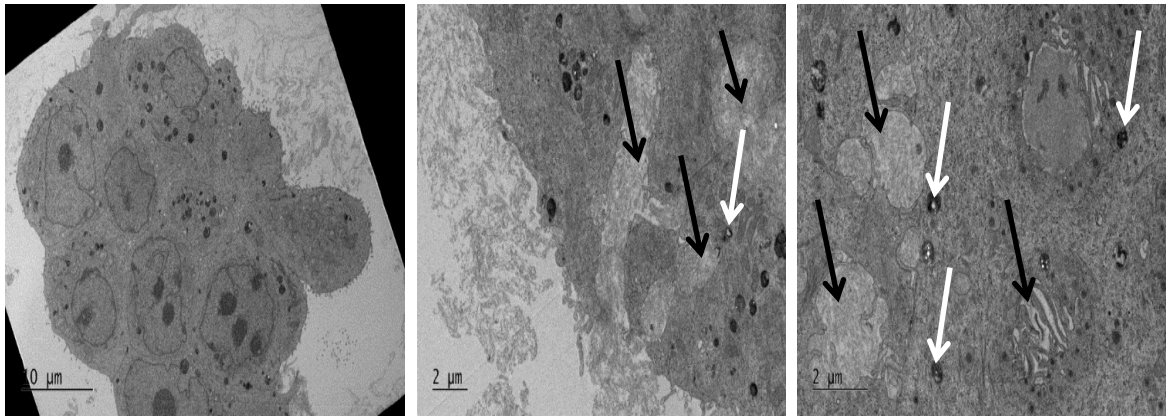


**Figure 5.12. TEM images of MCF-7 cells in PeptiGelAlpha1 after 14 days.** Cell-laden hydrogels were fixed and processed for TEM imaging. Black arrows denote internalised hydrogel within the cells. White arrows indicate autophagosomes. Scale bar = 10  $\mu\text{m}$  for left image and 2  $\mu\text{m}$  for middle and right images.

To investigate the internalisation of cell-laden hydrogel samples further, oscillatory rheology was carried out to determine if the mechanical properties were affected (**Figure 5.13**). Acellular PeptiGelAlpha1 samples incubated under standard cell culture conditions were used as a control. It was observed that the acellular material weakened over the 14-day culture duration, from 11510 Pa  $\pm$  4308 Pa after 1 day in culture, to 1912 Pa  $\pm$  478 Pa after 14 days ( $p < 0.0001$ ). When loaded with MCF-7 cells, a non-significant decrease was observed from day 1 to day 14 (3782 Pa  $\pm$  1358 Pa to 111 Pa  $\pm$  37 Pa;  $p > 0.05$ ). With MDA-MB-231 cells, there appeared to be no overall change in mechanical properties over time, from 1966 Pa  $\pm$  818 Pa after 1 day in culture to 1991 Pa  $\pm$  472 Pa after 14 days. Although non-significant, the decrease in mechanical properties observed in MCF-7 cell-laden samples is supported by the TEM images (**Figure 5.12**) where large portions of material were engulfed by the cells.

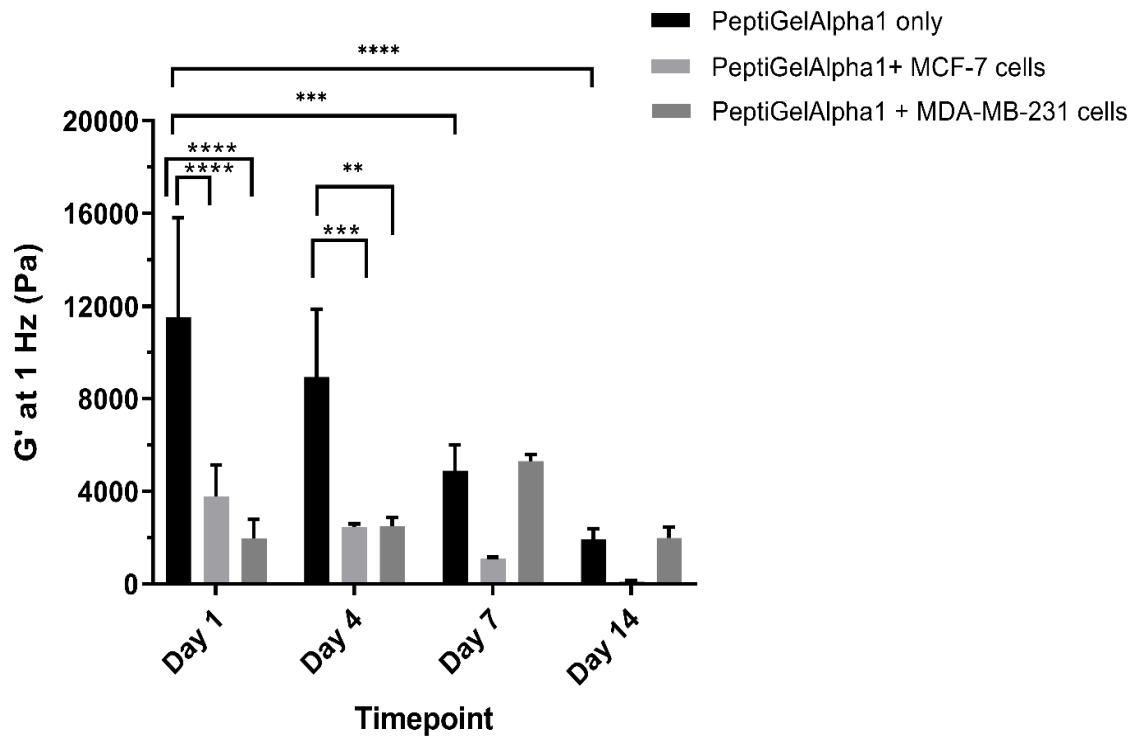


**Figure 5.13. Mechanical properties of acellular PeptiGelAlpha1 and MCF-7 and MDA-MB-231 cell-laden PeptiGelAlpha1 over 14 days in culture.** Acellular and cell-laden hydrogel samples were incubated under standard cell culture conditions (regular media changes, 37 °C, 20 % (v/v) O<sub>2</sub>, 5 % (v/v) CO<sub>2</sub>) for up to 14 days. At desired time points, samples were exposed to frequency sweeps of 0.01–10 Hz at 0.2 % strain using an oscillatory shear rheometer. Gap size = 500 μm. Temperature = 37 °C. Data are mean ± S.D. \*\* = p < 0.01, \*\*\* = p < 0.001, \*\*\*\* = p < 0.0001 using two-way ANOVA. N = 2 for MCF-7 samples, N = 1 for MDA-MB-231 samples.

To observe whether MCF-7 cancer cells were producing enzymes to degrade the material, an MMP-2 ELISA was carried out on supernatant collected from MCF-7 cell-laden PeptiGelAlpha1 samples. MMP-2 is a prominent enzyme in ECM dynamics and is well known for its role in tumour progression and metastasis, due to degradation of the surrounding tissue enabling invasion [308]. Production of MMP-2 appeared to significantly increase after 7 days, from 19.7 ng/mL ± 14.7 ng/mL at day 1 to 43.8 ng/mL ± 10.8 ng/mL (p < 0.05) (**Figure 5.14**). By day 14, the concentration of MMP-2 had decreased to 29.1 ng/mL ± 13.9 ng/mL.

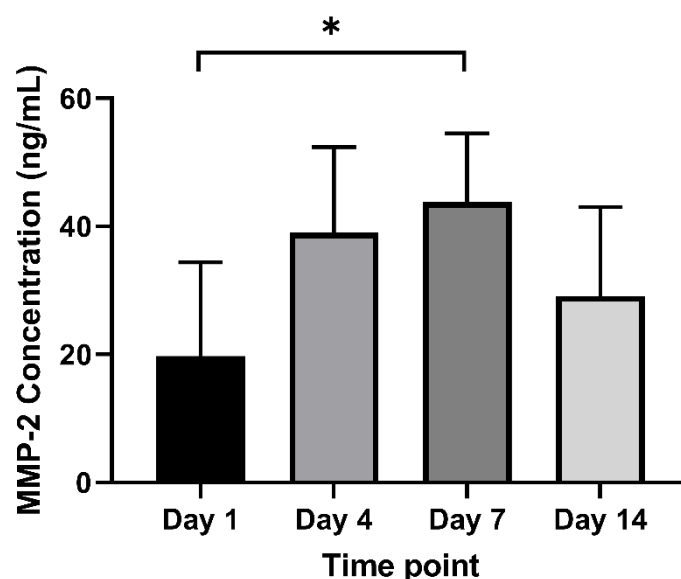


**Figure 5.14. MMP-2 production by MCF-7 cells cultured in PeptiGelAlpha1 over 14 days.** Cell culture supernatant samples collected from samples at each time point and MMP-2 concentration was measured using an ELISA assay. Acellular hydrogel was used as a blank and removed from all samples. A human MMP-2 standard curve was used to determine MMP-2 concentrations of samples. Data are mean  $\pm$  S.D. \* =  $p < 0.05$  using one-way ANOVA and post-hoc Tukey's test.  $N = 2$ .

### 5.2.6. Hypoxia Development

The generation of hypoxia within the centre of solid tumours is a result of the mass outgrowing the oxygen diffusion limit, causing an oxygen gradient from the centre to the tumour periphery [309]. Hypoxia triggers the cascade of events resulting in blood vessels to form within the tumour as a method of providing nutrients and oxygen to the growing tumour.

A fluorescent probe was used to detect hypoxic cells within PeptiGelAlpha1. The dye will only fluoresce in  $< 5\%$  (v/v)  $O_2$ . To establish that the assay was working correctly, MCF-7 cells encapsulated in PeptiGelAlpha1 were exposed to physiologically induced hypoxia (4% (v/v)  $O_2$ ) or chemically induced hypoxia (treatment with 150  $\mu M$  cobalt chloride) (**Figure 5.15**). Acellular hydrogel was used in both conditions as a control to show that the material was not interfering with the assay. Treatment with cobalt chloride was unable to generate hypoxia within MCF-7 cells, confirming that this method of hypoxia induction was not suitable for this assay (**Figure 5.15A & B**). On the other hand, when exposed to physiologically induced hypoxia, red fluorescence was observed within the cells, indicative of hypoxia development (**Figure 5.15C**). From the material only control, no fluorescence

was observed, indicating that the material did not produce any background fluorescence (Figure 5.15D).

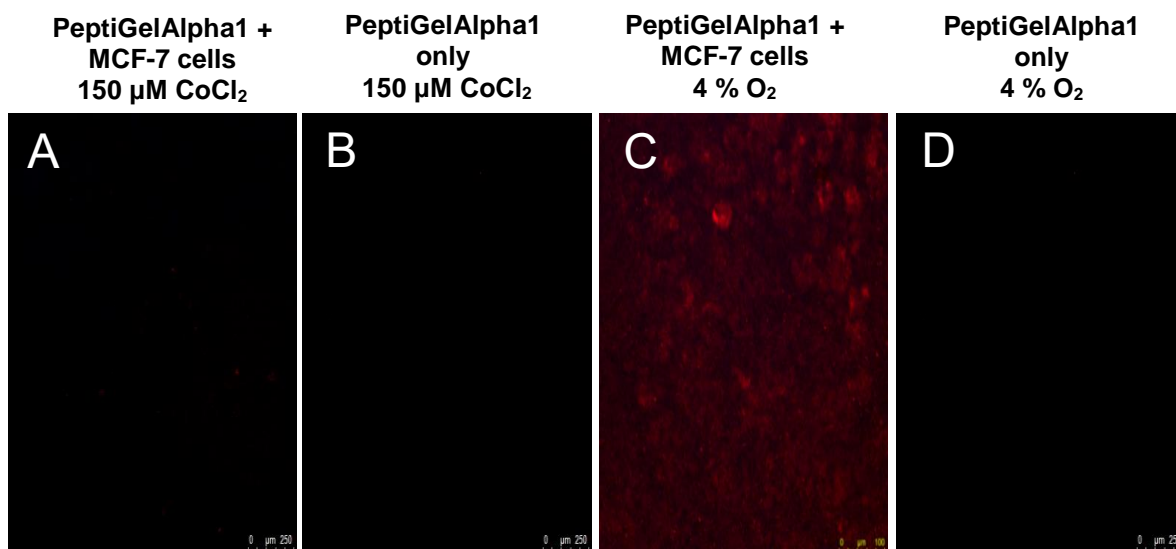


**Figure 5.15. Optimisation of the Image-iT Red Hypoxia staining procedure using chemically induced hypoxia and physiologically induced hypoxia (< 5 % (v/v) O<sub>2</sub>).** (A) PeptiGelAlpha1 and MCF-7 cells treated with 150 μM cobalt chloride. (B) PeptiGelAlpha1 treated with 150 μM cobalt chloride. (C) PeptiGelAlpha1 and MCF-7 cells exposed to 4 % (v/v) O<sub>2</sub>. (D) PeptiGelAlpha1 exposed to 4 % (v/v) O<sub>2</sub>. For chemically induced hypoxia, MCF-7 cells were exposed to 150 μM cobalt chloride for 48 hours. For physiologically induced hypoxia, MCF-7 cells incubated under hypoxic conditions (37 °C, 4 % (v/v) O<sub>2</sub>) for 48 hours. Samples were stained with 10 μM Image-iT Red Hypoxia Reagent and incubated for 1 hour at 37 °C. Samples were imaged using an inverted confocal microscope using wavelengths of 488 nm and 631 nm. Red = hypoxic cells. N = 2.

The assay was then used to observe if MCF-7 and MDA-MB-231 cells were becoming hypoxic when encapsulated within PeptiGelAlpha1 over time under standard cell culture conditions (Figure 5.16A). The images presented are the whole cell-laden hydrogel samples. After 1 day in culture, very few hypoxic cells were observed in both cell lines. The hypoxic cells that were present were located towards the periphery of the hydrogel. By day 7, more hypoxic MCF-7 cells were found towards the centre of the hydrogel and by day 14 there was a stark increase in the number of fluorescent cells, particularly within the spheroids formed. With MDA-MB-231 cells, more hypoxic cells were observed by day 14 but these were dispersed throughout the hydrogel. Quantification of hypoxic cells revealed that there was a significant increase in the number of hypoxic cells in both cell lines from day 1 to day 14 ( $p < 0.0001$ ) (Figure 5.17B). For the MCF-7 cell line, there was a

significant increase in hypoxic percentage area from day 1 to day 14 ( $p < 0.0001$ ) (Figure 5.16C). This was due to the formation of spheroids by this cell line. Overall, there was no increase in hypoxic percentage area in MDA-MB-231 cells, due to the cells remaining dispersed.

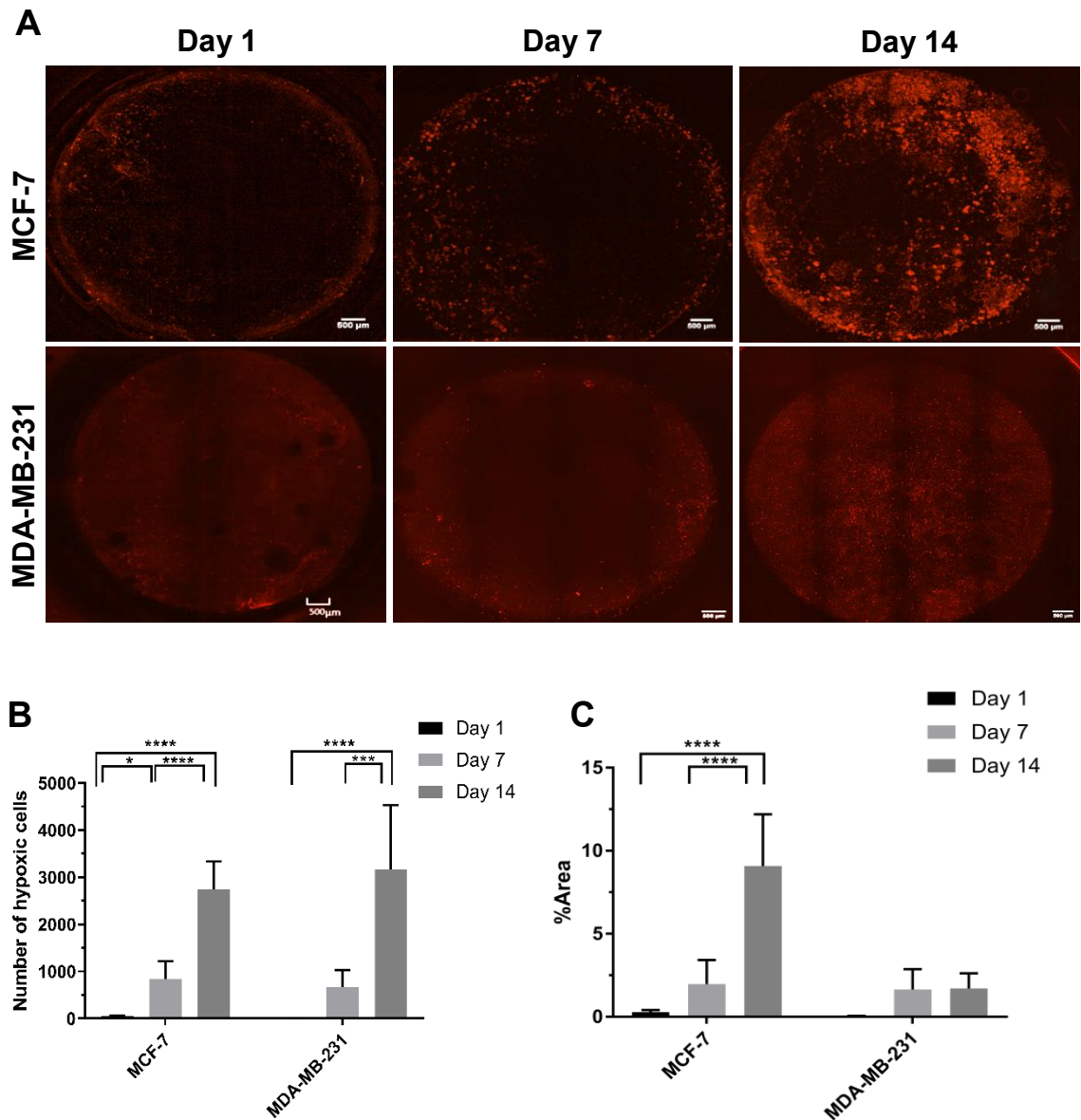


**Figure 5.16. Hypoxia detection and staining of MCF-7 and MDA-MB-231 cells in PeptiGelAlpha1 over 14 days.** (A) Fluorescence imaging of cell-laden hydrogel samples. Samples were stained with 10  $\mu\text{M}$  Image-iT Red Hypoxia Reagent and incubated for 1 hour at 37  $^{\circ}\text{C}$ . Red = hypoxic cells. Scale bar = 500  $\mu\text{m}$ . (B) Number of hypoxic cells in MCF-7/MDA-MB-231 cell-laden samples. ImageJ was used to quantify the number of hypoxic cells present in fluorescence images. (C) Percentage area of hypoxia in MCF-7/MDA-MB-231 cell-laden samples. ImageJ was used to quantify the percentage area of sample containing hypoxic cells. Data are mean  $\pm$  S.D. \* =  $p < 0.05$ , \*\*\* =  $p < 0.001$ , \*\*\*\* =  $p < 0.0001$  using two-way ANOVA and post-hoc Tukey's test. N = 3.

To further confirm that MCF-7 and MDA-MB-231 cells were becoming hypoxic within PeptiGelAlpha1, HIF1 $\alpha$  immunostaining was carried out on paraffin embedded sections. Positive staining was detected using a DAB chromagen, in which brown staining appeared if the protein was present. Under normoxic conditions, HIF1 $\alpha$  is inactivated by proteasomes and is located in the cell cytoplasm [97]. When the environment becomes hypoxic, the protein remains intact and translocates to the nucleus. Positive nuclear staining would thus indicate that the cells have become hypoxic. A cell pellet control for both cell lines revealed that cytoplasmic staining was mostly observed (**Appendix 4**).

For MCF-7 cell-laden PeptiGelAlpha1 samples, positive staining was observed within both the nucleus and the cytoplasm from 1 day in culture (**Figure 5.17**). As the cells aggregated, positive staining was abundant within the spheroids. In MDA-MB-231 cells, nuclear staining was observed after 7 days of culture, but in general, few cells presented positive staining.

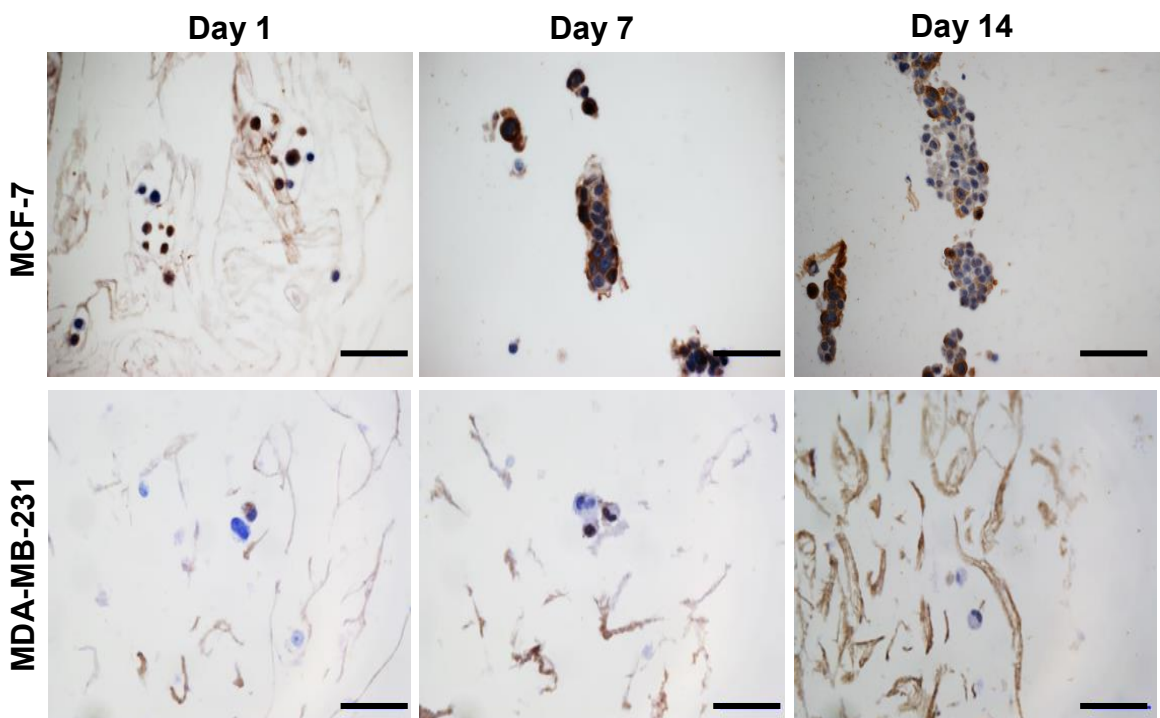


**Figure 5.17. Immunohistochemical staining of HIF1 $\alpha$  in MCF-7 and MDA-MB-231 cells in PeptiGelAlpha1 over 14 days.** Samples were sectioned at a thickness of 5.0  $\mu\text{m}$  and stained for HIF1 $\alpha$ . Positive staining was detected using a DAB substrate stain and counterstained using haematoxylin. Brown = positive staining. Blue = nuclei. Scale bar = 200  $\mu\text{m}$ . N = 2.

### 5.2.7. Epithelial to Mesenchymal Transition

To determine if expression of EMT related markers was affected by culture within PeptiGelAlpha1, immunohistochemistry of epithelial markers cytokeratin and E-cadherin, and mesenchymal markers N-cadherin and vimentin, was performed on sections of MCF-7 and MDA-MB-231 cell-laden PeptiGelAlpha1 samples. Positive staining was detected using a DAB chromagen, in which brown staining appeared if the protein was present. The surrounding hydrogel was weakly stained brown; however, negative controls (in which the primary antibody was omitted) showed that this was due to the DAB staining the hydrogel (**Appendix 2**). Cell pellet controls confirmed that positive staining was observed for MCF-7 cells for the E-cadherin, cytokeratin and vimentin markers but not for N-cadherin (**Appendix 4**). Positive staining was observed for MDA-MB-231 cells for cytokeratin and vimentin, but not for E-cadherin or N-cadherin (**Appendix 4**).

For PeptiGelAlpha1 samples, positive staining for E-cadherin was observed surrounding MCF-7 cells from 1 day of culture, indicative of cell-cell contacts (**Figure 5.18**). Strong positive staining was also observed for cytokeratin surrounding the cells at all time points. By day 14, when the cells had aggregated to form clusters, the staining was particularly strong on the periphery of the spheroids. For expression of mesenchymal markers, positive staining for vimentin was observed within the cell nuclei after 1 day in culture and throughout the 14-day culture period. For N-cadherin, no positive staining was observed after 1 day in culture. Weak staining was observed after 7 and 14 days in culture within the cytoplasm of the cell spheroids. Although it cannot be concluded from these data alone if EMT was occurring in MCF-7 cells within PeptiGelAlpha1, the native phenotype of the cell line was retained within the hydrogel.



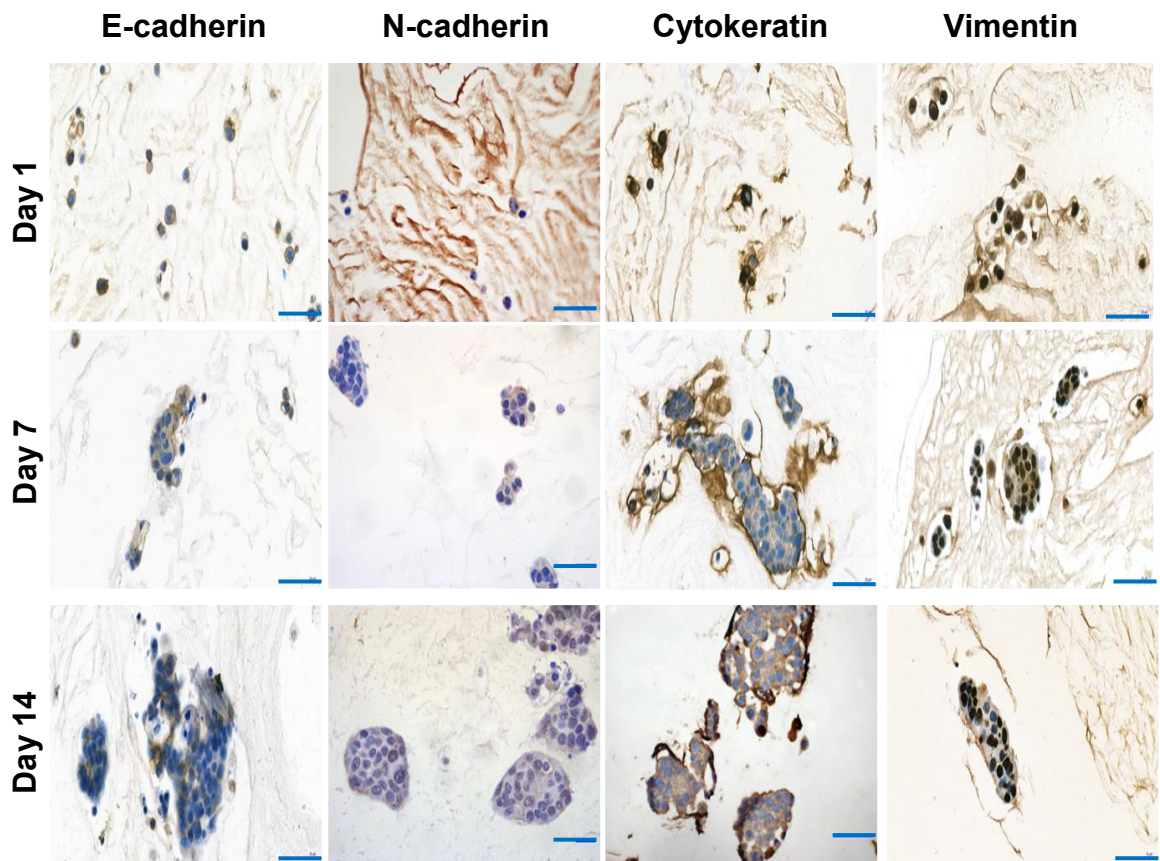


**Figure 5.18. Immunohistochemical staining of EMT markers in MCF-7 cells cultured in PeptiGelAlpha1 over 14 days.** Samples were sectioned at a thickness of 5.0  $\mu\text{m}$  and stained for epithelial markers (E-cadherin and cytokeratin) and mesenchymal markers (vimentin and N-cadherin). Positive staining was detected using a DAB substrate stain and counterstained using haematoxylin. Brown = positive staining. Blue = nuclei. Scale bar = 200  $\mu\text{m}$ . N = 2.

No positive staining was observed for E-cadherin in MDA-MB-231 cells throughout the 14-day culture period in PeptiGelAlpha1 (**Figure 5.19**). Positive staining, however, was observed for cytokeratin after 1 day in culture surrounding the cells and throughout the 14-day culture period. In regards to mesenchymal markers, strong positive staining was observed for vimentin at all three time points intracellularly. On the other hand, no positive staining was observed for N-cadherin at any time point within PeptiGelAlpha1. As observed with the MCF-7 cell line, it cannot be determined if EMT was occurring in MDA-MB-231 cells in PeptiGelAlpha1, although the native phenotype was retained.



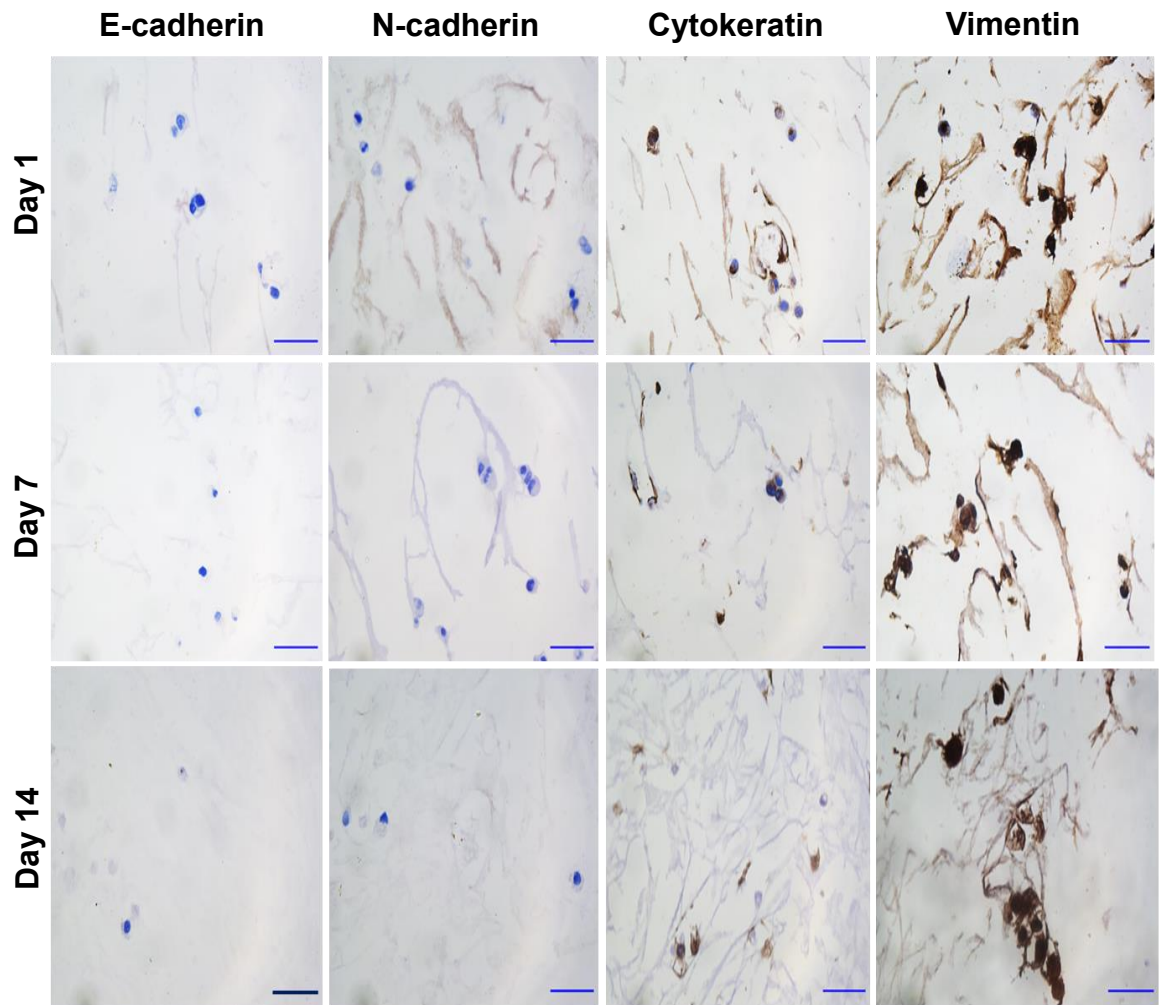


**Figure 5.19. Immunohistochemical staining of EMT markers in MDA-MB-231 cells cultured in PeptiGelAlpha1 over 14 days.** Samples were sectioned at a thickness of 5.0  $\mu\text{m}$  and stained for epithelial markers (E-cadherin and cytokeratin) and mesenchymal markers (vimentin and N-cadherin). Positive staining was detected using a DAB substrate stain and counterstained using haematoxylin. Brown = positive staining. Blue = nuclei. Scale bar = 200  $\mu\text{m}$ . N = 2.

### 5.2.8. Invasive Potential of MCF-7 & MDA-MB-231 Cells in PeptiGelAlpha1

To model the events underpinning invasion of surrounding tissues more closely, MCF-7 and MDA-MB-231 cell-laden PeptiGelAlpha1 samples were embedded in either collagen I or Matrigel and imaged over time. A schematic of the protocol used is depicted in **Figure 5.20**. Cells were imaged over a 21-day culture period.

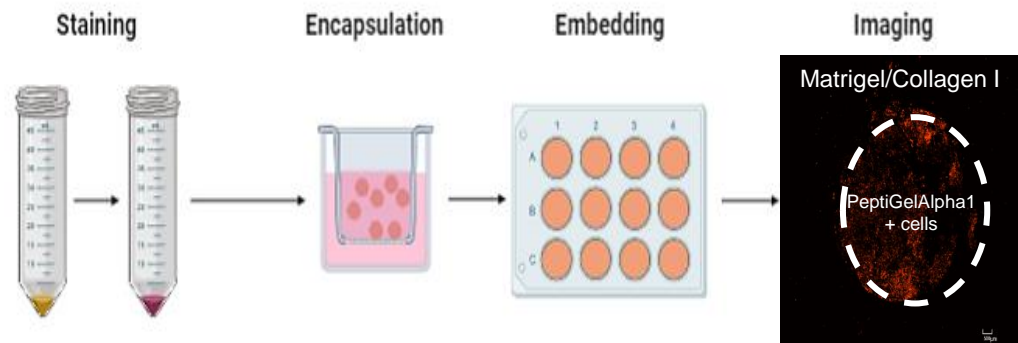


**Figure 5.20. Schematic of steps used for the embedded invasion assay.** Cells were pre-stained with the PKH26 Red Fluorescent Cell Linker Kit prior to encapsulation in PeptiGelAlpha1 in cell culture inserts. After 2 days in culture, cell-laden samples were removed from the inserts and placed in wells of a 24 well plate. The hydrogel was surrounded by collagen I or Matrigel. Live cell imaging was used to observe invasion. Created with BioRender.com.

MDA-MB-231 cells are a metastatic cell line and it was hypothesised that these cells would be more likely to invade collagen I or Matrigel compared with the MCF-7 cells. At day 0, MCF-7 and MDA-MB-231 cells were clearly within the PeptiGelAlpha1 material (**Figure 5.21**). After 7 days, small clusters of MCF-7 cells appeared to be budding and breaking away from the PeptiGelAlpha1 material into both collagen I and Matrigel. MDA-MB-231 cells remained within PeptiGelAlpha1. After 14 days, small colonies of MCF-7 cells separate from the PeptiGelAlpha1 construct were observed in Matrigel, with smaller clusters of cells observed in collagen I. MDA-MB-231 cells began to invade the collagen I matrix, but not Matrigel by this time point. By day 21, the Matrigel began to degrade so this was the final time point. MCF-7 cells were observed to form collective protrusions from the peptide hydrogel into Matrigel and collagen I, suggesting that the cells were actively breaking down the SAPH and invading the surrounding material. Surprisingly, this was not observed with MDA-MB-231 cells.

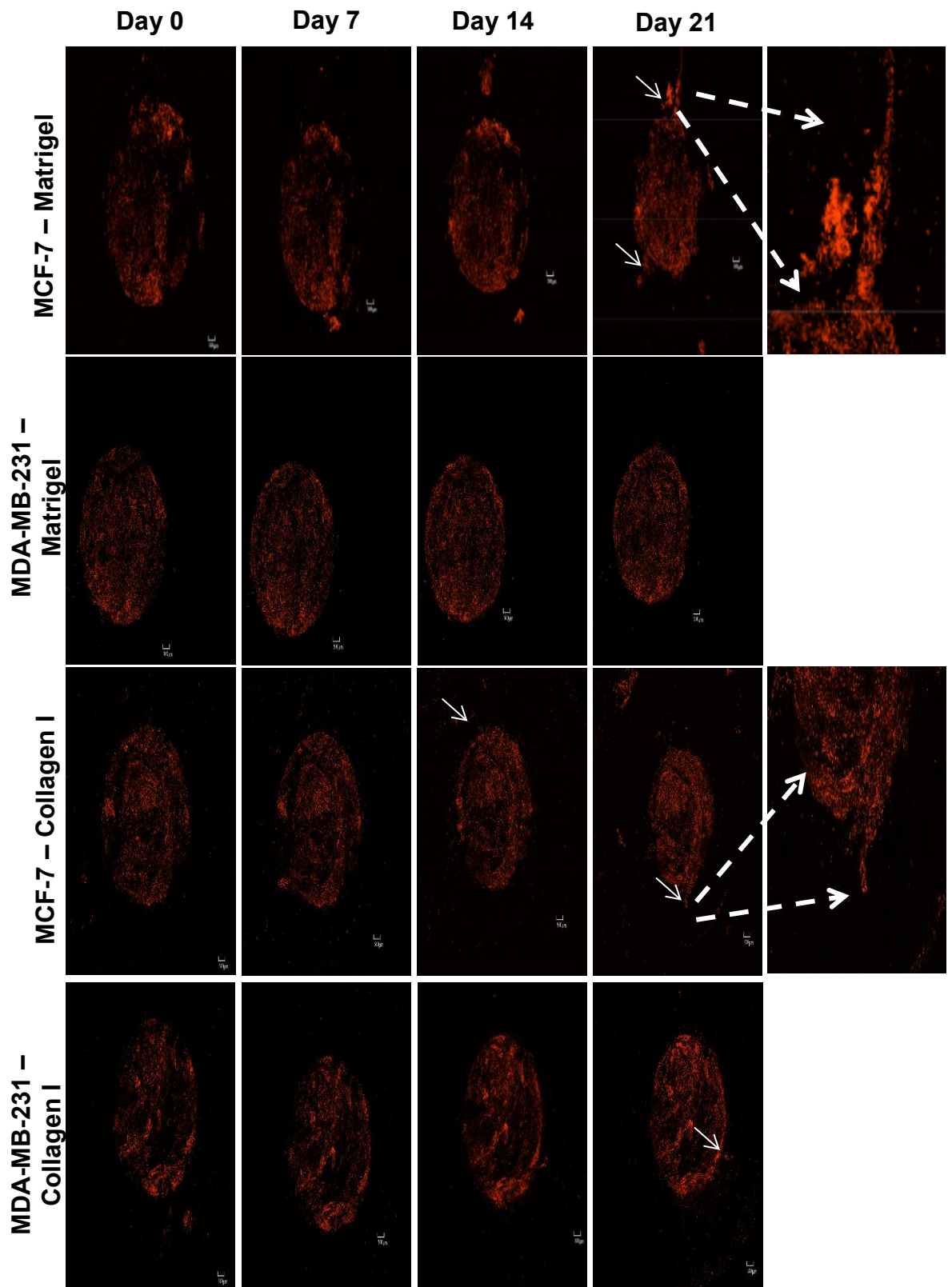


**Figure 5.21. Invasion of MCF-7 and MDA-MB-231 cells from PeptiGelAlpha1 into collagen I or Matrigel over 21 days.** Cells were pre-stained with the PKH26 Red Fluorescent Cell Linker Kit and cultured in PeptiGelAlpha1 for 2 days. Cell-laden samples were embedded in collagen I or Matrigel. Samples were imaged at each time point using an inverted confocal microscope. Solid arrows indicate cell invasion. Dashed arrows indicate expanded sections. Red = cell membrane. Scale bar = 500  $\mu\text{m}$ . N = 1.

Quantification of the images presented in **Figure 5.21** revealed that there was a significant increase in the number of invading MCF-7 cells into collagen I after 14 and 21 days, compared with 1 day (104.7 cells  $\pm$  15.1 cells vs 2156.5 cells  $\pm$  1077.5 cells and 2058.5 cells  $\pm$  297.5 cells respectively;  $p < 0.0001$ ) (**Figure 5.22**). A plateau was reached for invading MCF-7 cells by day 14 into collagen I. A significant increase in the number of invading MCF-7 cells into Matrigel was also observed after 14 and 21 days, increasing from 28.7 cells  $\pm$  51.0 cells to 743.3 cells  $\pm$  147.4 cells ( $p < 0.05$ ) and 1060  $\pm$  297 cells ( $p < 0.01$ ) respectively. For MDA-MB-231 cells, a significant increase was observed between 1 and 21 days in collagen I (84.5 cells  $\pm$  28.8 cells to 795.5 cells  $\pm$  247.7 cells;  $p < 0.05$ ) Whereas in Matrigel, no significant difference was observed in the number of invading cells over the 21-day culture period. These data suggested that both MCF-7 and MDA-MB-231 cells were more likely to invade collagen I from PeptiGelAlpha1 than Matrigel, and that the MCF-7 cells were more invasive than MDA-MB-231 cells.

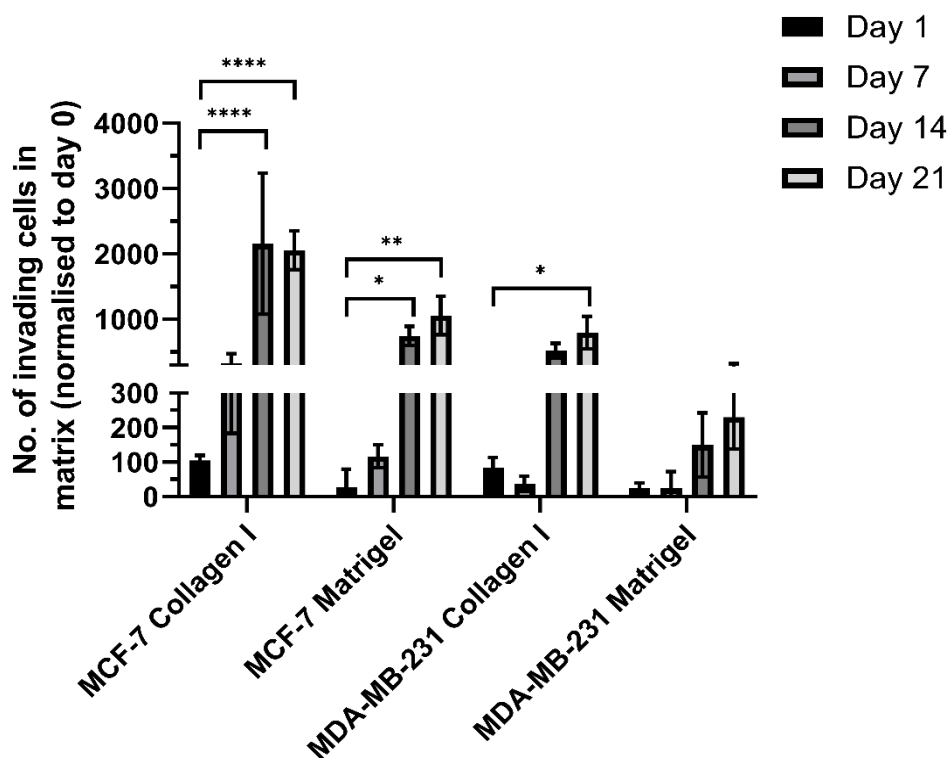


**Figure 5.22. Number of invading MCF-7 and MDA-MB-231 cells from PeptiGelAlpha1 into collagen I or Matrigel over 21 days.** ImageJ was used to quantify the number of invading cells in the surrounding matrix at each time point. Data were normalised to day 0. \* =  $p < 0.05$ , \*\* =  $p < 0.01$ , \*\*\*\* =  $p < 0.0001$ , using two-way ANOVA and post-hoc Tukey's test. Data are mean  $\pm$  S.D.

### 5.2.9. Cell Response to Anti-Cancer Drugs in PeptiGelAlpha1

To assess if PeptiGelAlpha1 could hinder the efficacy of anti-cancer drugs, MCF-7 and MDA-MB-231 cells were encapsulated in PeptiGelAlpha1 and exposed to tamoxifen or doxorubicin treatment. MCF-7 and MDA-MB-231 cells were cultured within PeptiGelAlpha1 at a density of  $1 \times 10^6$  cells/mL and as a monolayer culture in 24 well plates at a density of  $1 \times 10^5$  cells/mL. After 1 day in culture, samples were exposed to 100  $\mu$ M or 500  $\mu$ M tamoxifen or 100  $\mu$ M doxorubicin. 1 % DMSO was used as a vehicle control for TCP samples and no treatment controls were included. Samples were collected after 24 and 48 hours of exposure and processed for PicoGreen analysis (**Figure 5.23**).

There was no significant difference between untreated TCP samples and cells treated with 1 % DMSO for both MCF-7 and MDA-MB-231 cells after 24 and 48 hours, showing that the DMSO vehicle did not contribute towards the cytotoxic effects of tamoxifen and doxorubicin (**Figure 5.23A & B**). For MCF-7 cells cultured on TCP, treatment with 100  $\mu$ M tamoxifen resulted in decreased viability after 48 hours ( $2.26 \text{ ng/mL} \pm 3.59 \text{ ng/mL}$ ) compared with 24 hours exposure ( $14.05 \text{ ng/mL} \pm 1.00 \text{ ng/mL}$ ;  $p < 0.001$ ) and no treatment after 48 hours ( $20.73 \text{ ng/mL} \pm 3.58 \text{ ng/mL}$ ;  $p < 0.0001$ ) (**Figure 5.23A**). Treatment with 500  $\mu$ M tamoxifen resulted in reduced cell viability compared with untreated cells after 48 hours ( $6.84 \text{ ng/mL} \pm 1.58 \text{ ng/mL}$ ), but this was higher than that of 100  $\mu$ M tamoxifen. Treatment of MCF-7 cells on TCP with 100  $\mu$ M doxorubicin resulted in significantly reduced viability after 24 hours ( $4.18 \text{ ng/mL} \pm 2.48 \text{ ng/mL}$ ;  $p < 0.0001$ ) and 48 hours ( $2.82 \text{ ng/mL} \pm 0.69 \text{ ng/mL}$ ;  $p < 0.0001$ ) compared with untreated cells (**Figure 5.23C**). Little difference was observed with MDA-MB-231 cells treated with 100  $\mu$ M tamoxifen after 24 hours ( $11.66 \text{ ng/mL} \pm 3.59 \text{ ng/mL}$ ) and 48 hours ( $12.39 \text{ ng/mL} \pm 2.05 \text{ ng/mL}$ ) (**Figure 5.23B**). Both 24 and 48 hours exposure were significantly lower than that of untreated cells ( $p < 0.001$ ). Treatment with 500  $\mu$ M tamoxifen after 48 hours resulted in a significantly lower DNA concentration ( $0.52 \text{ ng/mL} \pm 1.68 \text{ ng/mL}$ ) than that of 100  $\mu$ M tamoxifen. Doxorubicin treatment of MDA-MB-231 cells resulted in significantly decreased DNA concentration compared with untreated cells after both 24 hours and 48 hours exposure, when cultured on TCP ( $p < 0.0001$ ) (**Figure 5.23D**).

Within PeptiGelAlpha1, a significant increase in DNA concentration was observed in untreated MCF-7 cells between 24 and 48 hours ( $55.2 \text{ ng/mL} \pm 1.93 \text{ ng/mL}$  vs  $274.2 \text{ ng/mL} \pm 16.6 \text{ ng/mL}$ ;  $p < 0.0001$ ) (**Figure 5.23E**). A significant increase in viability was also observed in 100  $\mu$ M and 500  $\mu$ M tamoxifen treated MCF-7 cells between 24 and

48 hours, although 48 hours exposure to both treatments was still significantly lower than untreated cells at 48 hours. Treatment with 100  $\mu$ M doxorubicin resulted in a greatly reduced DNA concentration after 48 hours of treatment. After 24 hours, there was no significant difference between any of the conditions used. A similar trend was observed with MDA-MB-231 cells (**Figure 5.23F**).

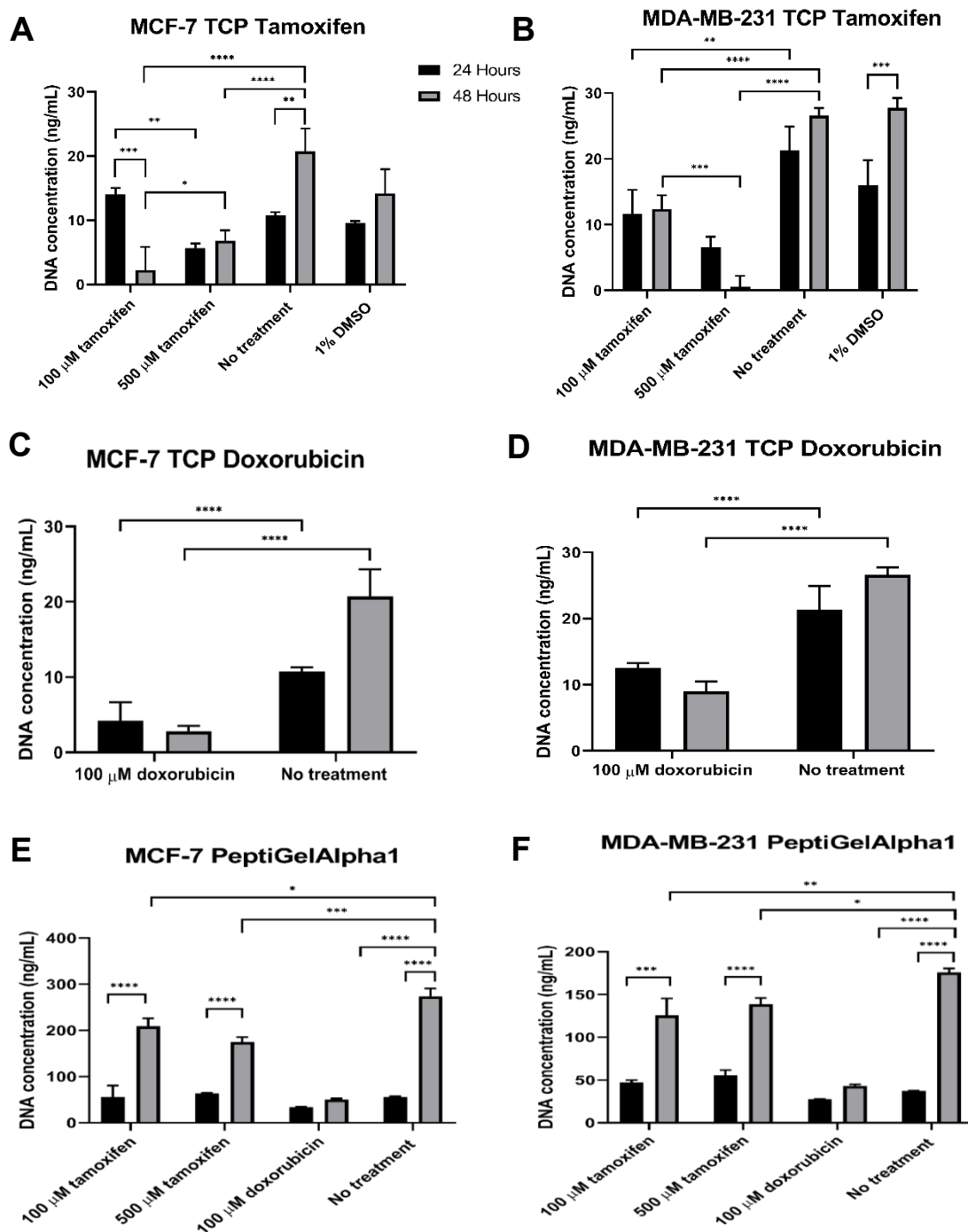


**Figure 5.23. Efficacy of anti-cancer drugs tamoxifen and doxorubicin on MCF-7 and MDA-MB-231 cells.** (A) MCF-7 cells cultured on TCP treated with 100–500  $\mu$ M tamoxifen. (B) MDA-MB-231 cells cultured on TCP treated with 100–500  $\mu$ M tamoxifen. (C) MCF-7 cells cultured on TCP treated with 100  $\mu$ M doxorubicin. (D) MDA-MB-231 cells cultured on TCP treated with 100  $\mu$ M doxorubicin. (E) MCF-7 cells cultured within PeptiGelAlpha1 treated with 100–500  $\mu$ M tamoxifen and 100  $\mu$ M doxorubicin. (F) MDA-MB-231 cells cultured within PeptiGelAlpha1 treated with 100–500  $\mu$ M tamoxifen and 100  $\mu$ M doxorubicin.  $1 \times 10^5$  cells/mL was used for TCP and  $1 \times 10^6$  cells/mL was used for PeptiGelAlpha1. PicoGreen analysis was performed and fluorescence values were converted to DNA concentration using a DNA concentration standard curve. \* =  $p < 0.05$ , \*\* =  $p < 0.01$ , \*\*\* =  $p < 0.001$ , \*\*\*\* =  $p < 0.0001$  using two-way ANOVA and post-hoc Tukey’s test. Data are mean  $\pm$  S.D. N = 1.

The efficacy of tamoxifen and doxorubicin on MCF-7 and MDA-MB-231 cells on TCP and within PeptiGelAlpha1 was directly compared (**Figure 5.24**). As different cell-seeding densities were used, data were interpreted as percentage of viable cells compared with the no treatment control. For MCF-7 cells, 3D culture in PeptiGelAlpha1 offered no protection against doxorubicin treatment compared with TCP, as a similar percentage of viable cells were observed for both time points ( $p > 0.05$ ) (**Figure 5.24A**). In regards to tamoxifen treatment, there was a significantly higher percentage of viable cells cultured in PeptiGelAlpha1 after 48 hours compared with TCP for 100  $\mu\text{M}$  ( $p < 0.05$ ). A higher percentage of viable cells was observed after 48 hours for 500  $\mu\text{M}$  tamoxifen but this was not significant ( $p > 0.05$ ) (**Figure 5.24A**). For MDA-MB-231 cells, as observed with MCF-7 cells, there was no difference observed in percentage viability in cells treated with doxorubicin between 2D and 3D culture ( $p > 0.05$ ) (**Figure 5.24B**). There was a significantly higher percentage of viable cells in 3D culture after 24 hours when treated with 100  $\mu\text{M}$  tamoxifen ( $p < 0.0001$ ). After 48 hours, there was a small, but non-significant increase with cells in 3D culture ( $p > 0.05$ ). For 500  $\mu\text{M}$  tamoxifen, a significantly higher percentage of cells was observed in PeptiGelAlpha1 after both 24 and 48 hours ( $p < 0.0001$ ) (**Figure 5.24B**). These data suggest that 3D culture in PeptiGelAlpha1 prevented uptake of tamoxifen, resulting in reduced efficacy.



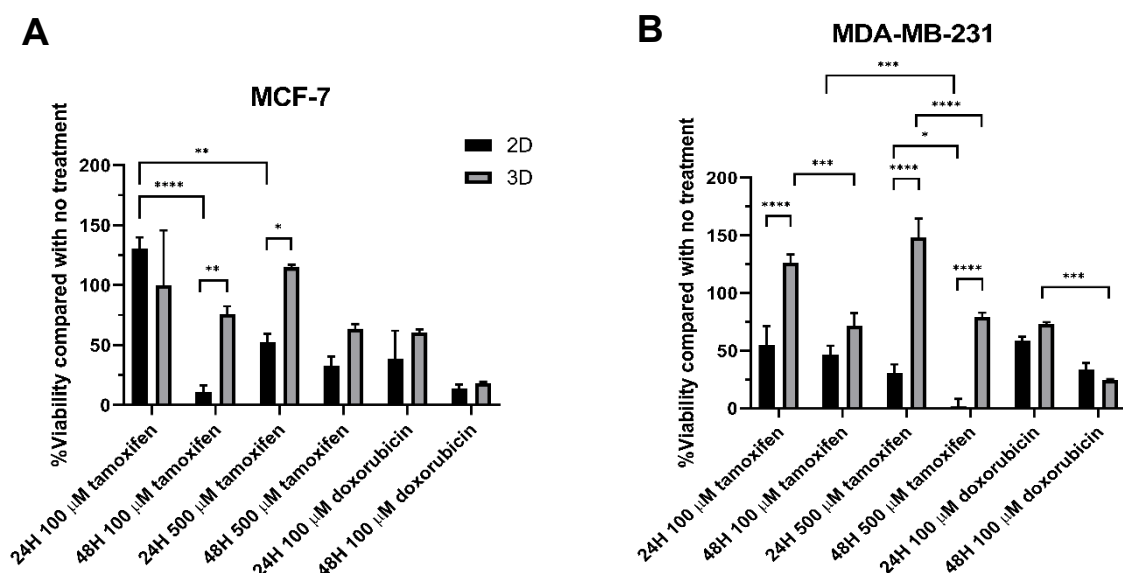


**Figure 5.24. Percentage viability of MCF-7 and MDA-MB-231 cells exposed to tamoxifen and doxorubicin treatment comparing 2D monolayer and 3D PeptiGelAlpha1 culture.** (A) MCF-7 cells. (B) MDA-MB-231 cells. MCF-7 and MDA-MB-231 cells were cultured on TCP ( $1 \times 10^5$  cells/mL) or within PeptiGelAlpha1 ( $1 \times 10^6$  cells/mL). After 1 day in culture, samples were exposed to 100–500  $\mu$ M tamoxifen, 100  $\mu$ M doxorubicin, or cell culture media. A no treatment control was included for TCP and PeptiGelAlpha1 and a 1 % DMSO vehicle control was included for TCP samples. Samples were collected after 24 hours and 48 hours of exposure. PicoGreen analysis was performed and raw fluorescence values were converted to DNA concentration using a standard curve of known DNA concentrations. Data were then converted to percentage viability compared with the no treatment control. \* =  $p < 0.05$ , \*\* =  $p < 0.01$ , \*\*\* =  $p < 0.001$ , \*\*\*\* =  $p < 0.0001$  using two-way ANOVA and post-hoc Tukey’s test. Data are mean  $\pm$  S.D. N = 1.

Cell morphology after exposure to tamoxifen and doxorubicin treatment was assessed by pre-staining the cells with the PKH26 Cell Linker Membrane Kit and imaging the cells at the designated time points. On TCP, MCF-7 cells without treatment exhibited an epithelioid morphology and were observed to aggregate into clusters (**Figure 5.25A**). The 1 % DMSO control showed no difference in cell morphology. When tamoxifen treatment was applied, cell morphology was rounded and cell density appeared sparser with 500  $\mu$ M tamoxifen. With 100  $\mu$ M doxorubicin treatment, cells appeared rounded and reduced in density. In PeptiGelAlpha1, untreated MCF-7 cells aggregated to form clusters and were rounded in morphology (**Figure 5.25B**). Treatment with tamoxifen or doxorubicin did not affect cell organisation or morphology, as there was no difference compared with the untreated control. No difference was observed for any condition between the two time points.

For the MDA-MB-231 cell line, untreated cells on TCP appeared elongated with a spindle-like morphology (**Figure 5.26A**). This was also observed with the 1 % DMSO control. When 100  $\mu$ M and 500  $\mu$ M tamoxifen was applied, cell morphology and density did not appear to have changed after 24 hours exposure. After 48 hours exposure, cell morphology appeared rounded with fewer cells present. Cells appeared rounded after exposure to 100  $\mu$ M doxorubicin after both 24 and 48 hours of exposure. Within PeptiGelAlpha1, untreated cells were mostly rounded and appeared dispersed throughout the hydrogel (**Figure 5.26B**). Exposure to tamoxifen and doxorubicin treatment appeared to have no effect on cell morphology or density after 24 and 48 hours of exposure, when encapsulated within PeptiGelAlpha1.

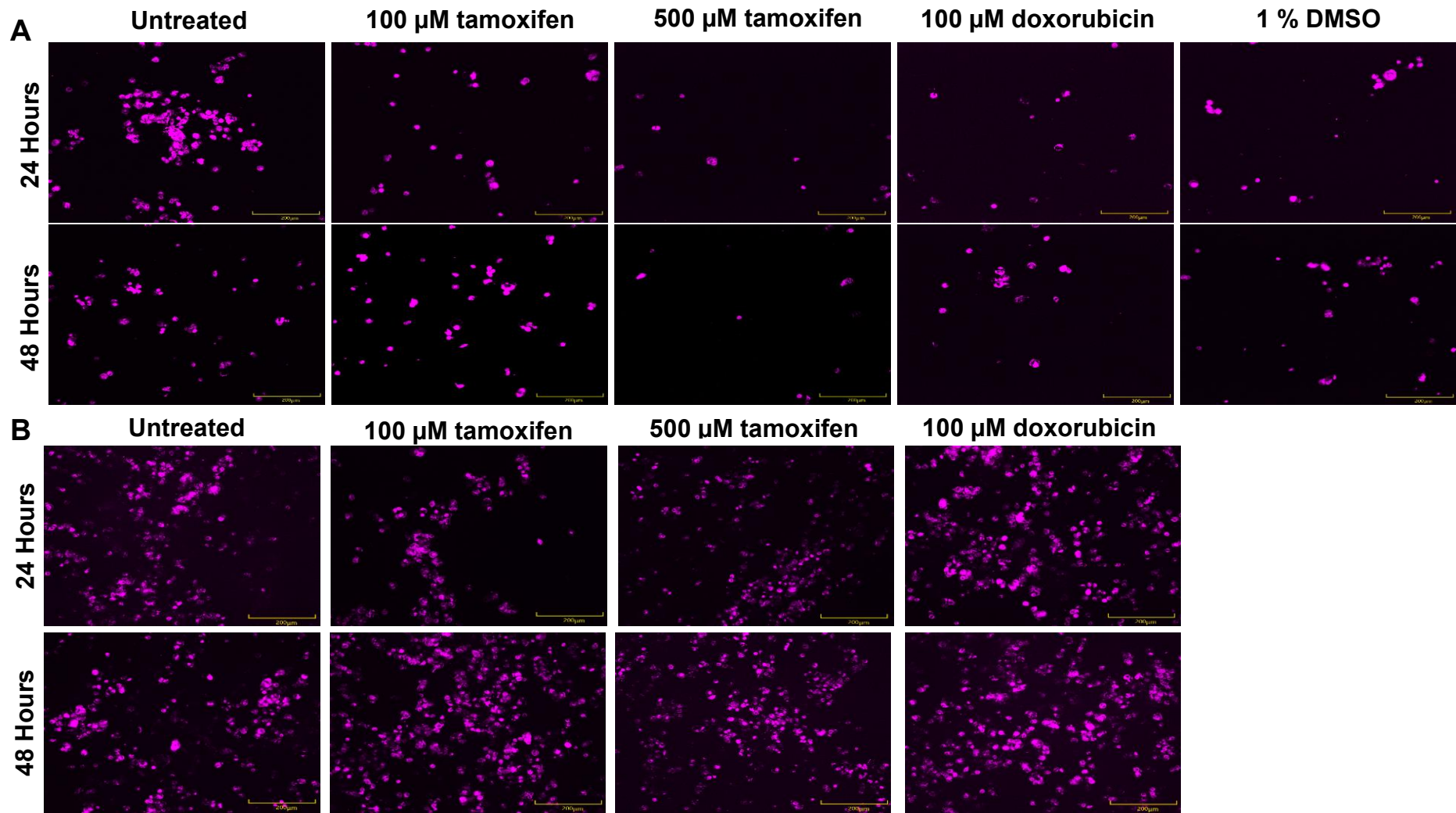


**Figure 5.25. Fluorescence imaging of MCF-7 cells exposed to tamoxifen and doxorubicin treatment after 24 and 48 hours. (A) Cells cultured on TCP ( $1 \times 10^5$  cells/mL). (B) Cells cultured within PeptiGelAlpha1 ( $1 \times 10^6$  cells/mL). Pink = cell membrane. N = 1.**

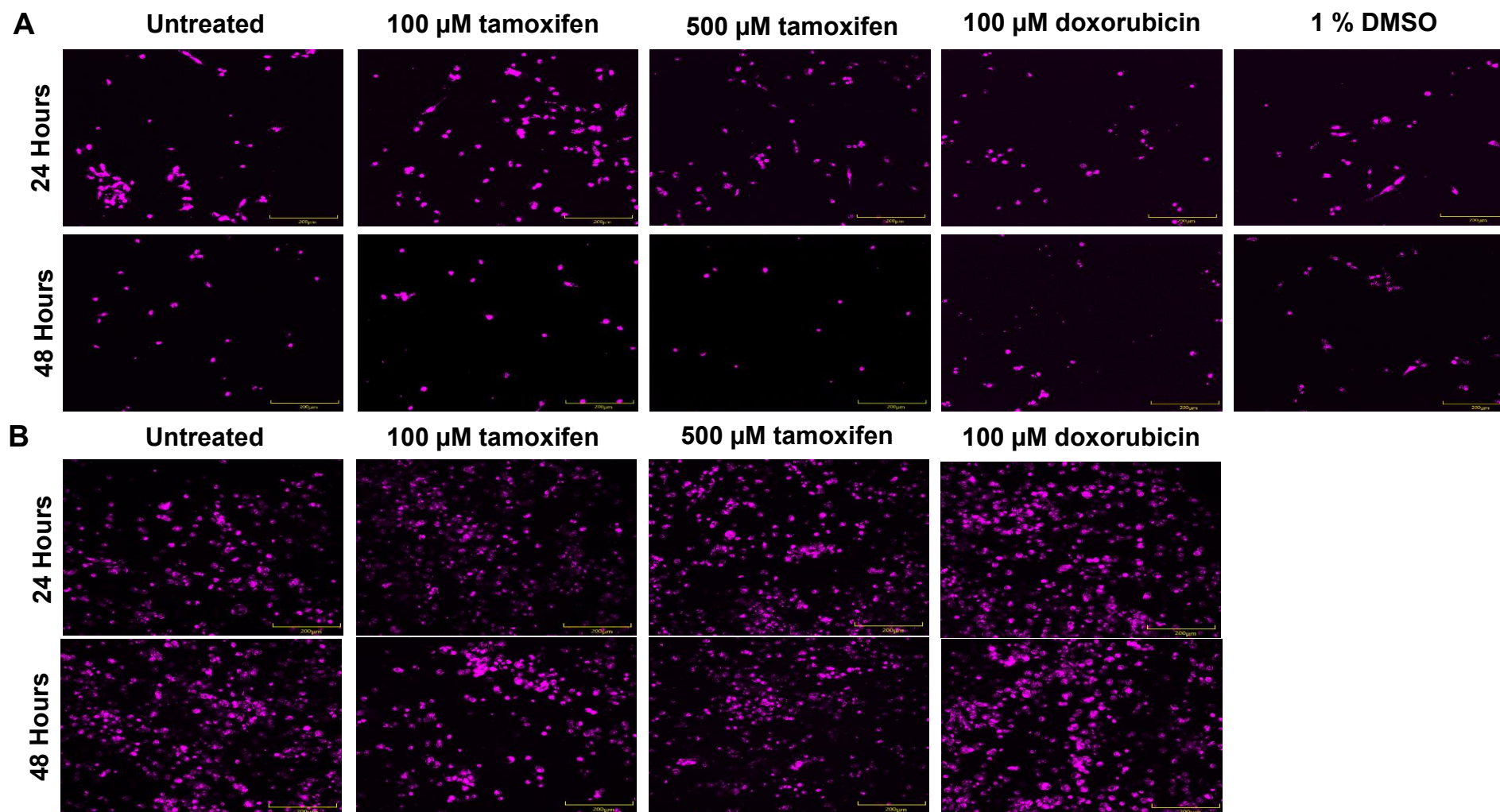


**Figure 5.26. Fluorescence imaging of MDA-MB-231 cells exposed to tamoxifen and doxorubicin treatment after 24 and 48 hours.** (A) Cells cultured on TCP ( $1 \times 10^5$  cells/mL). (B) Cells cultured within PeptiGelAlpha1 ( $1 \times 10^6$  cells/mL). Pink = cell membrane. N = 1.

To further investigate the efficacy of tamoxifen and doxorubicin on MCF-7 and MDA-MB-231 cells cultured within PeptiGelAlpha1, dose-response curves were generated by exposing cells to increasing concentrations of either drug (**Figure 5.27**). Cells were cultured in PeptiGelAlpha1 or on TCP for 24 hours, prior to exposure of 0.001–500  $\mu\text{M}$  tamoxifen or doxorubicin. Samples were collected after 48 hours and processed for PicoGreen analysis. To produce sigmoidal curves, the Y values were normalised using GraphPad software. This resulted in inflation of several of the error bars, which is not reflective of the data obtained. Data without normalisation are presented in **Appendix 7**.

In both 2D and 3D culture, MDA-MB-231 cells exhibited a sigmoidal response to increasing concentrations when exposed to doxorubicin, highlighted by little change in viability at lower concentrations before decreasing and plateauing at the highest concentrations (**Figure 5.27A**). The curve for MDA-MB-231 cells cultured in PeptiGelAlpha1 was shifted to the right, revealing that higher drug concentrations were needed to reduce cell viability. It was also noted that the threshold dose for cells cultured in 2D was much lower than that of 3D culture. When treating MDA-MB-231 cells with tamoxifen, a sigmoidal curve was observed for both 2D and 3D cultured cells (**Figure 5.27B**). The top plateau region for both datasets was similar, although the curve for 3D cultured cells was shifted slightly to the right. MCF-7 cells treated with doxorubicin exhibited no difference in response when comparing 2D and 3D cultured cells, although the curves appeared to be broader with the absence of a steep slope (**Figure 5.27C**). When MCF-7 cells were treated with tamoxifen, a sigmoidal response was observed for 2D cultured cells (**Figure 5.27D**). However, for 3D cultured cells, a classic sigmoidal dose-response curve was not observed.

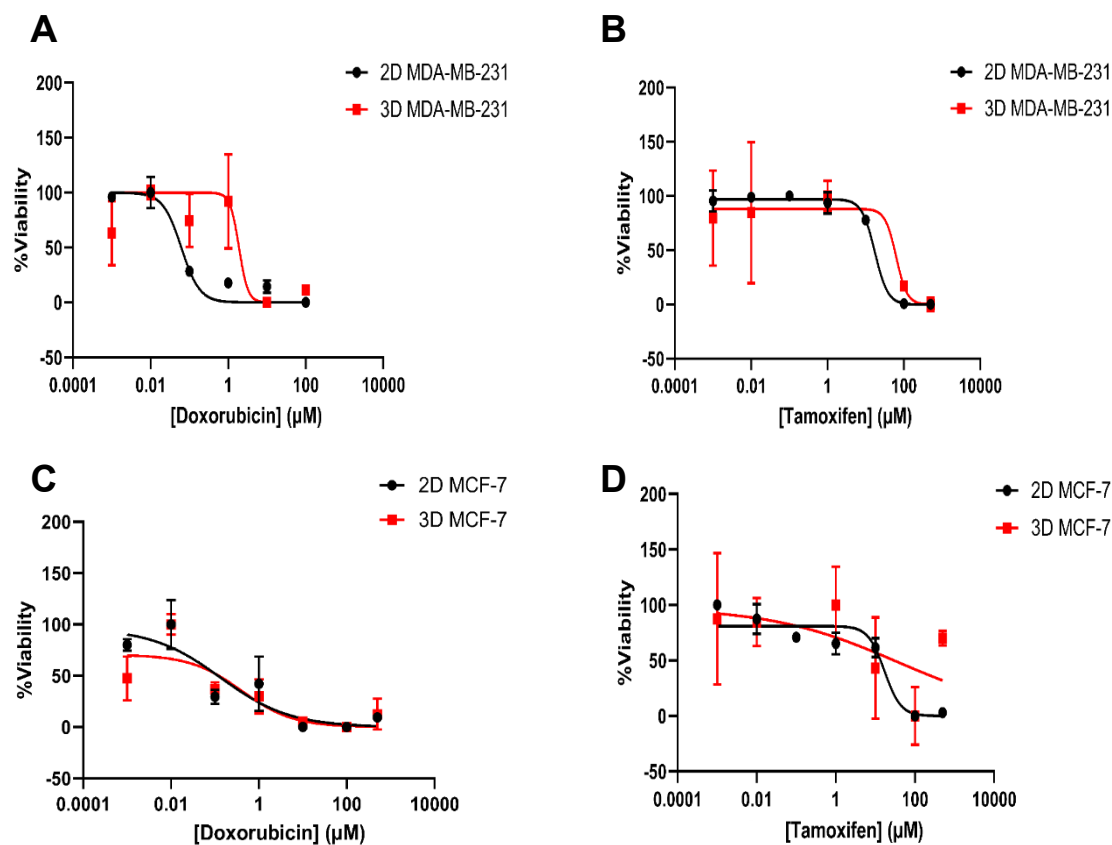


**Figure 5.27. Dose-response curves for MCF-7 and MDA-MB-231 cells in 2D and 3D in PeptiGelAlpha1.** (A) MDA-MB-231 cells treated with 0.001–500  $\mu\text{M}$  doxorubicin. (B) MDA-MB-231 cells treated with 0.001–500  $\mu\text{M}$  tamoxifen. (C) MCF-7 cells treated with 0.001–500  $\mu\text{M}$  doxorubicin. (D) MCF-7 cells treated with 0.001–500  $\mu\text{M}$  tamoxifen. Data are mean  $\pm$  S.D. Data are normalised. N = 1.

The dose-response curves presented in **Figure 5.27** were used to calculate the potency of tamoxifen and doxorubicin for both cell lines, known as the IC<sub>50</sub> values (**Table 5.1**). For doxorubicin treatment, no significant difference was observed between the 2D and 3D cultures, for both MCF-7 and MDA-MB-231 cells (**Figure 5.28A**). For tamoxifen treatment, no significant difference was observed for MCF-7 cells. However, for MDA-MB-231 cells, a 5-fold increase in concentration was needed to inhibit cell viability by 50 % in 3D cultured cells, from 16.7  $\mu\text{M} \pm 5.0 \mu\text{M}$  to 87.5  $\mu\text{M} \pm 1.05 \mu\text{M}$ . This difference was deemed to be statistically significant ( $p < 0.01$ ) (**Figure 5.28B**).

**Table 5.1. IC<sub>50</sub> values for MCF-7 and MDA-MB-231 cells cultured in 2D and 3D in PeptiGelAlpha1.** Data are mean ± S.E.M.

<b>Doxorubicin</b>				
	<b>MCF-7</b>		<b>MDA-MB-231</b>	
	2D	3D	2D	3D
IC <sub>50</sub> (μM)	0.1 ± 0.08	0.06 ± 0.06	0.06 ± 0.02	1.9 ± 14.5
<b>Tamoxifen</b>				
	<b>MCF-7</b>		<b>MDA-MB-231</b>	
	2D	3D	2D	3D
IC <sub>50</sub> (μM)	3.7 ± 2.1	5.4 ± 9.5	16.7 ± 5.0	87.5 ± 1.05

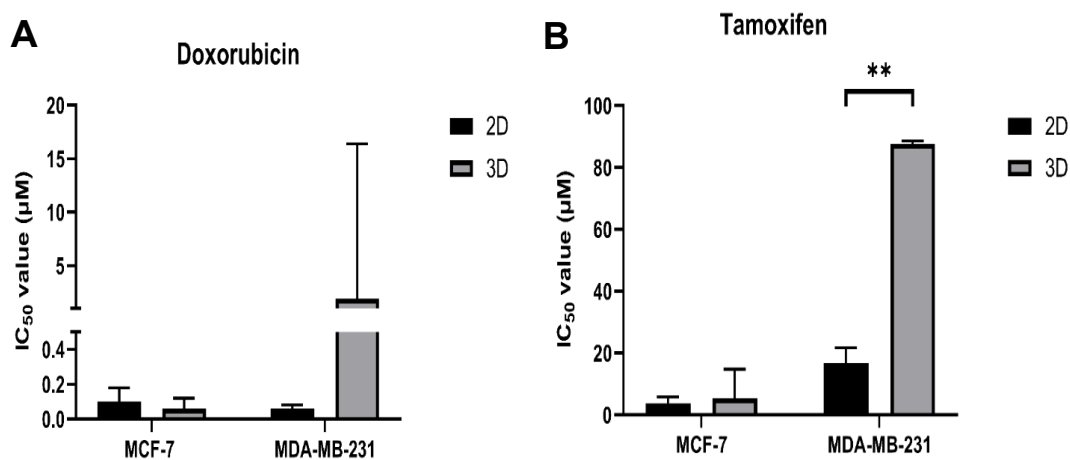


**Figure 5.28. IC<sub>50</sub> values for MCF-7 and MDA-MB-231 cells cultured in 2D and 3D in PeptiGelAlpha1.** (A) Doxorubicin. (B) Tamoxifen. Data are mean ± S.E.M. \*\* =  $p < 0.01$  using two-way ANOVA and post-hoc Sidak's test. N = 1.

## 5.3. Discussion

### 5.3.1. Viability and Proliferation of MCF-7 & MDA-MB-231 Cells within PeptiGelAlpha1

MCF-7 and MDA-MB-231 cells were observed to be viable and proliferating within PeptiGelAlpha1 for up to 14 days in culture, suggesting that this SAPH can support the long-term culture and growth of two breast cancer cell lines. LIVE/DEAD staining was used as a qualitative assay (**Figure 5.1**), but quantitative analysis could not be carried out due to cell aggregation. Therefore, PicoGreen analysis was used as a quantitative measure of cell growth (**Figure 5.3**). Other quantitative assays are available, such as quantifying metabolic activity with AlamarBlue [310], measuring adenosine triphosphate (ATP) activity with CellTiterGlo [311] and the lactate dehydrogenase (LDH) activity assay, measuring cytotoxicity [312]. Whilst the aforementioned assays provide direct and indirect measures of cell viability, they rely on adding the reagent directly to the cell culture media. For cells cultured on TCP, this is a rapid and simple method of assessing cell viability. However, with 3D samples, and in particular hydrogel samples, the issue lies in diffusion of the analyte into the cell culture media. This can result in an underestimation of cell viability.

To avoid this, PicoGreen was used as this relies on sacrificing and destroying the samples in order to quantify DNA content. PicoGreen analysis was achieved by digesting the peptide fibres with incubation of the enzyme pronase, which has been previously optimised for DNA recovery with peptide hydrogels [276]. Although the charge of the SAPH had been shown to interfere with DNA recovery, PeptiGelAlpha1 is neutrally charged, and as such, PicoGreen analysis could be used [276]. When comparing DNA recovery from cells encapsulated in PeptiGelAlpha1 and dPBS, this study showed that the material did not interfere with PicoGreen analysis (**Figure 5.2**). Optimisation of DNA recovery from SAPHs has previously been achieved using homogenisation to ensure complete cell lysis [276]. There was no access to a homogeniser in this study and as such, vortexing and freeze-thaw cycles were used to enable cell lysis, as used elsewhere for PicoGreen analysis of SAPH samples [313]. Ki67 immunohistochemical staining was used to supplement these data (**Figure 5.4**).

Naturally derived hydrogels such as hyaluronic acid [16], alginate [314] and collagen I [315] have been shown to support the viability of MCF-7 cells for up to 9 days. In regards to SAPH systems, previous studies have shown that this platform is suitable for MCF-7



culture; the SAPH h9e was found to support MCF-7 cells for up to 7 days in culture [27], and  $\beta$ -sheet forming FEFEFKFK also maintained the viability of MCF-7 cells for up to 7 days [29]. In regards to longer culture periods, one study using hydrogels formed from cellulose nanocrystals cultured MCF-7 cells for up to 15 days [316]. The data presented herein showed that PeptiGelAlpha1 could be a suitable candidate for the long-term growth of MCF-7 cells.

In regards to the MDA-MB-231 cells, the LIVE/DEAD staining and PicoGreen data showed that the cells were viable for up to 7 days (**Figure 5.1 & 5.3**). However, a large drop in DNA concentration from day 7 to day 14 was observed with the PicoGreen data (**Figure 5.3**). One study investigating MDA-MB-231 cells in Matrigel, collagen I and RADA16 showed that the cells became growth-arrested in RADA16 by day 5, observed by a decrease in proliferation and a plateau in cell number [28]. Other studies using MDA-MB-231 cells in hydrogel systems have used culture periods of predominantly up to 10 days [169,280,317]. It is possible that the decline in DNA concentration observed in this current study was due to cells migrating through the hydrogel towards the polyester membrane of the cell culture insert, resulting in a reduced number of cells in the hydrogel. Staining of the membrane was not carried out, but cell density did appear reduced in histological images (**Figure 5.5**), supporting this hypothesis.

Ki67 is typically used as a marker of cell proliferation and is actively expressed when cells are in the active stages of the cell cycle (G(1), S, G(2) and mitosis), and is absent when cells are in the rest phase G(0) [318]. Clinically, Ki67 is also a commonly used diagnostic marker in tumour detection, as it is commonly associated with tumour cell proliferation and growth [319]. The Ki67 proliferation index is used to indicate how rapidly a tumour is dividing, with a higher number of Ki67 positive cells indicative of a more aggressive tumour [320]. The data presented herein showed that MCF-7 and MDA-MB-231 cells were stained positive for Ki67 throughout the 14-day culture period (**Figure 5.4**). This showed that both cell lines were actively undergoing cell division within the hydrogel. Moreover, > 80 % of MCF-7 cells stained positive for Ki67 after 1 and 7 days in culture, but only 64.9 %  $\pm$  11.4 % of cells were Ki67 positive after 14 days. This drop in proliferative activity could be attributed to the large size of the MCF-7 spheroids formed by day 14; the growth may have plateaued resulting in growth-arrest and therefore some of the cells stopped proliferating. Cell senescence staining would be useful to determine if growth-arrest occurs within the cell spheroids. The MDA-MB-231 cell line stained highly

for Ki67 across the culture period; the percentage of Ki67 positive cells was much more consistent across the time points as these cells tended not to aggregate.

Previous studies have shown that cell pellets of 90 % and 100 % of MCF-7 and MDA-MB-231 cells respectively stained positively for Ki67 [321]. Positive staining for Ki67 was detected in MCF-7 spheroids encapsulated in h9e peptide hydrogel, although no quantification was carried out [27]. The Ki67 proliferation index of MCF-7 cells cultured on top of Matrigel for 4 days was measured to be 56.7 %, whereas 49.5 % of MDA-MB-231 cells were Ki67 positive [322]. A small proportion of MCF-7 cells encapsulated in bioprinted alginate-gelatin hydrogels were Ki67 positive over a 10-day period (< 20 %), whereas by day 10, ~ 40 % of MDA-MB-231 cells were Ki67 positive [323]. The authors of this study proposed that these Ki67 indexes were similar to that of native breast cancer tissue (10–30 %) [324], although other studies have shown that the Ki67 index of native breast cancer tissue samples can vary from 23.9 % to 50.9 %, dependent upon the stage of breast cancer [325]. The data provided herein showed that PeptiGelAlpha1 could support the proliferation of MCF-7 and MDA-MB-231 cells, and the Ki67 indexes were reduced compared with 2D culture [326], showing that 3D culture in SAPHs is much more physiologically relevant.

### **5.3.2. Organisation of MCF-7 & MDA-MB-231 Cells within PeptiGelAlpha1**

H&E staining and phalloidin staining of F-actin filaments showed that both cell lines behaved very differently within PeptiGelAlpha1; MCF-7 cells tended to aggregate and form large spheroids, whereas MDA-MB-231 cells remained dispersed, with loose clusters formed by day 14 (**Figure 5.5**). In collagen I, MCF-7 cells also formed large spheroids and MDA-MB-231 cells remained dispersed throughout the hydrogel, showing that both cell lines exhibited similar behavioural profiles in both collagen I and PeptiGelAlpha1 (**Figure 5.5**). This shows that a synthetic platform can provoke similar cell behaviour to that of a naturally derived hydrogel.

Quantification of MCF-7 spheroids revealed that after 14 days, MCF-7 cells tended to form larger spheroids with a greater number of cells in PeptiGelAlpha1 than collagen I (**Figure 5.7**). This correlates with the high proliferative activity discussed in **section 5.3.1**. This also shows that PeptiGelAlpha1 can support the long-term formation of MCF-7 spheroids, and that a synthetic platform can support a similar cell organisational profile to that of a naturally derived hydrogel. Spheroids formed by MCF-7 cells have been observed

in other SAPH systems [29,242]; the data in this study therefore support findings in the literature regarding MCF-7 cell behaviour in SAPHs.

Regarding MDA-MB-231 cells, their morphology has been shown to be particularly sensitive to the substrate or material in which the cells are cultured [28]. When cultured in PEG-fibrinogen hydrogels, MDA-MB-231 cells become elongated and stretched, whereas when 2 % PEG diacrylate was added, the cells were rounded in shape [327]. Moreover, F-actin staining of MDA-MB-231 cells showed a rounded morphology in 100 % alginate hydrogels, but elongation occurred when Matrigel was added [169]. The H&E staining and phalloidin staining of F-actin presented in these data showed that MDA-MB-231 cells were rounded in PeptiGelAlpha1, with a mixture of rounded and elongated morphologies within collagen I (**Figure 5.5 & Figure 5.8**). The rounded morphology exhibited in PeptiGelAlpha1 is possibly due to the lack of cell binding ligands and cues available. Therefore, the cells have nothing to attach to and thus cannot reorganise their cytoskeleton accordingly. MCF-7 cells, on the other hand, typically show a rounded morphology, as shown with this study, and thus do not require additional binding ligands [328]. Functionalising PeptiGelAlpha1 with a cell-binding motif such as RGD may be needed for MDA-MB-231 cells to retain their elongated morphology. This has been demonstrated with PEG-4-Thiol hydrogels, whereby MDA-MB-231 cells elongated when the hydrogel was functionalised with RGD or glycine-phenylalanine-hydroxyproline-glycine-glutamate-arginine (GFOGER), derived from collagen [317].

### **5.3.3. Extracellular Matrix Deposition**

Histological staining methods were used to determine if MCF-7 and MDA-MB-231 cells were depositing endogenously produced ECM within the SAPH. Gomori Trichrome staining was used to detect non-specific collagen production, which is stained green/blue. However, the hydrogel was also stained green/blue by the reagents, which made distinguishing collagen deposition from the hydrogel difficult (**Figure 5.9**). For MCF-7 cells, it was suggested that ECM was being produced by the cells, as pericellular ECM was observed surrounding the cells within the hydrogel. For MDA-MB-231 cell-laden sections, it was unclear whether the green staining surrounding the nuclei was ECM production or peptide matrix.

Collagen I immunohistochemical staining was therefore used to confirm that MDA-MB-231 cells were producing collagen, and collagen I was being specifically produced by MCF-7 cells (**Figure 5.10**). Collagen I constitutes the main component of the

breast tumour stroma and plays a large role in tumour progression, therefore its presence *in vitro* is indicative of normal cancer cell function and behaviour [329]. Positive staining for collagen I was observed after days 7 and 14 for MCF-7 cells, showing that PeptiGelAlpha could support ECM production by these cells. For MDA-MB-231 cells, no positive staining was observed for collagen I. A cell pellet control for collagen I was not performed on either cell line, but it is possible that the hydrogel was unable to support ECM production by MDA-MB-231 cells. Collagen I production by MCF-7 cells within the FEFEFKFK SAPH system has been detected previously after 7 days in immunofluorescence imaging, and after 10 days in immunohistochemical imaging [29]. These results support the findings presented in this study. One study performed Gomori Trichrome staining on MDA-MB-231 cells embedded in alginate-Matrigel hydrogels, however, no ECM production was observed [169]. To the author's knowledge, no other studies have investigated ECM production by MDA-MB-231 cells within hydrogel systems.

For other SAPH studies, total collagen production has been detected using a total collagen assay [236,313,330], and specific collagen I production has previously been detected using ELISA [21], reverse transcription-polymerase chain reaction (RT-PCR) [235], immunocytochemistry [29,235,313] and immunohistochemistry [21]. Although histological staining provides initial information on ECM component production as well as spatial context, it is not quantitative and does not provide information on gene expression of ECM components. Molecular techniques, such as RT-PCR and RNA sequencing, would be needed to provide gene expression data of ECM components produced by both cancer cell lines.

#### **5.3.4. Cell-Material Interactions**

To understand and observe how MCF-7 and MDA-MB-231 cells interact with the surrounding hydrogel, TEM imaging was used (**Figure 5.11**). It was revealed that MCF-7 cells appeared to internalise the peptide hydrogel fibres, with cells enveloping the material and vesicles containing hydrogel found within the cells (**Figure 5.12**). This was not observed with MDA-MB-231 cells, although cellular processes were observed to probe the hydrogel, indicative of cell-material interaction. With collagen I, internalisation of the material by either cell line was not observed, nor was any interaction observed. Anchoring of the fibrils to the cells was observed however, which correlates with the material contraction and subsequent high cell density observed, in fluorescence and histological imaging (**Figure 5.5 & 5.8**).

From the literature, peptide hydrogel entrapment by cells has been observed previously [216]. The authors found that MC3T3-E1 cells engulfed peptide amphiphilic hydrogel KGE as revealed by TEM imaging [216]. It was proposed that the cells were metabolising the fibres as a source of nutrients; follow up experiments found that lactate production was increased and glucose concentration was decreased in the supernatant of cell-laden samples compared with acellular samples. This suggests that these cells were metabolising the fibres as a source of nutrients [216]. Cancer cells *in vivo* typically scavenge the surrounding ECM and other cell types as a source of amino acids and glucose, to support the high metabolic demands of the tumour [331]. Another study found that macrophages internalised rhodamine labelled amphiphilic SAPH fibres which were located within the cytoplasm and lysosomes [332]. This occurred at both 37 °C and 4 °C and the process of internalising fibres in that study was shown to be passive and energy independent.

It is unclear why this phenomenon was occurring in MCF-7 cells alone in this current study. It may be due to the large spheroids formed, which may require additional glucose and amino acids than dispersed cells [333]. This event also may not have occurred with the collagen I hydrogel because the fibres were too large to engulf. As shown in **Table 4.2**, collagen I fibres measured  $12.0 \text{ nm} \pm 3.9 \text{ nm}$  in diameter, whilst PeptiGelAlpha1 fibres measured  $5.7 \text{ nm} \pm 1.4 \text{ nm}$ . This event has not been observed with cancer cells before, and therefore proposes a novel method to deliver anti-cancer drugs into cancer cells *in vitro*.

To further support these data, the mechanical properties of MCF-7 and MDA-MB-231 cell-laden and acellular SAPH samples were measured over time (**Figure 5.13**). Acellular PeptiGelAlpha1 was found to soften significantly over the 14-day culture period. This has previously been shown in other studies, whereby acellular PeptiGelAlpha1 weakened over time [23]. This could be due to frequent media washes removing peptide monomer from the hydrogel, therefore weakening the mechanical properties. With MCF-7 cells incorporated, softening of the hydrogel was accelerated and the hydrogels had almost completely degraded by day 14. Whereas with MDA-MB-231 cells, there was no overall change in mechanical properties from day 1 to day 14. Other studies investigating the mechanical properties of cell-laden SAPHs have produced mixed results, depending upon the cell type used. Bovine nucleus pulposus cell-laden FEFEFKFK SAPH samples were shown to weaken mechanically over a 14-day culture period, although a comparison with acellular samples was not carried out [235]. Conversely, chondrocyte-laden FEFEFKFK samples became stiffer over a 21-day culture period in another study [236]. Again, an acellular control was not included. Furthermore, after 28 days in culture, the G' of

synoviocyte-laden PeptiGelAlpha4 was observed to increase when compared with day 1 [22]. The cell type and SAPH used will collectively determine the fate of the hydrogel's mechanical properties in culture. The internalisation of the hydrogel fibres by MCF-7 cells could explain the reduced mechanical properties observed with this cell line in this current study.

MMP-2 ELISA data also corroborated these findings, as an increase in MMP-2 production was observed in cell culture supernatant from MCF-7 cell-laden PeptiGelAlpha1 samples between days 1 and 7, before declining slightly by day 14 (**Figure 5.14**). ELISA assays are highly sensitive and specific, ensuring that specific antigen-antibody reactions are occurring and that the antibody is not binding to non-specific proteins [334].

PeptiGelAlpha1 does not inherently contain any MMP-degradable cleavage sites, often incorporated when designing hydrogels to induce matrix remodelling and cell growth [335]. The increased production of MMP-2 suggests that the MCF-7 cells were actively remodelling the matrix and degrading the material. The localisation of peptide material within vesicles in the cells, as shown in **Figure 5.12**, could potentially be degraded hydrogel. MMP-2 production analysis was not carried out on MDA-MB-231 samples due to time constraints, but would be useful to perform to observe if there is a difference in MMP-2 production by the two cell lines. An MMP inhibitor was not included in the experiment as a negative control; inhibiting MMP activity would be useful to establish if internalisation of the hydrogel was determined by MMP activity. Previous studies using collagen I and Matrigel for ovarian cancer have shown that invasion of collagen I is MMP-dependent [336]. These data therefore support the notion that MCF-7 cells were remodelling PeptiGelAlpha1 via proteolytic degradation and internalisation.

### **5.3.5. Hypoxia Development**

Optimisation of the fluorescence-based hypoxia probe was achieved using a physiologically induced hypoxic control (< 5 % (v/v) O<sub>2</sub>) (**Figure 5.15**). An acellular control confirmed that PeptiGelAlpha1 did not interfere with the detection process. CoCl<sub>2</sub> is typically used as an inducer of hypoxia as it activates HIF1 $\alpha$  [337] and therefore is used as a reliable positive control for hypoxia experiments. However, chemical induction of hypoxia with CoCl<sub>2</sub> was not compatible with the fluorescence probe used in this study.

Fluorescence-based imaging showed that both MCF-7 and MDA-MB-231 cells became hypoxic within PeptiGelAlpha1 over a 14-day period, with a significant increase in the number of hypoxic cells in both cell lines, and a significant increase in percentage area

which was hypoxic with MCF-7 cells (**Figure 5.16**). The significant increase in hypoxic percentage area in MCF-7 cells was due to the spheroids formed by the cells, in which hypoxia could have been present in the centre of the spheroids. The hypoxic cells observed after 1 day of culture were observed on the periphery of the hydrogel; this could be due to variation in oxygen and glucose concentration and diffusion between the centre and periphery of the hydrogel/insert. *In vivo*, hypoxia typically occurs within the centre of the tumour, due to outgrowth of the oxygen diffusion limit. These data show that hypoxia did not occur within the centre of the cell-laden hydrogel, like *in vivo*, but instead by day 14, hypoxic cells were observed to be dispersed throughout the hydrogel in both cell lines. HIF1 $\alpha$  staining of both cell lines within the hydrogel also confirmed that the cells were becoming hypoxic over time (**Figure 5.17**).

In a study investigating MDA-MB-231 cells cultured in collagen I hydrogels, positive staining was observed for HIF1 $\alpha$  after 1 and 5 days in culture, particularly within the clusters formed, and quantitative RT-PCR confirmed that HIF1 $\alpha$  expression increased after 5 days in culture [280]. It is noted, however, that the hypoxic cells were only observed at the borders of the hydrogel, suggesting that hypoxia developed due to the variation in oxygen concentration in that study [280]. The majority of studies developing *in vitro* models of cancer and investigating hypoxia have artificially induced hypoxia to investigate the subsequent effect on cell behaviour and hallmarks of cancer [176,338], whereas very few have studied the spontaneous development of hypoxia in cancer cells within hydrogels [280]. One study investigating the impact of hypoxia discovered that when cultured in a hypoxic environment, MDA-MB-231 cells increased their extravasation potential when cultured within pre-formed HUVEC channels compared with normoxia [338]. Another study showed that MDA-MB-231 cells achieved optimal proliferation and invasion into the surrounding collagen I/Matrigel matrix under hypoxic conditions [176]. Clearly, culturing tumour cell-laden hydrogels in a hypoxic environment augments important features of cancer.

The observation of spontaneous and naturally occurring hypoxia in this study may be due to the hydrogel thickness; it has been shown that varying the hydrogel thickness results in changes in oxygen concentration and thus a change in oxygen gradient [339]. Another study has shown that an increased hydrogel thickness resulted in decreased dissolved oxygen concentrations, with hydrogels with thicknesses of  $> 2.5$  mm resulted in  $< 5$  % oxygen [340]. The thickness of hydrogel used in these data was not directly measured. However, considering a volume of 100  $\mu$ L hydrogel was used within a cell culture insert

with a surface area of 0.33 cm<sup>2</sup>, it is estimated that the hydrogel thickness used was ~ 2–3 mm. It is therefore possible that the cells were becoming hypoxic due to a lack of oxygen diffusion through the hydrogel. Oxygen consumption/concentration was not directly measured in this study, but it would be useful to determine how the oxygen concentration varies within different regions of the hydrogel. Culturing acellular alginate hydrogels with pimonidazole hydrochloride has previously been used to detect hypoxic regions [178].

### 5.3.6. Epithelial to Mesenchymal Transition

Immunohistochemical staining was used to determine if MCF-7 and MDA-MB-231 cells were undergoing EMT, or if their EMT profile was changing throughout their culture in PeptiGelAlpha1 (**Figure 5.18 & 5.19**). Epithelial markers E-cadherin and pan cytokeratin were chosen alongside mesenchymal markers vimentin and N-cadherin. These proteins were chosen as representative markers of the EMT process due to their respective presence in epithelial and mesenchymal cancer cells and relative change in expression during EMT [341]. As discussed in **section 2.2.4**, cancer cells undergo EMT in response to environmental cues, one of which is ECM stiffness [342]. It is possible that the stiffness of PeptiGelAlpha1, measured to be 12.7 kPa (**Figure 4.15B**), could have induced EMT in MCF-7 and MDA-MB-231 cells. As MDA-MB-231 cells typically exhibit high metastatic potential, it is possible that this cell line would be more likely to undergo EMT via stimulation by the matrix stiffness and hypoxia observed. Spontaneous EMT has been demonstrated in a study using MDA-MB-231 cells cultured within a gelatin methacrylamide and PLG fibre hydrogel-composite, whereby upregulation of mesenchymal markers vimentin, N-cadherin and fibronectin and downregulation of epithelial marker E-cadherin were observed. [343]. Another known stimulus for EMT is hypoxia [344]; as discussed in **section 5.3.5**, MCF-7 and MDA-MB-231 cells were becoming hypoxic within the hydrogel. Previous studies have shown that when cultured in a hypoxic environment within gelatin methacrylate hydrogels, cancer cells displayed decreased E-cadherin and increased vimentin expression, compared with normoxia [345].

Due to the stiffness of the hydrogel used and hypoxia occurring in both cell lines, it was expected that the cells would undergo EMT within PeptiGelAlpha1. For this study, however, staining alone was not sufficient to determine if both cell lines were becoming more mesenchymal-like within the hydrogel. Positive staining for E-cadherin and pan cytokeratin was observed in MCF-7 cells throughout the culture duration, confirming that PeptiGelAlpha1 could maintain the epithelial phenotype of this cell line (**Figure 5.18**). Weak positive staining for N-cadherin was observed, and was also present for vimentin.



Positive staining for vimentin was also observed in the cell pellet control (**Appendix 4**). Vimentin is not normally detected in MCF-7 cells in Western Blotting studies [346], however, it can be detected in paraffin wax-embedded epithelial tumour cells following antigen retrieval [347]. The weak positive staining for N-cadherin is not sufficient to confidently determine that MCF-7 cells were undergoing EMT and becoming more mesenchymal-like. For the MDA-MB-231 cells, positive staining for vimentin was observed, indicative of their high metastatic potential, but not N-cadherin (**Figure 5.19**). Positive staining for N-cadherin was not detected in the cell pellet control either (**Appendix 4**). EMT is a plastic process, which can occur only in a subpopulation of cancer cells. Therefore, it is possible that only some cells within the hydrogel were undergoing partial or full EMT. However, although it could not be determined if the cells were undergoing EMT, it was shown that both cell lines retained their phenotypes within the hydrogel. This supports the hypothesis that PeptiGelAlpha1 could maintain the phenotype of MCF-7 and MDA-MB-231 cells.

Molecular techniques such as Western Blotting and gene expression of EMT markers would be required to determine if EMT markers are upregulated or downregulated at the gene level within the hydrogel. TGF $\beta$  can be used as an artificial inducer of EMT *in vitro*, in order to study the EMT process and underlying molecular events within a synthetic system [348]. Further work using TGF $\beta$  and MCF-7 and MDA-MB-231 cells within PeptiGelAlpha1 would be useful to determine the EMT profile of the encapsulated cells.

### **5.3.7. Invasive Potential of MCF-7 & MDA-MB-231 Cells in PeptiGelAlpha1**

After having undergone EMT, metastasis begins by invasion of cancer cells into the surrounding tissue, by traversing the basement membrane and migrating towards blood vessels to be transported to other tissues or organs [349]. Modelling cancer cell invasion *in vitro* commonly involves the transwell migration assay and the embedded spheroid assay [350,351]. Both of these assays utilise cells responding and migrating towards a chemoattractant through a solid matrix. Although both assays provide important data regarding the invasive potential of migrating cancer cells, they are oversimplified in regards to the complex events involved in invasion *in vivo*.

To overcome the issues with the aforementioned assays, cancer cell-laden SAPH samples were embedded within collagen I or Matrigel to observe if the cells would degrade the SAPH and invade either material, to model cancer cell invasion *in vitro* (**Figure 5.21**). It was planned for the samples to be cultured for 28 days in total, but the Matrigel matrix

began to degrade by day 21, which was therefore used as the final time point. MCF-7 cells were observed to invade both collagen I and Matrigel, as shown by processes extending into the material. MCF-7 cell invasion was more prominent in collagen I than Matrigel, which has been shown previously with primary human breast tumour cells [352]. On the other hand, MDA-MB-231 cells exhibited limited invasive potential in PeptiGelAlpha1 compared with MCF-7 cells (**Figure 5.21**). The MDA-MB-231 cell line is typically used to study aggressive and metastatic breast cancer due to its triple negative receptor expression [353] and therefore exhibits high invasive potential. Previous studies investigating the invasive potential of MDA-MB-231 cells in SAPH systems showed that cell migration using the transwell assay was heavily reduced in RADA16, compared with collagen I and Matrigel [28]. It is possible that the lack of cell-binding sites and environmental cues in the SAPH alone results in a loss of malignant phenotype for MDA-MB-231 cells. Therefore, functionalising PeptiGelAlpha1, with cell-binding motifs such as RGD, could restore the invasive phenotype of MDA-MB-231 cells. MDA-MB-231 cells cultured in PEG-tetra-thiol hydrogels functionalised with RGDS peptide were found to be more elongated, compared with non-functionalised hydrogels [317]. The elongated morphology of the MDA-MB-231 cell line is related to the invasive potential of the cell line [169]. The rounded morphology of MDA-MB-231 cells in PeptiGelAlpha1 correlates with the lack of invasion observed (**Figure 5.6**). It is therefore suggested that PeptiGelAlpha1 alone may be more suitable for the study of early stages of breast cancer, with cell lines such as the MCF-7 cell line.

One factor to also consider is whether a non-cancerous cell line, such as the 3T3 fibroblast cell line, would also display invasive behaviour when used in this assay. Due to time constraints, this was not carried out, but would serve as a suitable control to optimise this assay. Furthermore, this assay could have been improved further by incorporating a stromal cell type into collagen I/Matrigel, such as fibroblasts or HUVECs and MSCs.

### **5.3.8. Cell Response to Anti-Cancer Drugs in PeptiGelAlpha1**

One of the main aims of the TME is to provide physical and chemical barriers preventing anti-cancer drugs from reaching the tumour cells. **Section 4.2.8** showed how doxorubicin diffusion was decreased in PeptiGelAlpha1. The efficacies of doxorubicin and tamoxifen were tested on MCF-7 and MDA-MB-231 cells encapsulated in PeptiGelAlpha1, compared with TCP after 24 and 48 hours exposure. Both MCF-7 and MDA-MB-231 cells in PeptiGelAlpha1 appeared to be resistant to tamoxifen treatment after 24 hours and 48 hours, compared with TCP. However, no significant difference in viability was

observed between cells cultured in PeptiGelAlpha1 and on TCP when treated with doxorubicin.

Tamoxifen works by inducing apoptosis of breast cancer cells via targeting the oestrogen receptor, which the MCF-7 cell line expresses [354]. Tamoxifen should therefore be effective in inhibiting proliferation of MCF-7 cells. When cultured on TCP, cell viability was reduced after 48 hours for 100  $\mu$ M tamoxifen, and after 24 hours for 500  $\mu$ M tamoxifen, compared with no treatment. When cultured in PeptiGelAlpha1, no difference was observed in viability between tamoxifen treated cells, and those that received no treatment. PeptiGelAlpha1 therefore acted as a barrier to tamoxifen treatment. The MDA-MB-231 cell line represents TNBC, due to the absence of the ER, PR and HER2 [25]. Therefore, it is unlikely to respond to tamoxifen treatment. These data showed that tamoxifen treatment did affect the viability of MDA-MB-231 cells on TCP, as > 50 % of cells were viable compared with untreated cells. Recent data have shown that tamoxifen can act independently of the ER and target MDA-MB-231 cells, via reversal of EMT [355]. This increases their sensitivity to chemotherapeutic drugs, explaining the decreased viability presented in this study. Encapsulation in PeptiGelAlpha1 did increase cell viability compared with 2D culture, showing that 3D culture in the SAPH can recapitulate hindered efficacy of some anti-cancer drugs.

However, no significant difference in viability was observed between cells cultured in PeptiGelAlpha1, and those on TCP when treated with doxorubicin, showing that PeptiGelAlpha1 offered no protection to doxorubicin treatment. Doxorubicin works by intercalating DNA and generating free radicals in cells, resulting in DNA and cellular damage [356]. As shown in **section 4.2.8**, doxorubicin diffusion was hindered throughout the hydrogel, with pockets of the drug being observed. The drug may be binding to the hydrogel, resulting in increased cytotoxicity in those specific regions. Due to time constraints, only one concentration of doxorubicin was tested on samples (100  $\mu$ M) and it is therefore possible that this was too potent. This concentration was chosen as it is more similar to treatment observed *in vivo* [357].

Dose-response curves were utilised to further investigate the efficacy of tamoxifen and doxorubicin in cells cultured in 2D and 3D (**Figure 5.27**). Due to time constraints, this experiment could only be carried out once and therefore would need repeating to provide conclusive evidence. Sigmoidal responses to increasing drug concentration were observed for 2D cultured MCF-7 and MDA-MB-231 cells for both tamoxifen and doxorubicin treatment, by which cell viability was unchanged at low concentrations, followed by a

decline as drug concentration increased, before plateauing at the highest concentrations. This dose-response relationship is typically observed in biological systems [358]. For cells cultured in 3D, the variability in data resulted in challenges fitting the data, particularly for MCF-7 cells treated with tamoxifen (**Figure 5.27D**).  $IC_{50}$  values were then calculated based on the dose-response data.  $IC_{50}$  estimates can be provided as relative or absolute values. The relative  $IC_{50}$  value is the concentration corresponding to a response midway between the estimates of the upper and lower plateaus, whilst the absolute  $IC_{50}$  value is the response corresponding to the 50 % control, related to the 0 % and 100 % assay controls [359]. The  $IC_{50}$  values calculated in this study were therefore reported as relative  $IC_{50}$  values. No significant difference could be determined between 2D and 3D cultured MCF-7 and MDA-MB-231 cells treated with doxorubicin, or for MCF-7 cells treated with tamoxifen. This is possibly due to the variability in 3D data, but more repeats will be needed to confirm this. However, a significant increase in the  $IC_{50}$  for MDA-MB-231 cells treated with tamoxifen was observed. This provides further proof that PeptiGelAlpha1 can act as a physical barrier to tamoxifen treatment. These data also support the notion that PeptiGelAlpha1 could not act as a barrier to doxorubicin treatment. Nonetheless, it must be noted that a single  $IC_{50}$  value for a compound is not sufficient to determine a drug's efficacy; more experimental repeats are needed to compare a range of  $IC_{50}$  values.

**Table 2.4** summarises the studies using SAPHs for *in vitro* cancer modelling, several of which have been investigated for anti-cancer drug efficacy profiling. Several studies have shown that the SAPH provides resistance to anti-cancer drugs [30,232,238], whilst others have shown increased sensitivity [32,240]. The chemotherapeutic drug in question, as well as the SAPH used, will determine the efficacy of the drug. Tamoxifen and doxorubicin have not been studied using SAPH systems previously, but the data presented in this study suggest that PeptiGelAlpha1 can offer protection from tamoxifen, but not doxorubicin.

## 5.4. Conclusions

Synthetic hydrogels used for *in vitro* modelling of cancer have the advantages of chemical definition and tuneable properties. However, the majority of *in vitro* studies used for cancer modelling (**Table 2.2 & 2.4**) fail to recapitulate key components of solid tumours and the TME. Therefore, they do not truly represent tumour-stroma interactions observed *in vivo*. Studies using SAPHs for *in vitro* modelling of cancer have not examined EMT status, cell-material interactions and hypoxia, such as in this study.

The results in Chapter 4 demonstrated that PeptiGelAlpha1 was composed of entangled nanofibres mimicking the ECM, had superior mechanical properties to collagen I and Matrigel, and was able to more faithfully mimic the stiffness of breast cancer tissue compared with the aforementioned hydrogels. It was also shown that PeptiGelAlpha1 acted as a physical barrier to doxorubicin diffusion and supported the viability of MCF-7 breast cancer cells. These findings therefore provided preliminary evidence that PeptiGelAlpha1 could act as a suitable platform, for modelling breast cancer *in vitro*.

This chapter aimed to determine if PeptiGelAlpha1 was suitable for the growth of MCF-7 and MDA-MB-231 breast cancer cells, and if the hydrogel maintained the viability and phenotype of both cell lines. Key features of solid tumours, such as hypoxia, invasion and ECM deposition, were investigated as well as the response of cells to anti-cancer drugs within the hydrogel.

In summary:

- PeptiGelAlpha1 was able to support the viability and proliferation of both MCF-7 and MDA-MB-231 cells.
- ECM deposition was observed in MCF-7 cells, but not MDA-MB-231 cells. MCF-7 cells organised themselves into large spheroids, whereas MDA-MB-231 cells remained dispersed.
- MCF-7 cells were observed to produce and deposit collagen I within the material, which was not observed with MDA-MB-231 cells.
- MCF-7 cells were observed to internalise the peptide hydrogel, which correlated with a decrease in mechanical properties and an increase in MMP-2 production.
- Both cell lines became hypoxic within the hydrogel.
- The hydrogel was able to maintain the phenotype of both cell lines, but the EMT status of the cells did not appear to change.

- MCF-7 cells successfully invaded collagen I and Matrigel from PeptiGelAlpha1. PeptiGelAlpha1 acted as a barrier to tamoxifen treatment, but not doxorubicin treatment.
- These findings show that PeptiGelAlpha1 could be a suitable platform for modelling of early breast cancer, such as using the MCF-7 cell line.

The formation of cell clusters by the MCF-7 cells, alongside ECM deposition and matrix remodelling, are consistent with stages of early breast cancer development. Whereas the distribution and migration of MDA-MB-231 cells through the hydrogel is concordant with metastatic breast cancer. The increased cell invasion of MCF-7 cells suggests that the cells were becoming more invasive and tumorigenic within PeptiGelAlpha1, suggestive of cancer progression.

Several points highlight the novelty of the work in this chapter. MCF-7 and MDA-MB-231 cells have not previously been used for 3D culture with PeptiGelAlpha1, and these data show that the material can support the viability and growth of both cell lines. Features of solid tumours such as hypoxia and cell invasion were also observed. MCF-7 cells within PeptiGelAlpha1 were observed to have a similar organisation profile to that of collagen I, showing that a synthetic platform can provoke similar cell behaviour to that of a natural hydrogel. Moreover, MCF-7 cells were observed to internalise the peptide hydrogel, which has not previously been shown with cancer cells and is thus demonstrated for the first time. This reveals a potential drug delivery method *in vitro* and *in vivo*. This could be achieved by exposing the cancer cells to drug-laden hydrogel and observing if the cells would internalise the laden hydrogel, and by injecting drug-laden PeptiGelAlpha1 into xenograft models of cancer. Preliminary data also suggested that the material provided resistance to tamoxifen treatment, which has not been observed before with this hydrogel.

Next steps involve investigating PeptiGelAlpha1 for culturing additional cell types to further mimic the stromal component of solid tumours, which will be investigated in **Chapter 6**.

# CHAPTER 6 – Stimulating Vasculature Formation by HUVECs and MSCs within Self-Assembling Peptide Hydrogels

## 6.1. Introduction

Inducing angiogenesis is one of the main hallmarks of cancer, due to its importance in tumour expansion and metastasis, thus augmenting disease progression [11]. The inclusion of vasculature *in vitro* when modelling solid tumours enables further replication of the TME, allowing tumour-stroma interactions to be mimicked and provides a potential barrier to chemotherapeutic drugs *in vitro*.

Tissue engineering blood vessel-like structures *in vitro* has been achieved using multiple strategies [360,361]. In this work, co-culture of HUVECs and MSCs were used to create tube-like structures, as this has been achieved successfully using collagen I hydrogels [26,243,252].

HUVECs are sensitive to the environment in which they are cultured, and consequently, tube formation by HUVECs is a delicate and multi-faceted process [362]. In order to form tube-like structures, ECs adhere to and break down the matrix by upregulation of MMPs, then sprout towards the angiogenic stimulus, followed by proliferation and migration towards the gradient [58,59]. The cells consequently reassemble and form intercellular contacts forming a lumen [58,59]. Accessory cells added such as pericytes stabilise the tubes formed by providing structural support.

SAPHs are synthetic by design and as such, do not inherently contain any binding sites or domains for cell attachment and reorganisation. Fine-tuning of the material is therefore required in order to guide and stimulate HUVECs to form vessel-like structures.

The goal of this 3D model is to create a tri-culture system of breast cancer cells, HUVECs and MSCs, to recapitulate vascularised breast tumour *in vitro* using a SAPH system. The focus of this Chapter is to investigate if a SAPH system can support vasculogenesis of HUVECs and MSCs *in vitro*, and what modifications are necessary to achieve this.

Modifications to PeptiGelAlpha1 (the SAPH used in Chapters 4 and 5) were investigated to observe how this affected behaviour of HUVECs and MSCs. Enrichment with laminin was used to determine if the IKVAV and YIGSR motifs found within the protein would provide HUVECs with binding sites to attach. The hydrophobicity of the SAPH was used to investigate if cells would prefer a more hydrophilic sequence. Functionalisation with

increasing concentrations of RGD was used to determine if an ECM derived binding motif could influence HUVEC and MSC morphology and behaviour in PeptiGelAlpha1.

HUVECs and MSCs were transduced using a lentiviral vector with RFP and GFP respectively to enable live-cell imaging. This was undertaken by Jekaterina Maksimcuka and the data collected were included in her thesis (2019) [363]. However, the transduction efficiency and GFP-MSC tri-lineage differentiation data have been included in **Appendix 8 and 9** respectively for reference.

The aims of this chapter are as follows:

- 1. To observe if conditioned media collected from cancer cells promotes the tube formation of HUVECs, via production of pro-angiogenic molecules such as VEGF.**
- 2. To observe if enrichment of SAPHs with ECM-derived laminin positively affects the tube formation of HUVECs.**
- 3. To observe if the hydrophobicity of SAPHs affects HUVEC behaviour.**
- 4. To observe how the cell-binding domain RGD affects HUVEC and MSC morphology, proliferation and phenotype.**
- 5. To observe if co-culture with cancer cells positively influences HUVEC and MSC morphology.**
- 6. To observe if RGD functionalisation affects the physical properties of PeptiGelAlpha1.**



## 6.2. Results

### 6.2.1. Effect of Cancer Cell Conditioned Media on HUVEC Tube Formation

HUVECs were exposed to conditioned media collected from MCF-7 cancer cells cultured in different platforms to observe if this would enhance angiogenesis compared with the positive control. The platforms used include: 2D monolayer culture, 3D suspension culture and 3D encapsulation in PeptiGelAlpha1, as well as cell culture media types of ECGM-2 and a 50:50 mixture of DMEM and ECGM-2. DMEM was not used on its own, as it was not able to support the tube formation of HUVECs (**Appendix 10**). This experiment was performed as a preliminary study to observe if a cancer cell conditioned media would positively influence the tube formation of HUVECs, prior to culture within PeptiGelAlpha1. The Angiogenesis Analyzer plugin on ImageJ was used to analyse and quantify fluorescent images of HUVECs [364], and the number of nodes, number of branches and total tube length were chosen as features of angiogenesis. The positive control was fully supplemented ECGM-2 and the negative control was fully supplemented ECGM-2 treated with 30  $\mu$ M suramin, an inhibitor of angiogenesis.

The images acquired are depicted in **Figure 6.1**. With the positive control, the HUVECs were observed to form an interconnected network of tubes, resembling blood vessels. The addition of 30  $\mu$ M suramin impeded the ability of HUVECs to form tubes, as shown by the absence of a network. The conditioned media types tested were also able to stimulate the reassembly of HUVECs into tubes. Compared with the positive control, there did not appear to be any changes in the gross morphology and network of HUVEC formed tubes. Quantification of the images was carried out (**Figure 6.2**). The number of nodes and total length of HUVEC formed tubes were significantly lower in the negative control when compared with the positive control ( $p < 0.0001$ ; **Figure 6.2A & B**). No significant difference was observed between the positive control and negative control in the number of branches ( $p > 0.05$ ; **Figure 6.2C**). Compared with the positive control, there was no significant difference with any of the conditioned media types in the number of nodes, number of branches or total tube length in HUVEC formed tubes ( $p > 0.05$ ).

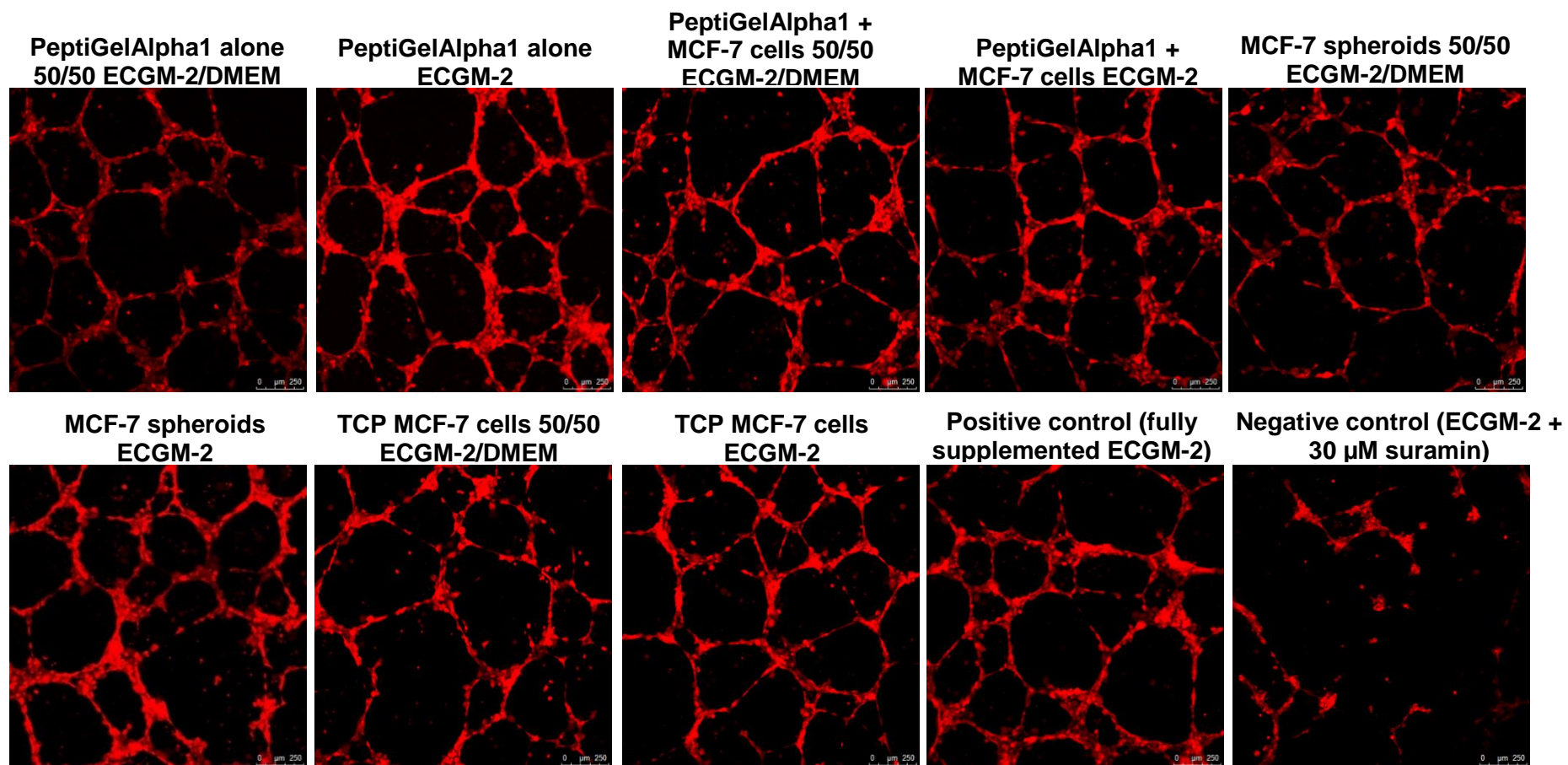


**Figure 6.1. Tube formation of HUVECs on Matrigel using conditioned media from MCF-7 cells.** Cell culture media was collected from MCF-7 cells cultured as spheroids in 96 well round bottomed plates in DMEM/ECGM-2, in PeptiGelAlpha1 in DMEM/ECGM-2 and TCP in DMEM/ECGM-2 for 4 days. PeptiGelAlpha1 was cultured in DMEM/ECGM-2 for 4 days without cells as a material control. RFP-HUVECs were cultured without FBS overnight and seeded onto 10 mg/mL Matrigel using each conditioned media type. A positive control of fully supplemented ECGM-2 and a negative control of ECGM-2 with 30  $\mu$ M suramin were used. Cells were incubated for 18 hours before fixation. Caption refers to conditioned media type used. Red = HUVECs. N = 1.

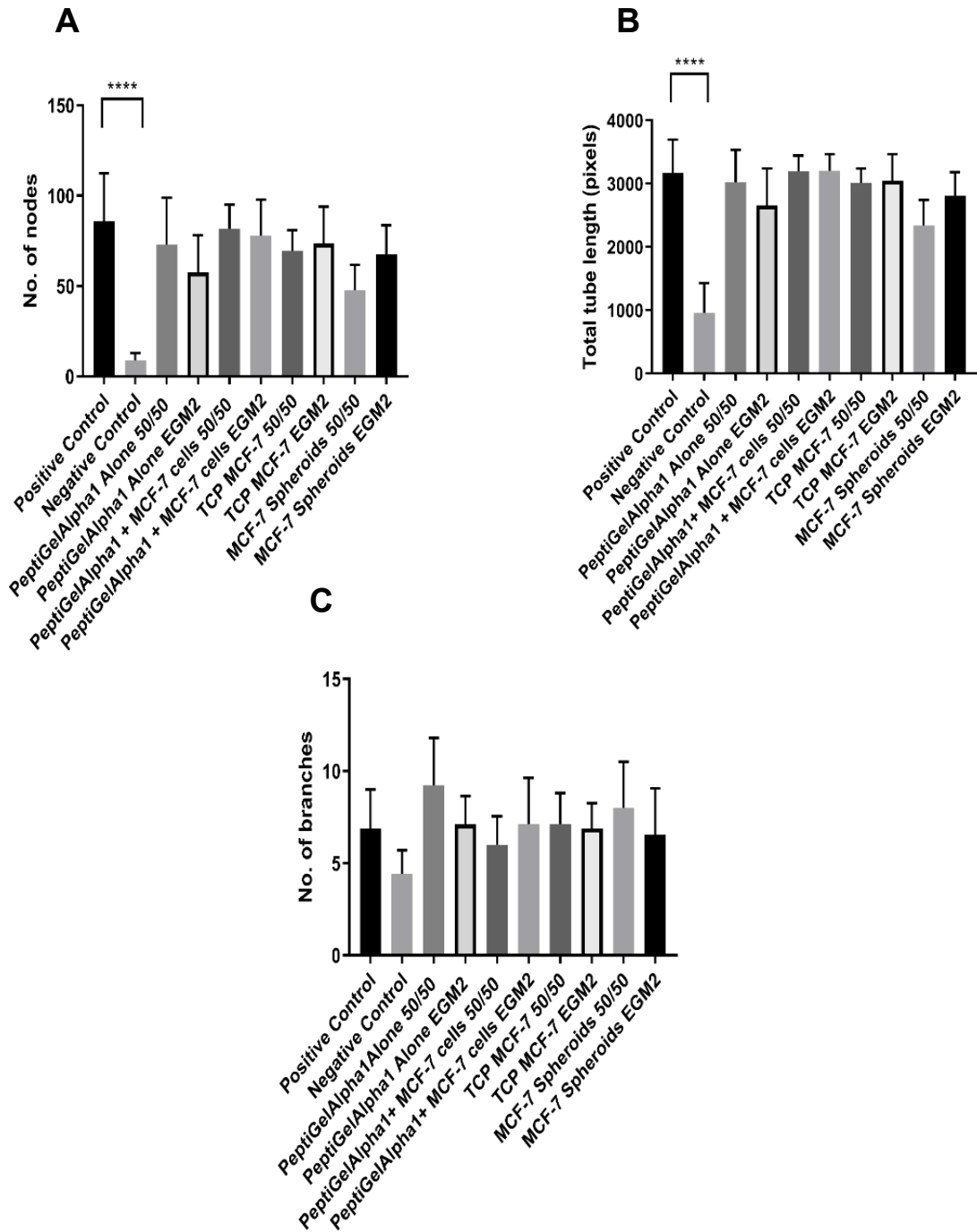


**Figure 6.2. Quantification of tube formation of HUVECs on Matrigel using conditioned media from MCF-7 cells.** (A) Number of nodes. (B) Total tube length (pixels). (C) Number of branches. Cells were incubated for 18 hours before fixation and subsequent imaging and analysis. \*\*\*\* =  $p < 0.0001$  using one-way ANOVA and post-hoc Tukey's test. Data are mean  $\pm$  S.D. N = 1.

All subsequent experiments in this chapter use ECGM-2 media for cell cultures.

### 6.2.2. Effect of Laminin Enrichment and Hydrophobicity of SAPHs on HUVEC Behaviour

Prior to 3D culture within PeptiGelAlpha1, RFP-HUVECs were cultured on top of the hydrogel initially to observe how these cells would respond to a peptide matrix environment. The effect of enriching PeptiGelAlpha1 with laminin was studied, alongside using a valine-based SAPH, V8, which is less hydrophobic than PeptiGelAlpha1. Enrichment of PeptiGelAlpha1 and V8 with the ECM protein laminin was used due to the presence of cell-binding domains RGD and YIGSR, which are thought to be responsible for the differentiation of ECs into tube-like structures by inducing cell attachment and cell-cell interactions [365]. Seeding HUVECs on TCP coated with increasing concentrations of laminin revealed that 50  $\mu\text{g/mL}$  was the optimal concentration to use due to high viability (**Appendix 11**) and significantly higher metabolic activity (**Appendix 12**) compared with TCP, 5 and 25  $\mu\text{g/mL}$  laminin. Moreover, this concentration has been used in 3D culture with collagen I hydrogels [366].

RFP-HUVECs were seeded on top of PeptiGelAlpha1  $\pm$  50  $\mu\text{g/mL}$  laminin, V8  $\pm$  50  $\mu\text{g/mL}$  laminin, collagen I + 50  $\mu\text{g/mL}$  laminin, collagen I + 90  $\mu\text{g/mL}$  fibronectin, and TCP (**Figure 6.3**). Cells were imaged over a 72-hour period. At 0 hours, the cells were mostly rounded in morphology with a high density present in all materials. After 72 hours, very few cells were present on PeptiGelAlpha1  $\pm$  laminin, with the cells remaining rounded, showing that the cells were unable to adhere to the matrix. This was also observed with V8  $\pm$  laminin, showing that a reduced hydrophobicity was not able to induce cell attachment. On collagen I + fibronectin, the cells had elongated and organised themselves into tube-like structures. Replacing fibronectin with laminin enhanced elongation and branching, with more cells adhering to the matrix. On TCP, the cells exhibited a typical cobblestone morphology and did not form tube-like structures. HUVEC behaviour was not affected by the addition of laminin to PeptiGelAlpha1, nor reduced hydrophobicity using a valine-based peptide sequence, but did appear to have a positive influence when added to collagen I.

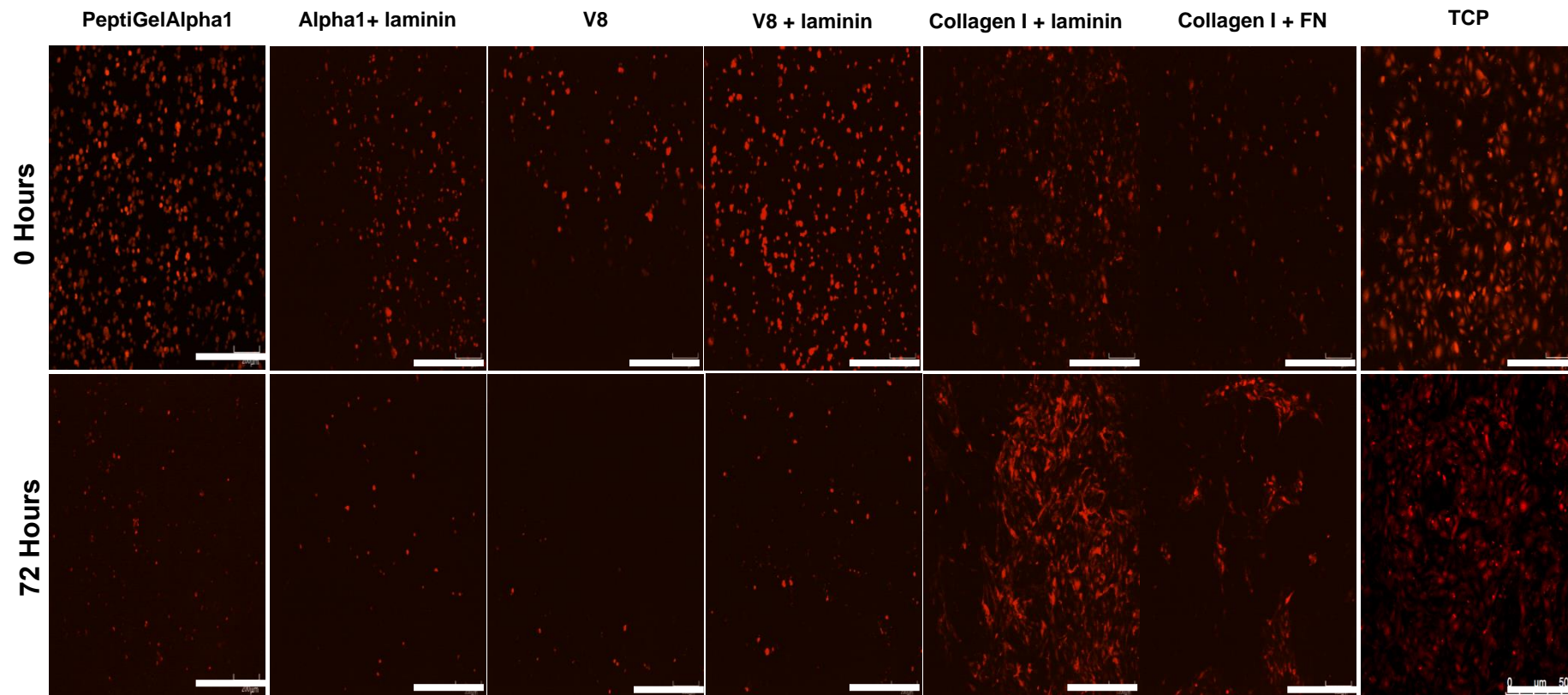


**Figure 6.3. Effect of ECM protein laminin and hydrophobicity of primary amino acid sequence on tube formation of HUVECs.** RFP-HUVECs were seeded on PeptiGelAlpha1  $\pm$  50  $\mu\text{g}/\text{mL}$  laminin, collagen I (1.5  $\text{mg}/\text{mL}$ ) + 50  $\mu\text{g}/\text{mL}$  laminin/90  $\mu\text{g}/\text{mL}$  fibronectin and TCP. Samples were imaged at 0 hours and 72 hours after seeding. Red = RFP-HUVECs. FN = fibronectin. Scale bar = 500  $\mu\text{m}$ . N = 1.

RFP-HUVEC attachment to each of the different substrates was quantified by measuring the percentage area covered after 72 hours in culture (**Figure 6.4**). On PeptiGelAlpha1 alone, there was a significant reduction in HUVECs on the material after 72 hours, from 10.3 %  $\pm$  3.9 % to 2.3 %  $\pm$  1.2 % ( $p < 0.0001$ ). No significant differences in area coverage were observed after 72 hours for cells cultured on PeptiGelAlpha1 + 50  $\mu$ g/mL laminin, V8  $\pm$  50  $\mu$ g/mL laminin or collagen I + 90  $\mu$ g/mL fibronectin ( $p > 0.05$ ). However, there was a significant increase in area coverage, for HUVECs cultured on collagen I + 50  $\mu$ g/mL laminin, from 9.8 %  $\pm$  0.7 % to 24.2 %  $\pm$  1.5 % after 72 hours ( $p < 0.0001$ ). A significant increase of HUVEC coverage was also observed on TCP, from 10.6 %  $\pm$  1.9 % to 23.7 %  $\pm$  2.9 % ( $p < 0.0001$ ).

When comparing HUVEC coverage between the different materials after 72 hours, no significant difference was observed between cells cultured on PeptiGelAlpha1  $\pm$  laminin or V8  $\pm$  laminin ( $p > 0.05$ ). A significant increase in HUVEC coverage was observed with collagen I + 50  $\mu$ g/mL laminin, compared with collagen I + 90  $\mu$ g/mL fibronectin, V8  $\pm$  50  $\mu$ g/mL laminin and PeptiGelAlpha1  $\pm$  50  $\mu$ g/mL laminin ( $p < 0.0001$ ).

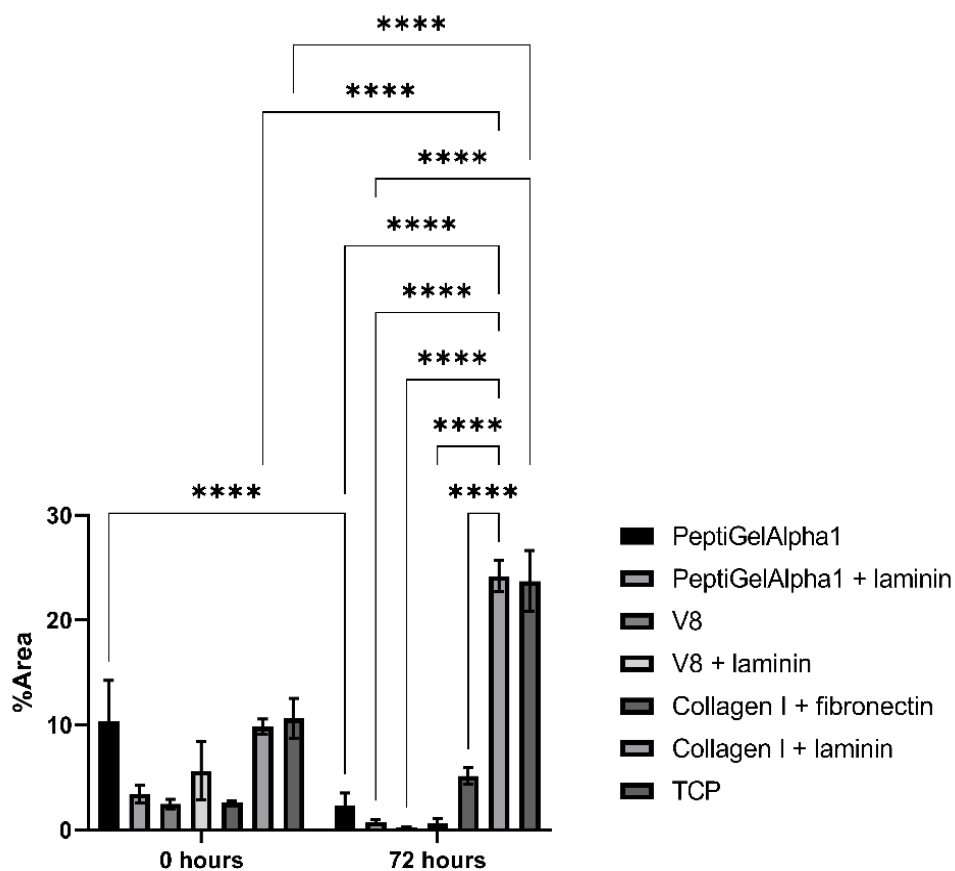


**Figure 6.4. Percentage area quantification of RFP-HUVECs cultured on different substrates.** Data are mean  $\pm$  S.D. \*\*\*\* =  $p < 0.0001$  using two-way ANOVA and post-hoc Tukey's test. N = 1.

### 6.2.3. Effect of RGD Functionalisation on HUVEC and MSC Morphology

RGD is a cell-binding motif originally isolated from the ECM protein fibronectin, and is well known for facilitating cell attachment [367]. PeptiGelAlpha1 functionalised with increasing concentrations of the RGD domain was investigated to observe if the HUVECs and MSCs would bind to the hydrogel via the binding motif and respond accordingly. 0.1, 1 and 10 % RGD were used to observe if low RGD concentrations could stimulate a response from HUVECs and MSCs and if this response was concentration-dependent. Collagen I + 90 µg/mL fibronectin was used as a positive control. Cells were encapsulated within the hydrogels for a 7-day period.

In collagen I + 90 µg/mL fibronectin, the HUVECs were observed to elongate and stretch and MSCs adopted a spindle shape after 1 day in culture (**Figure 6.5**). After 4 days, the HUVECs had organised themselves into tube-like structures. After 7 days, the tube formation by the HUVECs had regressed slightly. Cell density appeared to be high in the collagen I images due to contraction of the material by the cells (**Appendix 13**). In PeptiGelAlpha1 alone, both cell types remained rounded over the 7-day culture period. The addition of 0.1 % RGD did not appear to have any effect on cell behaviour, as both cell types were rounded over the 7 days in culture. With 1 % RGD, both the HUVECs and MSCs appeared to elongate and branch out, suggesting that they were responding to the RGD stimulus. This effect was enhanced when 10 % RGD was used, as by day 4, the MSCs were observed to extend processes into the material and the HUVECs appeared more elongated than the addition of 1 % RGD. These data suggest that the HUVECs and MSCs were positively responding to the RGD stimulus in a concentration-dependent manner.

To observe if the cell-seeding density had an effect on cell behaviour and if tube-like structures were more likely to form via increased cell-to-cell contacts, the cell-seeding density was increased from  $1 \times 10^6$  cells/mL (**Figure 6.5**) to  $2 \times 10^6$  cells/mL (**Figure 6.6**). Cell density appeared higher in all hydrogels used. In PeptiGelAlpha1 alone, both cell types remained rounded in morphology, with some spontaneous stretching of the MSCs observed after 7 days. Compared with the original cell-seeding density ( $1 \times 10^6$  cells/mL; **Figure 6.5**), there appeared to be no difference in HUVEC or MSC morphology with any of the RGD concentrations.



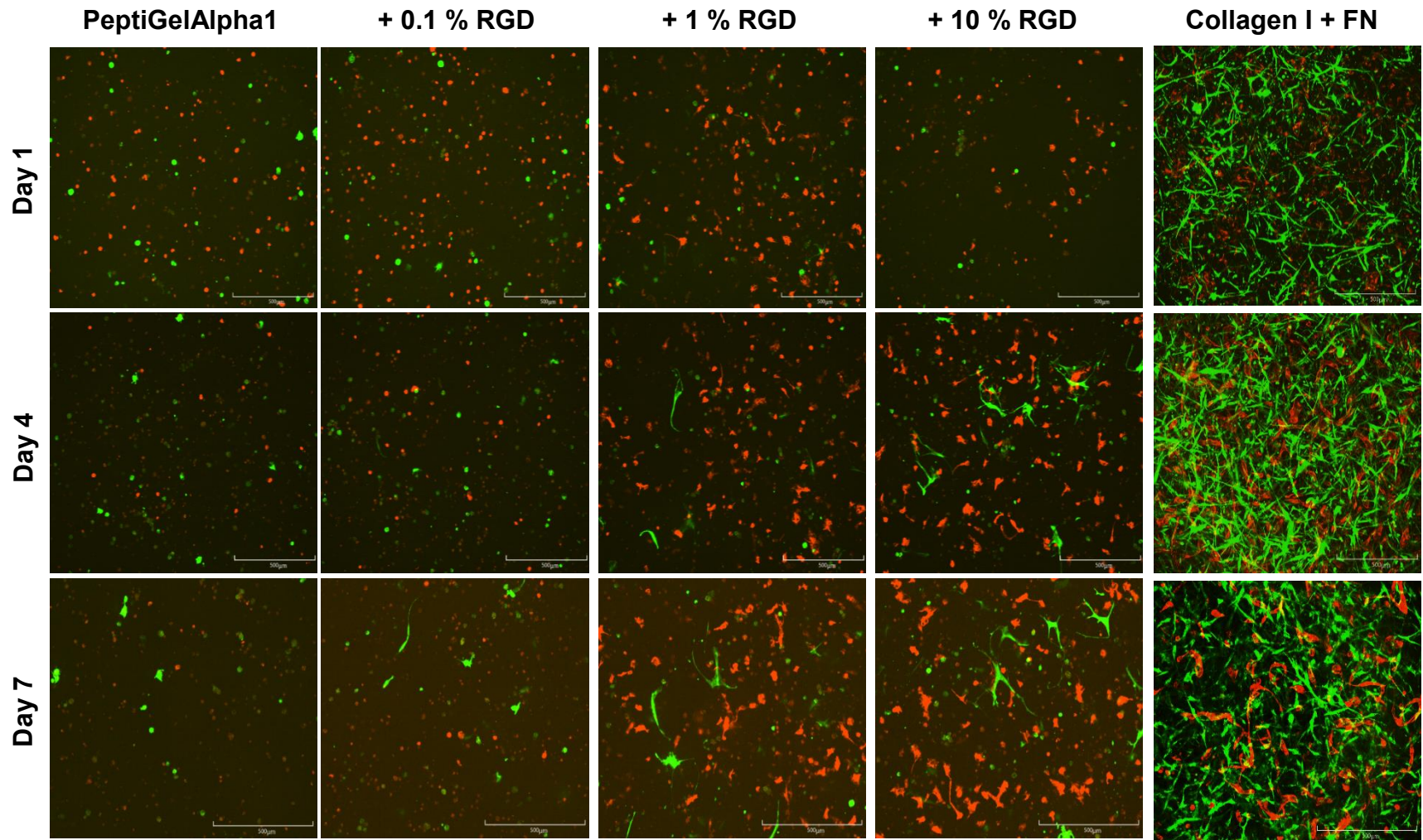


**Figure 6.5. Effect of cell-binding motif RGD on HUVEC and MSC behaviour.** RFP-HUVECs and GFP-MSCs were encapsulated within PeptiGelAlpha1  $\pm$  0.1 %, 1 % and 10 % RGD at a density of  $1 \times 10^6$  cells/mL (4:1 HUVEC:MSC ratio). Red = HUVECs. Green = MSCs. N = 2.



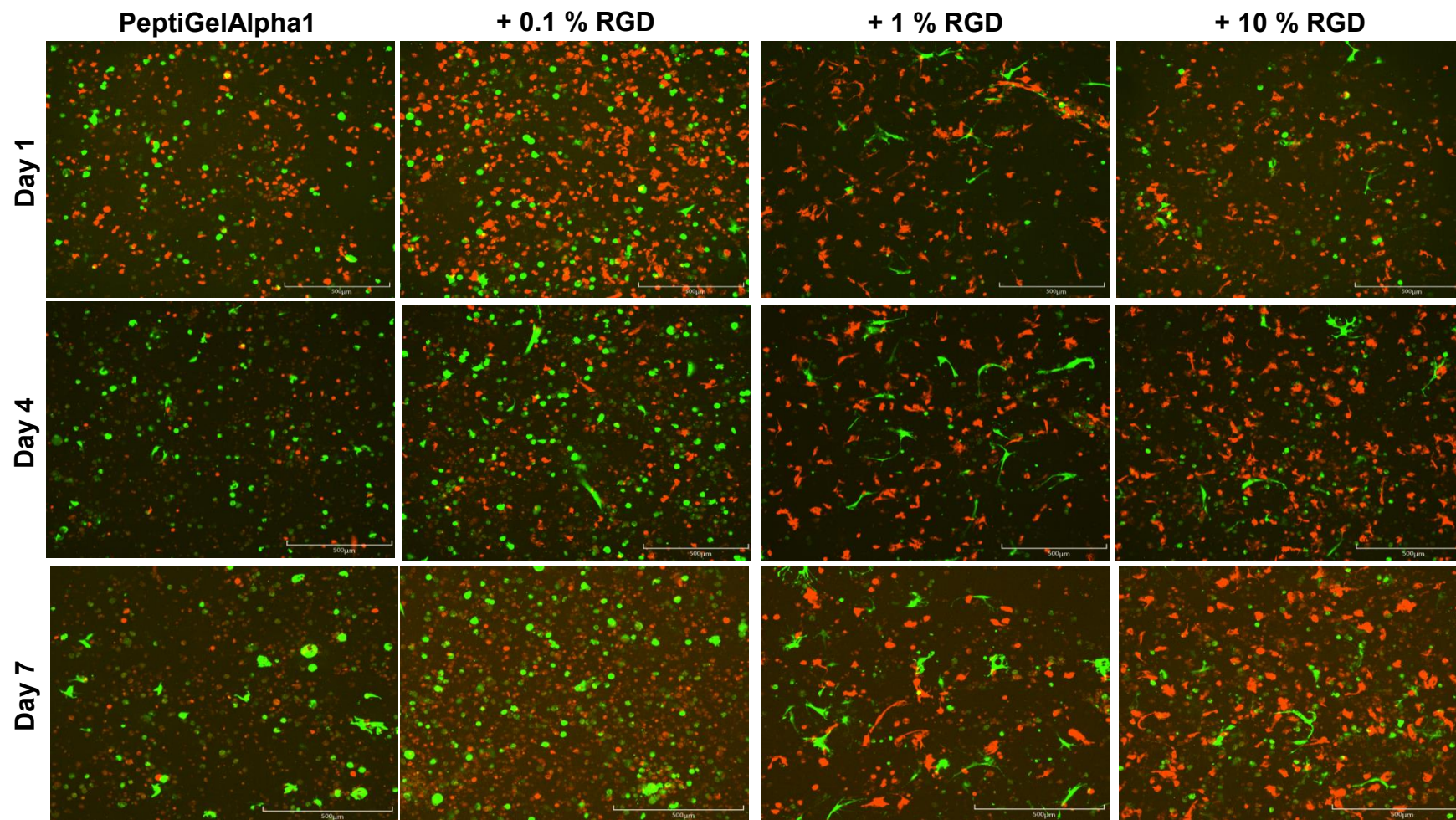


**Figure 6.6. Effect of cell-binding motif RGD and cell density on HUVEC and MSC behaviour.** RFP-HUVECs and GFP-MSCs were encapsulated within PeptiGelAlpha1  $\pm$  0.1 %, 1 % and 10 % RGD at a density of  $2 \times 10^6$  cells/mL (4:1 HUVEC:MSC ratio). Red = HUVECs. Green = MSCs. N = 2.

The effect of RGD concentration and cell-seeding density on HUVEC and MSC elongation after 7 days in culture was investigated by quantifying the circularity of cells (**Figure 6.7**). A round circle is given a circularity of 1, whereas a straight line has a circularity of 0 [368].

HUVECs seeded at a density of  $1 \times 10^6$  cells/mL (4 HUVECs:1 MSC) displayed a significantly decreased circularity when the RGD concentration was increased, compared with PeptiGelAlpha1 alone ( $p < 0.0001$ ) (**Figure 6.7A**). This same trend was also observed when a  $2 \times 10^6$  cells/mL density was used. However, no significant difference was observed between the same RGD concentrations at the different seeding densities, showing that the increased seeding density had no additional benefit on HUVEC morphology. For MSCs, when a  $1 \times 10^6$  cells/mL seeding density was used, the circularity was significantly decreased with 1 % and 10 % RGD ( $p < 0.0001$ ), but not for 0.1 % RGD ( $p > 0.05$ ) (**Figure 6.7B**). Whereas with a  $2 \times 10^6$  cells/mL seeding density, a significantly decreased circularity was observed with all RGD concentrations ( $p < 0.0001$ ). Again, there was no difference in circularity between the cell-seeding densities at any RGD concentration.

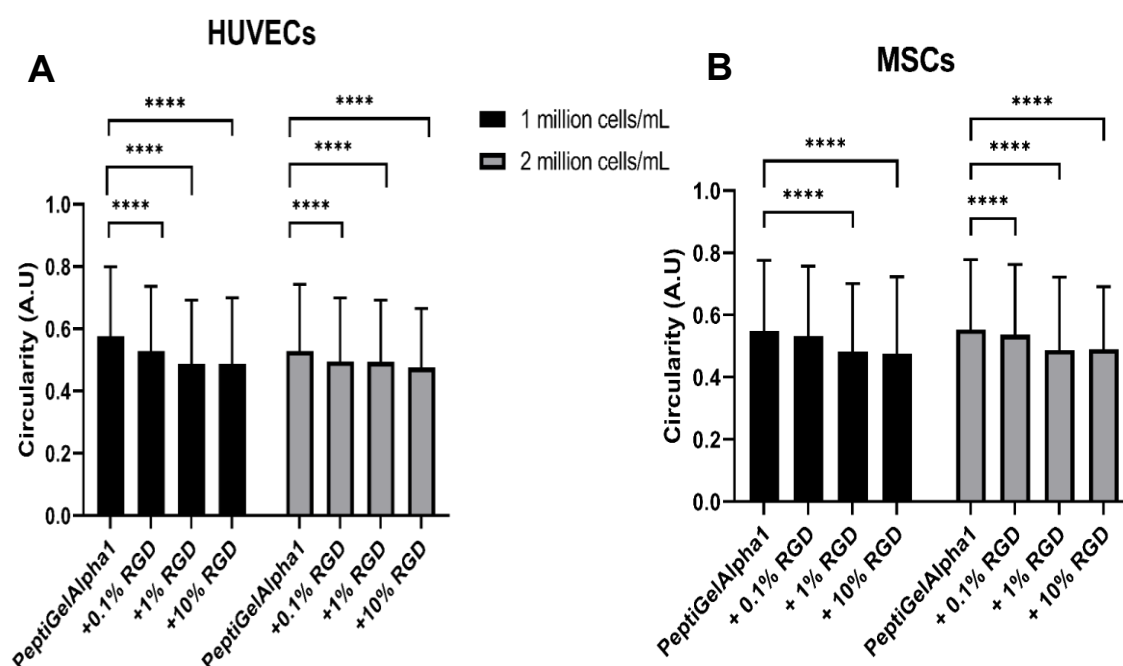


**Figure 6.7. Circularity quantification of (A) HUVECs and (B) MSCs in response to RGD concentration of PeptiGelAlpha1 and cell-seeding density after 7 days.**

Fluorescence images were analysed using ImageJ. Data are mean  $\pm$  S.D. \*\*\*\* =  $p < 0.0001$  using two-way ANOVA and post-hoc Tukey's test. N = 2.

Due to the lack of a positive response when 0.1 % RGD was incorporated, this concentration was not pursued further in subsequent experiments in this chapter. To investigate if a higher RGD concentration greater than 10 % could positively influence

HUVEC and MSC behaviour further, 40 % RGD was included. All subsequent experiments in this chapter use the original cell-seeding density of  $1 \times 10^6$  cells/mL.

The influence of MCF-7 breast cancer cells on HUVEC and MSC tube formation was investigated by tri-culturing all three cell lines simultaneously within PeptiGelAlpha1  $\pm$  1 %, 10 % and 40 % RGD (**Figure 6.8**). MCF-7 cells were pre-stained with the CellVue Claret Far Red Fluorescent Cell Linker Kit prior to hydrogel encapsulation to observe cells over time. Cells were imaged over a 7-day period.

In PeptiGelAlpha1 alone, all three cell types were rounded over the 7-day period, showing that culturing HUVECs and MSCs with MCF-7 cancer cells did not influence their behaviour or morphology. With 1 % and 10 % RGD, HUVECs and MSCs were observed to elongate by day 4 in culture. The MCF-7 cells remained rounded in the presence of RGD. When exposed to 40 % RGD, the majority of HUVECs and MSCs remained rounded, and the elongated morphology observed in 1 % and 10 % RGD was not as pronounced in 40 % RGD. It was also noted that cell elongation appeared to regress by day 7 in all materials. Within collagen I, the material had contracted after 1 day (**Figure 6.9**). HUVECs and MSCs were elongated but there was no evidence of tube formation. The MCF-7 cells were rounded in shape. After 4 days in culture, the HUVECs had organised themselves into large tube-like structures within the collagen material and were observed to protrude out of the collagen I constructs. In some cases, the MSCs were observed to align alongside the HUVEC formed tubes. The MCF-7 cells had aggregated to form clusters. By day 7, regression of the HUVEC tubes had occurred as only those on the periphery were still present.



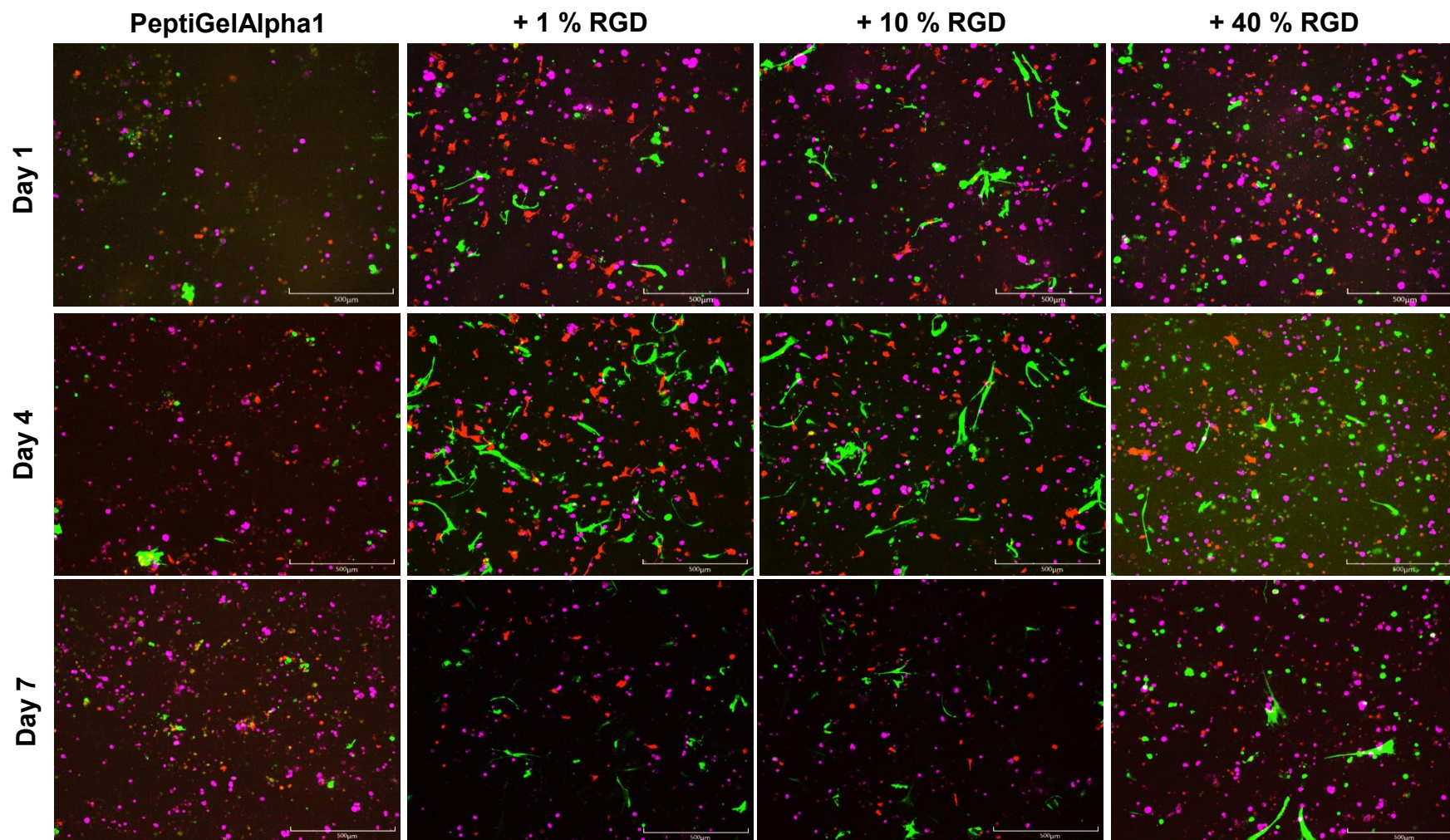


**Figure 6.8. Effect of RGD concentration and cancer cells on HUVEC and MSC behaviour.** RFP-HUVECs, GFP-MSCs and MCF-7 cells were encapsulated within PeptiGelAlpha1  $\pm$  1 %, 10 % and 40 % RGD at a density of  $1.5 \times 10^6$  cells/mL. Red = HUVECs. Green = MSCs. Pink = MCF-7. N = 2.

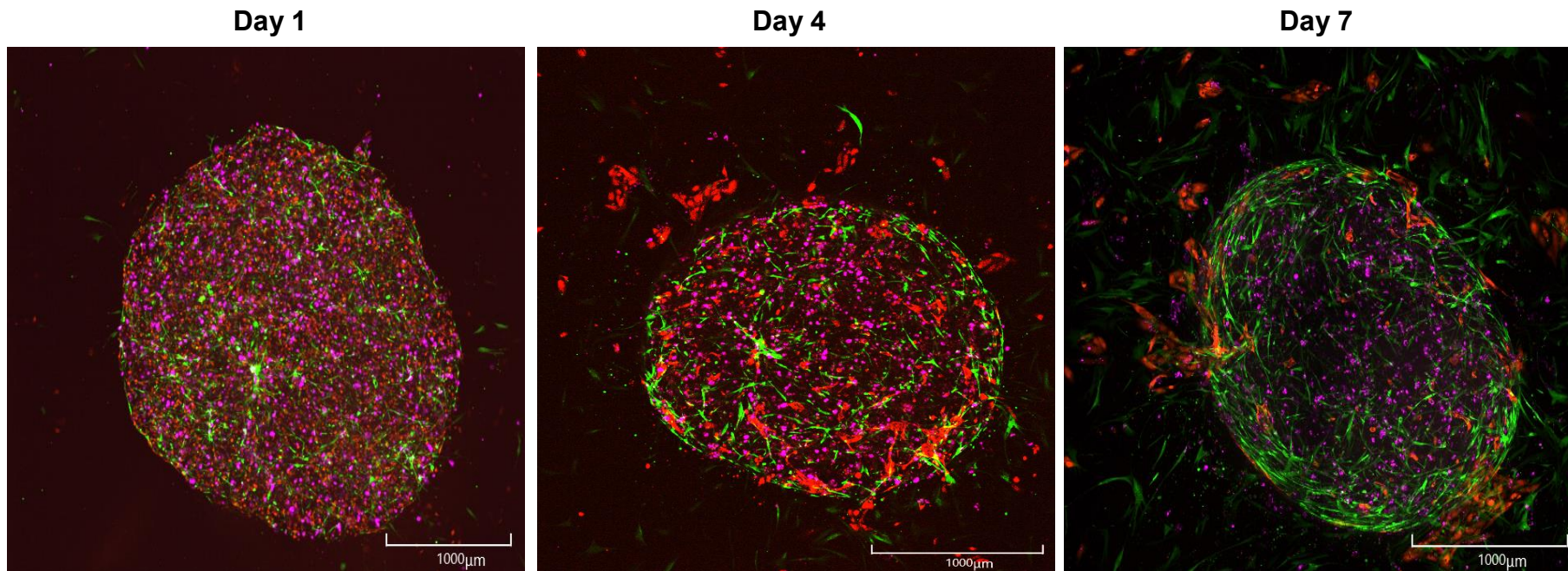


**Figure 6.9. Tri-culture of MCF-7 cancer cells, HUVECs and MSCs in collagen I + 90 μg/mL fibronectin.** RFP-HUVECs, GFP-MSCs and MCF-7 cells were encapsulated within collagen I + 90 μg/mL fibronectin at a density of  $1.5 \times 10^6$  cells/mL Red = HUVECs. Green = MSCs. Pink = MCF-7. N = 2.



#### 6.2.4. Effect of RGD Functionalisation on HUVEC and MSC Proliferation

To investigate the effect of RGD concentration on HUVEC and MSC growth, PicoGreen analysis was used on samples after 4 and 7 days in culture (**Figure 6.10**). After 4 days in culture, HUVEC and MSC DNA was significantly higher with 1 % RGD compared with PeptiGelAlpha1 alone ( $629.9 \text{ ng} \pm 140.8 \text{ ng}$  vs  $464.0 \text{ ng} \pm 35.3 \text{ ng}$ ;  $p < 0.01$ ). HUVEC and MSC DNA was significantly lower with 40 % RGD compared with PeptiGelAlpha1 alone ( $245.0 \text{ ng} \pm 80.1 \text{ ng}$  vs  $464.0 \text{ ng} \pm 35.3 \text{ ng}$ ;  $p < 0.01$ ). DNA yield was slightly higher with 10 % RGD than PeptiGelAlpha1 alone, but this increase was not significant. After 7 days, the DNA yield had declined considerably in all materials. No significant difference was observed between any of the materials, suggesting that the influence of RGD could not support the long-term culture of both cell types in PeptiGelAlpha1.

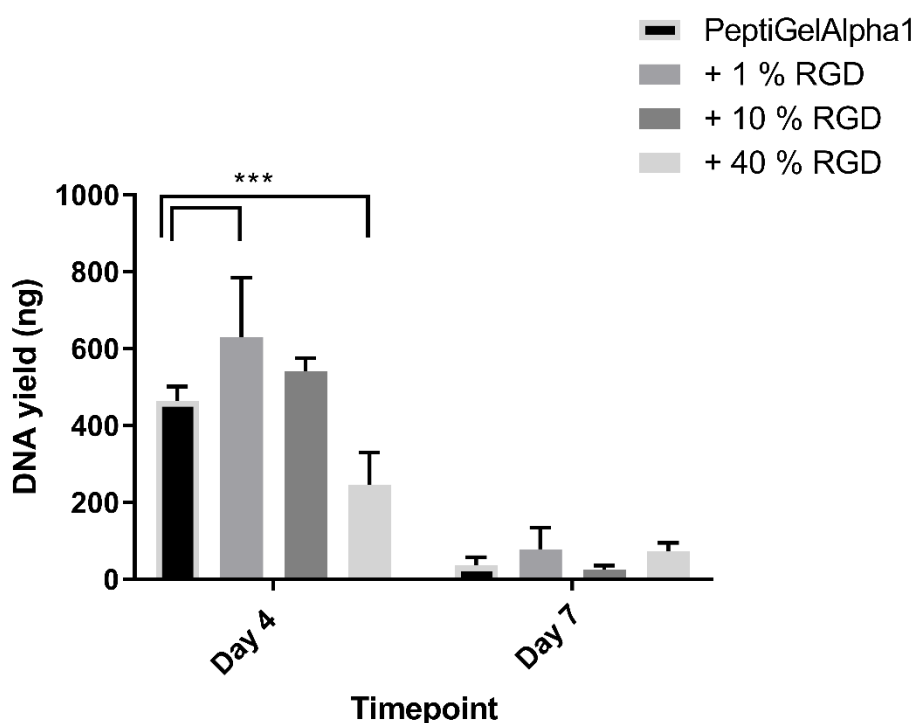


**Figure 6.10. PicoGreen analysis of HUVECs and MSCs encapsulated in PeptiGelAlpha1 ± 1 %, 10 % and 40 % RGD after 4 and 7 days in culture.** Cell-laden samples were digested and lysed using pronase, Triton-X treatment and exposure to a freeze-thaw cycle of  $-20 \text{ }^{\circ}\text{C}$ . PicoGreen solution was added to each sample and fluorescence was measured using a plate-reader at wavelengths of 480 nm and 520 nm. Acellular samples were used as blanks and removed from all samples. Data are mean  $\pm$  S.D. \*\*\* =  $p < 0.001$ , using two-way ANOVA and post-hoc Tukey's test. N = 1.

### 6.2.5. Effect of RGD Functionalisation on HUVEC Phenotype

CD31 is an EC marker, which is involved in tight junction formation and the integrity of the EC permeability barrier [369]. The presence of CD31 in HUVECs encapsulated in PeptiGelAlpha1, and the effect of RGD functionalisation, was investigated using immunohistochemical staining (**Figure 6.11**). Native HUVECs were observed to stain positively for CD31, as confirmed by a cell pellet control (**Appendix 4**). After 4 days in culture, HUVECs stained positive for CD31 in PeptiGelAlpha1 alone. This suggests that the native EC phenotype was retained within a synthetic hydrogel system, without any additional binding motifs. Positive staining for CD31 was observed with increasing concentrations of RGD, although the cell density appeared higher in 1 % and 10 % RGD samples, correlating with the cell proliferation data in **Figure 6.10**. Cell morphology was mostly rounded in the four materials.

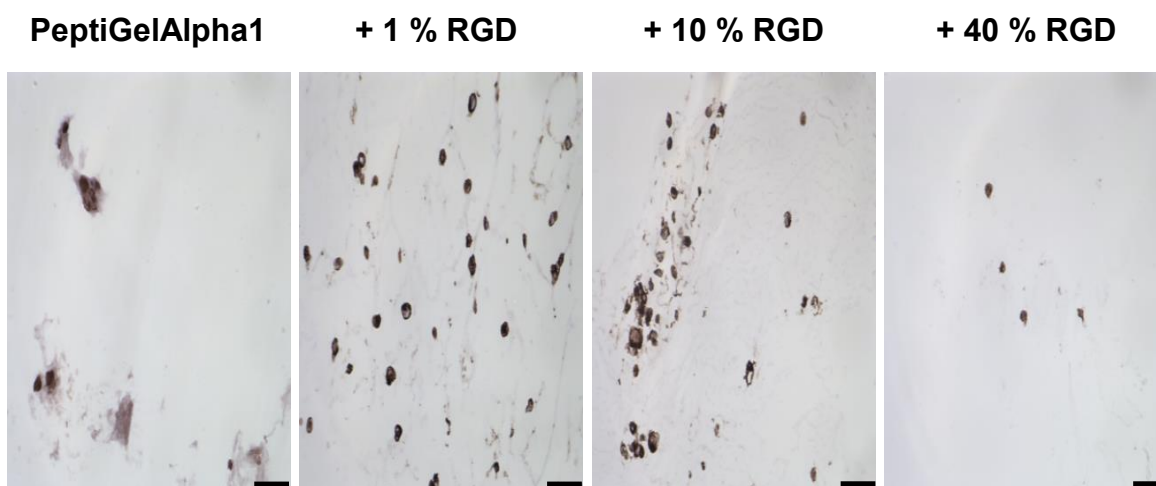


**Figure 6.11. CD31 immunostaining of HUVECs encapsulated in PeptiGelAlpha1 ± 1 %, 10 %, 40 % RGD after 4 days.** Cell-laden samples were fixed, processed for histological staining and embedded in paraffin wax. Samples were sectioned at a thickness of 5.0  $\mu\text{m}$  and stained for endothelial marker CD31. Positive staining was detected using a DAB substrate stain. Brown = positive staining. Blue = nuclei. Scale bar = 200  $\mu\text{m}$ . N = 1.

#### **6.2.6. Effect of RGD and IKVAV Functionalisation on HUVEC and MSC Behaviour**

IKVAV is a binding motif originally isolated from laminin, that has previously been used to promote tube formation of ECs [370]. PeptiGelAlpha1 functionalised with 15 % RGD and 15 % IKVAV was used to investigate the combined effect of RGD and IKVAV on HUVEC and MSC behaviour (Figure 6.12). 15 % RGD was used alongside 15 % IKVAV to observe if an enhanced response was observed > 10 % RGD, whilst limiting the total functionalisation percentage to < 40 %. Collagen I + 90 µg/mL fibronectin was used as a positive control. PeptiGelAlpha1 was used as a comparison. Cells were imaged over a 7-day period.

In collagen I + 90 µg/mL fibronectin, HUVECs were observed to elongate and differentiate into tube-like structures by day 4. MSCs were also observed to branch and align alongside the HUVECs by day 4. In PeptiGelAlpha1 alone, both cell types remained rounded throughout the 7-day culture period. With 15 % RGD and 15 % IKVAV, there was no evidence of elongation by either cell type, and the cells were indistinguishable from cells cultured in PeptiGelAlpha1.



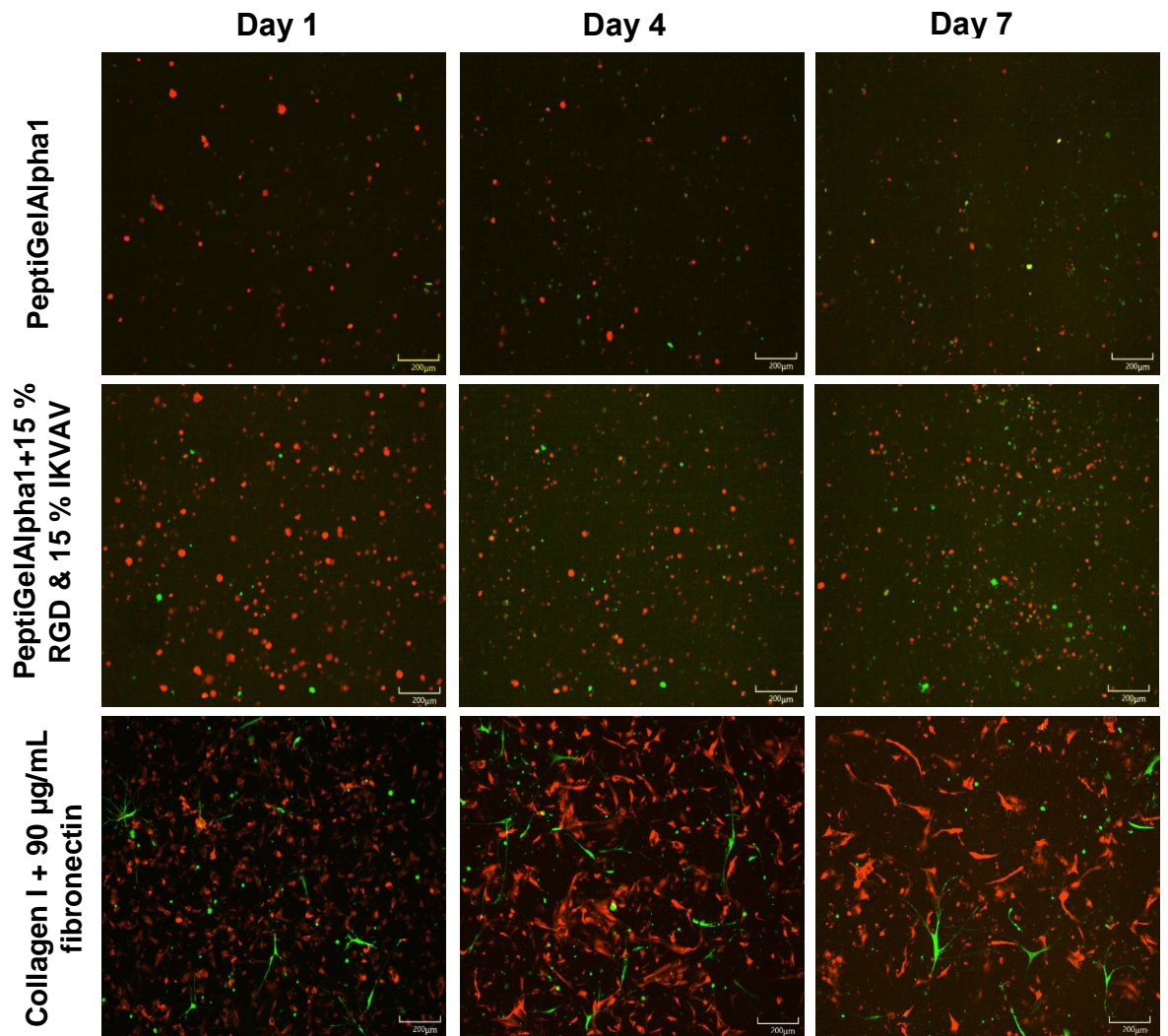


**Figure 6.12. Effect of cell-binding motifs RGD and IKVAV on HUVEC and MSC behaviour.** RFP-HUVECs and GFP-MSCs were encapsulated in PeptiGelAlpha1  $\pm$  15 % RGD & 15 % IKVAV at a density of  $1 \times 10^6$  cells/mL and imaged after 1, 4 and 7 days in culture. Collagen I + 90  $\mu$ g/mL fibronectin was used as a positive control. Red = HUVECs. Green = MSCs. N = 1.

### 6.2.7. Exploring HUVEC and MSC Interactions with RGD Functionalised PeptiGelAlpha1 via Integrin Binding

Cells bind to ECM proteins via transmembrane receptors called integrins, which facilitate adhesion between the cellular cytoskeleton and the matrix [371]. To observe if HUVECs and MSCs were binding to RGD functionalised PeptiGelAlpha1 via the  $\alpha5\beta1$  integrin, an anti- $\alpha5\beta1$  integrin antibody was used to block the integrin. PeptiGelAlpha1 + 10 % RGD was used as this concentration elicited the best response from HUVECs and MSCs, observed from other data described previously in this chapter (**Figure 6.5**). TCP alone and TCP pre-coated with 50  $\mu\text{g/mL}$  fibronectin were used as controls. Cells were incubated with the anti-human integrin  $\alpha5\beta1$  antibody for 45 minutes at 37 °C to initiate blocking, as used previously [213]. Samples were imaged after 4 days in culture.

In unblocked samples, HUVECs and MSCs were observed to adhere to TCP and fibronectin-coated TCP, as demonstrated by the cobblestone morphology displayed by HUVECs and MSCs adopting a spindle shape (**Figure 6.13**). In PeptiGelAlpha1 + 10 % RGD, HUVECs appeared elongated and MSCs displayed a branched morphology. When the  $\alpha5\beta1$  integrin was blocked, cells cultured on TCP appeared unaffected, as there was no change in morphology. On fibronectin-coated TCP, there appeared to be a reduction in MSC adhesion as the cells appeared more rounded compared with the unblocked control. HUVECs appeared to be greater in density, but morphology remained unaffected. With RGD enriched PeptiGelAlpha1, HUVECs again appeared greater in density with a greater degree of elongation compared with the unblocked samples. MSCs appeared unaffected by integrin blocking. These data suggest that blocking the  $\alpha5\beta1$  integrin had no detrimental effect on cell behaviour.

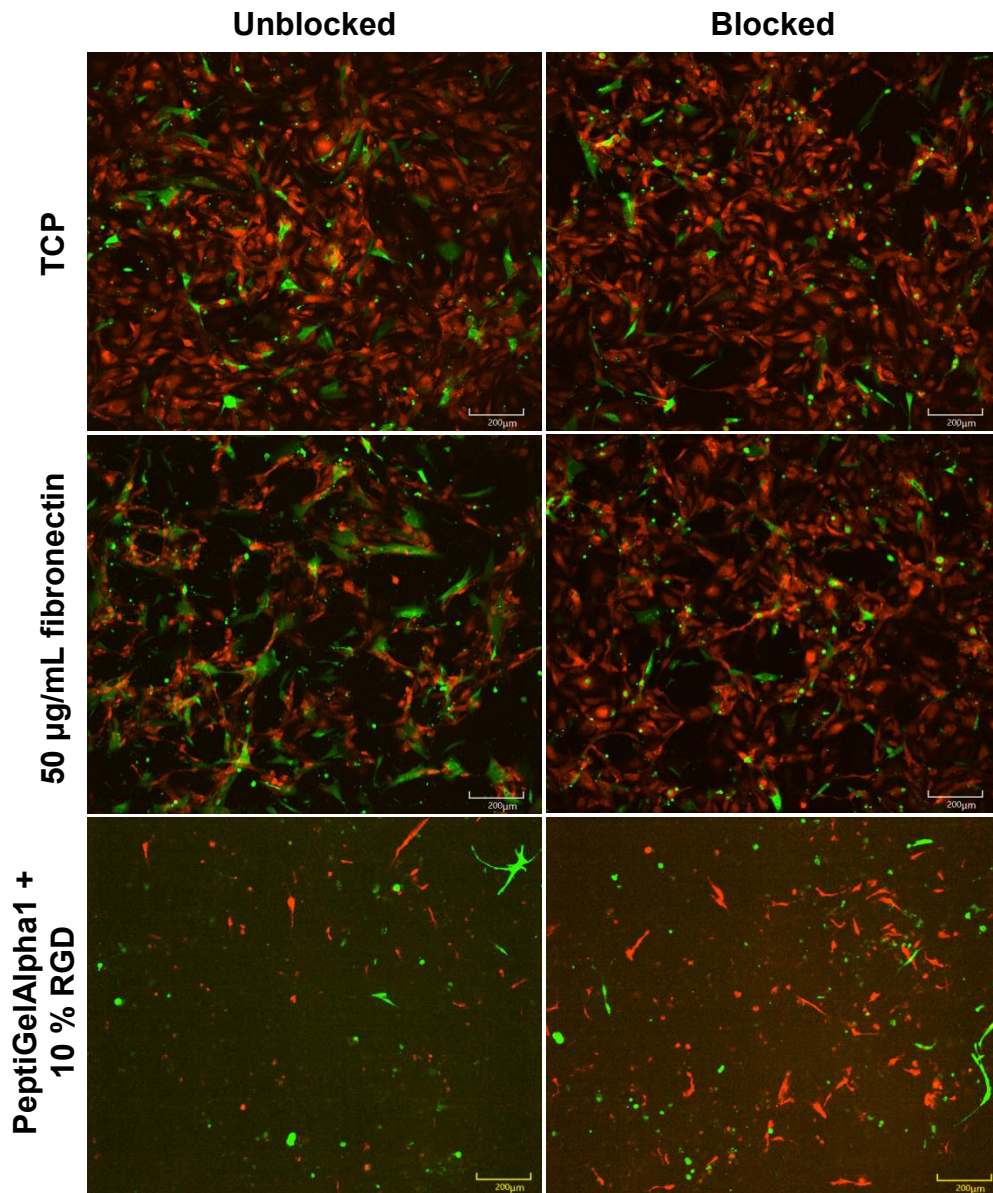


**Figure 6.13.  $\alpha 5\beta 1$  integrin blocking in HUVECs and MSCs.** RFP-HUVECs and GFP-MSCs were incubated in a mouse anti-human integrin  $\alpha 5\beta 1$  antibody using a dilution of 1:50 and a cell-seeding density of  $1 \times 10^6$  cells/mL at 37 °C for 45 minutes. Cells were subsequently seeded in PeptiGelAlpha1 + 10 % RGD and onto TCP  $\pm$  50  $\mu$ g/mL fibronectin. Samples were imaged after 4 days. Red = HUVECs. Green = MSCs. Scale bar = 200  $\mu$ m. N = 3.

### 6.2.8. Effect of RGD Functionalisation on PeptiGelAlpha1 Material Properties

The physical and chemical properties of RGD functionalised PeptiGelAlpha1 were characterised to observe if the inclusion of the RGD binding site affected the material. Beta-sheet formation was investigated to determine if the secondary structure of the hydrogel was affected by the RGD motif (**Figure 6.14**). A peak was observed at  $1620\text{ cm}^{-1}$  in the amide I region in PeptiGelAlpha1  $\pm 1\%$ , 10% and 40% RGD, indicative of  $\beta$ -sheet formation. This was accompanied by a small shoulder peak at approximately  $1690\text{ cm}^{-1}$  in all materials, showing that anti-parallel  $\beta$ -sheet formation was not affected by RGD functionalisation. With 10% and 40% RGD, a small shoulder vibration band was observed at  $1640\text{ cm}^{-1}$ , which was not present in PeptiGelAlpha1  $\pm 1\%$  RGD. This was attributed to random coils from the RGD sequence.

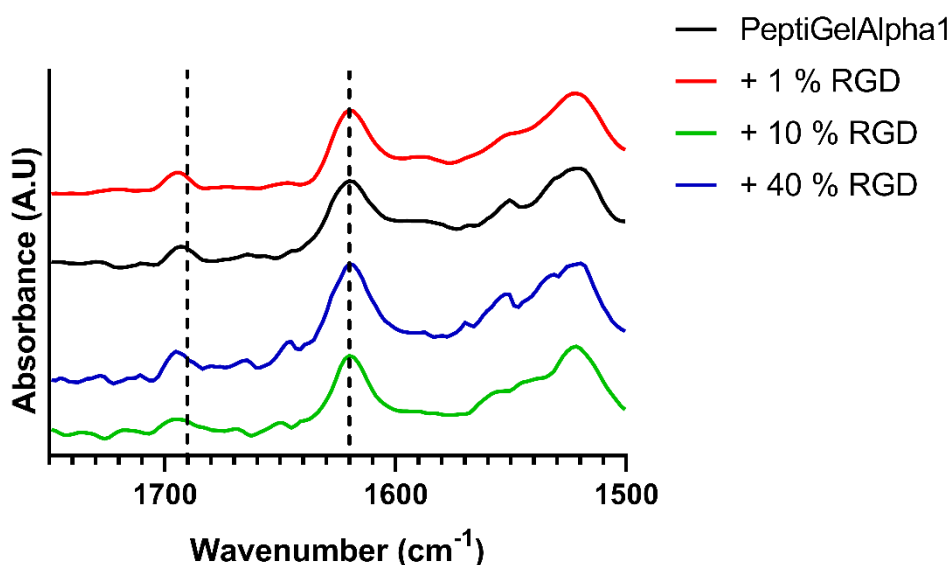


**Figure 6.14. AT-FTIR spectra of PeptiGelAlpha1  $\pm 1\%$ , 10% and 40% RGD.**

Dashed lines at  $1620\text{ cm}^{-1}$  and  $1690\text{ cm}^{-1}$  are indicative of  $\beta$ -sheet and anti-parallel  $\beta$ -sheet formation respectively. Spectra were collected over 256 scans using a resolution of  $4\text{ cm}^{-1}$ . HPLC grade water was used as a background control and removed from all spectra. OMNIC software was used to collect the spectra. Spectra were smoothed using 2<sup>nd</sup> order smoothing with an average number of 5 neighbours using GraphPad Prism 9.0 software. Data are representative spectra. N = 2.

The mechanical properties of RGD functionalised hydrogels, in the presence of media conditioning, were next investigated using oscillatory rheology (**Figure 6.15**). Frequency sweeps were carried out from 0.01–10 Hz at 0.2 % strain. The stiffness values reported are  $G'$  at 1 Hz. The stiffness of PeptiGelAlpha1 + 1 % RGD was significantly lower than that of PeptiGelAlpha1 (6183 Pa  $\pm$  317 Pa vs 7775 Pa  $\pm$  316 Pa;  $p < 0.01$ ). There was no significant difference between PeptiGelAlpha1 and PeptiGelAlpha1 + 10 % RGD (7712 Pa  $\pm$  648 Pa). PeptiGelAlpha1 + 40 % RGD was significantly lower than that of PeptiGelAlpha1 (5716 Pa  $\pm$  777 Pa vs 7775 Pa  $\pm$  316 Pa;  $p < 0.01$ ).

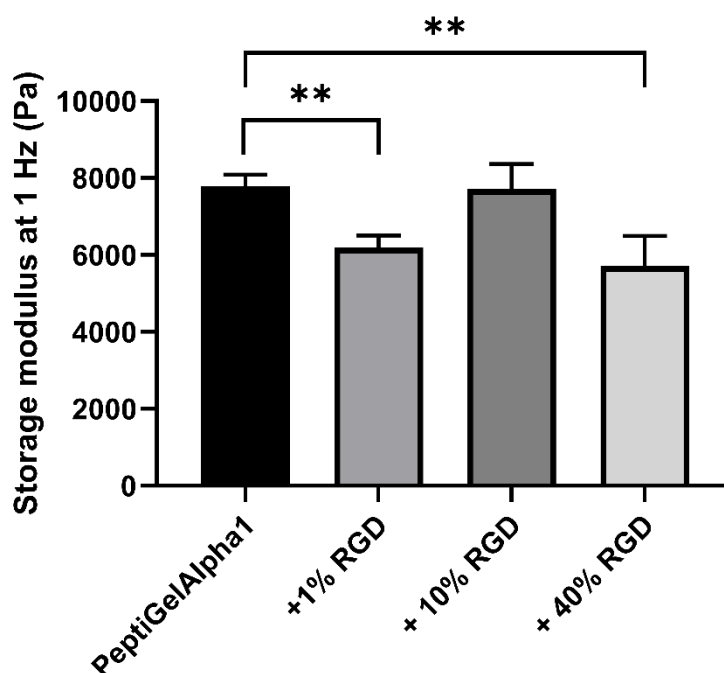


**Figure 6.15. Mechanical properties of PeptiGelAlpha1  $\pm$  1 %, 10 % and 40 % RGD with 18 hours media incubation.** Values were taken from frequency sweeps from 0.01–10 Hz at 0.2 % strain. Gap size = 500  $\mu$ m. Temperature = 37  $^{\circ}$ C. Data are mean  $\pm$  S.D. \*\* =  $p < 0.01$  using one-way ANOVA and post-hoc Tukey’s test. N = 1.

The nanofibre structure and diameter of RGD functionalised SAPHs were investigated using TEM imaging (**Figure 6.16**). As discussed previously in **section 4.2.6**, PeptiGelAlpha1 was shown to be composed of an entangled network of uniformly sized nanofibres. PeptiGelAlpha1  $\pm$  1 % and 40 % RGD stained darkly due to UA used as a contrast agent. PeptiGelAlpha1 + 10 % RGD fibres appeared white due to the camera detecting contaminants, which were darker than the peptide fibres. The incorporation of 1 %, 10 % and 40 % RGD did not appear to have an effect on the crude morphology of fibres, as the fibres were again forming an entangled network resembling ribbons



(**Figure 6.16**). The mesh of 40 % RGD did appear to be reduced compared with the other three hydrogels, with the fibres more densely packed and crowded.

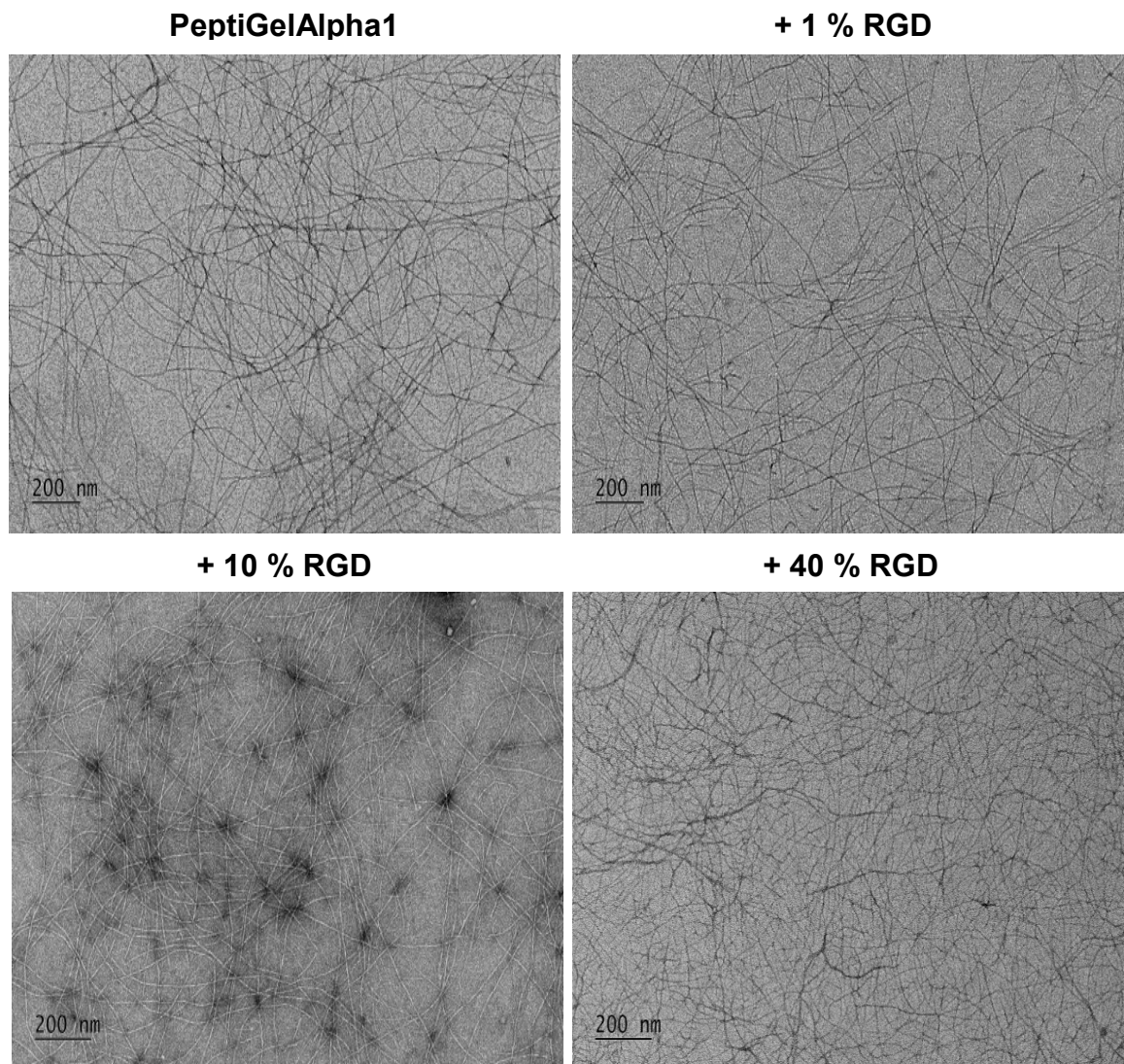


**Figure 6.16. TEM images of PeptiGelAlpha1 ± 1 %, 10 % and 40 % RGD.** Hydrogels were diluted 100x with HPLC grade water and placed onto a copper grid and exposed to 1 % (w/v) UA to improve contrast. Images were collected using a Gatan Orius SC1000 CCD camera. N = 2.

The fibre diameter of RGD functionalised SAPHs was quantified using ImageJ software from the images presented in **Figure 6.16** (**Figure 6.17**). PeptiGelAlpha1 fibres varied from 2.6–14.2 nm (**Figure 6.17A**). PeptiGelAlpha1 + 1 % RGD fibres did not differ much in diameter, with a range of 2.8–12.6 nm. Increasing the RGD concentration appeared to affect the range in fibre diameter, as PeptiGelAlpha1 + 10 % RGD fibres varied from 2.6–7.8 nm, and PeptiGelAlpha1 + 40 % RGD varied from 2.9–9.6 nm. This effect was accentuated further when comparing the average fibre diameters of all four materials (**Figure 6.17B**). The average fibre diameter of PeptiGelAlpha1 ( $5.9 \text{ nm} \pm 1.7 \text{ nm}$ ) was

significantly higher than + 1 % RGD (5.3 nm  $\pm$  1.5 nm;  $p < 0.0001$ ), + 10 % RGD (4.7 nm  $\pm$  0.9 nm;  $p < 0.0001$ ) and + 40 % RGD (4.8 nm  $\pm$  1.3 nm;  $p < 0.001$ ). The fibre diameter ranges and mean fibre diameters have been summarised in **Table 6.1**.

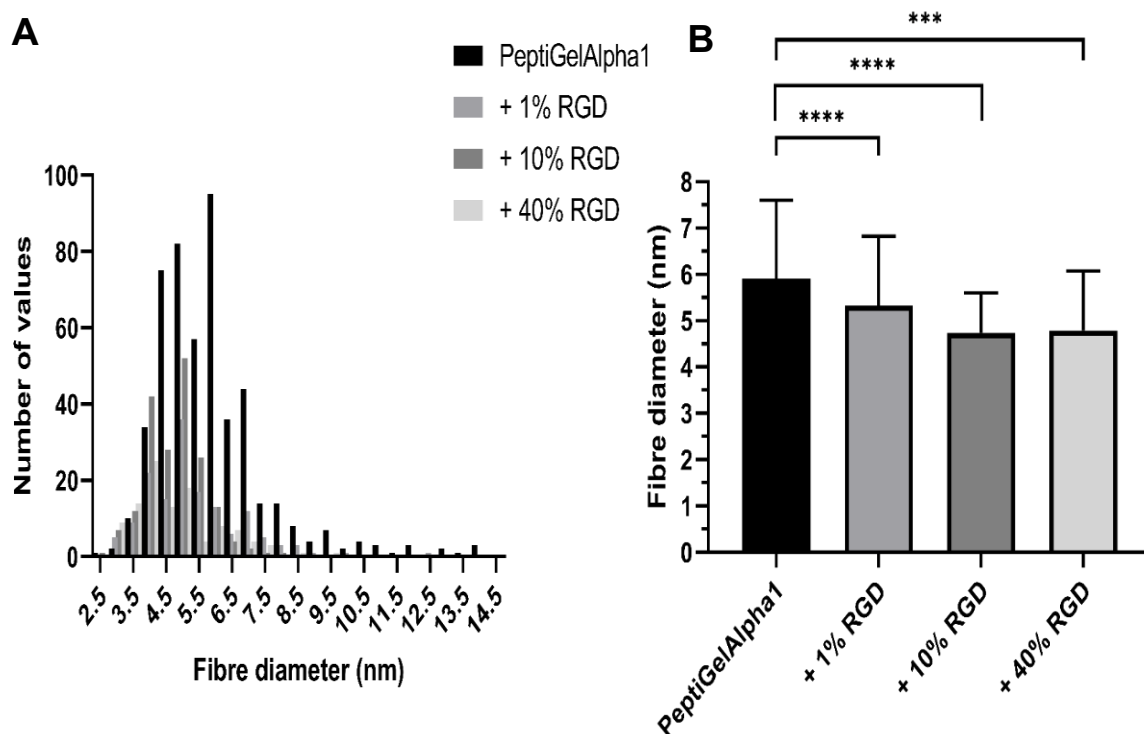


**Figure 6.17. Fibre diameters of PeptiGelAlpha1  $\pm$  1 %, 10 % and 40 % RGD.** (A) Frequency distribution of fibre diameters. (B) Mean fibre diameter quantification. Data are mean  $\pm$  S.D. \*\*\* =  $p < 0.001$ , \*\*\*\* =  $p < 0.0001$  using one-way ANOVA and post-hoc Tukey's test. N = 2.

**Table 6.1. Summary of mean fibre diameters and storage moduli at 1 Hz of PeptiGelAlpha1  $\pm$  1 %, 10 %, 40 % RGD.** Data are mean  $\pm$  S.D.

Hydrogel	Fibre diameter range (nm)	Mean fibre diameter (nm)	Storage moduli at 1 Hz (Pa)
PeptiGelAlpha1	2.6–14.2	5.9 $\pm$ 1.7	7775 $\pm$ 316
PeptiGelAlpha1 + 1 % RGD	2.8–12.6	5.3 $\pm$ 1.5	6183 $\pm$ 317
PeptiGelAlpha1 + 10 % RGD	2.6–7.8	4.7 $\pm$ 0.9	7711 $\pm$ 648
PeptiGelAlpha1 + 40 % RGD	2.9–9.6	4.8 $\pm$ 1.3	5716 $\pm$ 777

## 6.3. Discussion

### 6.3.1. Effect of Cancer Cell Conditioned Media on HUVEC Tube Formation

HUVECs readily organise themselves into tube-like structures when seeded on top of Matrigel (as well as exposure to specialist EC culture media) within 18 hours of culture [372,373]. Known as the tube formation assay, it is useful for assessing the efficacy of pro-angiogenic and anti-angiogenic compounds [374]. Cancer cells typically produce pro-angiogenic factors and molecules, such as VEGF [375]. It was hypothesised that conditioned media collected from MCF-7 cancer cells would be able to enhance HUVEC tube formation, compared with the positive control.

HUVECs seeded on top of Matrigel were exposed to cell culture media collected from MCF-7 cancer cells cultured under different conditions. When seeded on top of Matrigel and exposed to ECGM-2, HUVECs adhered to the material and organised themselves into primitive blood vessels. This shows the importance of the growth factors (EGF, FGF, VEGF and IGF) found within the cell culture media to stimulate tube formation of HUVECs. In this study, conditioning the cell culture media to cancer cells had no effect on tube formation by HUVECs (**Figure 6.1 & 6.2**). Data from other studies have produced mixed results. One study showed that HUVECs cultured in the presence of cancer cell conditioned media displayed significantly reduced motility [376]. Whereas glioma cell conditioned media promoted tube formation of brain ECs [377]. One study found, interestingly, that the cancer cell type has an effect on HUVEC tube formation; conditioned DMEM collected from MDA-MB-231 cancer cell was able to induce tube formation of HUVECs, whereas conditioned media collected from MCF-7, PC-3 and LNCaP cells could not [378]. This may be due to MDA-MB-231 cells producing higher concentrations of VEGF and MMP-9 compared with MCF-7 cells [379]. VEGF release by MCF-7 cells was not investigated in this study, although this may be the reason for the lack of difference in tube formation. It was also observed that HUVECs cultured in DMEM on top of Matrigel were rounded in morphology and did not form tubes (**Appendix 10**). As discussed earlier, this highlights the importance of the growth factors found within specialist EC culture media for EC tube formation. It also shows the sensitivity of HUVECs to the environment in which they are cultured, as seeding on top of Matrigel alone was not sufficient for tube formation.

Moreover, MCF-7 cells were cultured for 4 days prior to media collection. This time point was chosen to allow the cells to adhere and acclimatise to their designated culture platform



and to express pro-angiogenic molecules. A longer culture duration may have been needed for the cells to produce growth factors and proteins. Again, a VEGF release study using an ELISA would provide an optimum time point for media collection.

### **6.3.2. Influence of Laminin Enrichment of SAPHs on HUVEC Behaviour**

The addition of laminin to PeptiGelAlpha1 did not affect HUVEC behaviour (**Figure 6.3**). Laminin is believed to be a critical factor in inducing tube formation of HUVECs on Matrigel, due to the RGD and YIGSR binding motifs [365,380], and was thus investigated in this study. One study examining collagen I and the addition of laminin showed that laminin was able to induce intercellular contact between ECs, resembling tubes, whereas without laminin, ECs formed continuous sheets [366]. In this study, combining collagen I and laminin resulted in a higher HUVEC density and greater intercellular contacts than collagen I and fibronectin after 72 hours (**Figure 6.4**). This could be attributed to the YIGSR and IKVAV motifs provided by laminin, but could also be due to increased VEGF uptake due to increased  $\alpha 6$  integrin expression, which are known laminin receptors on ECs [366]. The lack of response observed in PeptiGelAlpha1 herein could be due to a number of reasons. The laminin protein was physically mixed into the hydrogel and it is possible that the shear stress exerted could have disrupted the structure, rendering it inert. It is also possible that the laminin binding domains were not available at the hydrogel surface and so the cells could not recognise and bind to them. Fluorescently labelling the laminin protein would reveal the location of the domains within the hydrogel and also if the protein remained intact.

### **6.3.3. Influence of SAPH Hydrophobicity on HUVEC Behaviour**

PeptiGelAlpha1 is based on alternating hydrophobic and hydrophilic residues. The overall hydrophobicity of SAPHs and the consequent effect on cell behaviour was investigated by utilising a valine-based hydrogel, named V8. In V8, the hydrophobic amino acid residues of PeptiGelAlpha1 are substituted with valine residues. Valine has a hydrophobicity index of 76, compared with the predominant hydrophobic amino acid in PeptiGelAlpha1, which has a score of 100 [381]. It was hypothesised that HUVECs would be able to adhere to a less hydrophobic surface, as cells prefer hydrophilic matrices [382]. Moreover, the hydrophobicity of SAPHs has previously been suggested to influence HUVEC behaviour [267].

Using the less hydrophobic SAPH V8, rather than PeptiGelAlpha1, was not able to positively influence HUVEC behaviour (**Figure 6.3 & 6.4**). It was also noted that after

72 hours, there was significantly less HUVEC coverage on PeptiGelAlpha1 alone, showing that the hydrogel could not support HUVEC growth. The hydrophobicity of primary amino acid sequences was determined using normalised values from the literature [381] and was not directly measured. Contact angle measurements are the most commonly used method to physically measure the hydrophobicity of a sample [383]. Typically, if a liquid is strongly attracted to a hydrophilic surface, the droplet will spread out and the contact angle will be close to zero. A greater contact angle correlates with a greater hydrophobicity [384]. As contact angle measurements were not carried out in this study, it is unknown if wettability differed between PeptiGelAlpha1 and V8, which may explain the similar results obtained. The hydrophobicity of the primary amino acid sequence of SAPHs has previously been suggested to affect tube formation of HUVECs. HUVECs cultured within RAD16-I and RAD16-II were able to attach to the matrix and organise into tube-like structures, whereas in KFE-8 and KLD-12, HUVECs remained rounded and clustered together [267]. The authors suggested that as KFE-8 and KLD-12 were more hydrophobic than RAD16-I and RAD16-II, proteins were adsorbing to the peptide fibre surface rather than being incorporated inside them during self-assembly, resulting in reduced binding sites for cells [267]. Physical measurements of hydrophobicity were not carried out on any of the hydrogels used, nor was this hypothesis followed up. Further work is needed to confirm if the physical hydrophobicity of a hydrogel sample correlates with the hydrophobicity of amino acid residues, as well as further investigating the relationship between SAPH hydrophobicity and HUVEC behaviour.

#### **6.3.4. Influence of Functionalisation of SAPHs on HUVEC and MSC Behaviour**

##### **6.3.4.1. HUVEC and MSC Morphology and Proliferation**

The influence of the RGD binding motif upon HUVEC and MSC behaviour within PeptiGelAlpha1 was investigated. Fluorescence-based imaging and quantifying cell shape by circularity measurements were used to investigate the effect of RGD functionalisation and cell-seeding density on cell behaviour. Circularity is a popular descriptor used in quantification of cell shape, in response to changing parameters affecting cell behaviour [385,386].

Functionalising PeptiGelAlpha1 with the RGD domain positively influenced elongation of HUVECs and MSCs in a concentration-dependent manner, but only up to a certain point (**Figure 6.5 & 6.8**). The addition of 0.1 % RGD had no effect on cell morphology, suggesting that insufficient RGD binding sites were present for the cells to attach.

However, a small but significantly reduced circularity was observed compared with PeptiGelAlpha1 alone (**Figure 6.7**). The addition of 1 % and 10 % RGD elicited a positive response, as shown by the fluorescence images (**Figure 6.5**), and circularity measurements (**Figure 6.7**), but 40 % RGD failed to stimulate elongation of the cells in the images presented (**Figure 6.8**). This response was supported with the PicoGreen data, with 1 % and 10 % RGD eliciting greater proliferation in HUVECs and MSCs than PeptiGelAlpha1 alone, and reduced proliferation observed with 40 % RGD (**Figure 6.10**). Increasing the cell-seeding density, from  $1 \times 10^6$  cells/mL to  $2 \times 10^6$  cells/mL, did not appear to stimulate the tube formation of HUVECs and MSCs under any of the conditions (**Figure 6.6 & 6.7**).

It was also observed that the inclusion of MCF-7 cancer cells did not affect HUVEC or MSC morphology with any of the RGD concentrations used, nor with PeptiGelAlpha1 alone (**Figure 6.8**). As discussed in **section 6.3.1**, it was unknown if the MCF-7 cells were expressing VEGF or other angiogenic growth factors, which could explain the lack of response by HUVECs and MSCs in the tri-culture system. It was also noted that the addition of the RGD domain did not affect MCF-7 cell morphology; this has been observed in other studies investigating functionalised hydrogels [328]

The benefits of functionalising synthetic hydrogels and SAPHs with ECM derived motifs for vasculature formation have previously been discussed in **section 2.6.3.3 & 2.6.4**. Functionalising PEG hydrogels [387], the Fmoc-FF SAPH [213] and the Q11 SAPH [239,388] with RGD domains have demonstrated that hydrogel functionalisation elicited a greater cell response compared to the unmodified hydrogel. The data in this study therefore support the findings in the literature that functionalisation of PeptiGelAlpha1, with low RGD concentrations (1 % and 10 %), could promote HUVEC and MSC behaviour. However, at 40 % RGD, there was no positive effect on cell behaviour. The diminished response observed with 40 % RGD presented could be due to saturation of the hydrogel network with binding sites, therefore the cells were unable to bind. This suggests that the network density could be a limiting factor in functionalising SAPHs. This limitation was shown previously when investigating RGD functionalisation on silicon surfaces, showing that  $6 \times 10^5$  RGD/mm<sup>2</sup>, or 100 % RGD, resulted in reduced EC adhesion compared with  $3 \times 10^5$  RGD/mm<sup>2</sup> [389]. The authors proposed that overcrowding of RGD ligands resulted in insufficient space for cell integrins to bind to the ligands effectively. The spacing of RGD ligands within the hydrogel was not investigated in this current study, but were assumed to be randomly distributed. Fluorescent labelling or gold conjugation coupled with TEM of RGD binding sites would determine the spatial arrangement of ligands within

the hydrogel [239,388,390]. Overcrowding of the SAPH network by binding sites would also explain the lack of cell response to PeptiGelAlpha1 functionalised with 15 % RGD and 15 % IKVAV (**Figure 6.12**). There is clearly an optimal density for functionalising hydrogels with ECM derived ligands to ensure maximal response from cells, without compromising cell behaviour. It was also noted that the DNA yield of HUVECs and MSCs diminished under all conditions after 7 days in culture, showing that the long-term culture of both cell types could not be maintained in PeptiGelAlpha1 alone or when functionalised with the RGD motif (**Figure 6.10**).

#### **6.3.4.2. HUVEC Phenotype**

The influence of RGD functionalisation on HUVEC phenotype was confirmed with CD31 immunostaining (**Figure 6.11**). Positive staining was consistently observed in PeptiGelAlpha1 and all RGD concentrations after 4 days in culture. CD31 has been widely used as a marker for EC phenotype when investigating ECs cultured using hydrogel systems [366,391]. The retention of CD31 in HUVECs in PeptiGelAlpha1 alone was promising, as it suggests that the unmodified hydrogel could still maintain the native EC phenotype. One study discovered that HUVECs cultured on the Q11 SAPH alone inconsistently expressed CD31 at cell-to-cell contacts; Q11-RGDS was used to investigate HUVEC behaviour but unfortunately, CD31 staining was not studied with RGD functionalised hydrogels [392]. In this current study, cell density appeared to be sparse in PeptiGelAlpha1 ± 40 % RGD images, further supporting the notion that the addition of 40 % RGD exerted no benefit to HUVEC behaviour. Cell density did appear more abundant with 1 % and 10 % RGD, which correlates with the PicoGreen data presented in **Figure 6.10**.

#### **6.3.4.3. $\alpha_5\beta_1$ Integrin Interaction**

To ascertain if HUVECs and MSCs were binding to the RGD domains directly via integrin activation within the hydrogel, integrin-blocking studies were carried out by incubating the cells with an anti-human  $\alpha_5\beta_1$  integrin antibody. The data presented showed that blocking this integrin did not affect the morphology of cells cultured in PeptiGelAlpha1 + 10 % RGD, TCP or 50  $\mu\text{g}/\text{mL}$  fibronectin, compared to unblocked samples (**Figure 6.13**). It was noted that the cells appeared more elongated with an increased density in blocked PeptiGelAlpha1 + 10 % RGD, which was surprising. One explanation is that the cells were not sufficiently blocked. The blocking procedure used was the same as described previously [213], in which cells were incubated with the same antibody for 45 minutes at 37 °C, prior to encapsulation within the hydrogel. In that study, the cell morphology was

rounded due to the blocked integrins unable to respond and attach to the RGD sites [213]. Integrin blocking may have been successful due to the hydrogel preparation starting as a liquid precursor, with the cells mixed in, prior to gelation at 37 °C [213]. This method ensures that the antibody remained in the cell suspension and the  $\alpha_5\beta_1$  integrins remained blocked throughout the culture duration. In this current study, a minimal volume of cell suspension was mixed into a preformed hydrogel. Due to the cell suspension volume being reduced after integrin blocking and prior to hydrogel encapsulation, it is possible that removal of the antibody resulted in restoration of integrin activity. However, the TCP and fibronectin coated TCP samples contained the original blocked cell suspension and no difference was observed between the blocked and unblocked samples.

Another factor may be that cells contain multiple integrins which recognise the RGD binding site;  $\alpha_5\beta_1$  is one of eight RGD-binding integrins [393]. The  $\alpha_5\beta_1$  integrin is often described as the ‘fibronectin receptor’ due to its high affinity for the RGD sequence in the fibronectin protein [394,395]. However, in the absence of the  $\alpha_5\beta_1$  integrin, other RGD recognising integrins can compensate, such as the  $\alpha_v\beta_3$  integrin which also binds to the RGD [396]. It is possible that blocking of the  $\alpha_5\beta_1$  integrin alone was not sufficient to reveal if HUVEC and MSC attachment to the RGD motifs was mediated by cell-integrin interactions. Dual blocking of both the  $\alpha_5\beta_1$  and  $\alpha_v\beta_3$  integrins could help elucidate the interactions of HUVECs and MSCs with RGD functionalised SAPHs.

### **6.3.5. RGD Functionalisation and Physico-Chemical Properties**

#### **6.3.5.1. Secondary Structure of RGD Functionalised PeptiGelAlpha1**

To observe if functionalising PeptiGelAlpha1 with the RGD motif affected the self-assembly and physical properties of the hydrogel, characterisation of the RGD functionalised PeptiGelAlpha1 hydrogels was carried out using the same techniques as described in Chapter 4. AT-FTIR analysis confirmed that anti-parallel  $\beta$  sheets were present in all RGD concentrations, confirming that the core secondary structure of the hydrogel was unaffected by functionalisation (**Figure 6.14**). This is concurrent with other studies using RGD functionalised ionic complementary SAPHs [213,397], in which  $\beta$ -sheet formation was not affected by the presence of RGD. The peak observed at 1640  $\text{cm}^{-1}$  in 10 % and 40 % RGD samples has been observed previously in RADA16-RGD and RADA16-IKVAV samples; the authors determined this peak was due to the presence of  $\alpha$ -helices or random coils [397]. A RADA16 only sample was not used

as a control, but this peak was not present in the PeptiGelAlpha1 spectra presented in this study, suggesting that this could be attributed to the binding motif.

### **6.3.5.2. Viscoelastic Behaviour of RGD Functionalised PeptiGelAlpha1**

The mechanical properties of RGD functionalised hydrogels were investigated using oscillatory rheology in the presence of media conditioning (**Figure 6.15**). PeptiGelAlpha1 + 1 % and 40 % RGD were measured to be significantly softer than PeptiGelAlpha1 alone. No significant difference was observed with + 10 % RGD. Previous studies have indicated that functionalisation of SAPHs with the RGD domain does significantly affect the mechanical properties. Zhou *et al* reported that increasing the percentage of Fmoc-RGD up to 30 % in the Fmoc-FF SAPH resulted in an increase in stiffness compared with a sample containing 0 % RGD [213]. However, 40 % and 50 % Fmoc-RGD resulted in softer hydrogels compared with 100 % Fmoc-FF [213]. Separate studies investigating the  $\beta$ -sheet forming SAPH KFE discovered that the stiffness of KFE was 10 times greater than that of KFE-RGD alone [398]. However, the stiffness of the  $\beta$ -turn forming SAPH Q11 was not affected by the presence of RGD [239].

The weakened mechanical properties shown with RGD functionalised PeptiGelAlpha1 in this study, and other  $\beta$ -sheet forming peptide hydrogels, could be explained by the interaction of the RGD motif with the self-assembling of the  $\beta$ -sheet nanofibres. As discussed in **section 6.3.5.1**, characteristic spectra of  $\beta$ -sheet forming SAPHs were observed in this study, but it could be possible that  $\beta$ -sheet content was reduced. One study found that functionalising  $\beta$ -sheet forming RADA16 with YIGSR and other laminin and collagen IV derived binding motifs, resulted in reduced  $\beta$ -sheet content as shown by CD spectra, although characteristic  $\beta$ -sheet spectra were observed [269]. Functionalisation with the RGD motif was not included in that study. It is thus possible that incorporation of an ECM derived ligand affects the lateral formation of  $\beta$ -sheet peptide fibres, resulting in a decreased mesh size and thus weakened mechanical properties. CD measurements were not carried out in this study, but would help elucidate this theory in more detail. The rheology data carried out in this study also showed that no difference in stiffness was observed between PeptiGelAlpha1 and + 10 % RGD; this could be due to the sample size used ( $n = 1$ ). More experimental repeats are therefore needed to confirm the effect of RGD functionalisation on SAPH mechanical properties.

### 6.3.5.3. Fibre Formation of RGD Functionalised PeptiGelAlpha1

Fibre formation of RGD functionalised PeptiGelAlpha1 was observed using TEM imaging (**Figure 6.16**). Compared with PeptiGelAlpha1, the presence of RGD at any concentration did not affect the gross morphology of nanofibres, which were observed as entangled ribbons. Quantification of TEM images revealed that RGD functionalisation did result in significantly reduced nanofibre diameter (**Figure 6.17B**). However, it is unclear whether the diameter of the peptide nanofibres would affect cell behaviour. Although the differences in fibre diameter were deemed to be significant, they were still small, with little difference observed in the ranges of fibre diameter (**Table 6.1**). Beta-sheet forming peptide hydrogels typically have a fibre thickness of 10–20 nm [219], although  $\beta$ -sheet forming hydrogels with fibre diameters of 3–5 nm have been reported [286]. Consequently, the fibre diameters of RGD functionalised PeptiGelAlpha1 appeared to be typical for this type of SAPH. In addition, the overall architecture of the hydrogels seemed to be largely unaffected by the presence of RGD. With 40 % RGD, however, the network appeared to be densely crowded. As discussed previously in **section 6.3.4.1**, labelling the RGD ligand with gold nanoparticles would enable visualisation of the binding motif within the peptide fibre network. This would also uncover the distribution of the binding motif and would reveal if the network was too crowded with 40 % RGD.

## 6.4. Conclusions

Tissue engineering blood vessels *in vitro* using HUVECs is challenging; HUVECs are notoriously delicate cells and are sensitive to the environment in which they are grown. Whilst some studies have fabricated vascular structures using HUVECs to recreate the vasculature component within tumours [399], focus on spontaneous formation of tube-like structures by HUVECs and MSCs was explored in this work.

Results in Chapter 5 showed that PeptiGelAlpha1 was able to support the viability and growth of MCF-7 and MDA-MB-231 breast cancer cells. Previous work has also shown that SAPH systems have been used successfully for the formation of primitive blood vessels by HUVECs [36,239,267]. PeptiGelAlpha1 had not been previously used for co-culture of HUVECs and MSCs; therefore, it was unknown if HUVECs and MSCs would spontaneously form tubes within the hydrogel alone, or if modifications to the material would be needed to promote this behaviour.

The aim of this chapter was to determine what modifications are needed to support HUVEC and MSC growth and vasculature formation within PeptiGelAlpha1.

In summary, none of the approaches used, nor the modifications made to PeptiGelAlpha1, were able to greatly induce tube-like structures and formation by HUVECs and MSCs. However, functionalisation with the RGD binding domain elicited the greatest response, as shown by the elongation and stretching of HUVECs and MSCs and increased proliferation. There was an initial concentration-dependent benefit to RGD functionalisation, however at 40 % RGD, it was noticed that the cell response to the RGD motif diminished. This was possibly due to saturation of the hydrogel network resulting in cells being unable to bind, suggesting that there may be a threshold value for functionalisation. CD31 expression was observed in the absence and presence of the RGD domain, showing that the hydrogel alone could support native HUVEC phenotype. Blocking of the  $\alpha 5\beta 1$  integrin was unable to determine if the cells were attaching to the RGD domain via this specific integrin. In conclusion, a multifaceted approach to modifying PeptiGelAlpha1 and more generally, SAPHs, is necessary for HUVEC and MSC tube formation.

The novelty of the work outlined in this chapter is found in the RGD functionalisation study, whereby the cell response to RGD functionalisation is concentration-dependent and the positive effect is lost at higher concentrations. This finding has been observed for the first time using this material, PeptiGelAlpha1, with the HUVEC and MSC cell types.



Moreover, the formation of vasculature has not been attempted before using this material, to the author's knowledge.

## CHAPTER 7 – Overall Conclusions and Future Work

### 7.1. Overall Conclusions

Anti-cancer drug development is hindered due to the lack of reliable *in vitro* models used in the development pipeline [400]. The simplicity of 2D *in vitro* models results in maximal therapeutic benefit exerted by novel drugs, due to the lack of barriers that are observed in tumours *in vivo* [9]. Developing representative 3D *in vitro* models that can recapitulate the TME will help streamline drug development, improving the data collected from *in vitro* research and supplementing *in vivo* studies [147]. Mimicking the TME *in vitro*, however, is a complex and difficult feat; the needs of numerous cell types and components need to be considered. Using a naturally derived hydrogel provides the cells with the binding cues typically found *in vivo*, and therefore there are few issues associated with co-culturing multiple cell types [183]. However, the limitations associated, such as weak mechanical properties and batch-to-batch variability, far outweigh the benefits, rendering them unsuitable for pharmaceutical applications and limit data reproducibility [180]. Using a synthetic system removes these impediments. Nonetheless, different cell types have individual environmental needs. Therefore, a biomaterial used must be able to maintain the native behaviour of multiple cell types. The issue thus lies in whether a synthetic system alone can support the phenotype and growth of these cells, and what material modifications are needed, as found within this thesis.

The overall aims of this thesis were as follows:

1. To identify the most appropriate SAPH candidate and characterise and compare the physical and mechanical properties of the chosen SAPH, PeptiGelAlpha1, with collagen I and Matrigel.
2. To investigate the growth and behaviour of MCF-7 and MDA-MB-231 breast cancer cell lines within the chosen SAPH, by exploring cell viability, phenotype, and organisation, as well as investigate if features of solid tumours could be mimicked.
3. To determine what modifications are needed to support HUVEC and MSC growth and tube formation within the chosen SAPH.

In response to **aim 1**, the data presented in **Chapter 4** have shown that PeptiGelAlpha1 was the most suitable material to use out of the SAPHs tested, due to its neutral charge, relatively stiff mechanical properties and biocompatibility with MCF-7 breast cancer cells.

PeptiGelAlpha1 was shown to be a shear-thinning and versatile material that was formed of entangled nanofibres mimicking that of the ECM. The fibre morphology and diameter of PeptiGelAlpha1 (2.6–14.2 nm) was uniform and homogeneous compared with collagen I (2.1–65.4 nm) and Matrigel (3.9–120.7 nm), due to its chemical definition. The mean fibre diameter of PeptiGelAlpha1 ( $5.7 \text{ nm} \pm 1.4 \text{ nm}$ ) was significantly smaller than that of collagen I ( $12.0 \text{ nm} \pm 3.9 \text{ nm}$ ) and Matrigel ( $20.1 \text{ nm} \pm 9.6 \text{ nm}$ ). PeptiGelAlpha1 exhibited superior mechanical properties ( $12,679.5 \text{ Pa} \pm 3224.0 \text{ Pa}$ ) to collagen I ( $27.8 \text{ Pa} \pm 0.8 \text{ Pa}$ ) and Matrigel ( $9.0 \text{ Pa} \pm 6.6 \text{ Pa}$ ) and was able to mimic the stiffness of breast tumour tissue, more closely. The viscoelastic properties of PeptiGelAlpha1 were more sensitive to media conditioning than collagen I and Matrigel, with an increase in stiffness observed due to charge screening. Recovery experiments showed that Matrigel was not able to deform and recover following cycles of low and high shear, impeding the applications of this material. On the other hand, collagen I and PeptiGelAlpha1 were able to deform and recover following alternating cycles of high and low shear. However, media conditioning detrimentally affected the recovery profile of PeptiGelAlpha1, resulting in the system crashing. Nonetheless, without media conditioning, PeptiGelAlpha1 could withstand high shear and recover to form a hydrogel, and therefore could be suitable for applications including: 3D printing, injection and cell encapsulation. PeptiGelAlpha1 also acted as a physical barrier to doxorubicin penetration, as shown by confocal and multi-photon imaging. PeptiGelAlpha1 therefore demonstrated appropriate material properties for modelling breast tumours.

For **aim 2**, as shown in **Chapter 5**, MCF-7 and MDA-MB-231 cells were viable and proliferated within the hydrogel over the 14-day period observed. Ki67 immunohistochemistry showed that both cell lines were actively dividing within PeptiGelAlpha1. MCF-7 cells aggregated to form large spheroids within the SAPH, in a similar manner to the collagen I hydrogel, whereas MDA-MB-231 cells remained dispersed. Both cell lines became hypoxic within the hydrogel, with an increase in number of hypoxic cells observed over the 14-day culture. For MCF-7 cells, however, the formation of cell spheroids resulted in an increase in percentage area that was hypoxic. The EMT status of both cell lines was not observed to change over the culture duration, as shown by immunohistochemical staining, therefore it cannot be concluded from these data alone if the EMT status of the cells was changing. However, the native phenotype of MCF-7 and MDA-MB-231 cells was retained, with positive staining observed for E-cadherin and cytokeratin (MCF-7 cells), and vimentin and cytokeratin (MDA-MB-231 cells) within PeptiGelAlpha1. TEM imaging revealed that MCF-7 cells were internalising

the peptide hydrogel, which was not observed with collagen I, nor was this observed with the MDA-MB-231 cell line. This was supported by weakened mechanical properties of MCF-7 cell laden samples and increased MMP-2 production, suggesting that MCF-7 cells were remodelling the peptide hydrogel by proteolytic degradation. MCF-7 cells were observed to be highly invasive when cultured within PeptiGelAlpha1, as shown by invasion into collagen I and Matrigel hydrogels, but this was not observed with MDA-MB-231 cells. Preliminary data showed that MCF-7 and MDA-MB-231 cells cultured in PeptiGelAlpha1 were resistant to tamoxifen treatment compared with 2D monolayer cultures, suggesting that 3D culture using a SAPH system could reflect drug sensitivity observed *in vivo*. It was noted that PeptiGelAlpha1 appeared to be a more appropriate platform for culturing MCF-7 cells than MDA-MB-231 cells. This was highlighted by the invasive potential of MCF-7 cells into collagen I and Matrigel hydrogels, remodelling of the PeptiGelAlpha1 matrix and ECM deposition, which were not observed with MDA-MB-231 cells. It is possible that PeptiGelAlpha1 alone could not support the malignant phenotype of this cell line, and that functionalisation with a cell-binding domain such as RGD may be necessary. PeptiGelAlpha1 alone therefore may be more suited for modelling early stages of breast cancer, such as with MCF-7 cells. Events of cancer progression, such as hypoxia, invasion, resistance to anti-cancer drugs and ECM remodelling, were observed with this system. PeptiGelAlpha1 could therefore be a suitable platform for modelling early breast cancer, and more widely, the TME.

For **aim 3**, presented in **Chapter 6**, none of the modifications made to PeptiGelAlpha1 in this work were able to induce tube formation by HUVECs and MSCs. MCF-7 cancer cell conditioned media did not positively influence HUVEC tube formation when cultured on Matrigel. Laminin enrichment of SAPH and the hydrophobicity of the amino acid sequence did not exert any benefit to HUVEC behaviour. However, compared with fibronectin enrichment, laminin did promote HUVEC attachment to collagen I. Functionalisation of PeptiGelAlpha1 with 1 % and 10 % RGD was able to elicit HUVEC and MSC attachment and elongation, whereas no benefit was observed with 0.1 % and 40 % RGD. Increasing the cell-seeding density did not stimulate HUVECs and MSCs to form tube-like structures, nor did tri-culturing with MCF-7 cancer cells. After 4 days in culture, 1 % and 10 % RGD functionalisation resulted in increased DNA concentration of HUVECs and MSCs. After 7 days, DNA yield appeared to reduce, showing that RGD functionalisation was not sufficient to maintain the long-term growth of HUVECs and MSCs within PeptiGelAlpha1. CD31 expression was retained in HUVECs in the absence and presence of RGD functionalisation, showing that HUVEC phenotype was maintained.

The benefits of RGD-mediated cell attachment were concentration-dependent; it is likely that crowding of the network with ligands resulted in cells no longer able to recognise and attach to the matrix. This was highlighted by the rounded morphology of HUVECs and MSCs when cultured in PeptiGelAlpha1 functionalised with 15 % RGD and 15 % IKVAV. It could not be concluded if the cells were attaching to the RGD domains specifically by integrin binding. However, RGD functionalisation did not have any effect on  $\beta$ -sheet formation or fibre morphology, but the mechanical properties were affected. Given the sensitivity of HUVECs, it is likely that a multi-faceted approach is needed to stimulate tube formation of HUVECs and MSCs within PeptiGelAlpha1, such as by combining RGD functionalisation with softer mechanical properties and growth factor supplementation.

It was hypothesised that an ionic complementary SAPH system would be able to support the 3D culture, growth and *in vitro* modelling of the MCF-7 and MDA-MB-231 breast cancer cell lines, as well as support tube formation of HUVECs and MSCs, with appropriate material modifications if needed. The data presented in this thesis support the hypothesis that PeptiGelAlpha1 is a suitable candidate for MCF-7 and MDA-MB-231 cell growth and 3D culture. However, MCF-7 cells appeared to be more active within the hydrogel than MDA-MB-231 cells, therefore the data in this thesis support the hypothesis that PeptiGelAlpha1 may be more appropriate for *in vitro* modelling of early stage breast cancer cell lines. Regarding HUVEC and MSC behaviour, RGD functionalisation was able to stimulate cell elongation and increase proliferation, but was not sufficient to promote tube formation. Therefore, more work is needed to support the hypothesis that PeptiGelAlpha1 alone is suitable for modelling vasculature formation *in vitro* using HUVECs and MSCs.

The novelty of this research lies in several findings and approaches. As a chemically defined platform, PeptiGelAlpha1 exhibited a uniform nanofibre architecture, and superior mechanical properties compared to collagen I and Matrigel. The recovery profiles of collagen I and Matrigel were characterised for the first time. Two breast cancer cell lines (MCF-7 and MDA-MB-231) representing different stages of the disease were used, alongside HUVECs and MSCs to mimic vasculature *in vitro*. None of these cell lines have been used previously with this commercially available hydrogel. Internalisation of the peptide hydrogel fibres by MCF-7 cells has not been observed previously with a cancer cell line and therefore offers a novel approach of drug delivery *in vitro*. Preliminary data suggested that the hydrogel could impede the efficacy of tamoxifen treatment *in vitro*. RGD functionalisation offered a concentration-dependent benefit to HUVEC and MSC

behaviour, but only up to a certain point. Saturation of the hydrogel network with cell-binding motifs is therefore a factor to consider when designing functionalised hydrogels.

The implications of this work hold significance for several research fields. Firstly, biomaterials and tissue engineering researchers can benefit from the viscoelastic behaviour and nanofibre diameter data presented in **Chapter 4** of PeptiGelAlpha1, collagen I and Matrigel, helping users make an informed choice about which platform is most suitable for their own research. The MCF-7 and MDA-MB-231 cell lines are commonly used in breast cancer research; therefore their encapsulation and subsequent behaviour profiles within PeptiGelAlpha1, as demonstrated in **Chapter 5**, can allow for the probing of tumour progression mechanisms in synthetic 3D *in vitro* platforms. The drug efficacy data also support the notion that SAPHs can act as a physical barrier to chemotherapeutic drugs, aiding drug development research. The RGD functionalisation study can aid the design of hydrogels for tissue engineering applications, and provide a stepping-stone for the fabrication of tissue engineered blood vessels within SAPHs, as presented in **Chapter 6**. As well, SAPH users can also benefit from the assays presented herein and adopt these into their own research.

In conclusion, the findings in this thesis provide proof that PeptiGelAlpha1 could be used for *in vitro* modelling of early breast cancer and that events of tumour progression, such as hypoxia, invasion and drug resistance are reliably mimicked. PeptiGelAlpha1 is potentially a more suitable material for developing *in vitro* models of breast cancer compared with naturally derived hydrogels, due to its chemical definition and relevant mechanical properties. However, PeptiGelAlpha1 alone may be more suitable for modelling early breast cancer, whilst functionalisation of the hydrogel may be required to maintain the invasive/malignant phenotype of the MDA-MB-231 and other invasive breast cancer cell lines. Whilst RGD functionalisation resulted in HUVEC and MSC elongation and increased cell density, it was not sufficient for the cells to differentiate into tube-like structures. More work is therefore needed to identify the parameters to induce angiogenesis within PeptiGelAlpha1 and similar systems. These data have implications for research into 3D *in vitro* modelling of cancer, tissue engineering blood vessels *in vitro*, hydrogel design and pharmaceutical development of anti-cancer drugs.

## 7.2. Future Work

In regards to future work, gene expression studies of EMT markers need to be carried out to establish if the EMT status of the cells is changing when encapsulated in PeptiGelAlpha1, such as by using RNA sequencing or RT-PCR. In addition, artificially inducing EMT with TGF $\beta$  would enable exploration of EMT mechanisms using a 3D synthetic platform. To explore the hypoxia data further, measuring oxygen concentration in different regions of the hydrogel would reveal if the cells were becoming hypoxic due to reduced oxygen diffusion spatially. This could be achieved using fluorescent microparticles [401] or using an electrode-based oxygen microsensor [402]. Exploring why the MCF-7 cells were taking up the hydrogel would provide some insight into cell-material interactions and nutrient scavenging *in vitro*, as well as determine if the cells would internalise drug-laden hydrogel. Lysosome activity of MCF-7 cells and atomic force microscopy-infrared spectroscopy (AFM-IR) mapping were initially pursued to explore this further, but time constraints resulted in suspension of this work. Lysosome activity would determine if the hydrogel was being metabolised and degraded within the cell organelles, which is observed with nutrient scavenging *in vivo* [331]. AFM-IR mapping would couple imaging of the cell-laden hydrogel with analysing the IR spectra of specific regions within the sample [403]. Both of the aforementioned approaches alongside quantifying glucose consumption and lactic acid production, which have previously been utilised to investigate peptide fibre entrapment by cells [216], would determine if the cells were scavenging the hydrogel for additional nutrients. TEM imaging with MCF-7 cell-laden hydrogel samples exposed to chemotherapeutic drug treatment in the cell culture media would reveal if the cells would internalise drug-laden hydrogel. The downstream effects of this could be analysed by observing if this affects the efficacy profile of the drug, and observing if the drug reaches the centre of the spheroids formed by the MCF-7 cells. This could be supplemented further by incorporating nanoparticles containing anti-cancer drugs into the hydrogel, to observe if the cells would internalise these alongside the hydrogel.

More work is needed to confidently assess if PeptiGelAlpha1 can act as a physical barrier to anti-cancer drugs, particularly tamoxifen treatment. Further repeats of drug efficacy experiments and dose-response curves are needed to provide a range of IC<sub>50</sub> values. This would reliably determine the efficacy of tamoxifen and doxorubicin with PeptiGelAlpha1. Performing drug efficacy experiments at later time points, such as after 14 days in culture when the MCF-7 cells have formed large spheroids, would reveal if the culture period and spheroid size has any bearing on drug sensitivity.

Further work is also needed to establish how to induce tube formation by HUVECs and MSCs within SAPHs and identify the parameters needed. In regards to functionalisation with ECM derived binding motifs, labelling of the ligand with gold or a fluorescent protein would enable ligand distribution and network density to be observed. This would help determine the threshold concentration at which network saturation occurs, for a binding motif such as the RGD domain. Further work needs to determine if HUVECs and MSCs were responding to the RGD stimulus via integrin binding; dual blocking of the  $\alpha_5\beta_1$  and  $\alpha_v\beta_3$  integrins would help to explore this further.

Factors that were not studied in this project to stimulate HUVEC and MSC growth include matrix stiffness and the influence of growth factors. Alongside functionalisation, growth factor supplementation within the hydrogel as well as softer mechanical properties may be necessary. Although VEGF, IGF, FGF and EGF were included in the ECGM-2 cell culture media, it is possible that the growth factors could not diffuse through the hydrogel.

Enriching the hydrogel with angiogenic growth factors from within may be necessary to induce tube formation of HUVECs and MSCs, as used with previous studies [30]. Diluting PeptiGelAlpha1 to weaken the mechanical properties would determine if HUVECs and MSCs would respond to a softer environment. One factor, which was also not considered, was the influence of pH on cell growth. PeptiGelAlpha1 has a pH of 4 before the addition of cell culture media [21]; cells encapsulated therefore experience this relatively acidic environment prior to media conditioning. It is possible that the primary HUVECs and MSCs are too sensitive for this pH. A SAPH with an initial physiological pH may be necessary to support the growth of these cell types. Rather than inducing spontaneous angiogenesis, fabricating vascular networks using 3D printing could offer a solution, as seen with other studies [15,175].

To fully mimic the TME, additional cell types such as fibroblasts and white blood cells, need to be incorporated. Future work should explore if PeptiGelAlpha1 can support the growth and viability of these stromal cells by using the LIVE/DEAD and PicoGreen assays utilised in this thesis. Investigating breast to bone metastasis by incorporating bone cells would also enhance the complexity of this model [404]. One approach to mimic the stromal component (including vasculature) would be to surround the cancer cell-laden hydrogel with another SAPH containing the stromal cells, as seen in other studies modelling the TME *in vitro* [30,323,405,406].



Furthermore, performing rheological and histological studies on *ex vivo* breast tumour tissue samples and comparison with this *in vitro* model would confirm if PeptiGelAlpha1 could indeed mimic the stiffness and histoarchitecture of breast tumour tissue.

Exploring the use of cell lines representing cancers from other tissues within PeptiGelAlpha1 would also be worthwhile, to investigate if the material can mimic other tumour types *in vitro*. This would expand the versatility of this hydrogel and allow comparisons to be made between cell lines from different cancer types, in regards to disease progression and drug efficacy.

Personalised medicine is becoming more commonplace to identify chemotherapeutic drugs that will target the patient's cells *in vitro*, instead of trialling them directly in the clinic. A 3D synthetic platform, such as PeptiGelAlpha1, would be a suitable candidate as a platform for this use, due to its chemical definition [407]. It would be useful to determine how primary cancer cells respond when cultured within PeptiGelAlpha1, as a logical step towards using the hydrogel as a platform for streamlining selection of an anti-cancer drug [408].

## CHAPTER 8 – References

- [1] F. Bray, J. Ferlay, I. Soerjomataram, R.L. Siegel, L.A. Torre, A. Jemal, Global cancer statistics 2018: GLOBOCAN estimates of incidence and mortality worldwide for 36 cancers in 185 countries, *CA. Cancer J. Clin.* 68 (2018) 394–424. <https://doi.org/10.3322/caac.21492>.
- [2] C.A. Klein, Cancer progression and the invisible phase of metastatic colonization, *Nat. Rev. Cancer.* 20 (2020) 681–694. <https://doi.org/10.1038/s41568-020-00300-6>.
- [3] K.D. Miller, R.L. Siegel, C.C. Lin, A.B. Mariotto, J.L. Kramer, J.H. Rowland, K.D. Stein, R. Alteri, A. Jemal, Cancer treatment and survivorship statistics, 2016, *CA. Cancer J. Clin.* 66 (2016) 271–289. <https://doi.org/10.3322/caac.21349>.
- [4] K.D. Miller, L. Nogueira, A.B. Mariotto, J.H. Rowland, K.R. Yabroff, C.M. Alfano, A. Jemal, J.L. Kramer, R.L. Siegel, Cancer treatment and survivorship statistics, 2019, *CA. Cancer J. Clin.* 69 (2019) 363–385. <https://doi.org/10.3322/caac.21565>.
- [5] F.R. Balkwill, M. Capasso, T. Hagemann, The tumor microenvironment at a glance, *J. Cell Sci.* 125 (2013).
- [6] A.W. Holle, J.L. Young, J.P. Spatz, In vitro cancer cell–ECM interactions inform in vivo cancer treatment, *Adv. Drug Deliv. Rev.* 97 (2016) 270–279. <https://doi.org/10.1016/J.ADDR.2015.10.007>.
- [7] S. Roberts, V. Speirs, Advances in the development of improved animal-free models for use in breast cancer biomedical research, *Biophys. Rev.* 9 (2017) 321–327. <https://doi.org/10.1007/s12551-017-0276-4>.
- [8] L. Gurski, N. Petrelli, X. Jia, 3D matrices for anti-cancer drug testing and development, *Oncology.* (2010). <https://pdfs.semanticscholar.org/37ea/af4f0202f10994e76ac6aa028228050934cd.pdf> (accessed April 19, 2017).
- [9] S. Breslin, L. O’Driscoll, Three-dimensional cell culture: the missing link in drug discovery, *Drug Discov. Today.* 18 (2013) 240–249. <https://doi.org/10.1016/j.drudis.2012.10.003>.
- [10] R.M. Sutherland, J.A. McCredie, W.R. Inch, Growth of multicell spheroids in tissue culture as a model of nodular carcinomas., *J. Natl. Cancer Inst.* 46 (1971) 113–20. <http://www.ncbi.nlm.nih.gov/pubmed/5101993> (accessed May 30, 2017).
- [11] D. Hanahan, R.A. Weinberg, Hallmarks of Cancer: The Next Generation, *Cell.* 144 (2011) 646–674. <https://doi.org/10.1016/j.cell.2011.02.013>.
- [12] D.W. Hutmacher, Biomaterials offer cancer research the third dimension, *Nat. Mater.* 9 (2010) 90–93. <https://doi.org/10.1038/nmat2619>.
- [13] C.J. Lovitt, T.B. Shelper, V.M. Avery, Doxorubicin resistance in breast cancer cells is mediated by extracellular matrix proteins, *BMC Cancer.* 18 (2018) 41. <https://doi.org/10.1186/s12885-017-3953-6>.
- [14] T. Magdeldin, V. López-Dávila, J. Pape, G.W.W. Cameron, M. Emberton, M. Loizidou, U. Cheema, Engineering a vascularised 3D in vitro model of cancer progression, *Sci. Rep.* 7 (2017) 44045. <https://doi.org/10.1038/srep44045>.

- [15] S. Han, S. Kim, Z. Chen, H.K. Shin, S.Y. Lee, H.E. Moon, S.H. Paek, S. Park, 3D bioprinted vascularized tumour for drug testing, *Int. J. Mol. Sci.* 21 (2020). <https://doi.org/10.3390/ijms21082993>.
- [16] A. Suo, W. Xu, Y. Wang, T. Sun, L. Ji, J. Qian, Dual-degradable and injectable hyaluronic acid hydrogel mimicking extracellular matrix for 3D culture of breast cancer MCF-7 cells, *Carbohydr. Polym.* 211 (2019) 336–348. <https://doi.org/10.1016/j.carbpol.2019.01.115>.
- [17] X. Ding, H. Zhao, Y. Li, A.L. Lee, Z. Li, M. Fu, C. Li, Y.Y. Yang, P. Yuan, Synthetic peptide hydrogels as 3D scaffolds for tissue engineering, *Adv. Drug Deliv. Rev.* 160 (2020) 78–104. <https://doi.org/10.1016/j.addr.2020.10.005>.
- [18] S. Zhang, Emerging biological materials through molecular self-assembly, *Biotechnol. Adv.* 20 (2002) 321–339. [https://doi.org/10.1016/S0734-9750\(02\)00026-5](https://doi.org/10.1016/S0734-9750(02)00026-5).
- [19] D.F. Williams, On the mechanisms of biocompatibility, *Biomaterials.* 29 (2008) 2941–2953. <https://doi.org/10.1016/j.biomaterials.2008.04.023>.
- [20] J.E. Gough, A. Saiani, A.F. Miller, Peptide hydrogels: mimicking the extracellular matrix, *Bioinspired, Biomim. Nanobiomaterials.* 1 (2012) 4–12. <https://doi.org/10.1680/bbn.11.00007>.
- [21] D. Kumar, V.L. Workman, M. O'Brien, J. McLaren, L. White, K. Raganath, F. Rose, A. Saiani, J.E. Gough, Peptide Hydrogels-A Tissue Engineering Strategy for the Prevention of Oesophageal Strictures, *Adv. Funct. Mater.* 27 (2017) 1702424. <https://doi.org/10.1002/adfm.201702424>.
- [22] A. Imere, C. Ligorio, M. O'Brien, J.K.F. Wong, M. Domingos, S.H. Cartmell, Engineering a cell-hydrogel-fibre composite to mimic the structure and function of the tendon synovial sheath, *Acta Biomater.* (2020). <https://doi.org/10.1016/j.actbio.2020.11.017>.
- [23] A. Faroni, V.L. Workman, A. Saiani, A.J. Reid, Self-Assembling Peptide Hydrogel Matrices Improve the Neurotrophic Potential of Human Adipose-Derived Stem Cells, *Adv. Healthc. Mater.* (2019) 1900410. <https://doi.org/10.1002/adhm.201900410>.
- [24] Ş. Comşa, A.M. Cîmpean, M. Raica, The Story of MCF-7 Breast Cancer Cell Line: 40 years of Experience in Research., *Anticancer Res.* 35 (2015) 3147–54. <http://www.ncbi.nlm.nih.gov/pubmed/26026074> (accessed June 15, 2017).
- [25] K.J. Chavez, S. V. Garimella, S. Lipkowitz, Triple negative breast cancer cell lines: One tool in the search for better treatment of triple negative breast cancer, *Breast Dis.* 32 (2010) 35–48. <https://doi.org/10.3233/BD-2010-0307>.
- [26] N. Koike, D. Fukumura, O. Gralla, P. Au, J.S. Schechner, R.K. Jain, Tissue engineering: Creation of long-lasting blood vessels, *Nature.* 428 (2004) 138–139. <https://doi.org/10.1038/428138a>.
- [27] H. Huang, Y. Ding, X.S. Sun, T.A. Nguyen, Peptide hydrogelation and cell encapsulation for 3D culture of MCF-7 breast cancer cells., *PLoS One.* 8 (2013) e59482. <https://doi.org/10.1371/journal.pone.0059482>.
- [28] K. Mi, G. Wang, Z. Liu, Z. Feng, B. Huang, X. Zhao, Influence of a Self-

- Assembling Peptide, RADA16, Compared with Collagen I and Matrigel on the Malignant Phenotype of Human Breast-Cancer Cells in 3D Cultures and *in vivo*, *Macromol. Biosci.* 9 (2009) 437–443. <https://doi.org/10.1002/mabi.200800262>.
- [29] J.C. Ashworth, J.L. Thompson, J.R. James, C.E. Slater, S. Pijuan-Galitó, K. Lis-Slimak, R.J. Holley, K.A. Meade, A. Thompson, K.P. Arkill, M. Tassieri, A.J. Wright, G. Farnie, C.L.R. Merry, Peptide gels of fully-defined composition and mechanics for probing cell-cell and cell-matrix interactions *in vitro*, *Matrix Biol.* 85–86 (2020) 15–33. <https://doi.org/10.1016/j.matbio.2019.06.009>.
- [30] C.L. Hedegaard, C. Redondo-Gómez, B.Y. Tan, K.W. Ng, D. Loessner, A. Mata, Peptide-protein coassembling matrices as a biomimetic 3d model of ovarian cancer, *Sci. Adv.* 6 (2020). <https://doi.org/10.1126/sciadv.abb3298>.
- [31] G. Benton, G. DeGray, H.K. Kleinman, J. George, I. Arnaoutova, *In vitro* microtumors provide a physiologically predictive tool for breast cancer therapeutic screening., *PLoS One.* 10 (2015) e0123312. <https://doi.org/10.1371/journal.pone.0123312>.
- [32] P. Worthington, K.M. Drake, Z. Li, A.D. Napper, D.J. Pochan, S.A. Langhans, Beta-hairpin hydrogels as scaffolds for high-throughput drug discovery in three-dimensional cell culture, (2017). <https://doi.org/10.1016/j.ab.2017.07.024>.
- [33] P. Worthington, D.J. Pochan, S.A. Langhans, Peptide Hydrogels – Versatile Matrices for 3D Cell Culture in Cancer Medicine, *Front. Oncol.* 5 (2015) 92. <https://doi.org/10.3389/fonc.2015.00092>.
- [34] D.A. Narmoneva, O. Oni, A.L. Sieminski, S. Zhang, J.P. Gertler, R.D. Kamm, R.T. Lee, Self-assembling short oligopeptides and the promotion of angiogenesis, *Biomaterials.* 26 (2005) 4837–4846. <https://doi.org/10.1016/j.biomaterials.2005.01.005>.
- [35] C. Tang, X. Shao, B. Sun, W. Huang, X. Zhao, The effect of self-assembling peptide RADA16-I on the growth of human leukemia cells *in vitro* and in nude mice., *Int. J. Mol. Sci.* 10 (2009) 2136–45. <https://doi.org/10.3390/ijms10052136>.
- [36] A.L. Sieminski, A.A.S. Was, A.G. Kim, A.H. Gong, A.R.D. Kamm, The Stiffness of Three-dimensional Ionic Self-assembling Peptide Gels Affects the Extent of Capillary-like Network Formation, (2007). <https://doi.org/10.1007/s12013-007-0046-1>.
- [37] X. Dai, H. Cheng, Z. Bai, J. Li, Breast cancer cell line classification and Its relevance with breast tumor subtyping, *J. Cancer.* 8 (2017) 3131–3141. <https://doi.org/10.7150/jca.18457>.
- [38] J.P. Jung, J. V. Moyano, J.H. Collier, Multifactorial optimization of endothelial cell growth using modular synthetic extracellular matrices, *Integr. Biol.* 3 (2011) 185. <https://doi.org/10.1039/c0ib00112k>.
- [39] R.L. Saunders, D.A. Hammer, Assembly of Human Umbilical Vein Endothelial Cells on Compliant Hydrogels., *Cell. Mol. Bioeng.* 3 (2010) 60–67. <https://doi.org/10.1007/s12195-010-0112-4>.
- [40] A. Khademhosseini, R. Langer, A decade of progress in tissue engineering, *Nat. Protoc.* 11 (2016) 1775–1781. <https://doi.org/10.1038/nprot.2016.123>.

- [41] D.F. Williams, On the nature of biomaterials, *Biomaterials*. 30 (2009) 5897–5909. <https://doi.org/10.1016/j.biomaterials.2009.07.027>.
- [42] J. Whitlow, A. Paul, A. Polini, Bioactive materials: Definitions and application in tissue engineering and regeneration therapy, in: *Adv. Struct. Mater.*, Springer Verlag, 2016: pp. 1–17. [https://doi.org/10.1007/978-3-319-44249-5\\_1](https://doi.org/10.1007/978-3-319-44249-5_1).
- [43] K.H. Benam, S. Dauth, B. Hassell, A. Herland, A. Jain, K.J. Jang, K. Karalis, H.J. Kim, L. MacQueen, R. Mahmoodian, S. Musah, Y.S. Torisawa, A.D. Van Der Meer, R. Villenave, M. Yadid, K.K. Parker, D.E. Ingber, Engineered in vitro disease models, *Annu. Rev. Pathol. Mech. Dis.* 10 (2015) 195–262. <https://doi.org/10.1146/annurev-pathol-012414-040418>.
- [44] D. Hanahan, R.A. Weinberg, The Hallmarks of Cancer Review evolve progressively from normalcy via a series of pre, *Cell*. 100 (2000) 57–70. [http://ac.els-cdn.com/S0092867400816839/1-s2.0-S0092867400816839-main.pdf?\\_tid=016082f6-2f21-11e7-a68d-00000aacb35e&acdnat=1493720626\\_be7908404fc126b022dd0422c3cd0ef8](http://ac.els-cdn.com/S0092867400816839/1-s2.0-S0092867400816839-main.pdf?_tid=016082f6-2f21-11e7-a68d-00000aacb35e&acdnat=1493720626_be7908404fc126b022dd0422c3cd0ef8) (accessed May 2, 2017).
- [45] F. Runa, S. Hamalian, K. Meade, P. Shisgal, P.C. Gray, J.A. Kelber, Tumor Microenvironment Heterogeneity: Challenges and Opportunities, (n.d.). <https://doi.org/10.1007/s40610-017-0073-7>.
- [46] M. Junttila, F. de Sauvage, Influence of tumour micro-environment heterogeneity on therapeutic response, *Nature*. 501 (2013) 346–354. <https://doi.org/10.1038/nature12626>.
- [47] J. Winkler, A. Abisoye-Ogunniyan, K.J. Metcalf, Z. Werb, Concepts of extracellular matrix remodelling in tumour progression and metastasis, *Nat. Commun.* 11 (2020). <https://doi.org/10.1038/s41467-020-18794-x>.
- [48] S. Kaushik, M.W. Pickup, V.M. Weaver, From transformation to metastasis: deconstructing the extracellular matrix in breast cancer., *Cancer Metastasis Rev.* 35 (2016) 655–667. <https://doi.org/10.1007/s10555-016-9650-0>.
- [49] P. Lu, V.M. Weaver, Z. Werb, The extracellular matrix: A dynamic niche in cancer progression, *J. Cell Biol.* 196 (2012). <http://jcb.rupress.org/content/196/4/395> (accessed April 19, 2017).
- [50] J. Insua-Rodríguez, T. Oskarsson, The extracellular matrix in breast cancer, *Adv. Drug Deliv. Rev.* 97 (2016) 41–55. <https://doi.org/10.1016/j.addr.2015.12.017>.
- [51] I. Acerbi, L. Cassereau, I. Dean, Q. Shi, A. Au, C. Park, Y.Y. Chen, J. Liphardt, E.S. Hwang, V.M. Weaver, Human breast cancer invasion and aggression correlates with ECM stiffening and immune cell infiltration., *Integr. Biol. (Camb)*. 7 (2015) 1120–34. <https://doi.org/10.1039/c5ib00040h>.
- [52] J. Fenner, A.C. Stacer, F. Winterroth, T.D. Johnson, K.E. Luker, G.D. Luker, Macroscopic Stiffness of Breast Tumors Predicts Metastasis, *Sci. Rep.* 4 (2015) 5512. <https://doi.org/10.1038/srep05512>.
- [53] C. Rianna, P. Kumar, M. Radmacher, The role of the microenvironment in the biophysics of cancer, *Semin. Cell Dev. Biol.* 73 (2018) 107–114. <https://doi.org/10.1016/J.SEMCDB.2017.07.022>.

- [54] M. Egeblad, Z. Werb, New functions for the matrix metalloproteinases in cancer progression, *Nat. Rev. Cancer.* 2 (2002) 161–174. <https://doi.org/10.1038/nrc745>.
- [55] C. Gialeli, A.D. Theocharis, N.K. Karamanos, Roles of matrix metalloproteinases in cancer progression and their pharmacological targeting, *FEBS J.* 278 (2011) 16–27. <https://doi.org/10.1111/j.1742-4658.2010.07919.x>.
- [56] P. Schedin, P.J. Keely, Mammary gland ECM remodeling, stiffness, and mechanosignaling in normal development and tumor progression., *Cold Spring Harb. Perspect. Biol.* 3 (2011) a003228. <https://doi.org/10.1101/cshperspect.a003228>.
- [57] A. Jabłońska-Trypuć, M. Matejczyk, S. Rosochacki, Matrix metalloproteinases (MMPs), the main extracellular matrix (ECM) enzymes in collagen degradation, as a target for anticancer drugs, *J. Enzyme Inhib. Med. Chem.* 31 (2016) 177–183. <https://doi.org/10.3109/14756366.2016.1161620>.
- [58] G.E. Davis, D.R. Senger, Endothelial extracellular matrix: Biosynthesis, remodeling, and functions during vascular morphogenesis and neovessel stabilization, *Circ. Res.* 97 (2005) 1093–1107. <https://doi.org/10.1161/01.RES.0000191547.64391.e3>.
- [59] T.H. Adair, J.-P. Montani, Overview of Angiogenesis, (2010). <https://www.ncbi.nlm.nih.gov/books/NBK53238/> (accessed July 9, 2020).
- [60] Y. Mao, E.T. Keller, D.H. Garfield, K. Shen, J. Wang, Stromal cells in tumor microenvironment and breast cancer., *Cancer Metastasis Rev.* 32 (2013) 303–15. <https://doi.org/10.1007/s10555-012-9415-3>.
- [61] E. Sahai, I. Astsaturov, E. Cukierman, D.G. DeNardo, M. Egeblad, R.M. Evans, D. Fearon, F.R. Greten, S.R. Hingorani, T. Hunter, R.O. Hynes, R.K. Jain, T. Janowitz, C. Jorgensen, A.C. Kimmelman, M.G. Kolonin, R.G. Maki, R.S. Powers, E. Puré, D.C. Ramirez, R. Scherz-Shouval, M.H. Sherman, S. Stewart, T.D. Tlsty, D.A. Tuveson, F.M. Watt, V. Weaver, A.T. Weeraratna, Z. Werb, A framework for advancing our understanding of cancer-associated fibroblasts, *Nat. Rev. Cancer.* 20 (2020) 174–186. <https://doi.org/10.1038/s41568-019-0238-1>.
- [62] C.E. Weber, A.N. Kothari, P.Y. Wai, N.Y. Li, J. Driver, M.A.C. Zapf, C.A. Franzen, G.N. Gupta, C. Osipo, A. Zlobin, W.K. Syn, J. Zhang, P.C. Kuo, Z. Mi, Osteopontin mediates an MZF1-TGF- $\beta$ 1-dependent transformation of mesenchymal stem cells into cancer-associated fibroblasts in breast cancer, *Oncogene.* 34 (2015) 4821–4833. <https://doi.org/10.1038/onc.2014.410>.
- [63] N. Dumont, B. Liu, R.A. Defilippis, H. Chang, J.T. Rabban, A.N. Karnezis, J.A. Tjoe, J. Marx, B. Parvin, T.D. Tlsty, Breast fibroblasts modulate early dissemination, tumorigenesis, and metastasis through alteration of extracellular matrix characteristics, *Neoplasia (United States).* 15 (2013) 249–262. <https://doi.org/10.1593/neo.121950>.
- [64] T. Liu, C. Han, S. Wang, P. Fang, Z. Ma, L. Xu, R. Yin, Cancer-associated fibroblasts: An emerging target of anti-cancer immunotherapy, *J. Hematol. Oncol.* 12 (2019) 86. <https://doi.org/10.1186/s13045-019-0770-1>.
- [65] K.J. Cullen, H.S. Smith, S. Hill, N. Rosen, M.E. Lippman, Growth Factor Messenger RNA Expression by Human Breast Fibroblasts from Benign and Malignant Lesions, *Cancer Res.* 51 (1991).

- [66] L. Tao, G. Huang, H. Song, Y. Chen, L. Chen, Cancer associated fibroblasts: An essential role in the tumor microenvironment (review), *Oncol. Lett.* 14 (2017) 2611–2620. <https://doi.org/10.3892/ol.2017.6497>.
- [67] S.J. Turley, V. Cremasco, J.L. Astarita, Immunological hallmarks of stromal cells in the tumour microenvironment, *Nat. Rev. Immunol.* 15 (2015) 669–682. <https://doi.org/10.1038/nri3902>.
- [68] V. Chew, H.C. Toh, J.-P. Abastado, Immune Microenvironment in Tumor Progression: Characteristics and Challenges for Therapy, *J. Oncol.* 2012 (2012) 1–10. <https://doi.org/10.1155/2012/608406>.
- [69] L. Hui, Y. Chen, Tumor microenvironment: Sanctuary of the devil, *Cancer Lett.* 368 (2015) 7–13. <https://doi.org/10.1016/j.canlet.2015.07.039>.
- [70] P. Carmeliet, R.K. Jain, Angiogenesis in cancer and other diseases, *Nature*, Publ. Online 14 Sept. 2000; | Doi10.1038/35025220. 407 (2000) 249. <https://doi.org/10.1038/35025220>.
- [71] A.S. Chung, J. Lee, N. Ferrara, Targeting the tumour vasculature: insights from physiological angiogenesis, *Nat. Rev. Cancer.* 10 (2010) 505–514. <https://doi.org/10.1038/nrc2868>.
- [72] M.B. Schaaf, A.D. Garg, P. Agostinis, Defining the role of the tumor vasculature in antitumor immunity and immunotherapy article, *Cell Death Dis.* 9 (2018) 1–14. <https://doi.org/10.1038/s41419-017-0061-0>.
- [73] S.M. Weis, D.A. Cheresh, Tumor angiogenesis: molecular pathways and therapeutic targets, *Nat. Med.* 17 (2011) 1359–1370. <https://doi.org/10.1038/nm.2537>.
- [74] N. Makrilia, T. Lappa, V. Xyla, I. Nikolaidis, K. Syrigos, The role of angiogenesis in solid tumours: an overview., *Eur. J. Intern. Med.* 20 (2009) 663–71. <https://doi.org/10.1016/j.ejim.2009.07.009>.
- [75] S. Krishna Priya, R.P. Nagare, V.S. Sneha, C. Sidhanth, S. Bindhya, P. Manasa, T.S. Ganesan, Tumour angiogenesis-Origin of blood vessels, *Int. J. Cancer.* 139 (2016) 729–735. <https://doi.org/10.1002/ijc.30067>.
- [76] F. Hillen, A.W. Griffioen, Tumour vascularization: sprouting angiogenesis and beyond, *Cancer Metastasis Rev.* 26 (2007) 489–502. <https://doi.org/10.1007/s10555-007-9094-7>.
- [77] V. Estrella, T. Chen, M. Lloyd, J. Wojtkowiak, H.H. Cornell, A. Ibrahim-Hashim, K. Bailey, Y. Balagurunathan, J.M. Rothberg, B.F. Sloane, J. Johnson, R.A. Gatenby, R.J. Gillies, Acidity generated by the tumor microenvironment drives local invasion., *Cancer Res.* 73 (2013) 1524–35. <https://doi.org/10.1158/0008-5472.CAN-12-2796>.
- [78] B.C. Prager, Q. Xie, S. Bao, J.N. Rich, Cell Stem Cell Perspective Cancer Stem Cells: The Architects of the Tumor Ecosystem, *Stem Cell.* 24 (2019) 41–53. <https://doi.org/10.1016/j.stem.2018.12.009>.
- [79] M. Saitoh, Involvement of partial EMT in cancer progression, *J. Biochem.* 164 (2018) 257–264. <https://doi.org/10.1093/jb/mvy047>.
- [80] F.M. Davis, T.A. Stewart, E.W. Thompson, G.R. Monteith, Targeting EMT in

- cancer: opportunities for pharmacological intervention, *Trends Pharmacol. Sci.* 35 (2014) 479–488. <https://doi.org/10.1016/j.tips.2014.06.006>.
- [81] A.I. Riggio, K.E. Varley, A.L. Welm, The lingering mysteries of metastatic recurrence in breast cancer, *Br. J. Cancer.* 124 (2021) 13–26. <https://doi.org/10.1038/s41416-020-01161-4>.
- [82] C.L. Chaffer, B.P. San Juan, E. Lim, R.A. Weinberg, EMT, cell plasticity and metastasis, *Cancer Metastasis Rev.* 35 (2016) 645–654. <https://doi.org/10.1007/s10555-016-9648-7>.
- [83] E. Romeo, C.A. Caserta, C. Rumio, F. Marcucci, The Vicious Cross-Talk between Tumor Cells with an EMT Phenotype and Cells of the Immune System, *Cells.* 8 (2019) 460. <https://doi.org/10.3390/cells8050460>.
- [84] T. Shibue, R.A. Weinberg, EMT, CSCs, and drug resistance: the mechanistic link and clinical implications, *Nat. Rev. Clin. Oncol.* 14 (2017) 611. <https://doi.org/10.1038/NRCLINONC.2017.44>.
- [85] B. De Craene, G. Berx, Regulatory networks defining EMT during cancer initiation and progression, *Nat. Rev. Cancer.* 13 (2013) 97–110. <https://doi.org/10.1038/nrc3447>.
- [86] P. Bronsert, K. Enderle-Ammour, M. Bader, S. Timme, M. Kuehs, A. Csanadi, G. Kayser, I. Kohler, D. Bausch, J. Hoepfner, U. Hopt, T. Keck, E. Stickeler, B. Passlick, O. Schilling, C. Reiss, Y. Vashist, T. Brabletz, J. Berger, J. Lotz, J. Olesch, M. Werner, U. Wellner, Cancer cell invasion and EMT marker expression: a three-dimensional study of the human cancer-host interface, *J. Pathol.* 234 (2014) 410–422. <https://doi.org/10.1002/path.4416>.
- [87] I. Pastushenko, C. Blanpain, EMT Transition States during Tumor Progression and Metastasis., *Trends Cell Biol.* 29 (2019) 212–226. <https://doi.org/10.1016/j.tcb.2018.12.001>.
- [88] A.Z. Ayob, T.S. Ramasamy, Cancer stem cells as key drivers of tumour progression, *J. Biomed. Sci.* 25 (2018) 20. <https://doi.org/10.1186/s12929-018-0426-4>.
- [89] S. Liu, Y. Cong, D. Wang, Y. Sun, L. Deng, Y. Liu, R. Martin-Trevino, L. Shang, S.P. McDermott, M.D. Landis, S. Hong, A. Adams, R. D'Angelo, C. Ginestier, E. Charafe-Jauffret, S.G. Clouthier, D. Birnbaum, S.T. Wong, M. Zhan, J.C. Chang, M.S. Wicha, Breast Cancer Stem Cells Transition between Epithelial and Mesenchymal States Reflective of their Normal Counterparts, *Stem Cell Reports.* 2 (2014) 78–91. <https://doi.org/10.1016/j.stemcr.2013.11.009>.
- [90] H. Korkaya, S. Liu, M.S. Wicha, Breast cancer stem cells, cytokine networks, and the tumor microenvironment., *J. Clin. Invest.* 121 (2011) 3804–9. <https://doi.org/10.1172/JCI57099>.
- [91] C. Ciardiello, A. Leone, A. Budillon, The Crosstalk between Cancer Stem Cells and Microenvironment Is Critical for Solid Tumor Progression: The Significant Contribution of Extracellular Vesicles, *Stem Cells Int.* 2018 (2018) 1–11. <https://doi.org/10.1155/2018/6392198>.
- [92] O. Tredan, C.M. Galmarini, K. Patel, I.F. Tannock, Drug Resistance and the Solid Tumor Microenvironment, *JNCI J. Natl. Cancer Inst.* 99 (2007) 1441–1454. <https://doi.org/10.1093/jnci/djm135>.



- [93] A.J. Rice, E. Cortes, D. Lachowski, B.C.H. Cheung, S.A. Karim, J.P. Morton, A. Del Río Hernández, Matrix stiffness induces epithelial-mesenchymal transition and promotes chemoresistance in pancreatic cancer cells., *Oncogenesis*. 6 (2017) e352. <https://doi.org/10.1038/oncsis.2017.54>.
- [94] C.-H. Heldin, K. Rubin, K. Pietras, A. Östman, High interstitial fluid pressure — an obstacle in cancer therapy, *Nat. Rev. Cancer*. 4 (2004) 806–813. <https://doi.org/10.1038/nrc1456>.
- [95] K.M. Comerford, T.J. Wallace, J. Karhausen, N.A. Louis, M.C. Montalto, S.P. Colgan, Hypoxia-inducible factor-1-dependent regulation of the multidrug resistance (MDR1) gene., *Cancer Res*. 62 (2002) 3387–94. <http://www.ncbi.nlm.nih.gov/pubmed/12067980> (accessed September 30, 2019).
- [96] S. Taylor, E.P. Spugnini, Y.G. Assaraf, T. Azzarito, C. Rauch, S. Fais, Microenvironment acidity as a major determinant of tumor chemoresistance: Proton pump inhibitors (PPIs) as a novel therapeutic approach, *Drug Resist. Updat*. 23 (2015) 69–78. <https://doi.org/10.1016/J.DRUP.2015.08.004>.
- [97] K.M. Bailey, J.W. Wojtkowiak, A.I. Hashim, R.J. Gillies, Targeting the Metabolic Microenvironment of Tumors, *Adv. Pharmacol*. 65 (2012) 63–107. <https://doi.org/10.1016/B978-0-12-397927-8.00004-X>.
- [98] A.W. Holle, J.L. Young, J.P. Spatz, In vitro cancer cell-ECM interactions inform in vivo cancer treatment, *Adv. Drug Deliv. Rev*. 97 (2016). <https://doi.org/10.1016/j.addr.2015.10.007>.
- [99] J.P. Yang, Y.D. Liao, D.M. Mai, P. Xie, Y.Y. Qiang, L.S. Zheng, M.Y. Wang, Y. Mei, D.F. Meng, L. Xu, L. Cao, Q. Yang, X.X. Yang, W.B. Wang, L.X. Peng, B.J. Huang, C.N. Qian, Tumor vasculogenic mimicry predicts poor prognosis in cancer patients: a meta-analysis, *Angiogenesis*. 19 (2016) 191–200. <https://doi.org/10.1007/s10456-016-9500-2>.
- [100] T. Liu, B. Sun, X. Zhao, Y. Li, Q. Gu, X. Dong, F. Liu, OCT4 expression and vasculogenic mimicry formation positively correlate with poor prognosis in human breast cancer, *Int. J. Mol. Sci*. 15 (2014) 19634–19649. <https://doi.org/10.3390/ijms151119634>.
- [101] C.J.H. Kramer, K.M.H. Vangangelt, G.W. van Pelt, T.J.A. Dekker, R.A.E.M. Tollenaar, W.E. Mesker, The prognostic value of tumour–stroma ratio in primary breast cancer with special attention to triple-negative tumours: a review, *Breast Cancer Res. Treat*. 173 (2019) 55–64. <https://doi.org/10.1007/s10549-018-4987-4>.
- [102] X. Zhao, J. Qu, Y. Sun, J. Wang, X. Liu, F. Wang, H. Zhang, W. Wang, X. Ma, X. Gao, S. Zhang, Prognostic significance of tumor-associated macrophages in breast cancer: a meta-analysis of the literature, *Oncotarget*. 8 (2017) 30576–30586. <https://doi.org/10.18632/oncotarget.15736>.
- [103] X. Zhang, Y. Lin, 542PResponse of apatinib in progressive radioactive iodine-refractory differentiated thyroid cancer: One-year follow-up study, *Ann. Oncol*. 28 (2017). <https://doi.org/10.1093/annonc/mdx725>.
- [104] C. Polydorou, F. Mpekris, P. Papageorgis, C. Voutouri, T. Stylianopoulos, Pifrenidone normalizes the tumor microenvironment to improve chemotherapy, *Oncotarget*. 8 (2017) 24506–24517. <https://doi.org/10.18632/oncotarget.15534>.

- [105] B. Diop-Frimpong, V.P. Chauhan, S. Krane, Y. Boucher, R.K. Jain, Losartan inhibits collagen I synthesis and improves the distribution and efficacy of nanotherapeutics in tumors., *Proc. Natl. Acad. Sci. U. S. A.* 108 (2011) 2909–14. <https://doi.org/10.1073/pnas.1018892108>.
- [106] R. Coulson, S.H. Liew, A.A. Connelly, N.S. Yee, S. Deb, B. Kumar, A.C. Vargas, S.A. O’Toole, A.C. Parslow, A. Poh, T. Putoczki, R.J. Morrow, M. Alorro, K.A. Lazarus, E.F.W. Yeap, K.L. Walton, C.A. Harrison, N.J. Hannan, A.J. George, C.D. Clyne, M. Ernst, A.M. Allen, A.L. Chand, R. Coulson, S.H. Liew, A.A. Connelly, N.S. Yee, S. Deb, B. Kumar, A.C. Vargas, S.A. O’Toole, A.C. Parslow, A. Poh, T. Putoczki, R.J. Morrow, M. Alorro, K.A. Lazarus, E.F.W. Yeap, K.L. Walton, C.A. Harrison, N.J. Hannan, A.J. George, C.D. Clyne, M. Ernst, A.M. Allen, A.L. Chand, The angiotensin receptor blocker, Losartan, inhibits mammary tumor development and progression to invasive carcinoma, *Oncotarget.* 8 (2017) 18640–18656. <https://doi.org/10.18632/oncotarget.15553>.
- [107] R. Edmondson, J.J. Broglie, A.F. Adcock, L. Yang, Three-dimensional cell culture systems and their applications in drug discovery and cell-based biosensors., *Assay Drug Dev. Technol.* 12 (2014) 207–18. <https://doi.org/10.1089/adt.2014.573>.
- [108] H. HogenEsch, A.Y. Nikitin, Challenges in pre-clinical testing of anti-cancer drugs in cell culture and in animal models., *J. Control. Release.* 164 (2012) 183–6. <https://doi.org/10.1016/j.jconrel.2012.02.031>.
- [109] U. McDermott, S. V. Sharma, J. Settleman, High-Throughput Lung Cancer Cell Line Screening for Genotype-Correlated Sensitivity to an EGFR Kinase Inhibitor, *Methods Enzymol.* 438 (2008) 331–341. [https://doi.org/10.1016/S0076-6879\(07\)38023-3](https://doi.org/10.1016/S0076-6879(07)38023-3).
- [110] A. Amelian, K. Wasilewska, D. Megias, K. Winnicka, Application of standard cell cultures and 3D in vitro tissue models as an effective tool in drug design and development, *Pharmacol. Reports.* 69 (2017) 861–870. <https://doi.org/10.1016/J.PHAREP.2017.03.014>.
- [111] K. Tanner, M.M. Gottesman, Beyond 3D culture models of cancer, *Sci. Transl. Med.* 7 (2015). <https://doi.org/10.1126/scitranslmed.3009367>.
- [112] X. Xu, M.C. Farach-Carson, X. Jia, Three-dimensional in vitro tumor models for cancer research and drug evaluation., *Biotechnol. Adv.* 32 (2014) 1256–68. <https://doi.org/10.1016/j.biotechadv.2014.07.009>.
- [113] L. Hutchinson, R. Kirk, High drug attrition rates—where are we going wrong?, *Nat. Rev. Clin. Oncol.* 8 (2011) 189–190. <https://doi.org/10.1038/nrclinonc.2011.34>.
- [114] H. Ledford, US cancer institute to overhaul tumour cell lines, *Nature.* 530 (2016) 391–391. <https://doi.org/10.1038/nature.2016.19364>.
- [115] B.A. Ruggeri, F. Camp, S. Miknyoczki, Animal models of disease: Pre-clinical animal models of cancer and their applications and utility in drug discovery, *Biochem. Pharmacol.* 87 (2014) 150–161. <https://doi.org/10.1016/j.bcp.2013.06.020>.
- [116] S.E. Gould, M.R. Junttila, F.J. de Sauvage, Translational value of mouse models in oncology drug development, *Nat. Med.* 21 (2015) 431–439. <https://doi.org/10.1038/nm.3853>.

- [117] L.H. Mengelbier, D. Bexell, D. Sehic, C.D. Ciornei, D. Gisselsson, Orthotopic Wilms tumor xenografts derived from cell lines reflect limited aspects of tumor morphology and clinical characteristics, *Pediatr. Blood Cancer*. 61 (2014) 1949–1954. <https://doi.org/10.1002/pbc.25131>.
- [118] L. Pompili, M. Porru, C. Caruso, A. Biroccio, C. Leonetti, Patient-derived xenografts: a relevant preclinical model for drug development., *J. Exp. Clin. Cancer Res*. 35 (2016) 189. <https://doi.org/10.1186/s13046-016-0462-4>.
- [119] Y. Zhang, G. Zhang, X. Sun, K. Cao, C. Ma, N. Nan, G. Yang, M. Yu, X. Wang, Establishment of a murine breast tumor model by subcutaneous or orthotopic implantation, *Oncol. Lett*. 15 (2018) 6233–6240. <https://doi.org/10.3892/ol.2018.8113>.
- [120] O.M. Rashid, M. Nagahashi, S. Ramachandran, C.I. Dumur, J.C. Schaum, A. Yamada, T. Aoyagi, S. Milstien, S. Spiegel, K. Takabe, Is tail vein injection a relevant breast cancer lung metastasis model?, *J. Thorac. Dis*. 5 (2013) 385–92. <https://doi.org/10.3978/j.issn.2072-1439.2013.06.17>.
- [121] M. Paez-Ribes, S. Man, P. Xu, R.S. Kerbel, Development of Patient Derived Xenograft Models of Overt Spontaneous Breast Cancer Metastasis: A Cautionary Note., *PLoS One*. 11 (2016) e0158034. <https://doi.org/10.1371/journal.pone.0158034>.
- [122] C. Krepler, K. Sproesser, P. Brafford, M. Beqiri, B. Garman, M. Xiao, B. Shannan, A. Watters, M. Perego, G. Zhang, A. Vultur, X. Yin, Q. Liu, I.N. Anastopoulos, B. Wubbenhorst, M.A. Wilson, W. Xu, G. Karakousis, M. Feldman, X. Xu, R. Amaravadi, T.C. Gangadhar, D.E. Elder, L.E. Haydu, J.A. Wargo, M.A. Davies, Y. Lu, G.B. Mills, D.T. Frederick, M. Barzily-Rokni, K.T. Flaherty, D.S. Hoon, M. Guarino, J.J. Bennett, R.W. Ryan, N.J. Petrelli, C.L. Shields, M. Terai, T. Sato, A.E. Aplin, A. Roesch, D. Darr, S. Angus, R. Kumar, E. Halilovic, G. Caponigro, S. Jeay, J. Wuerthner, A. Walter, M. Ocker, M.B. Boxer, L. Schuchter, K.L. Nathanson, M. Herlyn, A Comprehensive Patient-Derived Xenograft Collection Representing the Heterogeneity of Melanoma, *Cell Rep*. 21 (2017) 1953–1967. <https://doi.org/10.1016/j.celrep.2017.10.021>.
- [123] H. Gao, J.M. Korn, S. Ferretti, J.E. Monahan, Y. Wang, M. Singh, C. Zhang, C. Schnell, G. Yang, Y. Zhang, O.A. Balbin, S. Barbe, H. Cai, F. Casey, S. Chatterjee, D.Y. Chiang, S. Chuai, S.M. Cogan, S.D. Collins, E. Dammassa, N. Ebel, M. Embry, J. Green, A. Kauffmann, C. Kowal, R.J. Leary, J. Lehar, Y. Liang, A. Loo, E. Lorenzana, E. Robert McDonald, M.E. McLaughlin, J. Merkin, R. Meyer, T.L. Naylor, M. Patawaran, A. Reddy, C. Röelli, D.A. Ruddy, F. Salangsang, F. Santacroce, A.P. Singh, Y. Tang, W. Tinetto, S. Tobler, R. Velazquez, K. Venkatesan, F. Von Arx, H.Q. Wang, Z. Wang, M. Wiesmann, D. Wyss, F. Xu, H. Bitter, P. Atadja, E. Lees, F. Hofmann, E. Li, N. Keen, R. Cozens, M.R. Jensen, N.K. Pryer, J.A. Williams, W.R. Sellers, High-throughput screening using patient-derived tumor xenografts to predict clinical trial drug response, *Nat. Med*. 21 (2015) 1318–1325. <https://doi.org/10.1038/nm.3954>.
- [124] Y.S. DeRose, G. Wang, Y.-C. Lin, P.S. Bernard, S.S. Buys, M.T.W. Ebbert, R. Factor, C. Matsen, B.A. Milash, E. Nelson, L. Neumayer, R.L. Randall, I.J. Stijleman, B.E. Welm, A.L. Welm, Tumor grafts derived from women with breast cancer authentically reflect tumor pathology, growth, metastasis and disease outcomes, *Nat. Med*. 17 (2011) 1514–1520. <https://doi.org/10.1038/nm.2454>.

- [125] J. Maykel, J.H. Liu, H. Li, L.D. Shultz, D.L. Greiner, J. Houghton, NOD-scidII2rg (tm1Wjl) and NOD-Rag1 (null) Il2rg (tm1Wjl) : a model for stromal cell-tumor cell interaction for human colon cancer., *Dig. Dis. Sci.* 59 (2014) 1169–79. <https://doi.org/10.1007/s10620-014-3168-5>.
- [126] V.E. Schneeberger, V. Allaj, E.E. Gardner, J.T. Poirier, C.M. Rudin, Quantitation of Murine Stroma and Selective Purification of the Human Tumor Component of Patient-Derived Xenografts for Genomic Analysis., *PLoS One.* 11 (2016) e0160587. <https://doi.org/10.1371/journal.pone.0160587>.
- [127] N.E. Sharpless, R.A. DePinho, The mighty mouse: genetically engineered mouse models in cancer drug development, *Nat. Rev. Drug Discov.* 5 (2006) 741–754. <https://doi.org/10.1038/nrd2110>.
- [128] K. Politi, W. Pao, How genetically engineered mouse tumor models provide insights into human cancers., *J. Clin. Oncol.* 29 (2011) 2273–81. <https://doi.org/10.1200/JCO.2010.30.8304>.
- [129] R.D. Cardiff, M.R. Anver, B.A. Gusterson, L. Hennighausen, R.A. Jensen, M.J. Merino, S. Rehm, J. Russo, F.A. Tavassoli, L.M. Wakefield, J.M. Ward, J.E. Green, The mammary pathology of genetically engineered mice: the consensus report and recommendations from the Annapolis meeting†, *Oncogene.* 19 (2000) 968–988. <https://doi.org/10.1038/sj.onc.1203277>.
- [130] D.P. Hollern, M.R. Swiatnicki, E.R. Andrechek, Histological subtypes of mouse mammary tumors reveal conserved relationships to human cancers, *PLOS Genet.* 14 (2018) e1007135. <https://doi.org/10.1371/journal.pgen.1007135>.
- [131] D. Rodenhizer, T. Dean, E. D’Arcangelo, A.P. McGuigan, The Current Landscape of 3D In Vitro Tumor Models: What Cancer Hallmarks Are Accessible for Drug Discovery?, *Adv. Healthc. Mater.* 7 (2018) 1701174. <https://doi.org/10.1002/adhm.201701174>.
- [132] C.G. Gahmberg, S.C. Fagerholm, S.M. Nurmi, T. Chavakis, S. Marchesan, M. Grönholm, Regulation of integrin activity and signalling, *Biochim. Biophys. Acta - Gen. Subj.* 1790 (2009) 431–444. <https://doi.org/10.1016/j.bbagen.2009.03.007>.
- [133] B.M. Baker, C.S. Chen, Deconstructing the third dimension-how 3D culture microenvironments alter cellular cues, *J. Cell Sci.* 125 (2012) 3015–3024. <https://doi.org/10.1242/jcs.079509>.
- [134] C.F. Guimarães, L. Gasperini, A.P. Marques, R.L. Reis, The stiffness of living tissues and its implications for tissue engineering, *Nat. Rev. Mater.* (2020) 1–20. <https://doi.org/10.1038/s41578-019-0169-1>.
- [135] A.J. Engler, S. Sen, H.L. Sweeney, D.E. Discher, Matrix Elasticity Directs Stem Cell Lineage Specification, *Cell.* 126 (2006) 677–689. <https://doi.org/10.1016/j.cell.2006.06.044>.
- [136] S.L. Ham, R. Joshi, P.S. Thakuri, H. Tavana, Liquid-based three-dimensional tumor models for cancer research and drug discovery., *Exp. Biol. Med. (Maywood).* 241 (2016) 939–54. <https://doi.org/10.1177/1535370216643772>.
- [137] W. Asghar, R. El Assal, H. Shafiee, S. Pitteri, R. Paulmurugan, U. Demirci, Engineering cancer microenvironments for in vitro 3-D tumor models, *Mater. Today.* 18 (2015) 539–553. <https://doi.org/10.1016/j.mattod.2015.05.002>.

- [138] J.M. Kelm, N.E. Timmins, C.J. Brown, M. Fussenegger, L.K. Nielsen, Method for generation of homogeneous multicellular tumor spheroids applicable to a wide variety of cell types, *Biotechnol. Bioeng.* 83 (2003) 173–180. <https://doi.org/10.1002/bit.10655>.
- [139] A. Amann, M. Zwierzina, G. Gamerith, M. Bitsche, J.M. Huber, G.F. Vogel, M. Blumer, S. Koeck, E.J. Pechriggl, J.M. Kelm, W. Hilbe, H. Zwierzina, Development of an Innovative 3D Cell Culture System to Study Tumour - Stroma Interactions in Non-Small Cell Lung Cancer Cells, *PLoS One.* 9 (2014) e92511. <https://doi.org/10.1371/journal.pone.0092511>.
- [140] Y.-C. Tung, A.Y. Hsiao, S.G. Allen, Y. Torisawa, M. Ho, S. Takayama, High-throughput 3D spheroid culture and drug testing using a 384 hanging drop array, *Analyst.* 136 (2011) 473–478. <https://doi.org/10.1039/C0AN00609B>.
- [141] C. Morabito, N. Steimberg, G. Mazzoleni, S. Guarnieri, G. Fanò-Illic, M.A. Marigliò, RCCS Bioreactor-Based Modelled Microgravity Induces Significant Changes on *In Vitro* 3D Neuroglial Cell Cultures, *Biomed Res. Int.* 2015 (2015) 1–14. <https://doi.org/10.1155/2015/754283>.
- [142] J. Bin Kim, R. Stein, M.J. O’Hare, Three-dimensional in vitro tissue culture models of breast cancer — a review, *Breast Cancer Res. Treat.* 85 (2004) 281–291. <https://doi.org/10.1023/B:BREA.0000025418.88785.2b>.
- [143] M. Ingram, G.B. Techy, R. Saroufeem, O. Yazan, K.S. Narayan, T.J. Goodwin, G.F. Spaulding, Three-dimensional growth patterns of various human tumor cell lines in simulated microgravity of a NASA bioreactor, *Vitr. Cell. Dev. Biol. - Anim.* 33 (1997) 459–466. <https://doi.org/10.1007/s11626-997-0064-8>.
- [144] W.L. Haisler, D.M. Timm, J.A. Gage, H. Tseng, T.C. Killian, G.R. Souza, Three-dimensional cell culturing by magnetic levitation, *Nat. Protoc.* 8 (2013) 1940–1949. <https://doi.org/10.1038/nprot.2013.125>.
- [145] H. Jaganathan, J. Gage, F. Leonard, S. Srinivasan, G.R. Souza, B. Dave, B. Godin, Three-Dimensional In Vitro Co-Culture Model of Breast Tumor using Magnetic Levitation, *Sci. Rep.* 4 (2014) 6468. <https://doi.org/10.1038/srep06468>.
- [146] G.R. Souza, J.R. Molina, R.M. Raphael, M.G. Ozawa, D.J. Stark, C.S. Levin, L.F. Bronk, J.S. Ananta, J. Mandelin, M.-M. Georgescu, J.A. Bankson, J.G. Gelovani, T.C. Killian, W. Arap, R. Pasqualini, Three-dimensional tissue culture based on magnetic cell levitation, *Nat. Nanotechnol.* 5 (2010) 291–296. <https://doi.org/10.1038/nnano.2010.23>.
- [147] M. Zanoni, F. Piccinini, C. Arienti, A. Zamagni, S. Santi, R. Polico, A. Bevilacqua, A. Tesei, 3D tumor spheroid models for in vitro therapeutic screening: a systematic approach to enhance the biological relevance of data obtained, *Sci. Rep.* 6 (2016) 19103. <https://doi.org/10.1038/srep19103>.
- [148] K. Han, S.E. Pierce, A. Li, K. Spees, G.R. Anderson, J.A. Seoane, Y.H. Lo, M. Dubreuil, M. Olivas, R.A. Kamber, M. Wainberg, K. Kostyrko, M.R. Kelly, M. Yousefi, S.W. Simpkins, D. Yao, K. Lee, C.J. Kuo, P.K. Jackson, A. Sweet-Cordero, A. Kundaje, A.J. Gentles, C. Curtis, M.M. Winslow, M.C. Bassik, CRISPR screens in cancer spheroids identify 3D growth-specific vulnerabilities, *Nature.* 580 (2020) 136–141. <https://doi.org/10.1038/s41586-020-2099-x>.
- [149] C.R. Thoma, M. Zimmermann, I. Agarkova, J.M. Kelm, W. Krek, 3D cell culture

systems modeling tumor growth determinants in cancer target discovery, *Adv. Drug Deliv. Rev.* 69–70 (2014) 29–41. <https://doi.org/10.1016/j.addr.2014.03.001>.

- [150] S.P. Pathi, C. Kowalczewski, R. Tadipatri, C. Fischbach, A Novel 3-D Mineralized Tumor Model to Study Breast Cancer Bone Metastasis, *PLoS One*. 5 (2010) e8849. <https://doi.org/10.1371/journal.pone.0008849>.
- [151] M. Rabionet, M. Yeste, T. Puig, J. Ciurana, Electrospinning PCL Scaffolds Manufacture for Three-Dimensional Breast Cancer Cell Culture, *Polymers (Basel)*. 9 (2017) 328. <https://doi.org/10.3390/polym9080328>.
- [152] E.L.S. Fong, S.E. Lamhamedi-Cherradi, E. Burdett, V. Ramamoorthy, A.J. Lazar, F.K. Kasper, M.C. Farach-Carson, D. Vishwamitra, E.G. Demicco, B.A. Menegaz, H.M. Amin, A.G. Mikos, J.A. Ludwig, Modeling Ewing sarcoma tumors in vitro with 3D scaffolds, *Proc. Natl. Acad. Sci. U. S. A.* 110 (2013) 6500–6505. <https://doi.org/10.1073/pnas.1221403110>.
- [153] Z. Liu, G. Vunjak-Novakovic, Modeling tumor microenvironments using custom-designed biomaterial scaffolds, *Curr. Opin. Chem. Eng.* 11 (2016) 94–105. <https://doi.org/10.1016/j.coche.2016.01.012>.
- [154] S. Totti, M.C. Allenby, S.B. Dos Santos, A. Mantalaris, E.G. Velliou, A 3D bioinspired highly porous polymeric scaffolding system for: In vitro simulation of pancreatic ductal adenocarcinoma, *RSC Adv.* 8 (2018) 20928–20940. <https://doi.org/10.1039/c8ra02633e>.
- [155] L. Gu, D.J. Mooney, Biomaterials and emerging anticancer therapeutics: engineering the microenvironment., *Nat. Rev. Cancer.* 16 (2015). <https://doi.org/10.1038/nrc.2015.3>.
- [156] Q. Chai, Y. Jiao, X. Yu, Hydrogels for Biomedical Applications: Their Characteristics and the Mechanisms behind Them, *Gels*. 3 (2017) 6. <https://doi.org/10.3390/gels3010006>.
- [157] J.R. Tse, A.J. Engler, Preparation of hydrogel substrates with tunable mechanical properties, *Curr. Protoc. Cell Biol.* Chapter 10 (2010). <https://doi.org/10.1002/0471143030.cb1016s47>.
- [158] S. Sultan, A.P. Mathew, 3D printed scaffolds with gradient porosity based on a cellulose nanocrystal hydrogel, *Nanoscale*. 10 (2018) 4421–4431. <https://doi.org/10.1039/c7nr08966j>.
- [159] K.A. Burgess, C. Frati, K. Meade, J. Gao, L. Castillo Diaz, D. Madeddu, G. Graiani, S. Cavalli, A.F. Miller, D. Oceandy, F. Quaini, A. Saiani, Functionalised peptide hydrogel for the delivery of cardiac progenitor cells, *Mater. Sci. Eng. C.* 119 (2021) 111539. <https://doi.org/10.1016/j.msec.2020.111539>.
- [160] M.P. Lutolf, J.L. Lauer-Fields, H.G. Schmoekel, A.T. Metters, F.E. Weber, G.B. Fields, J.A. Hubbell, Synthetic matrix metalloproteinase-sensitive hydrogels for the conduction of tissue regeneration: Engineering cell-invasion characteristics, *Proc. Natl. Acad. Sci. U. S. A.* 100 (2003) 5413–5418. <https://doi.org/10.1073/pnas.0737381100>.
- [161] E. Caló, V. V. Khutoryanskiy, Biomedical applications of hydrogels: A review of patents and commercial products, *Eur. Polym. J.* 65 (2015) 252–267. <https://doi.org/10.1016/j.eurpolymj.2014.11.024>.

- [162] C.H. Streuli, N. Bailey, M.J. Bissell, Control of mammary epithelial differentiation: basement membrane induces tissue-specific gene expression in the absence of cell-cell interaction and morphological polarity, *J. Cell Biol.* 115 (1991) 1383–1395. <https://doi.org/10.1083/jcb.115.5.1383>.
- [163] G. Benton, I. Arnaoutova, J. George, H.K. Kleinman, J. Koblinski, Matrigel: From discovery and ECM mimicry to assays and models for cancer research, *Adv. Drug Deliv. Rev.* 79 (2014). <https://doi.org/10.1016/j.addr.2014.06.005>.
- [164] H.K. Kleinman, G.R. Martin, Matrigel: Basement membrane matrix with biological activity, *Semin. Cancer Biol.* 15 (2005) 378–386. <https://doi.org/10.1016/j.semcancer.2005.05.004>.
- [165] F. Travascio, Composition and Function of the Extracellular Matrix in the Human Body, InTech, 2016. <https://doi.org/10.5772/61601>.
- [166] K. Stock, M.F. Estrada, S. Vidic, K. Gjerde, A. Rudisch, V.E. Santo, M. Barbier, S. Blom, S.C. Arundkar, I. Selvam, A. Osswald, Y. Stein, S. Gruenewald, C. Brito, W. van Weerden, V. Rotter, E. Boghaert, M. Oren, W. Sommergruber, Y. Chong, R. de Hoogt, R. Graeser, Capturing tumor complexity in vitro: Comparative analysis of 2D and 3D tumor models for drug discovery, *Sci. Rep.* 6 (2016) 28951. <https://doi.org/10.1038/srep28951>.
- [167] V. Hongisto, S. Jernström, V. Fey, J.-P. Mpindi, K. Kleivi Sahlberg, O. Kallioniemi, M. Perälä, High-Throughput 3D Screening Reveals Differences in Drug Sensitivities between Culture Models of JIMT1 Breast Cancer Cells, *PLoS One.* 8 (2013) e77232. <https://doi.org/10.1371/journal.pone.0077232>.
- [168] C. Godugu, A.R. Patel, U. Desai, T. Andey, A. Sams, M. Singh, Algimatrix™ Based 3D Cell Culture System as an In-Vitro Tumor Model for Anticancer Studies, *PLoS One.* 8 (2013) e53708. <https://doi.org/10.1371/journal.pone.0053708>.
- [169] M. Cavo, M. Caria, I. Pulsoni, F. Beltrame, M. Fato, S. Scaglione, A new cell-laden 3D Alginate-Matrigel hydrogel resembles human breast cancer cell malignant morphology, spread and invasion capability observed “in vivo,” *Sci. Rep.* 8 (2018) 5333. <https://doi.org/10.1038/s41598-018-23250-4>.
- [170] O. Chaudhuri, S.T. Koshy, C. Branco da Cunha, J.-W. Shin, C.S. Verbeke, K.H. Allison, D.J. Mooney, Extracellular matrix stiffness and composition jointly regulate the induction of malignant phenotypes in mammary epithelium., *Nat. Mater.* 13 (2014) 970–8. <https://doi.org/10.1038/nmat4009>.
- [171] J.N. Beck, A. Singh, A.R. Rothenberg, J.H. Elisseeff, A.J. Ewald, The independent roles of mechanical, structural and adhesion characteristics of 3D hydrogels on the regulation of cancer invasion and dissemination, *Biomaterials.* 34 (2013) 9486–9495. <https://doi.org/10.1016/j.biomaterials.2013.08.077>.
- [172] M.J. Paszek, N. Zahir, K.R. Johnson, J.N. Lakins, G.I. Rozenberg, A. Gefen, C.A. Reinhart-King, S.S. Margulies, M. Dembo, D. Boettiger, D.A. Hammer, V.M. Weaver, Tensional homeostasis and the malignant phenotype, *Cancer Cell.* 8 (2005) 241–254. <https://doi.org/10.1016/j.ccr.2005.08.010>.
- [173] M. Anguiano, X. Morales, C. Castilla, A.R. Pena, C. Ederra, M. Martínez, M. Ariz, M. Esparza, H. Amaveda, M. Mora, N. Movilla, J.M.G. Aznar, I. Cortés-Domínguez, C. Ortiz-de-Solorzano, The use of mixed collagen-Matrigel matrices of increasing complexity recapitulates the biphasic role of cell adhesion in cancer cell

migration: ECM sensing, remodeling and forces at the leading edge of cancer invasion, *PLoS One*. 15 (2020) e0220019.  
<https://doi.org/10.1371/journal.pone.0220019>.

- [174] S. Gorgieva, V. Kokol, Collagen- vs. Gelatine-Based Biomaterials and Their Biocompatibility: Review and Perspectives, in: *Biomater. Appl. Nanomedicine, InTech*, 2011. <https://doi.org/10.5772/24118>.
- [175] D.F.D. Campos, A.B. Marquez, C. O'seanain, H. Fischer, A. Blaeser, M. Vogt, D. Corallo, S. Aveic, Exploring cancer cell behavior in vitro in three-dimensional multicellular bioprintable collagen-based hydrogels, *Cancers (Basel)*. 11 (2019). <https://doi.org/10.3390/cancers11020180>.
- [176] G. Benton, G. DeGray, H.K. Kleinman, J. George, I. Arnaoutova, In vitro microtumors provide a physiologically predictive tool for breast cancer therapeutic screening., *PLoS One*. 10 (2015) e0123312.  
<https://doi.org/10.1371/journal.pone.0123312>.
- [177] A.H. Kesarwala, J.L. Carter, G.H. Read, N. Miura, K. Yamamoto, J.B. Mitchell, M. Krishna, Alginate Hydrogels for Three-Dimensional Culture and Real-Time Monitoring of Cancer Cell Metabolism and Radiation Response, *Int. J. Radiat. Oncol.* 99 (2017) S148. <https://doi.org/10.1016/j.ijrobp.2017.06.342>.
- [178] G.H. Read, N. Miura, J.L. Carter, K.T. Kines, K. Yamamoto, N. Devasahayam, J.Y. Cheng, K.A. Camphausen, M.C. Krishna, A.H. Kesarwala, Three-dimensional alginate hydrogels for radiobiological and metabolic studies of cancer cells, *Colloids Surfaces B Biointerfaces*. 171 (2018) 197–204.  
<https://doi.org/10.1016/j.colsurfb.2018.06.018>.
- [179] Y.L. Kassim, E. Al Tawil, C. Buquet, D. Le Cerf, J. PierreVannier, Three Dimensional Tumor Engineering by Co-Culture of Breast Tumor and Endothelial Cells Using a Hyaluronic Acid Hydrogel Model, *J. Clin. Exp. Oncol.* 06 (2017).  
<https://doi.org/10.4172/2324-9110.1000194>.
- [180] S.R. Caliri, J.A. Burdick, A practical guide to hydrogels for cell culture, *Nat. Methods*. 13 (2016) 405–414. <https://doi.org/10.1038/nmeth.3839>.
- [181] M. Farokhi, F. Jonidi Shariatzadeh, A. Solouk, H. Mirzadeh, Alginate Based Scaffolds for Cartilage Tissue Engineering: A Review, *Int. J. Polym. Mater. Polym. Biomater.* 69 (2020) 230–247. <https://doi.org/10.1080/00914037.2018.1562924>.
- [182] J. Ivanovska, T. Zehnder, P. Lennert, B. Sarker, A.R. Boccaccini, A. Hartmann, R. Schneider-Stock, R. Detsch, Biofabrication of 3D Alginate-Based Hydrogel for Cancer Research: Comparison of Cell Spreading, Viability, and Adhesion Characteristics of Colorectal HCT116 Tumor Cells, *Tissue Eng. Part C Methods*. 22 (2016) 708–715. <https://doi.org/10.1089/ten.tec.2015.0452>.
- [183] Y. Li, E. Kumacheva, Hydrogel microenvironments for cancer spheroid growth and drug screening, *Sci. Adv.* 4 (2018) eaas8998.  
<https://doi.org/10.1126/sciadv.aas8998>.
- [184] S. Pradhan, I. Hassani, W.J. Seeto, E.A. Lipke, PEG-fibrinogen hydrogels for three-dimensional breast cancer cell culture, *J. Biomed. Mater. Res. Part A*. 105 (2017) 236–252. <https://doi.org/10.1002/jbm.a.35899>.
- [185] M.K. Livingston, M.M. Morgan, W.T. Daly, W.L. Murphy, B.P. Johnson, D.J.



- Beebe, M. Virumbrales-Muñoz, Evaluation of PEG-Based Hydrogel Influence on Estrogen-Receptor-Driven Responses in MCF7 Breast Cancer Cells, *ACS Biomater. Sci. Eng.* 5 (2019) 6089–6098. <https://doi.org/10.1021/acsbiomaterials.9b00480>.
- [186] L.J. Bray, M. Binner, A. Holzheu, J. Friedrichs, U. Freudenberg, D.W. Hutmacher, C. Werner, Multi-parametric hydrogels support 3D in vitro bioengineered microenvironment models of tumour angiogenesis, *Biomaterials*. 53 (2015) 609–620. <https://doi.org/10.1016/j.biomaterials.2015.02.124>.
- [187] H. Wang, J. Qian, Y. Zhang, W. Xu, J. Xiao, A. Suo, Growth of MCF-7 breast cancer cells and efficacy of anti-angiogenic agents in a hydroxyethyl chitosan/glycidyl methacrylate hydrogel., *Cancer Cell Int.* 17 (2017) 55. <https://doi.org/10.1186/s12935-017-0424-8>.
- [188] R.J. Jerrell, A. Parekh, Polyacrylamide gels for invadopodia and traction force assays on cancer cells, *J. Vis. Exp.* (2015). <https://doi.org/10.3791/52343>.
- [189] S. Syed, J. Schober, A. Blanco, S.P. Zustiak, Morphological adaptations in breast cancer cells as a function of prolonged passaging on compliant substrates, *PLoS One*. 12 (2017). <https://doi.org/10.1371/journal.pone.0187853>.
- [190] S. Koutsopoulos, Self-assembling peptide nanofiber hydrogels in tissue engineering and regenerative medicine: Progress, design guidelines, and applications, *J. Biomed. Mater. Res. Part A*. 104 (2016) 1002–1016. <https://doi.org/10.1002/jbm.a.35638>.
- [191] S. Fleming, R. V. Ulijn, Design of nanostructures based on aromatic peptide amphiphiles, *Chem. Soc. Rev.* 43 (2014) 8150–8177. <https://doi.org/10.1039/C4CS00247D>.
- [192] S. Zhang, Fabrication of novel biomaterials through molecular self-assembly, *Nat. Biotechnol.* 21 (2003) 1171–1178. <https://doi.org/10.1038/nbt874>.
- [193] B. Alberts, A. Johnson, J. Lewis, M. Raff, K. Roberts, P. Walter, *The Shape and Structure of Proteins*, (2002). <https://www.ncbi.nlm.nih.gov/books/NBK26830/> (accessed June 5, 2017).
- [194] C. Aronsson, S. Dånmark, F. Zhou, P. Öberg, K. Enander, H. Su, D. Aili, Self-sorting heterodimeric coiled coil peptides with defined and tuneable self-assembly properties, *Sci. Rep.* 5 (2015). <https://doi.org/10.1038/srep14063>.
- [195] J.S. Rudra, J.H. Collier, Self-assembling biomaterials, in: *Compr. Biomater.*, Elsevier, 2011: pp. 77–94. <https://doi.org/10.1016/b978-0-08-055294-1.00063-5>.
- [196] A. Saiani, A. Mohammed, H. Frielinghaus, R. Collins, N. Hodson, C.M. Kielty, M.J. Sherratt, A.F. Miller, Self-assembly and gelation properties of  $\alpha$ -helix versus  $\beta$ -sheet forming peptides, *Soft Matter*. 5 (2009) 193–202. <https://doi.org/10.1039/b811288f>.
- [197] A. Dasgupta, J.H. Mondal, D. Das, Peptide hydrogels, *RSC Adv.* 3 (2013) 9117–9149. <https://doi.org/10.1039/c3ra40234g>.
- [198] S. Eskandari, T. Guerin, I. Toth, R.J. Stephenson, Recent advances in self-assembled peptides: Implications for targeted drug delivery and vaccine engineering, *Adv. Drug Deliv. Rev.* 110–111 (2017) 169–187. <https://doi.org/10.1016/j.addr.2016.06.013>.

- [199] J. Lu, X. Wang, Biomimetic self-assembling peptide hydrogels for tissue engineering applications, in: *Adv. Exp. Med. Biol.*, Springer New York LLC, 2018: pp. 297–312. [https://doi.org/10.1007/978-981-13-0445-3\\_18](https://doi.org/10.1007/978-981-13-0445-3_18).
- [200] J. Chen, X. Zou, Self-assemble peptide biomaterials and their biomedical applications, *Bioact. Mater.* 4 (2019) 120–131. <https://doi.org/10.1016/j.bioactmat.2019.01.002>.
- [201] E.F. Banwell, E.S. Abelardo, D.J. Adams, M.A. Birchall, A. Corrigan, A.M. Donald, M. Kirkland, L.C. Serpell, M.F. Butler, D.N. Woolfson, Rational design and application of responsive  $\alpha$ -helical peptide hydrogels, *Nat. Mater.* 8 (2009) 596–600. <https://doi.org/10.1038/nmat2479>.
- [202] N. Mehrban, B. Zhu, F. Tamagnini, F.I. Young, A. Wasmuth, K.L. Hudson, A.R. Thomson, M.A. Birchall, A.D. Randall, B. Song, D.N. Woolfson, Functionalized  $\alpha$ -Helical Peptide Hydrogels for Neural Tissue Engineering, *ACS Biomater. Sci. Eng.* 1 (2015) 431–439. <https://doi.org/10.1021/acsbiomaterials.5b00051>.
- [203] M. Rivas, L.J. Del Valle, C. Alemán, J. Puiggalí, Peptide self-assembly into hydrogels for biomedical applications related to hydroxyapatite, *Gels.* 5 (2019). <https://doi.org/10.3390/gels5010014>.
- [204] C.E. Stotz, E.M. Topp, Applications of model  $\beta$ -hairpin peptides, *J. Pharm. Sci.* 93 (2004) 2881–2894. <https://doi.org/10.1002/jps.20188>.
- [205] J.P. Schneider, D.J. Pochan, B. Ozbas, K. Rajagopal, L. Pakstis, J. Kretsinger, Responsive Hydrogels from the Intramolecular Folding and Self-Assembly of a Designed Peptide, (2002). <https://doi.org/10.1021/ja027993g>.
- [206] J.K. Kretsinger, L.A. Haines, B. Ozbas, D.J. Pochan, J.P. Schneider, Cytocompatibility of self-assembled  $\beta$ -hairpin peptide hydrogel surfaces, *Biomaterials.* 26 (2005) 5177–5186. <https://doi.org/10.1016/j.biomaterials.2005.01.029>.
- [207] B. Ozbas, J. Kretsinger, K. Rajagopal, J.P. Schneider, D.J. Pochan, Salt-triggered peptide folding and consequent self-assembly into hydrogels with tunable modulus, *Macromolecules.* 37 (2004) 7331–7337. <https://doi.org/10.1021/ma0491762>.
- [208] R. V. Rughani, J.R. Schneider, Molecular design of  $\beta$ -hairpin peptides for material construction, *MRS Bull.* 33 (2008) 530–535. <https://doi.org/10.1557/mrs2008.106>.
- [209] N. Yadav, M.K. Chauhan, V.S. Chauhan, Short to ultrashort peptide-based hydrogels as a platform for biomedical applications, *Biomater. Sci.* 8 (2020) 84–100. <https://doi.org/10.1039/c9bm01304k>.
- [210] M. Reches, E. Gazit, Casting metal nanowires within discrete self-assembled peptide nanotubes, *Science* (80-. ). 300 (2003) 625–627. <https://doi.org/10.1126/science.1082387>.
- [211] S.M. Acuña, M.C. Veloso, P.G. Toledo, Self-assembly of diphenylalanine-based nanostructures in water and electrolyte solutions, *J. Nanomater.* 2018 (2018). <https://doi.org/10.1155/2018/8140954>.
- [212] V. Jayawarna, M. Ali, T.A. Jowitt, A.F. Miller, A. Saiani, J.E. Gough, R.V. Ulijn, Nanostructured Hydrogels for Three-Dimensional Cell Culture Through Self-Assembly of Fluorenylmethoxycarbonyl–Dipeptides, *Adv. Mater.* 18 (2006) 611–

614. <https://doi.org/10.1002/adma.200501522>.

- [213] M. Zhou, A.M. Smith, A.K. Das, N.W. Hodson, R.F. Collins, R. V. Ulijn, J.E. Gough, Self-assembled peptide-based hydrogels as scaffolds for anchorage-dependent cells, *Biomaterials*. 30 (2009) 2523–2530. <https://doi.org/10.1016/J.BIOMATERIALS.2009.01.010>.
- [214] F. Qiu, Y. Chen, C. Tang, X. Zhao, Amphiphilic peptides as novel nanomaterials: Design, self-assembly and application, *Int. J. Nanomedicine*. 13 (2018) 5003–5022. <https://doi.org/10.2147/IJN.S166403>.
- [215] S.E. Paramonov, H.W. Jun, J.D. Hartgerink, Self-assembly of peptide-amphiphile nanofibers: The roles of hydrogen bonding and amphiphilic packing, *J. Am. Chem. Soc.* 128 (2006) 7291–7298. <https://doi.org/10.1021/ja060573x>.
- [216] E. Beniash, J.D. Hartgerink, H. Storrie, J.C. Stendahl, S.I. Stupp, Self-assembling peptide amphiphile nanofiber matrices for cell entrapment, *Acta Biomater.* 1 (2005) 387–397. <https://doi.org/10.1016/j.actbio.2005.04.002>.
- [217] J.C. Stendahl, M.S. Rao, M.O. Guler, S.I. Stupp, Intermolecular Forces in the Self-Assembly of Peptide Amphiphile Nanofibers, *Adv. Funct. Mater.* 16 (2006) 499–508. <https://doi.org/10.1002/adfm.200500161>.
- [218] S. Zhang, C. Lockshin, A. Herbert, E. Winter, A. Rich, Zuotin, a putative Z-DNA binding protein in *Saccharomyces cerevisiae*., *EMBO J.* 11 (1992) 3787–96. <http://www.ncbi.nlm.nih.gov/pubmed/1396572> (accessed June 6, 2017).
- [219] S. Zhang, T. Holmes, C. Lockshin, A. Rich, Spontaneous assembly of a self-complementary oligopeptide to form a stable macroscopic membrane., *Proc. Natl. Acad. Sci. U. S. A.* 90 (1993) 3334–8. <https://doi.org/10.1073/PNAS.90.8.3334>.
- [220] S. Zhang, T.C. Holmes, C.M. DiPersio, R.O. Hynes, X. Su, A. Rich, Self-complementary oligopeptide matrices support mammalian cell attachment, *Biomaterials*. 16 (1995) 1385–1393. [https://doi.org/10.1016/0142-9612\(95\)96874-Y](https://doi.org/10.1016/0142-9612(95)96874-Y).
- [221] Y. Loo, S. Zhang, C.A.E. Hauser, From short peptides to nanofibers to macromolecular assemblies in biomedicine, *Biotechnol. Adv.* 30 (2012) 593–603. <https://doi.org/10.1016/j.biotechadv.2011.10.004>.
- [222] E.J. Leon, N. Verma, S. Zhang, D.A. Lauffenburger, R.D. Kamm, Mechanical properties of a self-assembling oligopeptide matrix., *J. Biomater. Sci. Polym. Ed.* 9 (1998) 297–312. <http://www.ncbi.nlm.nih.gov/pubmed/9556763> (accessed December 26, 2017).
- [223] S. Jun, Y. Hong, H. Imamura, B.-Y. Ha, J. Bechhoefer, P. Chen, Self-Assembly of the Ionic Peptide EAK16: The Effect of Charge Distributions on Self-Assembly, *Biophys. J.* 87 (2004) 1249–1259. <https://doi.org/10.1529/biophysj.103.038166>.
- [224] Y. Hong, R.L. Legge, S. Zhang, P. Chen, Effect of Amino Acid Sequence and pH on Nanofiber Formation of Self-Assembling Peptides EAK16-II and EAK16-IV, *Biomacromolecules*. 4 (2003) 1433–1442. <https://doi.org/10.1021/bm0341374>.
- [225] M.R. Caplan, E.M. Schwartzfarb, S. Zhang, R.D. Kamm, D.A. Lauffenburger, Control of self-assembling oligopeptide matrix formation through systematic variation of amino acid sequence, *Biomaterials*. 23 (2002) 219–227.

[https://doi.org/10.1016/S0142-9612\(01\)00099-0](https://doi.org/10.1016/S0142-9612(01)00099-0).

- [226] F. Koch, M. Müller, F. König, N. Meyer, J. Gattlen, U. Pieves, K. Peters, B. Kreikemeyer, S. Mathes, S. Saxer, Mechanical characteristics of beta sheet-forming peptide hydrogels are dependent on peptide sequence, concentration and buffer composition, *R. Soc. Open Sci.* 5 (2018). <https://doi.org/10.1098/rsos.171562>.
- [227] H. Kaur, P. Sharma, N. Patel, V.K. Pal, S. Roy, Accessing Highly Tunable Nanostructured Hydrogels in a Short Ionic Complementary Peptide Sequence via pH Trigger, *Langmuir*. 36 (2020) 12107–12120. <https://doi.org/10.1021/acs.langmuir.0c01472>.
- [228] M. Tokunaga, M.-L. Liu, T. Nagai, K. Iwanaga, K. Matsuura, T. Takahashi, M. Kanda, N. Kondo, P. Wang, A.T. Naito, I. Komuro, Implantation of cardiac progenitor cells using self-assembling peptide improves cardiac function after myocardial infarction., *J. Mol. Cell. Cardiol.* 49 (2010) 972–83. <https://doi.org/10.1016/j.yjmcc.2010.09.015>.
- [229] H.B. Henriksson, M. Hagman, M. Horn, A. Lindahl, H. Brisby, Investigation of different cell types and gel carriers for cell-based intervertebral disc therapy, *in vitro* and *in vivo* studies, *J. Tissue Eng. Regen. Med.* 6 (2012) 738–747. <https://doi.org/10.1002/term.480>.
- [230] Y. Sun, Y. Zhang, L. Tian, Y. Zhao, D. Wu, W. Xue, S. Ramakrishna, W. Wu, L. He, Self-assembly behaviors of molecular designer functional RADA16-I peptides: influence of motifs, pH, and assembly time, *Biomed. Mater.* 12 (2016) 015007. <https://doi.org/10.1088/1748-605X/12/1/015007>.
- [231] A. Markey, V.L. Workman, I.A. Bruce, T.J. Woolford, B. Derby, A.F. Miller, S.H. Cartmell, A. Saiani, Peptide hydrogel *in vitro* non-inflammatory potential, *J. Pept. Sci.* 23 (2017) 148–154. <https://doi.org/10.1002/psc.2940>.
- [232] Z. Yang, X. Zhao, A 3D model of ovarian cancer cell lines on peptide nanofiber scaffold to explore the cell-scaffold interaction and chemotherapeutic resistance of anticancer drugs., *Int. J. Nanomedicine.* 6 (2011) 303–10. <https://doi.org/10.2147/IJN.S15279>.
- [233] K. Mi, Z. Xing, CD44(+)/CD24(-) breast cancer cells exhibit phenotypic reversion in three-dimensional self-assembling peptide RADA16 nanofiber scaffold., *Int. J. Nanomedicine.* 10 (2015) 3043–53. <https://doi.org/10.2147/IJN.S66723>.
- [234] H. Song, Y.-Z. Han, G.-H. Cai, F.-S. Tang, Z.-H. Yang, D.-S. Ao, A. Zhou, The effects of self-assembling peptide RADA16 hydrogel on malignant phenotype of human hepatocellular carcinoma cell., *Int. J. Clin. Exp. Med.* 8 (2015) 14906–15. <http://www.ncbi.nlm.nih.gov/pubmed/26628972> (accessed April 3, 2017).
- [235] S. Wan, S. Borland, S.M. Richardson, C.L.R. Merry, A. Saiani, J.E. Gough, Self-assembling peptide hydrogel for intervertebral disc tissue engineering, *Acta Biomater.* 46 (2016) 29–40. <https://doi.org/10.1016/j.actbio.2016.09.033>.
- [236] A. Mujeeb, A.F. Miller, A. Saiani, J.E. Gough, Self-assembled octapeptide scaffolds for in vitro chondrocyte culture, *Acta Biomater.* 9 (2013) 4609–4617. <https://doi.org/10.1016/J.ACTBIO.2012.08.044>.
- [237] H. Huang, J. Shi, J. Laskin, Z. Liu, D.S. McVey, X.S. Sun, Design of a shear-thinning recoverable peptide hydrogel from native sequences and application for

influenza H1N1 vaccine adjuvant, *Soft Matter*. 7 (2011) 8905–8912.  
<https://doi.org/10.1039/c1sm05157a>.

- [238] J. Xu, G. Qi, C. Sui, W. Wang, X. Sun, 3D h9e peptide hydrogel: An advanced three-dimensional cell culture system for anticancer prescreening of chemopreventive phenolic agents, *Toxicol. Vitro*. 61 (2019) 104599.  
<https://doi.org/10.1016/j.tiv.2019.104599>.
- [239] J.P. Jung, A.K. Nagaraj, E.K. Fox, J.S. Rudra, J.M. Devgun, J.H. Collier, Co-assembling peptides as defined matrices for endothelial cells., *Biomaterials*. 30 (2009) 2400–10. <https://doi.org/10.1016/j.biomaterials.2009.01.033>.
- [240] K.M. Hainline, F. Gu, J.F. Handley, Y.F. Tian, Y. Wu, L. de Wet, D.J. Vander Griend, J.H. Collier, Self-Assembling Peptide Gels for 3D Prostate Cancer Spheroid Culture, *Macromol. Biosci*. 19 (2019) e1800249.  
<https://doi.org/10.1002/mabi.201800249>.
- [241] M. Sheikholeslam, S.D. Wheeler, K.G. Duke, M. Marsden, M. Pritzker, P. Chen, Peptide and peptide-carbon nanotube hydrogels as scaffolds for tissue & 3D tumor engineering, *Acta Biomater*. (2017).  
<https://doi.org/10.1016/J.ACTBIO.2017.12.012>.
- [242] H. Huang, Y. Ding, X.S. Sun, T.A. Nguyen, Peptide hydrogelation and cell encapsulation for 3D culture of MCF-7 breast cancer cells., *PLoS One*. 8 (2013) e59482. <https://doi.org/10.1371/journal.pone.0059482>.
- [243] O. Tsigkou, I. Pomerantseva, J.A. Spencer, P.A. Redondo, A.R. Hart, E. O’Doherty, Y. Lin, C.C. Friedrich, L. Daheron, C.P. Lin, C.A. Sundback, J.P. Vacanti, C. Neville, Engineered vascularized bone grafts., *Proc. Natl. Acad. Sci. U. S. A.* 107 (2010) 3311–6. <https://doi.org/10.1073/pnas.0905445107>.
- [244] D.G. Belair, J.A. Whisler, J. Valdez, J. Velazquez, J.A. Molenda, V. Vickerman, R. Lewis, C. Daigh, T.D. Hansen, D.A. Mann, J.A. Thomson, L.G. Griffith, R.D. Kamm, M.P. Schwartz, W.L. Murphy, Human Vascular Tissue Models Formed from Human Induced Pluripotent Stem Cell Derived Endothelial Cells, *Stem Cell Rev. Reports*. 11 (2015) 511–525. <https://doi.org/10.1007/s12015-014-9549-5>.
- [245] S. Hauser, F. Jung, J. Pietzsch, Human Endothelial Cell Models in Biomaterial Research, *Trends Biotechnol*. 35 (2017) 265–277.  
<https://doi.org/10.1016/j.tibtech.2016.09.007>.
- [246] I. Kocherova, A. Bryja, P. Mozdziak, A. Angelova Volponi, M. Dyszkiewicz-Konwińska, H. Piotrowska-Kempisty, P. Antosik, D. Bukowska, M. Bruska, D. Iżycki, M. Zabel, M. Nowicki, B. Kempisty, Human Umbilical Vein Endothelial Cells (HUVECs) Co-Culture with Osteogenic Cells: From Molecular Communication to Engineering Prevascularised Bone Grafts, *J. Clin. Med*. 8 (2019) 1602. <https://doi.org/10.3390/jcm8101602>.
- [247] R. Costa-Almeida, P.L. Granja, R. Soares, S.G. Guerreiro, Cellular strategies to promote vascularisation in tissue engineering applications, *Eur. Cells Mater*. 28 (2014) 51–67. <https://doi.org/10.22203/eCM.v028a05>.
- [248] F. Saleh, M. Whyte, P. Genever, Effects of endothelial cells on human mesenchymal stem cell activity in a three-dimensional in vitro model, *Eur. Cells Mater*. 22 (2011) 242–257. <https://doi.org/10.22203/eCM.v022a19>.

- [249] R. Hass, C. Kasper, S. Böhm, R. Jacobs, Different populations and sources of human mesenchymal stem cells (MSC): A comparison of adult and neonatal tissue-derived MSC, *Cell Commun. Signal.* 9 (2011). <https://doi.org/10.1186/1478-811X-9-12>.
- [250] M. Crisan, S. Yap, L. Casteilla, C.W. Chen, M. Corselli, T.S. Park, G. Andriolo, B. Sun, B. Zheng, L. Zhang, C. Norotte, P.N. Teng, J. Traas, R. Schugar, B.M. Deasy, S. Badylak, H.J. Buhring, J.P. Giacobino, L. Lazzari, J. Huard, B. Péault, A Perivascular Origin for Mesenchymal Stem Cells in Multiple Human Organs, *Cell Stem Cell.* 3 (2008) 301–313. <https://doi.org/10.1016/j.stem.2008.07.003>.
- [251] H. Gerhardt, C. Betsholtz, Endothelial-pericyte interactions in angiogenesis, *Cell Tissue Res.* 314 (2003) 15–23. <https://doi.org/10.1007/s00441-003-0745-x>.
- [252] P. Au, J. Tam, D. Fukumura, R.K. Jain, Bone marrow derived mesenchymal stem cells facilitate engineering of long-lasting functional vasculature, *Blood.* 111 (2008) 4551–4558. <https://doi.org/10.1182/blood-2007-10-118273>.
- [253] G.P. Duffy, T. Ahsan, T. O'Brien, F. Barry, R.M. Nerem, Bone marrow-derived mesenchymal stem cells promote angiogenic processes in a time- and dose-Dependent manner in vitro, *Tissue Eng. - Part A.* 15 (2009) 2459–2470. <https://doi.org/10.1089/ten.tea.2008.0341>.
- [254] W. Chen, X. Liu, Q. Chen, C. Bao, L. Zhao, Z. Zhu, H.H.K. Xu, Angiogenic and osteogenic regeneration in rats via calcium phosphate scaffold and endothelial cell co-culture with human bone marrow mesenchymal stem cells (MSCs), human umbilical cord MSCs, human induced pluripotent stem cell-derived MSCs and human embryonic stem cell-derived MSCs, *J. Tissue Eng. Regen. Med.* 12 (2018) 191–203. <https://doi.org/10.1002/term.2395>.
- [255] H. Li, R. Daculsi, M. Grellier, R. Bareille, C. Bourget, M. Remy, J. Amedee, The Role of Vascular Actors in Two Dimensional Dialogue of Human Bone Marrow Stromal Cell and Endothelial Cell for Inducing Self-Assembled Network, *PLoS One.* 6 (2011) e16767. <https://doi.org/10.1371/journal.pone.0016767>.
- [256] J.P. Califano, C.A. Reinhart-King, A Balance of Substrate Mechanics and Matrix Chemistry Regulates Endothelial Cell Network Assembly, *Cell. Mol. Bioeng.* 1 (2008) 122–132. <https://doi.org/10.1007/s12195-008-0022-x>.
- [257] J.J. Moon, J.E. Saik, R.A. Poché, J.E. Leslie-Barbick, S.H. Lee, A.A. Smith, M.E. Dickinson, J.L. West, Biomimetic hydrogels with pro-angiogenic properties, *Biomaterials.* 31 (2010) 3840–3847. <https://doi.org/10.1016/j.biomaterials.2010.01.104>.
- [258] N. Yamamura, R. Sudo, M. Ikeda, K. Tanishita, Effects of the mechanical properties of collagen gel on the in vitro formation of microvessel networks by endothelial cells, *Tissue Eng.* 13 (2007) 1443–1453. <https://doi.org/10.1089/ten.2006.0333>.
- [259] B.N. Mason, A. Starchenko, R.M. Williams, L.J. Bonassar, C.A. Reinhart-King, Tuning three-dimensional collagen matrix stiffness independently of collagen concentration modulates endothelial cell behavior, *Acta Biomater.* 9 (2013) 4635–4644. <https://doi.org/10.1016/j.actbio.2012.08.007>.
- [260] C.O. Crosby, J. Zoldan, Mimicking the physical cues of the ECM in angiogenic biomaterials, *Regen. Biomater.* 6 (2019) 61–73. <https://doi.org/10.1093/rb/rbz003>.

- [261] L.S. Wang, F. Lee, J. Lim, C. Du, A.C.A. Wan, S.S. Lee, M. Kurisawa, Enzymatic conjugation of a bioactive peptide into an injectable hyaluronic acid-tyramine hydrogel system to promote the formation of functional vasculature, *Acta Biomater.* 10 (2014) 2539–2550. <https://doi.org/10.1016/j.actbio.2014.02.022>.
- [262] L.A. Rocha, E.D. Gomes, J.L. Afonso, S. Granja, F. Baltazar, N.A. Silva, M.S. Shoichet, R.A. Sousa, D.A. Learmonth, A.J. Salgado, In vitro Evaluation of ASCs and HUVECs Co-cultures in 3D Biodegradable Hydrogels on Neurite Outgrowth and Vascular Organization, *Front. Cell Dev. Biol.* 8 (2020) 489. <https://doi.org/10.3389/fcell.2020.00489>.
- [263] J. Su, S.C. Satchell, J.A. Wertheim, R.N. Shah, Poly(ethylene glycol)-crosslinked gelatin hydrogel substrates with conjugated bioactive peptides influence endothelial cell behavior, *Biomaterials.* 201 (2019) 99–112. <https://doi.org/10.1016/j.biomaterials.2019.02.001>.
- [264] R. Suntornnond, E.Y.S. Tan, J. An, C.K. Chua, A highly printable and biocompatible hydrogel composite for direct printing of soft and perfusable vasculature-like structures, *Sci. Rep.* 7 (2017) 1–11. <https://doi.org/10.1038/s41598-017-17198-0>.
- [265] R.K. Singh, D. Seliktar, A.J. Putnam, Capillary morphogenesis in PEG-collagen hydrogels, *Biomaterials.* 34 (2013) 9331–9340. <https://doi.org/10.1016/j.biomaterials.2013.08.016>.
- [266] Y.C. Chen, R.Z. Lin, H. Qi, Y. Yang, H. Bae, J.M. Melero-Martin, A. Khademhosseini, Functional human vascular network generated in photocrosslinkable gelatin methacrylate hydrogels, *Adv. Funct. Mater.* 22 (2012) 2027–2039. <https://doi.org/10.1002/adfm.201101662>.
- [267] A.L. Sieminski, C.E. Semino, H. Gong, R.D. Kamm, Primary sequence of ionic self-assembling peptide gels affects endothelial cell adhesion and capillary morphogenesis, *J. Biomed. Mater. Res. Part A.* 87A (2008) 494–504. <https://doi.org/10.1002/jbm.a.31785>.
- [268] X. Wang, A. Horii, S. Zhang, P.J. Gallagher, P. de Lanerolle, D.A. Cheresh, B. Trimarco, C. Pedone, E.B. Lavik, D. Junker, J.M. Häufel, C. Carvalho, M. Heberer, G. Germann, B. Vollmar, M.D. Menger, Designer functionalized self-assembling peptide nanofiber scaffolds for growth, migration, and tubulogenesis of human umbilical vein endothelial cells, *Soft Matter.* 4 (2008) 2388. <https://doi.org/10.1039/b807155a>.
- [269] E. Genové, C. Shen, S. Zhang, C.E. Semino, The effect of functionalized self-assembling peptide scaffolds on human aortic endothelial cell function, *Biomaterials.* 26 (2005) 3341–3351. <https://doi.org/10.1016/j.biomaterials.2004.08.012>.
- [270] W.K. Surewicz, H.H. Mantsch, D. Chapman, Determination of protein secondary structure by Fourier transform infrared spectroscopy: A critical assessment, *Biochemistry.* 32 (1993) 389–394. <https://doi.org/10.1021/bi00053a001>.
- [271] S.E. Glassford, B. Byrne, S.G. Kazarian, Recent applications of ATR FTIR spectroscopy and imaging to proteins, *Biochim. Biophys. Acta - Proteins Proteomics.* 1834 (2013) 2849–2858. <https://doi.org/10.1016/j.bbapap.2013.07.015>.
- [272] S. Sathaye, A. Mbi, C. Sonmez, Y. Chen, D.L. Blair, J.P. Schneider, D.J. Pochan,

Rheology of peptide- and protein-based physical hydrogels: Are everyday measurements just scratching the surface?, *Wiley Interdiscip. Rev. Nanomedicine Nanobiotechnology*. 7 (2015) 34–68. <https://doi.org/10.1002/wnan.1299>.

- [273] C. Yan, D.J. Pochan, Rheological properties of peptide-based hydrogels for biomedical and other applications., *Chem. Soc. Rev.* 39 (2010) 3528–40. <https://doi.org/10.1039/b919449p>.
- [274] L. Graham, J.M. Orenstein, Processing tissue and cells for transmission electron microscopy in diagnostic pathology and research, *Nat. Protoc.* 2 (2007) 2439–2450. <https://doi.org/10.1038/nprot.2007.304>.
- [275] A.I. Dragan, J.R. Casas-Finet, E.S. Bishop, R.J. Strouse, M.A. Schenerman, C.D. Geddes, Characterization of PicoGreen interaction with dsDNA and the origin of its fluorescence enhancement upon binding., *Biophys. J.* 99 (2010) 3010–9. <https://doi.org/10.1016/j.bpj.2010.09.012>.
- [276] K.A. Burgess, V.L. Workman, M.A. Elsayy, A.F. Miller, D. Oceandy, A. Saiani, RNA extraction from self-assembling peptide hydrogels to allow qPCR analysis of encapsulated cells, *PLoS One*. 13 (2018) e0197517. <https://doi.org/10.1371/journal.pone.0197517>.
- [277] K.L. Cox, V. Devanarayan, A. Kriauciunas, J. Manetta, C. Montrose, S. Sittampalam, *Immunoassay Methods*, Eli Lilly & Company and the National Center for Advancing Translational Sciences, 2004. <http://www.ncbi.nlm.nih.gov/pubmed/22553884> (accessed January 28, 2021).
- [278] M. V. Monteiro, V.M. Gaspar, L.P. Ferreira, J.F. Mano, Hydrogel 3D in vitro tumor models for screening cell aggregation mediated drug response , *Biomater. Sci.* 8 (2020) 1855–1864. <https://doi.org/10.1039/c9bm02075f>.
- [279] N.H. Barrak, M.A. Khajah, Y.A. Luqmani, Hypoxic environment may enhance migration/penetration of endocrine resistant MCF7- derived breast cancer cells through monolayers of other non-invasive cancer cells in vitro, *Sci. Rep.* 10 (2020). <https://doi.org/10.1038/s41598-020-58055-x>.
- [280] C.S. Szot, C.F. Buchanan, J.W. Freeman, M.N. Rylander, 3D in vitro bioengineered tumors based on collagen I hydrogels, *Biomaterials*. 32 (2011) 7905–7912. <https://doi.org/10.1016/j.biomaterials.2011.07.001>.
- [281] C. Ligorio, M. Zhou, J.K. Wychowaniec, X. Zhu, C. Bartlam, A.F. Miller, A. Vijayaraghavan, J.A. Hoyland, A. Saiani, Graphene oxide containing self-assembling peptide hybrid hydrogels as a potential 3D injectable cell delivery platform for intervertebral disc repair applications, *Acta Biomater.* 92 (2019) 92–103. <https://doi.org/10.1016/J.ACTBIO.2019.05.004>.
- [282] K.A. Burgess, A.F. Miller, D. Oceandy, A. Saiani, Western blot analysis of cells encapsulated in self-assembling peptide hydrogels, *Biotechniques*. 63 (2017) 253–260. <https://doi.org/10.2144/000114617>.
- [283] L. Ying, Q. Meng, C. Yi, W. Wei, Designing the mechanical properties of peptide-based supramolecular hydrogels for biomedical applications, 57 (2014) 849–858. <https://doi.org/10.1007/s11433-014-5427-z>.
- [284] D. Roberts, C. Rochas, A. Saiani, A.F. Miller, Effect of Peptide and Guest Charge on the Structural, Mechanical and Release Properties of  $\beta$ -Sheet Forming Peptides,



(n.d.). <https://doi.org/10.1021/la303328p>.

- [285] H. Yang, S. Yang, J. Kong, A. Dong, S. Yu, Obtaining information about protein secondary structures in aqueous solution using Fourier transform IR spectroscopy, *Nat. Protoc.* 10 (2015) 382–396. <https://doi.org/10.1038/nprot.2015.024>.
- [286] J.K. Wychowaniec, A.M. Smith, C. Ligorio, O.O. Mykhaylyk, A.F. Miller, A. Saiani, Role of sheet-edge interactions in  $\beta$ -sheet self-assembling peptide hydrogels, *Biomacromolecules*. (2020) [acs.biomac.0c00229](https://doi.org/10.1021/acs.biomac.0c00229).  
<https://doi.org/10.1021/acs.biomac.0c00229>.
- [287] J.M. Zuidema, C.J. Rivet, R.J. Gilbert, F.A. Morrison, A protocol for rheological characterization of hydrogels for tissue engineering strategies, *J. Biomed. Mater. Res. Part B Appl. Biomater.* 102 (2014) 1063–1073.  
<https://doi.org/10.1002/jbm.b.33088>.
- [288] A. Scelsi, B. Bochicchio, A. Smith, V.L. Workman, L.A. Castillo Diaz, A. Saiani, A. Pepe, Tuning of hydrogel stiffness using a two-component peptide system for mammalian cell culture, *J. Biomed. Mater. Res. - Part A*. 107 (2019) 535–544.  
<https://doi.org/10.1002/jbm.a.36568>.
- [289] G. Zuber, S.J. Prestrelski, K. Benedek, Application of Fourier transform infrared spectroscopy to studies of aqueous protein solutions, *Anal. Biochem.* 207 (1992) 150–156. [https://doi.org/10.1016/0003-2697\(92\)90516-A](https://doi.org/10.1016/0003-2697(92)90516-A).
- [290] N.J. Greenfield, Using circular dichroism spectra to estimate protein secondary structure, *Nat. Protoc.* 1 (2007) 2876–2890. <https://doi.org/10.1038/nprot.2006.202>.
- [291] C.G. Golding, L.L. Lamboo, D.R. Beniac, T.F. Booth, The scanning electron microscope in microbiology and diagnosis of infectious disease, *Sci. Rep.* 6 (2016) 1–8. <https://doi.org/10.1038/srep26516>.
- [292] S. Thiberge, A. Nechushtan, D. Sprinzak, O. Gileadi, V. Behar, O. Zik, Y. Chowers, S. Michaeli, J. Schlessinger, E. Moses, Scanning electron microscopy of cells and tissues under fully hydrated conditions, *Proc. Natl. Acad. Sci. U. S. A.* 101 (2004) 3346–3351. <https://doi.org/10.1073/pnas.0400088101>.
- [293] P.C. Nalam, N.N. Gosvami, M.A. Caporizzo, R.J. Composto, R.W. Carpick, Nanorheology of hydrogels using direct drive force modulation atomic force microscopy, *Soft Matter*. 11 (2015) 8165–8178. <https://doi.org/10.1039/c5sm01143d>.
- [294] M.L. Oyen, Mechanical characterisation of hydrogel materials, *Int. Mater. Rev.* 59 (2014) 44–59. <https://doi.org/10.1179/1743280413Y.0000000022>.
- [295] J.M. Zuidema, C.J. Rivet, R.J. Gilbert, F.A. Morrison, A protocol for rheological characterization of hydrogels for tissue engineering strategies, *J. Biomed. Mater. Res. Part B Appl. Biomater.* 102 (2014) 1063–1073.  
<https://doi.org/10.1002/jbm.b.33088>.
- [296] Y.L. Yang, L.J. Kaufman, Rheology and confocal reflectance microscopy as probes of mechanical properties and structure during collagen and collagen/hyaluronan self-assembly, *Biophys. J.* 96 (2009) 1566–1585.  
<https://doi.org/10.1016/j.bpj.2008.10.063>.
- [297] P.A. Janmey, P.C. Georges, S. Hvidt, Basic Rheology for Biologists, *Methods Cell Biol.* 83 (2007) 1–27. [https://doi.org/10.1016/S0091-679X\(07\)83001-9](https://doi.org/10.1016/S0091-679X(07)83001-9).

- [298] C. Yan, A. Altunbas, T. Yucel, R.P. Nagarkar, J.P. Schneider, D.J. Pochan, Injectable solid hydrogel: Mechanism of shear-thinning and immediate recovery of injectable  $\beta$ -hairpin peptide hydrogels, *Soft Matter*. 6 (2010) 5143–5156. <https://doi.org/10.1039/c0sm00642d>.
- [299] A. Buxboim, I.L. Ivanovska, D.E. Discher, Matrix elasticity, cytoskeletal forces and physics of the nucleus: How deeply do cells “feel” outside and in?, *J. Cell Sci.* 123 (2010) 297–308. <https://doi.org/10.1242/jcs.041186>.
- [300] A. Samani, J. Zubovits, D. Plewes, Elastic moduli of normal and pathological human breast tissues: an inversion-technique-based investigation of 169 samples, *Phys. Med. Biol.* 52 (2007) 1565–1576. <https://doi.org/10.1088/0031-9155/52/6/002>.
- [301] P. Deptuła, D. Łysik, K. Pogoda, M. Cieśluk, A. Namiot, J. Mystkowska, G. Król, S. Głuszek, P.A. Janmey, R. Bucki, Tissue Rheology as a Possible Complementary Procedure to Advance Histological Diagnosis of Colon Cancer, *ACS Biomater. Sci. Eng.* 6 (2020) 5620–5631. <https://doi.org/10.1021/acsbiomaterials.0c00975>.
- [302] C. Madsen, T. Cox, Relative Stiffness Measurements of Tumour Tissues by Shear Rheology, *BIO-PROTOCOL*. 7 (2017). <https://doi.org/10.21769/BioProtoc.2265>.
- [303] S. Shah, A. Chandra, A. Kaur, N. Sabnis, A. Lacko, Z. Gryczynski, R. Fudala, I. Gryczynski, Fluorescence properties of doxorubicin in PBS buffer and PVA films, *J. Photochem. Photobiol. B Biol.* 170 (2017) 65–69. <https://doi.org/10.1016/j.jphotobiol.2017.03.024>.
- [304] D.R. Miller, J.W. Jarrett, A.M. Hassan, A.K. Dunn, Deep tissue imaging with multiphoton fluorescence microscopy, *Curr. Opin. Biomed. Eng.* 4 (2017) 32–39. <https://doi.org/10.1016/j.cobme.2017.09.004>.
- [305] Shedding light on deep tissue: Multiphoton microscopy | Science | AAAS, (n.d.). <https://www.sciencemag.org/features/2019/03/shedding-light-deep-tissue-multiphoton-microscopy> (accessed November 27, 2020).
- [306] J.E. Welsh, Animal Models for Studying Prevention and Treatment of Breast Cancer, in: *Anim. Model. Study Hum. Dis.*, Elsevier Inc., 2013: pp. 997–1018. <https://doi.org/10.1016/B978-0-12-415894-8.00040-3>.
- [307] B. Raphael, T. Khalil, V.L. Workman, A. Smith, C.P. Brown, C. Streuli, A. Saiani, M. Domingos, 3D cell bioprinting of self-assembling peptide-based hydrogels, *Mater. Lett.* 190 (2017) 103–106. <https://doi.org/10.1016/J.MATLET.2016.12.127>.
- [308] W. Dong, H. Li, Y. Zhang, H. Yang, M. Guo, L. Li, T. Liu, Matrix metalloproteinase 2 promotes cell growth and invasion in colorectal cancer, *Acta Biochim. Biophys. Sin. (Shanghai)*. 43 (2011) 840–848. <https://doi.org/10.1093/abbs/gmr085>.
- [309] M. Allen, J. Louise Jones, Jekyll and Hyde: the role of the microenvironment on the progression of cancer, *J. Pathol.* 223 (2011) 163–177. <https://doi.org/10.1002/path.2803>.
- [310] S.N. Rampersad, Multiple applications of alamar blue as an indicator of metabolic function and cellular health in cell viability bioassays, *Sensors (Switzerland)*. 12 (2012) 12347–12360. <https://doi.org/10.3390/s120912347>.

- [311] L. Peternel, M. Kotnik, A. Preželj, U. Urleb, Comparison of 3 cytotoxicity screening assays and their application to the selection of novel antibacterial hits, *J. Biomol. Screen.* 14 (2009) 142–150. <https://doi.org/10.1177/1087057108329452>.
- [312] S. Kaja, A.J. Payne, Y. Naumchuk, P. Koulen, Quantification of lactate dehydrogenase for cell viability testing using cell lines and primary cultured astrocytes, *Curr. Protoc. Toxicol.* 2017 (2017) 1–10. <https://doi.org/10.1002/cptx.21>.
- [313] L.A. Castillo Diaz, M. Elsayy, A. Saiani, J.E. Gough, A.F. Miller, Osteogenic differentiation of human mesenchymal stem cells promotes mineralization within a biodegradable peptide hydrogel, *J. Tissue Eng.* 7 (2016) 204173141664978. <https://doi.org/10.1177/2041731416649789>.
- [314] M. Cavo, M. Fato, L. Peñuela, F. Beltrame, R. Raiteri, S. Scaglione, Microenvironment complexity and matrix stiffness regulate breast cancer cell activity in a 3D in vitro model, *Sci. Rep.* 6 (2016) 35367. <https://doi.org/10.1038/srep35367>.
- [315] G. Benton, G. DeGray, H.K. Kleinman, J. George, I. Arnaoutova, In vitro microtumors provide a physiologically predictive tool for breast cancer therapeutic screening., *PLoS One.* 10 (2015) e0123312. <https://doi.org/10.1371/journal.pone.0123312>.
- [316] Y. Li, N. Khuu, A. Gevorkian, S. Sarjinsky, H. Therien-Aubin, Y. Wang, S. Cho, E. Kumacheva, Supramolecular Nanofibrillar Thermoreversible Hydrogel for Growth and Release of Cancer Spheroids, *Angew. Chemie Int. Ed.* 56 (2017) 6083–6087. <https://doi.org/10.1002/anie.201610353>.
- [317] L.A. Sawicki, E.M. Ovadia, L. Pradhan, J.E. Cowart, K.E. Ross, C.H. Wu, A.M. Kloxin, Tunable synthetic extracellular matrices to investigate breast cancer response to biophysical and biochemical cues., *APL Bioeng.* 3 (2019) 016101. <https://doi.org/10.1063/1.5064596>.
- [318] T. Scholzen, J. Gerdes, The Ki-67 protein: From the known and the unknown, *J. Cell. Physiol.* 182 (2000) 311–322. [https://doi.org/10.1002/\(SICI\)1097-4652\(200003\)182:3<311::AID-JCP1>3.0.CO;2-9](https://doi.org/10.1002/(SICI)1097-4652(200003)182:3<311::AID-JCP1>3.0.CO;2-9).
- [319] L.T. Li, G. Jiang, Q. Chen, J.N. Zheng, Predic Ki67 is a promising molecular target in the diagnosis of cancer (Review), *Mol. Med. Rep.* 11 (2015) 1566–1572. <https://doi.org/10.3892/mmr.2014.2914>.
- [320] L. Li, G. Jiang, Q. Chen, J. Zheng, Ki67 is a promising molecular target in the diagnosis of cancer (Review), *Mol. Med. Rep.* (2014). <https://doi.org/10.3892/mmr.2014.2914>.
- [321] K. Subik, J.-F. Lee, L. Baxter, T. Strzepak, D. Costello, P. Crowley, L. Xing, M.-C. Hung, T. Bonfiglio, D.G. Hicks, P. Tang, The Expression Patterns of ER, PR, HER2, CK5/6, EGFR, Ki-67 and AR by Immunohistochemical Analysis in Breast Cancer Cell Lines., *Breast Cancer (Auckl).* 4 (2010) 35–41. <http://www.ncbi.nlm.nih.gov/pubmed/20697531> (accessed April 25, 2017).
- [322] P.A. Kenny, G.Y. Lee, C.A. Myers, R.M. Neve, J.R. Semeiks, P.T. Spellman, K. Lorenz, E.H. Lee, M.H. Barcellos-Hoff, O.W. Petersen, J.W. Gray, M.J. Bissell, The morphologies of breast cancer cell lines in three-dimensional assays correlate with their profiles of gene expression., *Mol. Oncol.* 1 (2007) 84–96. <https://doi.org/10.1016/j.molonc.2007.02.004>.

- [323] E.M. Langer, B.L. Allen-Petersen, S.M. King, N.D. Kendsersky, M.A. Turnidge, G.M. Kuziel, R. Riggers, R. Samatham, T.S. Amery, S.L. Jacques, B.C. Sheppard, J.E. Korkola, J.L. Muschler, G. Thibault, Y.H. Chang, J.W. Gray, S.C. Presnell, D.G. Nguyen, R.C. Sears, Modeling Tumor Phenotypes In Vitro with Three-Dimensional Bioprinting, *Cell Rep.* 26 (2019) 608-623.e6. <https://doi.org/10.1016/j.celrep.2018.12.090>.
- [324] R. Nishimura, T. Osako, Y. Okumura, M. Hayashi, Y. Totoyozumi, N. Arima, Ki-67 as a prognostic marker according to breast cancer subtype and a predictor of recurrence time in primary breast cancer, *Exp. Ther. Med.* 1 (2010) 747–754. <https://doi.org/10.3892/etm.2010.133>.
- [325] A.A. Hashmi, K.A. Hashmi, M. Irfan, S.M. Khan, M.M. Edhi, J.P. Ali, S.K. Hashmi, H. Asif, N. Faridi, A. Khan, Ki67 index in intrinsic breast cancer subtypes and its association with prognostic parameters, *BMC Res. Notes.* 12 (2019) 605. <https://doi.org/10.1186/s13104-019-4653-x>.
- [326] K. Subik, J.-F. Lee, L. Baxter, T. Strzepak, D. Costello, P. Crowley, L. Xing, M.-C. Hung, T. Bonfiglio, D.G. Hicks, P. Tang, The Expression Patterns of ER, PR, HER2, CK5/6, EGFR, Ki-67 and AR by Immunohistochemical Analysis in Breast Cancer Cell Lines., *Breast Cancer (Auckl).* 4 (2010) 35–41. <http://www.ncbi.nlm.nih.gov/pubmed/20697531> (accessed May 26, 2017).
- [327] S. Pradhan, I. Hassani, W.J. Seeto, E.A. Lipke, PEG-fibrinogen Hydrogels for Three-dimensional Breast Cancer Cell Culture, (n.d.). <https://doi.org/10.1002/jbm.a.35899>.
- [328] A. V. Taubenberger, L.J. Bray, B. Haller, A. Shaposhnykov, M. Binner, U. Freudenberg, J. Guck, C. Werner, 3D extracellular matrix interactions modulate tumour cell growth, invasion and angiogenesis in engineered tumour microenvironments, *Acta Biomater.* 36 (2016). <https://doi.org/10.1016/j.actbio.2016.03.017>.
- [329] S. Xu, H. Xu, W. Wang, S. Li, H. Li, T. Li, W. Zhang, X. Yu, L. Liu, The role of collagen in cancer: From bench to bedside, *J. Transl. Med.* 17 (2019) 1–22. <https://doi.org/10.1186/s12967-019-2058-1>.
- [330] L.A. Castillo Diaz, A. Saiani, J.E. Gough, A.F. Miller, Human osteoblasts within soft peptide hydrogels promote mineralisation in vitro, *J. Tissue Eng.* 5 (2014) 204173141453934. <https://doi.org/10.1177/2041731414539344>.
- [331] B.T. Finicle, V. Jayashankar, A.L. Edinger, Nutrient scavenging in cancer, *Nat. Rev. Cancer.* 18 (2018) 619–633. <https://doi.org/10.1038/s41568-018-0048-x>.
- [332] P.K. Vemula, J.E. Kohler, A. Blass, M. Williams, C. Xu, L. Chen, S.R. Jadhav, G. John, D.I. Soybel, J.M. Karp, Self-assembled hydrogel fibers for sensing the multi-compartment intracellular milieu, *Sci. Rep.* 4 (2014) 1–9. <https://doi.org/10.1038/srep04466>.
- [333] P.M.R. Pereira, N. Berisha, N.V.S.D.K. Bhupathiraju, R. Fernandes, J.P.C. Tomé, C.M. Drain, Cancer cell spheroids are a better screen for the photodynamic efficiency of glycosylated photosensitizers, *PLoS One.* 12 (2017) e0177737. <https://doi.org/10.1371/journal.pone.0177737>.
- [334] S. Sakamoto, W. Putalun, S. Vimolmangkang, W. Phoolcharoen, Y. Shoyama, H. Tanaka, S. Morimoto, Enzyme-linked immunosorbent assay for the

quantitative/qualitative analysis of plant secondary metabolites, *J. Nat. Med.* 72 (2018) 32–42. <https://doi.org/10.1007/s11418-017-1144-z>.

- [335] Y. Kumada, N.A. Hammond, S. Zhang, Functionalized scaffolds of shorter self-assembling peptides containing MMP-2 cleavable motif promote fibroblast proliferation and significantly accelerate 3-D cell migration independent of scaffold stiffness, *Soft Matter*. 6 (2010) 5073–5079. <https://doi.org/10.1039/c0sm00333f>.
- [336] K.L. Sodek, T.J. Brown, M.J. Ringuette, Collagen I but not Matrigel matrices provide an MMP-dependent barrier to ovarian cancer cell penetration, *BMC Cancer*. 8 (2008) 223. <https://doi.org/10.1186/1471-2407-8-223>.
- [337] D. Wu, P. Yotnda, Induction and testing of hypoxia in cell culture., *J. Vis. Exp.* (2011). <https://doi.org/10.3791/2899>.
- [338] J. Song, A. Miermont, C.T. Lim, R.D. Kamm, A 3D microvascular network model to study the impact of hypoxia on the extravasation potential of breast cell lines., *Sci. Rep.* 8 (2018) 17949. <https://doi.org/10.1038/s41598-018-36381-5>.
- [339] D.M. Lewis, M.R. Blatchley, K.M. Park, S. Gerecht, O<sub>2</sub>-controllable hydrogels for studying cellular responses to hypoxic gradients in three dimensions in vitro and in vivo, *Nat. Protoc.* 12 (2017) 1620–1638. <https://doi.org/10.1038/nprot.2017.059>.
- [340] K.M. Park, S. Gerecht, Hypoxia-inducible hydrogels, *Nat. Commun.* 5 (2014) 4075. <https://doi.org/10.1038/ncomms5075>.
- [341] H. Škovierová, T. Okajčėková, J. Strnáděl, E. Vidomanová, E. Halašová, Molecular regulation of epithelial-to-mesenchymal transition in tumorigenesis (Review), *Int. J. Mol. Med.* 41 (2018) 1187–1200. <https://doi.org/10.3892/ijmm.2017.3320>.
- [342] L. Fattet, H.Y. Jung, M.W. Matsumoto, B.E. Aubol, A. Kumar, J.A. Adams, A.C. Chen, R.L. Sah, A.J. Engler, E.B. Pasquale, J. Yang, Matrix Rigidity Controls Epithelial-Mesenchymal Plasticity and Tumor Metastasis via a Mechanoresponsive EPHA2/LYN Complex, *Dev. Cell.* 54 (2020) 302-316.e7. <https://doi.org/10.1016/j.devcel.2020.05.031>.
- [343] M. Pal, H. Chen, B.H. Lee, J.Y.H. Lee, Y.S. Yip, N.S. Tan, L.P. Tan, Epithelial-mesenchymal transition of cancer cells using bioengineered hybrid scaffold composed of hydrogel/3D-fibrous framework, *Sci. Rep.* 9 (2019). <https://doi.org/10.1038/s41598-019-45384-9>.
- [344] S.Y. Tam, V.W.C. Wu, H.K.W. Law, Hypoxia-Induced Epithelial-Mesenchymal Transition in Cancers: HIF-1 $\alpha$  and Beyond, *Front. Oncol.* 10 (2020) 486. <https://doi.org/10.3389/fonc.2020.00486>.
- [345] Y. Wang, S. Mirza, S. Wu, J. Zeng, W. Shi, H. Band, V. Band, B. Duan, 3D hydrogel breast cancer models for studying the effects of hypoxia on epithelial to mesenchymal transition, *Oncotarget*. 9 (2018) 32191–32203. <https://doi.org/10.18632/oncotarget.25891>.
- [346] C.Y. Liu, H.H. Lin, M.J. Tang, Y.K. Wang, Vimentin contributes to epithelial-mesenchymal transition cancer cell mechanics by mediating cytoskeletal organization and focal adhesion maturation, *Oncotarget*. 6 (2015) 15966–15983. <https://doi.org/10.18632/oncotarget.3862>.
- [347] B. Robinson-Bennett, A. Han, Role of Immunohistochemistry in Elucidating Lung

Cancer Metastatic to the Ovary from Primary Ovarian Carcinoma, *Handb. Immunohistochem. Situ Hybrid. Hum. Carcinomas.* 4 (2006) 537–545.  
[https://doi.org/10.1016/S1874-5784\(05\)80116-3](https://doi.org/10.1016/S1874-5784(05)80116-3).

- [348] B.J. Gill, D.L. Gibbons, L.C. Roudsari, J.E. Saik, Z.H. Rizvi, J.D. Roybal, J.M. Kurie, J.L. West, A synthetic matrix with independently tunable biochemistry and mechanical properties to study epithelial morphogenesis and EMT in a lung adenocarcinoma model, *Cancer Res.* 72 (2012) 6013–6023.  
<https://doi.org/10.1158/0008-5472.CAN-12-0895>.
- [349] A.G. Clark, D.M. Vignjevic, Modes of cancer cell invasion and the role of the microenvironment, *Curr. Opin. Cell Biol.* 36 (2015) 13–22.  
<https://doi.org/10.1016/j.ceb.2015.06.004>.
- [350] J. Marshall, Transwell ® invasion assays, *Methods Mol. Biol.* 769 (2011) 97–110.  
[https://doi.org/10.1007/978-1-61779-207-6\\_8](https://doi.org/10.1007/978-1-61779-207-6_8).
- [351] M. Vinci, C. Box, S.A. Eccles, Three-dimensional (3D) tumor spheroid invasion assay, *J. Vis. Exp.* 2015 (2015). <https://doi.org/10.3791/52686>.
- [352] K.V. Nguyen-Ngoc, K.J. Cheung, A. Brenot, E.R. Shamir, R.S. Gray, W.C. Hines, P. Yaswen, Z. Werb, A.J. Ewald, ECM microenvironment regulates collective migration and local dissemination in normal and malignant mammary epithelium, *Proc. Natl. Acad. Sci. U. S. A.* 109 (2012).  
<https://doi.org/10.1073/pnas.1212834109>.
- [353] K. Liu, P.A. Newbury, B.S. Glicksberg, W.Z.D. Zeng, S. Paithankar, E.R. Andrechek, B. Chen, Evaluating cell lines as models for metastatic breast cancer through integrative analysis of genomic data, *Nat. Commun.* 10 (2019) 1–12.  
<https://doi.org/10.1038/s41467-019-10148-6>.
- [354] W. Li, X. Shi, Y. Xu, J. Wan, S. Wei, R. Zhu, Tamoxifen promotes apoptosis and inhibits invasion in estrogen-positive breast cancer MCF-7 cells, *Mol. Med. Rep.* 16 (2017) 478–484. <https://doi.org/10.3892/mmr.2017.6603>.
- [355] Q. Wang, Y. Cheng, Y. Wang, Y. Fan, C. Li, Y. Zhang, Y. Wang, Q. Dong, Y. Ma, Y. e. Teng, X. Qu, Y. Liu, Tamoxifen reverses epithelial-mesenchymal transition by demethylating miR-200c in triple-negative breast cancer cells, *BMC Cancer.* 17 (2017). <https://doi.org/10.1186/s12885-017-3457-4>.
- [356] C.F. Thorn, C. Oshiro, S. Marsh, T. Hernandez-Boussard, H. McLeod, T.E. Klein, R.B. Altman, Doxorubicin pathways: Pharmacodynamics and adverse effects, *Pharmacogenet. Genomics.* 21 (2011) 440–446.  
<https://doi.org/10.1097/FPC.0b013e32833ffb56>.
- [357] J.G. Van oosterwijk, B. Herpers, D. Meijer, I.H. Briaire-de bruijn, A.M. Cleton-jansen, H. Gelderblom, B. Van de water, J.V.M.G. Bée, Restoration of chemosensitivity for doxorubicin and cisplatin in chondrosarcoma in vitro: BCL-2 family members cause chemoresistance, *Ann. Oncol.* 23 (2012) 1617–1626.  
<https://doi.org/10.1093/annonc/mdr512>.
- [358] G. Jones, Fitting and handling dose response data, *J. Comput. Aided. Mol. Des.* 29 (2015) 1–11. <https://doi.org/10.1007/s10822-014-9752-0>.
- [359] J.L. Sebaugh, Guidelines for accurate EC50/IC50 estimation, *Pharm. Stat.* 10 (2011) 128–134. <https://doi.org/10.1002/pst.426>.

- [360] R.E. Ayata, S. Chabaud, M. Auger, R. Pouliot, Behaviour of endothelial cells in a tridimensional in vitro environment, *Biomed Res. Int.* 2015 (2015). <https://doi.org/10.1155/2015/630461>.
- [361] K. Chwalek, M. V. Tsurkan, U. Freudenberg, C. Werner, Glycosaminoglycan-based hydrogels to modulate heterocellular communication in in vitro angiogenesis models, *Sci. Rep.* 4 (2014). <https://doi.org/10.1038/srep04414>.
- [362] V. Mastrullo, W. Cathery, E. Velliou, P. Madeddu, P. Campagnolo, Angiogenesis in Tissue Engineering: As Nature Intended?, *Front. Bioeng. Biotechnol.* 8 (2020) 188. <https://doi.org/10.3389/fbioe.2020.00188>.
- [363] J. Maksimcuka, Bioactive scaffold-based tissue engineering strategies for orthopaedic applications, The University of Manchester, 2019. <https://www.escholar.manchester.ac.uk/item/?pid=uk-ac-man-scw:322337>.
- [364] G. Carpentier, S. Berndt, S. Ferratge, W. Rasband, M. Cuendet, G. Uzan, P. Albanese, Angiogenesis Analyzer for ImageJ — A comparative morphometric analysis of “Endothelial Tube Formation Assay” and “Fibrin Bead Assay,” *Sci. Rep.* 10 (2020) 11568. <https://doi.org/10.1038/s41598-020-67289-8>.
- [365] D.S. Grant, K. Tashiro, B. Segui-Real, Y. Yamada, G.R. Martin, H.K. Kleinman, Two different laminin domains mediate the differentiation of human endothelial cells into capillary-like structures in vitro., *Cell.* 58 (1989) 933–43. [https://doi.org/10.1016/0092-8674\(89\)90945-8](https://doi.org/10.1016/0092-8674(89)90945-8).
- [366] K. Stamati, J. V. Priestley, V. Mudera, U. Cheema, Laminin promotes vascular network formation in 3D in vitro collagen scaffolds by regulating VEGF uptake, *Exp. Cell Res.* 327 (2014) 68–77. <https://doi.org/10.1016/J.YEXCR.2014.05.012>.
- [367] S. Takahashi, M. Leiss, M. Moser, T. Ohashi, T. Kitao, D. Heckmann, A. Pfeifer, H. Kessler, J. Takagi, H.P. Erickson, R. Fässler, The RGD motif in fibronectin is essential for development but dispensable for fibril assembly, *J. Cell Biol.* 178 (2007). <http://jcb.rupress.org/content/178/1/167.long> (accessed May 6, 2017).
- [368] G. Thurston, B. Jaggi, B. Palcic, Measurement of cell motility and morphology with an automated microscope system, *Cytometry.* 9 (1988) 411–417. <https://doi.org/10.1002/cyto.990090502>.
- [369] P. Lertkiatmongkol, D. Liao, H. Mei, Y. Hu, P.J. Newman, Endothelial functions of platelet/endothelial cell adhesion molecule-1 (CD31), *Curr. Opin. Hematol.* 23 (2016) 253–259. <https://doi.org/10.1097/MOH.0000000000000239>.
- [370] M. Nakamura, M. Mie, H. Mihara, M. Nakamura, E. Kobatake, Construction of multi-functional extracellular matrix proteins that promote tube formation of endothelial cells, *Biomaterials.* 29 (2008) 2977–2986. <https://doi.org/10.1016/j.biomaterials.2008.04.006>.
- [371] E.H.J. Danen, Integrins: An Overview of Structural and Functional Aspects, (2013). <https://www.ncbi.nlm.nih.gov/books/NBK6259/> (accessed August 3, 2020).
- [372] L.A. Marquez-Curtis, A.B. Sultani, L.E. McGann, J.A.W. Elliott, Beyond membrane integrity: Assessing the functionality of human umbilical vein endothelial cells after cryopreservation, *Cryobiology.* 72 (2016) 183–190. <https://doi.org/10.1016/j.cryobiol.2016.05.005>.

- [373] D. Guidolin, G. Albertin, D. Ribatti, Exploring in vitro angiogenesis by image analysis and mathematical modeling, Undefined. (2010).
- [374] K.L. DeCicco-Skinner, G.H. Henry, C. Cataisson, T. Tabib, J.C. Gwilliam, N.J. Watson, E.M. Bullwinkle, L. Falkenburg, R.C. O'Neill, A. Morin, J.S. Wiest, Endothelial cell tube formation assay for the in vitro study of angiogenesis., *J. Vis. Exp.* (2014) e51312. <https://doi.org/10.3791/51312>.
- [375] M. De Palma, D. Biziato, T. V. Petrova, Microenvironmental regulation of tumour angiogenesis, *Nat. Rev. Cancer.* 17 (2017) 457–474. <https://doi.org/10.1038/nrc.2017.51>.
- [376] C. Gialeli, M. Viola, D. Barbouri, D. Kletsas, A. Passi, N.K. Karamanos, Dynamic interplay between breast cancer cells and normal endothelium mediates the expression of matrix macromolecules, proteasome activity and functional properties of endothelial cells ☆, (2014). <https://doi.org/10.1016/j.bbagen.2014.02.019>.
- [377] H. Cai, Y. Xue, Z. Li, Y. Hu, Z. Wang, W. Liu, Z. Li, Y. Liu, Roundabout4 suppresses glioma-induced endothelial cell proliferation, migration and tube formation in vitro by inhibiting VEGFR2-mediated PI3K/AKT and FAK signaling pathways, *Cell. Physiol. Biochem.* 35 (2015) 1689–1705. <https://doi.org/10.1159/000373982>.
- [378] T. Liu, M. Jabbes, J.R. Nedrow-Byers, L.Y. Wu, J.N. Bryan, C.E. Berkman, Detection of prostate-specific membrane antigen on HUVECs in response to breast tumor-conditioned medium, *Int. J. Oncol.* 38 (2011) 1349–1355. <https://doi.org/10.3892/ijo.2011.946>.
- [379] X.Y. Wang, J.X. Tan, M. Vasse, B. Delpech, G.S. Ren, Comparison of hyaluronidase expression, invasiveness and tubule formation promotion in ER (-) and ER (+) breast cancer cell lines in vitro, *Chin. Med. J. (Engl).* 122 (2009) 1300–1304. <https://doi.org/10.3760/cma.j.issn.0366-6999.2009.11.012>.
- [380] Y. Kubota, H.K. Kleinman, G.R. Martin, T.J. Lawley, Role of laminin and basement membrane in the morphological differentiation of human endothelial cells into capillary-like structures., *J. Cell Biol.* 107 (1988) 1589–98. <http://www.ncbi.nlm.nih.gov/pubmed/3049626> (accessed November 12, 2017).
- [381] O.D. Monera, T.J. Sereda, N.E. Zhou, C.M. Kay, R.S. Hodges, Relationship of sidechain hydrophobicity and  $\alpha$ -helical propensity on the stability of the single-stranded amphipathic  $\alpha$ -helix, *J. Pept. Sci.* 1 (1995) 319–329. <https://doi.org/10.1002/psc.310010507>.
- [382] K. Webb, V. Hlady, P.A. Tresco, Relative importance of surface wettability and charged functional groups on NIH 3T3 fibroblast attachment, spreading, and cytoskeletal organization, *J. Biomed. Mater. Res.* 41 (1998) 422–430. [https://doi.org/10.1002/\(SICI\)1097-4636\(19980905\)41:3<422::AID-JBM12>3.0.CO;2-K](https://doi.org/10.1002/(SICI)1097-4636(19980905)41:3<422::AID-JBM12>3.0.CO;2-K).
- [383] C. Zhu, Y. Gao, H. Li, S. Meng, L. Li, J.S. Francisco, X.C. Zeng, Characterizing hydrophobicity of amino acid side chains in a protein environment via measuring contact angle of a water nanodroplet on planar peptide network, *Proc. Natl. Acad. Sci. U. S. A.* 113 (2016) 12946–12951. <https://doi.org/10.1073/pnas.1616138113>.
- [384] Appendix C: Contact Angle Goniometry, *Surf. Des. Appl. Biosci. Nanotechnol.*

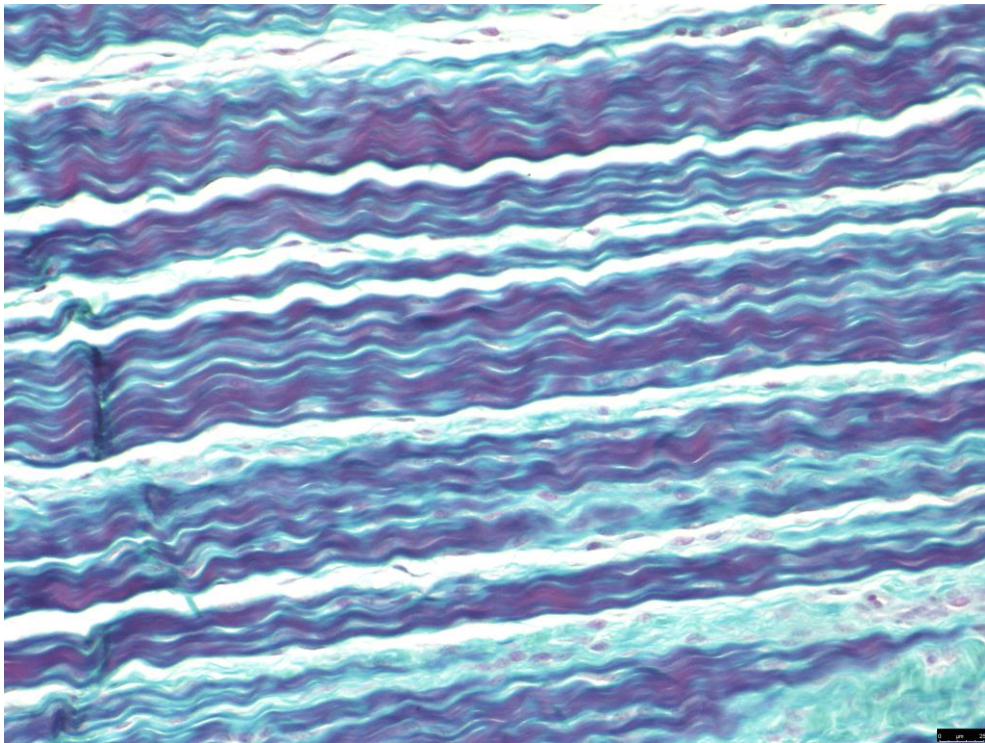


(2009) 471–473. <https://doi.org/doi:10.1002/9783527628599.app3>.

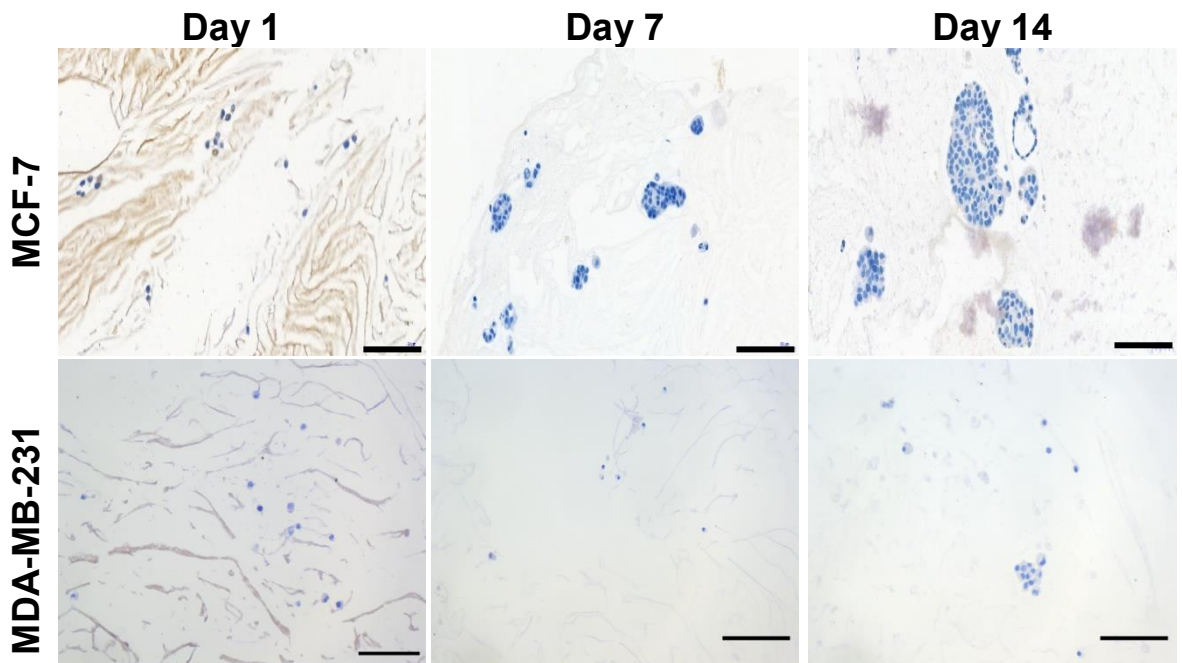
- [385] M. Hart, J. Lauer, M. Selig, M. Hanak, B. Walters, B. Rolauffs, Shaping the Cell and the Future: Recent Advancements in Biophysical Aspects Relevant to Regenerative Medicine, *J. Funct. Morphol. Kinesiol.* 3 (2017) 2. <https://doi.org/10.3390/jfmk3010002>.
- [386] T. Uynuk-Ool, M. Rothdiener, B. Walters, M. Hegemann, J. Palm, P. Nguyen, T. Seeger, U. Stöckle, J.P. Stegemann, W.K. Aicher, B. Kurz, M.L. Hart, G. Klein, B. Rolauffs, The geometrical shape of mesenchymal stromal cells measured by quantitative shape descriptors is determined by the stiffness of the biomaterial and by cyclic tensile forces, *J. Tissue Eng. Regen. Med.* 11 (2017) 3508–3522. <https://doi.org/10.1002/term.2263>.
- [387] J. Zhu, R.E. Marchant, Design properties of hydrogel tissue-engineering scaffolds, *Expert Rev. Med. Devices.* 8 (2011) 607–626. <https://doi.org/10.1586/erd.11.27>.
- [388] J.Z. Gasiowski, J.H. Collier, Directed intermixing in multicomponent self-assembling biomaterials, *Biomacromolecules.* 12 (2011) 3549–3558. <https://doi.org/10.1021/bm200763y>.
- [389] G. Le Saux, A. Magenau, T. Böcking, K. Gaus, J.J. Gooding, The Relative Importance of Topography and RGD Ligand Density for Endothelial Cell Adhesion, *PLoS One.* 6 (2011) e21869. <https://doi.org/10.1371/journal.pone.0021869>.
- [390] M.K. Lee, M.H. Rich, J. Lee, H. Kong, A bio-inspired, microchanneled hydrogel with controlled spacing of cell adhesion ligands regulates 3D spatial organization of cells and tissue, *Biomaterials.* 58 (2015) 26–34. <https://doi.org/10.1016/j.biomaterials.2015.04.014>.
- [391] J.J. Moon, J.E. Saik, R.A. Poché, J.E. Leslie-Barbick, S.H. Lee, A.A. Smith, M.E. Dickinson, J.L. West, Biomimetic hydrogels with pro-angiogenic properties, *Biomaterials.* 31 (2010) 3840–3847. <https://doi.org/10.1016/j.biomaterials.2010.01.104>.
- [392] J.P. Jung, J.L. Jones, S.A. Cronier, J.H. Collier, Modulating the mechanical properties of self-assembled peptide hydrogels via native chemical ligation, *Biomaterials.* 29 (2008) 2143–2151. <https://doi.org/10.1016/j.biomaterials.2008.01.008>.
- [393] M. Barczyk, S. Carracedo, D. Gullberg, Integrins., *Cell Tissue Res.* 339 (2010) 269–80. <https://doi.org/10.1007/s00441-009-0834-6>.
- [394] E.H.J. Danen, P. Sonneveld, C. Brakebusch, R. Fässler, A. Sonnenberg, The fibronectin-binding integrins  $\alpha 5\beta 1$  and  $\alpha v\beta 3$  differentially modulate RhoA-GTP loading, organization of cell matrix adhesions, and fibronectin fibrillogenesis, *J. Cell Biol.* 159 (2002) 1071–1086. <https://doi.org/10.1083/jcb.200205014>.
- [395] S. Maude, E. Ingham, A. Aggeli, Biomimetic self-assembling peptides as scaffolds for soft tissue engineering, *Nanomedicine.* 8 (2013) 823–847. <https://doi.org/10.2217/nnm.13.65>.
- [396] J.T. Yang, R.O. Hynes, Fibronectin receptor functions in embryonic cells deficient in  $\alpha 5\beta 1$  integrin can be replaced by  $\alpha(v)$  integrins, *Mol. Biol. Cell.* 7 (1996) 1737–1748. <https://doi.org/10.1091/mbc.7.11.1737>.

- [397] Y. Sun, W. Li, X. Wu, N. Zhang, Y. Zhang, S. Ouyang, X. Song, X. Fang, R. Seeram, W. Xue, L. He, W. Wu, Functional Self-Assembling Peptide Nanofiber Hydrogels Designed for Nerve Degeneration, *ACS Appl. Mater. Interfaces*. 8 (2016) 2348–2359. <https://doi.org/10.1021/acsami.5b11473>.
- [398] M.D. Stevenson, H. Piristine, N.J. Hoglebe, T.M. Nocera, M.W. Boehm, R.K. Reen, K.W. Koelling, G. Agarwal, A.L. Sarang-Sieminski, K.J. Gooch, A self-assembling peptide matrix used to control stiffness and binding site density supports the formation of microvascular networks in three dimensions, *Acta Biomater.* (2013). <https://doi.org/10.1016/j.actbio.2013.04.002>.
- [399] C. Vyas, R. Pereira, B. Huang, F. Liu, W. Wang, P. Bartolo, Engineering the vasculature with additive manufacturing, *Curr. Opin. Biomed. Eng.* 2 (2017) 1–13. <https://doi.org/10.1016/j.cobme.2017.05.008>.
- [400] V.E. Santo, S.P. Rebelo, M.F. Estrada, P.M. Alves, E. Boghaert, C. Brito, Drug screening in 3D in vitro tumor models: overcoming current pitfalls of efficacy read-outs, *Biotechnol. J.* 12 (2017). <https://doi.org/10.1002/biot.201600505>.
- [401] M.A. Acosta, P. Ymele-Leki, Y. V. Kostov, J.B. Leach, Fluorescent microparticles for sensing cell microenvironment oxygen levels within 3D scaffolds, *Biomaterials*. 30 (2009) 3068–3074. <https://doi.org/10.1016/j.biomaterials.2009.02.021>.
- [402] H. Niu, C. Li, Y. Guan, Y. Dang, X. Li, Z. Fan, J. Shen, L. Ma, J. Guan, High oxygen preservation hydrogels to augment cell survival under hypoxic condition, *Acta Biomater.* 105 (2020) 56–67. <https://doi.org/10.1016/j.actbio.2020.01.017>.
- [403] A. Dazzi, C.B. Prater, AFM-IR: Technology and applications in nanoscale infrared spectroscopy and chemical imaging, *Chem. Rev.* 117 (2017) 5146–5173. <https://doi.org/10.1021/acs.chemrev.6b00448>.
- [404] L.J. Bray, C. Secker, B. Murekatete, J. Sievers, M. Binner, P.B. Welzel, C. Werner, Three-dimensional in vitro hydro- and cryogel-based cell-culture models for the study of breast-cancer metastasis to bone, *Cancers (Basel)*. 10 (2018) 292. <https://doi.org/10.3390/cancers10090292>.
- [405] P. Gupta, P.A. Pérez-Mancera, H. Kocher, A. Nisbet, G. Schettino, E.G. Velliou, A Novel Scaffold-Based Hybrid Multicellular Model for Pancreatic Ductal Adenocarcinoma—Toward a Better Mimicry of the in vivo Tumor Microenvironment, *Front. Bioeng. Biotechnol.* 8 (2020) 290. <https://doi.org/10.3389/fbioe.2020.00290>.
- [406] L.C. Roudsari, S.E. Jeffs, A.S. Witt, B.J. Gill, J.L. West, A 3D Poly(ethylene glycol)-based Tumor Angiogenesis Model to Study the Influence of Vascular Cells on Lung Tumor Cell Behavior, *Sci. Rep.* 6 (2016) 32726. <https://doi.org/10.1038/srep32726>.
- [407] E.L.S. Fong, T.B. Toh, H. Yu, E.K.H. Chow, 3D Culture as a Clinically Relevant Model for Personalized Medicine, *SLAS Technol.* 22 (2017) 245–253. <https://doi.org/10.1177/2472630317697251>.
- [408] E.S. Sokol, D.H. Miller, A. Breggia, K.C. Spencer, L.M. Arendt, P.B. Gupta, Growth of human breast tissues from patient cells in 3D hydrogel scaffolds, *Breast Cancer Res.* 18 (2016). <https://doi.org/10.1186/s13058-016-0677-5>.

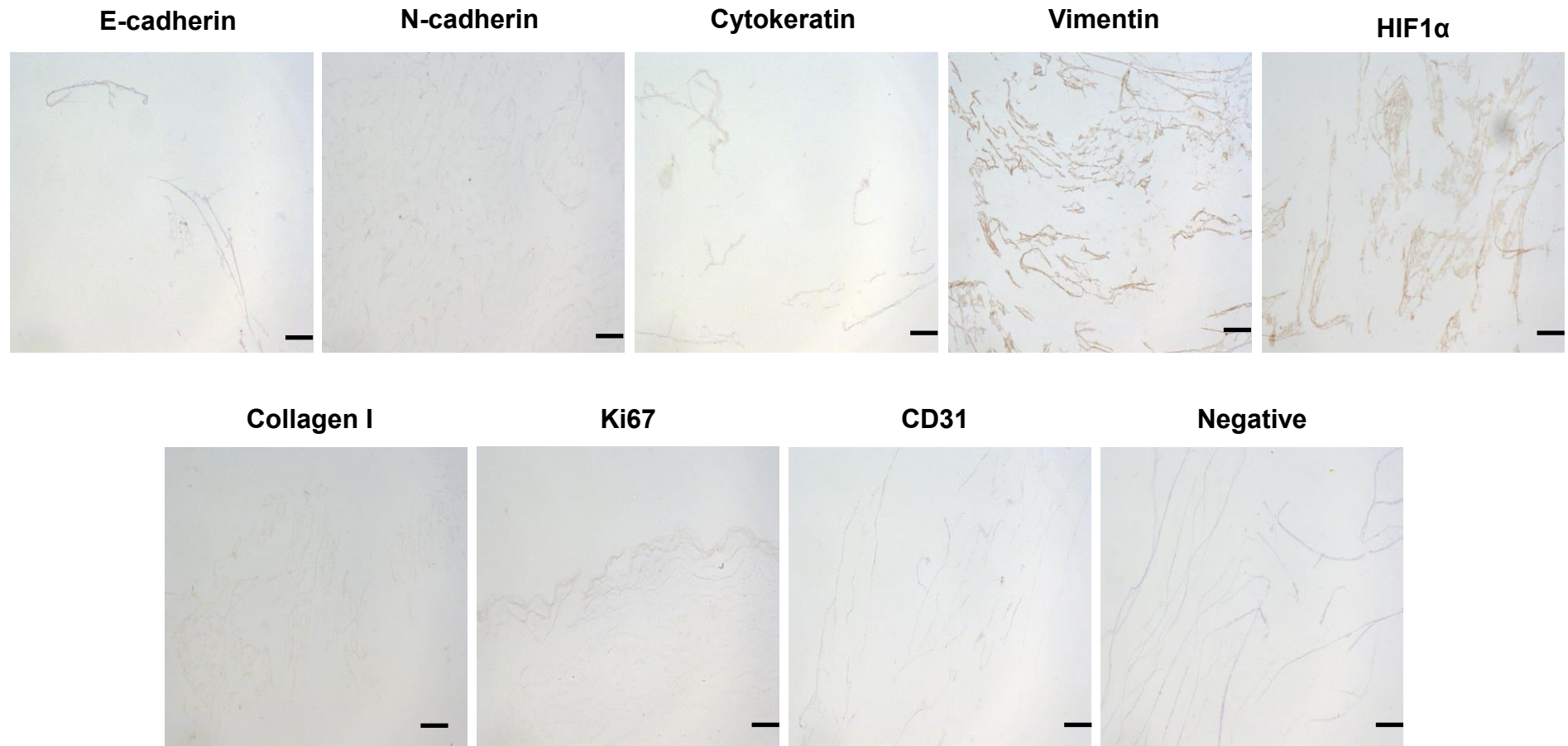
## CHAPTER 9 – Appendix



**Appendix 1. Positive control for Gomori Trichrome staining.** Pig anterior cruciate ligament was used. Green = collagen. Blue = nuclei. Scale bar = 25  $\mu$ m.

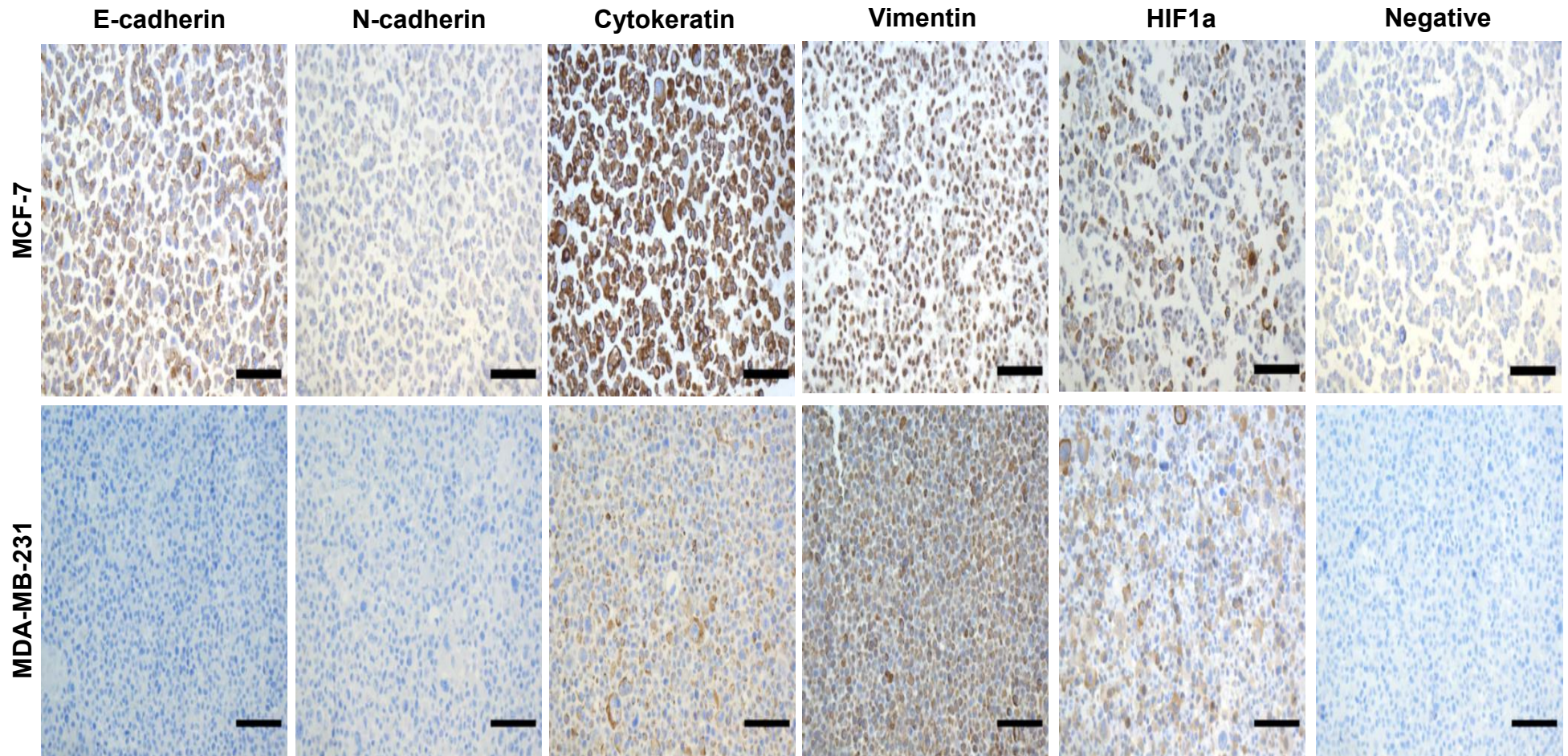


**Appendix 2. Representative negative controls of MCF-7 and MDA-MB-231 cells encapsulated in PeptiGelAlpha1.** The primary antibody was omitted from immunohistochemistry staining and all subsequent steps were carried out as normal. Brown = DAB staining. Blue = nuclei. Scale bar = 200  $\mu$ m.



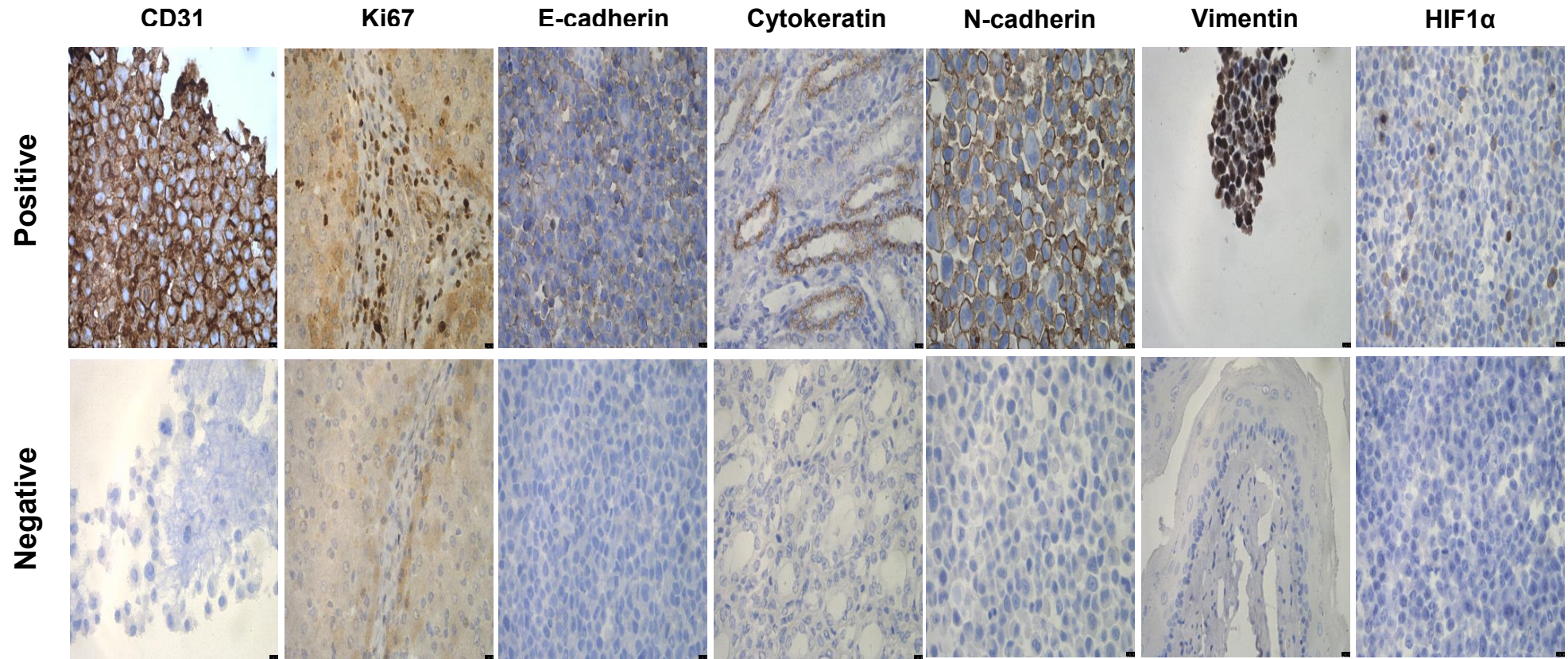
**Appendix 3. Acellular PeptiGelAlpha1 controls for immunohistochemistry staining.** Acellular samples were treated with the primary antibody and all subsequent steps were carried out as normal. Brown = DAB staining. Scale bar = 50  $\mu$ m.



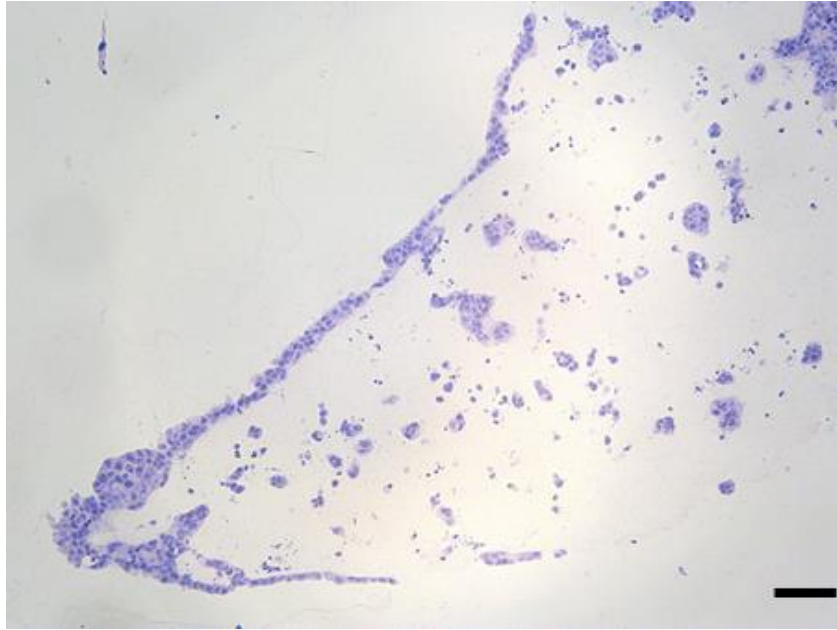


**Appendix 4. MCF-7 and MDA-MB-231 cell pellet controls for E-cadherin, N-cadherin, pan cytokeratin, vimentin and HIF1 $\alpha$ .** Brown = positive staining. Blue = nuclei. Scale bar = 200  $\mu$ m.



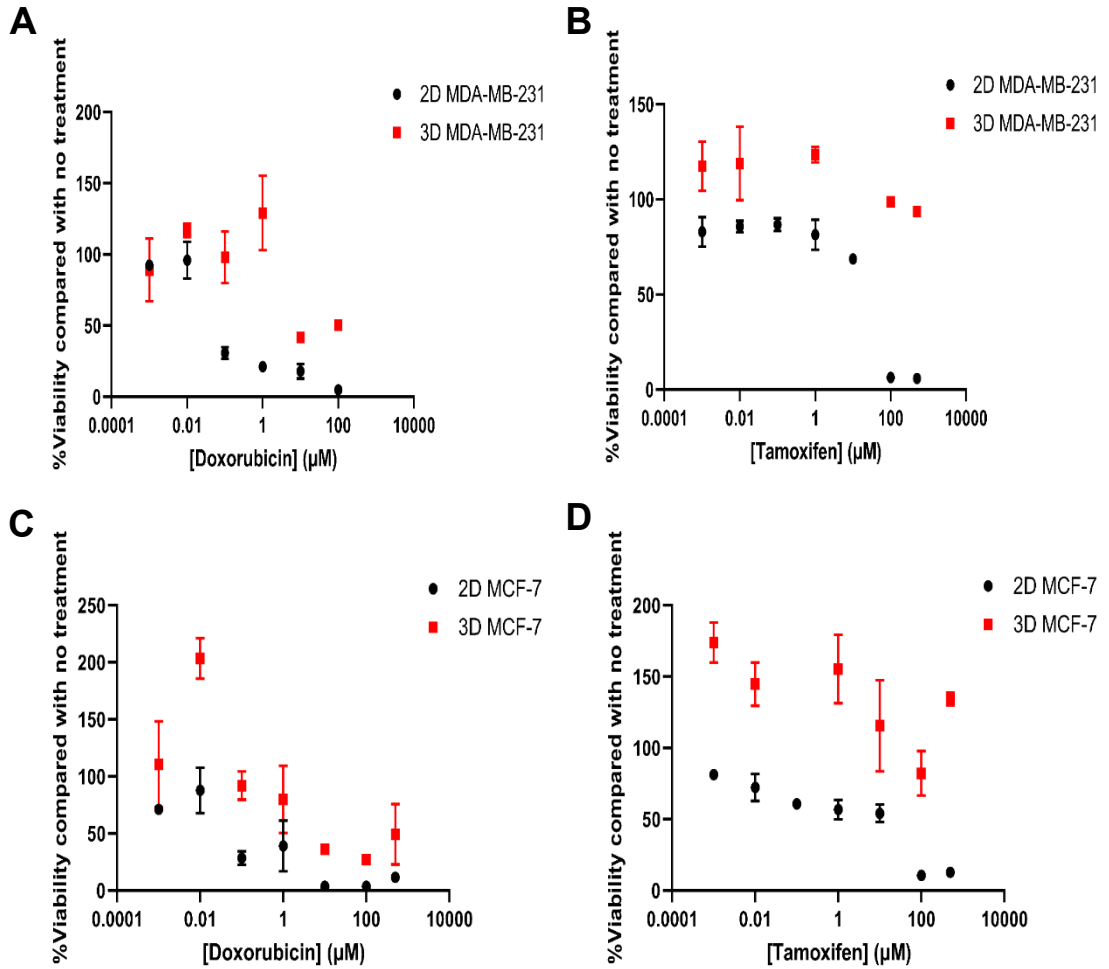


**Appendix 5. Positive control images for immunohistochemistry.** CD31 = HUVEC cell pellet. Ki67 = rat liver. E-cadherin = LNCaP cell pellet. Cytokeratin = pig kidney. N-cadherin = PC3 cell pellet. Vimentin = rat oesophagus. HIF1 $\alpha$  = LNCaP cell pellet. Brown = positive staining. Blue = nuclei. Scale bar = 10  $\mu$ m.

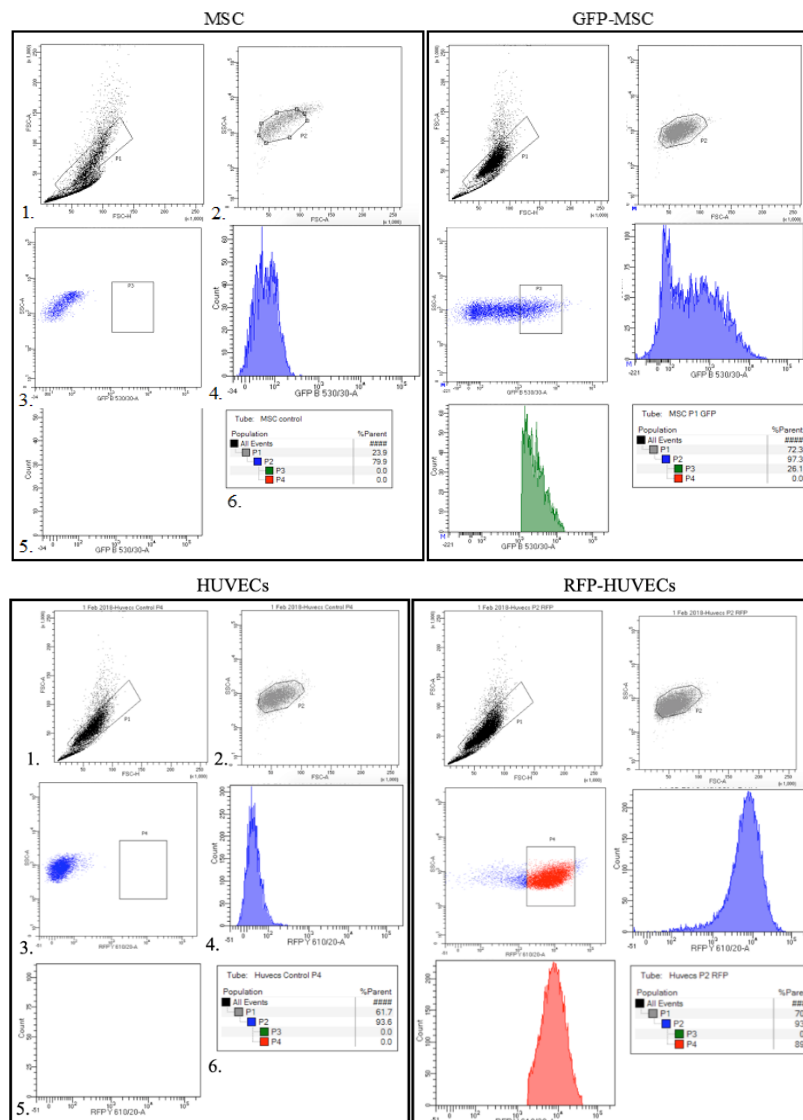


**Appendix 6. Contraction of collagen I by MCF-7 cells.** Nuclei = blue. Scale bar = 100  $\mu\text{m}$ .



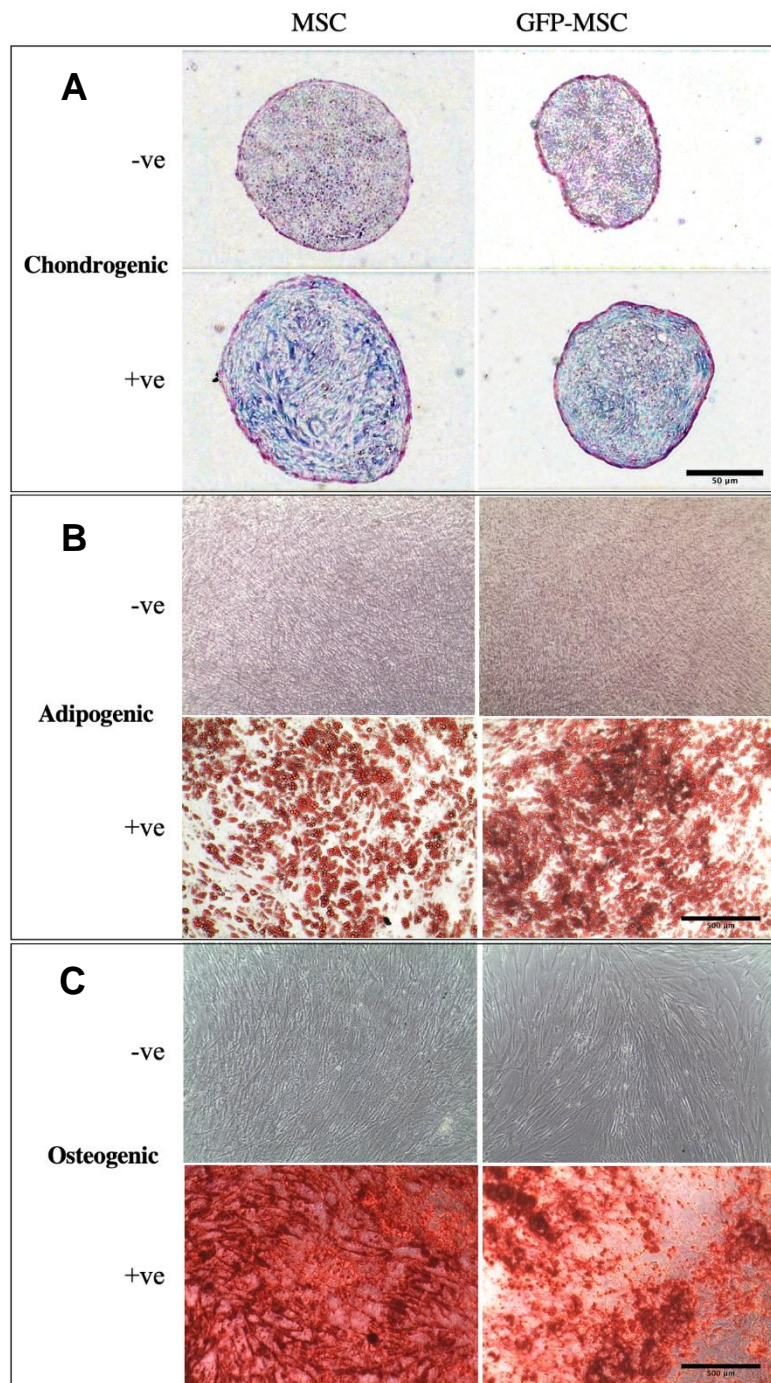


**Appendix 7. Dose-response curves without normalisation of Y values.** (A) MDA-MB-231 cells treated with doxorubicin. (B) MDA-MB-231 cells treated with tamoxifen. (C) MCF-7 cells treated with doxorubicin. (D) MCF-7 cells treated with tamoxifen. Data are presented as percentage viability compared with no treatment due to different cell-seeding densities used with 2D and 3D culture. Data are mean  $\pm$  S.D.

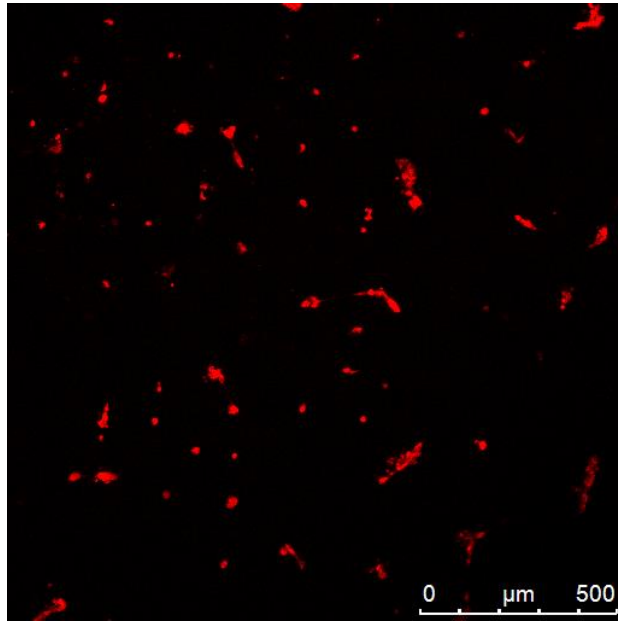


### Appendix 8. Steps for sorting GFP-MSCs and RFP-HUVECs using fluorescence activated cell sorting (FACS).

(1) Forward vs height scatter histogram to identify single cells. (2) Forward vs side scatter histogram to identify intact cells. (3) Single intact fluorescent cells. (4) Number of fluorescent cells. (5) Selected region for sorting. (6) Final percentage of each event. HUVECs and MSCs were used as controls. 89.5 % of RFP-HUVECs and 26.1 % of GFP-MSCs were successfully isolated and sorted. These data were taken from Jekaterina Maksimcuka's thesis (2019) [363].

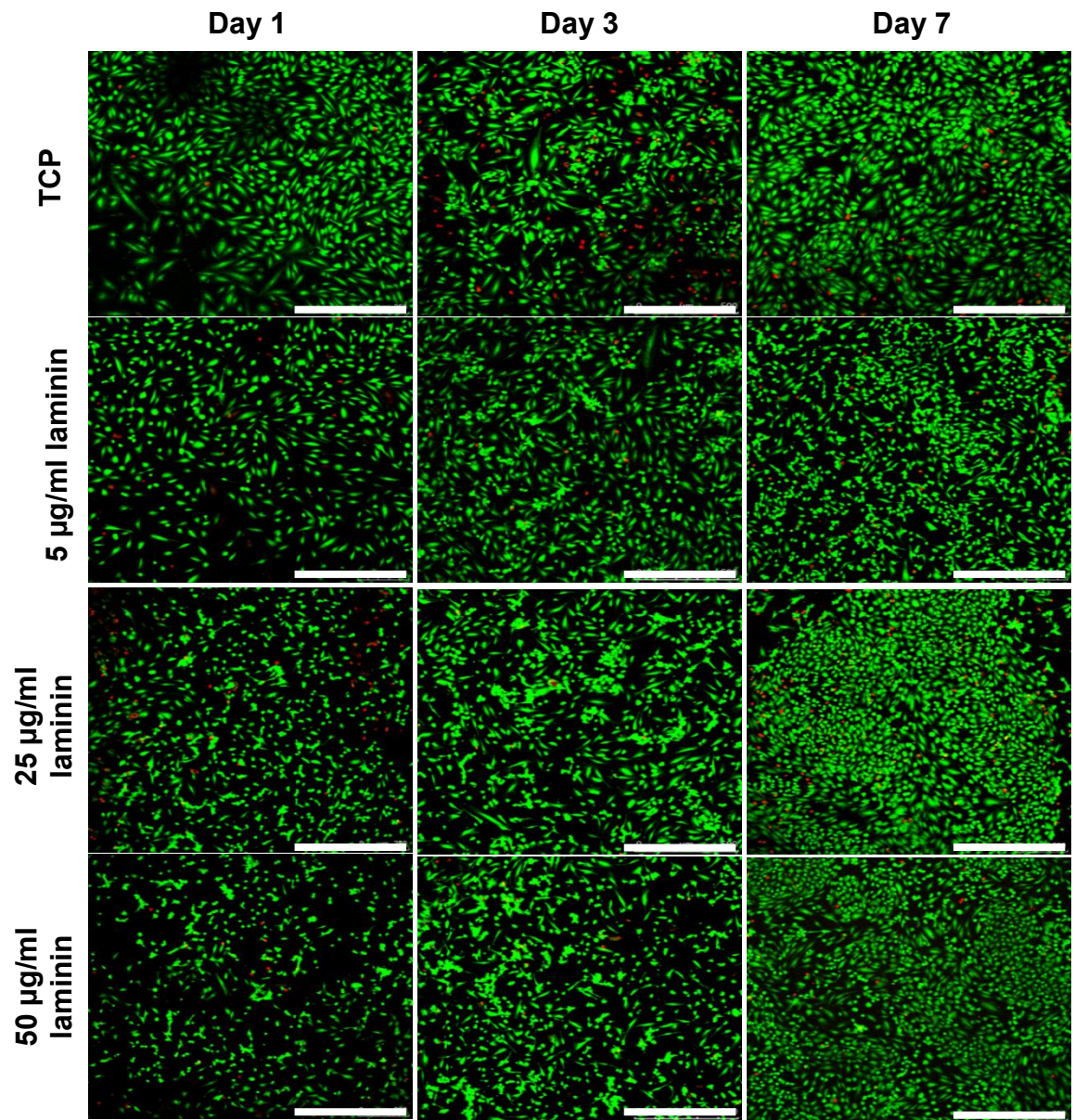


**Appendix 9. Tri-lineage differentiation of MSCs and GFP-MSCs.** (A) Chondrogenic differentiation. Blue = positive staining. (B) Adipogenic differentiation. Red = positive staining. (C) Osteogenic differentiation. Red = positive staining. N = 3. These data were taken from Jekaterina Maksimcuka's thesis (2019) [363].

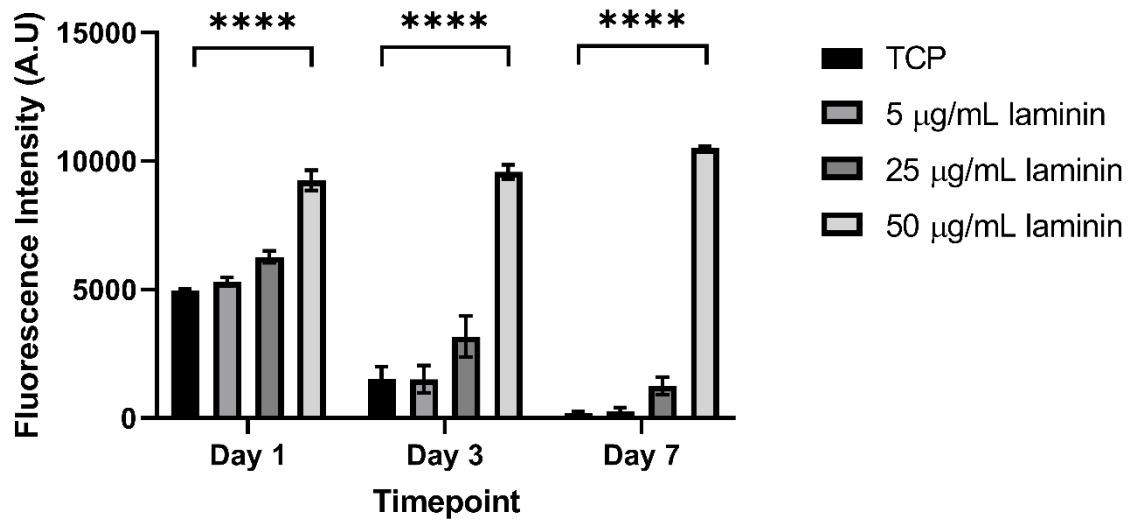


**Appendix 10. RFP-HUVECs cultured on top of Matrigel in the presence of DMEM.**  
Cells were incubated for 18 hours before fixation. Red = HUVECs.

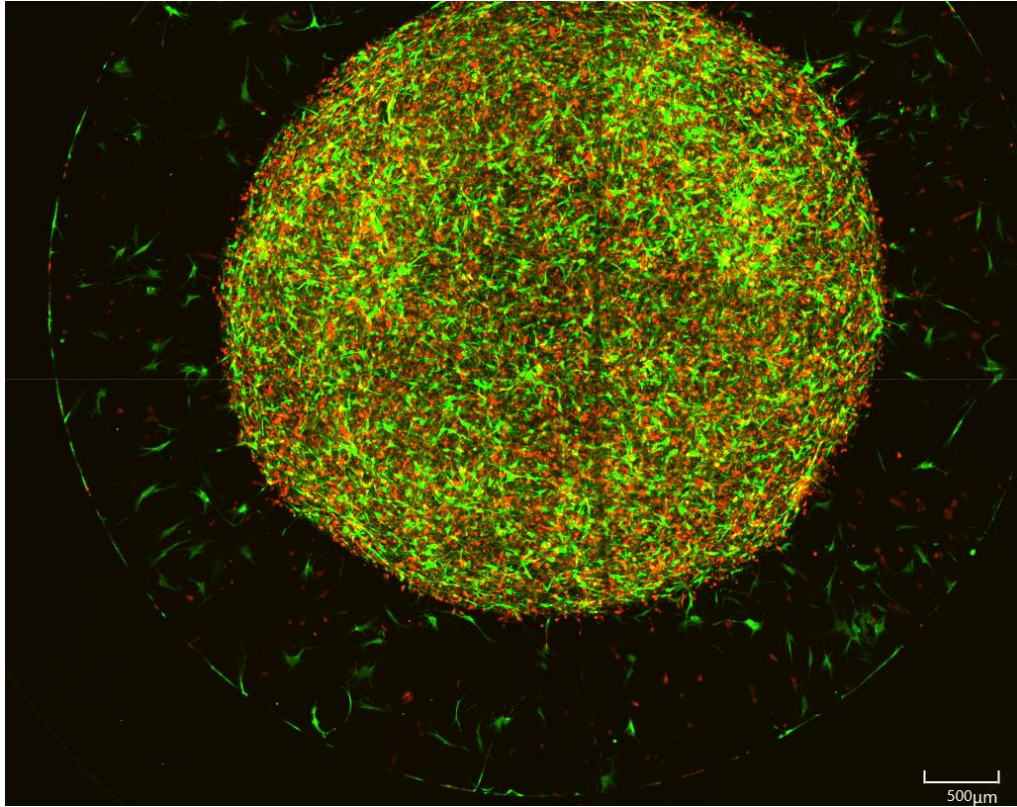




**Appendix 11. LIVE/DEAD staining of HUVECs seeded on TCP ± 5, 25 and 50 µg/mL laminin over 7 days. Green = live cells. Red = dead cells. Scale bar = 500 µm. N = 6.**



**Appendix 12. Metabolic activity of HUVECs seeded on laminin-coated TCP over 7 days.** Data are mean  $\pm$  S.D. \*\*\*\* =  $p < 0.0001$  using two-way ANOVA and post-hoc Tukey's test. N = 6.



**Appendix 13. Contraction of collagen I by HUVECs and MSCs.** RFP-HUVECs and GFP-MSCs were cultured in collagen I + 90 μg/mL fibronectin after 1 day in culture using a density of  $1 \times 10^6$  cells/mL (4:1 HUVEC:MSC ratio) . Red = RFP-HUVECs. Green = GFP-MSCs.